Homogenization and Characterization of Additive Manufactured Dielectric Crystals for High-Frequency Electromagnetic Applications

Hehenberger, S.P.

DOI
10.4233/uuid:c854c11b-331d-4d9a-accb-18aee281bf25

Publication date
2025

Document Version
Final published version

Citation (APA)
Hehenberger, S. P. (2025). *Homogenization and Characterization of Additive Manufactured Dielectric Crystals for High-Frequency Electromagnetic Applications*. [Dissertation (TU Delft), Delft University of Technology]. https://doi.org/10.4233/uuid:c854c11b-331d-4d9a-accb-18aee281bf25

Homogenization and Characterization of Additive Manufactured Dielectric Crystals for High-Frequency Electromagnetic Applications

Simon Philipp Hehenberger

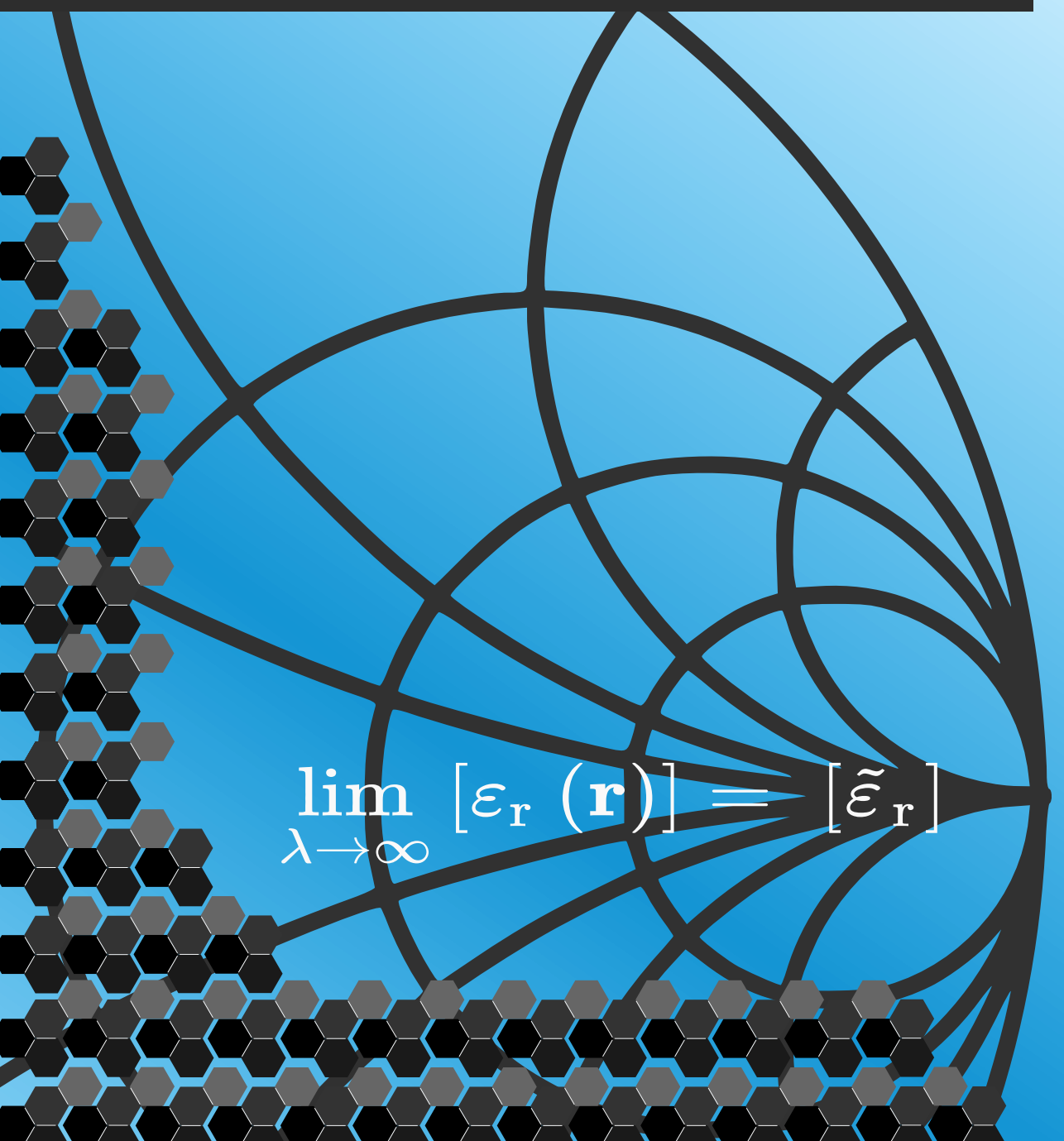

Homogenization and Characterization of Additive Manufactured Dielectric Crystals for High-Frequency Electromagnetic Applications

Homogenization and Characterization of Additive Manufactured Dielectric Crystals for High-Frequency Electromagnetic Applications

Dissertation

for the purpose of obtaining the degree of doctor
at Delft University of Technology
by the authority of the Rector Magnificus, Prof. dr. ir. T.H.J.J. van der Hagen,
chair of the Board for Doctorates
to be defended publicly on
Monday 15th September 2025 at 15:00 o'clock

by

Simon Philipp HEHENBERGER

Master of Science in Electronics and Information Technology,
Johannes Kepler University, Austria
born in Rohrbach, Austria

This dissertation has been approved by the promotors.

Composition of the doctoral committee:

Rector Magnificus,	Chairperson
Prof. dr. A. G. Yarovoy,	Delft University of Technology, promotor
Dr. Y. Aslan,	Delft University of Technology, copromotor
Dr. S. Caizzone,	German Aerospace Center, external advisor
Independent members:	
Prof. dr. ir. E. C. Slob,	Delft University of Technology
Prof. dr. Leo C. N. Vreede,	Delft University of Technology
Prof. dr. ir. A. B. Smolders,	Eindhoven University of Technology
Assoc. prof. M. García-Vigueras,	University of Rennes, France
Reserve member:	
Dr. C. M. F. Viellard-Boutry,	Delft University of Technology

Keywords: Additive Manufacturing, Periodic Dielectrics, Dielectric Crystal, Homogenization, Characterization, Effective Permittivity Tensor, Material Synthesis, Antenna, Filter, Bandgap

Printed by: Ipskamp Printing, Enschede, The Netherlands.

Front & Back: Design by Simon Philipp Hehenberger.

ISBN / EAN: 978-97-6473-908-4

An electronic version of this dissertation is available at
`http://repository.tudelft.nl/`.

Author e-mail: simon.hehenberger@dlr.de

To curiosity and learning, to growth and achievement,
to my younger self who dared to start,
and my present self who persevered.

Contents

Summary

Today, state-of-the-art device manufacturing for high-frequency (HF) electromagnetic (EM) applications is primarily dominated by subtractive techniques, including milling, laser cutting, electric discharge machining, and chemical etching, among others. While these methods are well established and enable remarkable accuracy, they are fundamentally constrained in terms of the geometric complexity they can achieve. The growing demand for more compact, efficient, and high-bandwidth EM devices challenges these limitations. Consequently, there has been a surge in alternative manufacturing techniques that leverage three-dimensional space to unlock additional design freedoms. The present work explores the unique capabilities of extrusion-based additive manufacturing (AM) to realize complex periodic dielectric structures for modern high-frequency EM applications. Specifically, this thesis investigates the homogenization, characterization, and practical implementation of periodic dielectric structures—also referred to as dielectric crystals—for advanced EM applications at microwave and millimeter-wave frequencies.

The thesis opens with a comprehensive review of AM applications in HF electromagnetics, highlighting significant potential while also identifying critical gaps in the current state of the art. These gaps guide the original contributions of the presented research, summarized below.

First, a comprehensive overview and comparison of homogenization and experimental characterization techniques for evaluating dielectric material properties is provided. While literature offers treatments on numerous analytical, numerical, and experimental methods, there is a lack of a systematic comparison tailored specifically to AM periodic dielectric structures. This thesis bridges that gap by rigorously comparing selected homogenization methods against experimental characterization results. It provides an analysis of the advantages and limitations of each approach and identifies their suitability for analysing AM periodic dielectrics.

Second, the impact of additive fabrication on the anisotropy of dielectric material properties is studied. The phenomenon of mechanical anisotropy resulting from the layer-by-layer additive fabrication approach is well-documented in literature, while its implications for dielectric properties remain unexplored. The presented research addresses this critical gap by thoroughly investigating the effective permittivity tensor. For this purpose, an analytical model is presented and its predictions validated through numerical simulations and experimental characterization using various materials and printing parameters. The results confirm significant anisotropy with negative birefringence, aligning well with theoretical predictions.

Third, although previous studies have utilized volumetric infill variations to influence the effective dielectric properties of periodic structures, the fundamental connection between crystallographic theory and dielectric behavior has remained largely unexplored. This thesis systematically investigates how lattice symmetries affect the effective permittivity tensor. A detailed parametric study of selected Bravais lattices and crystal centerings

is conducted, demonstrating precise control over dielectric anisotropy. These findings are confirmed experimentally through careful characterization of several lattice structures exhibiting distinct uniaxial and biaxial anisotropic properties.

Fourth, spatially modulated dielectric structures have mostly been employed in graded-index (GRIN) lenses for long-wavelength applications. This work expands significantly beyond this scope, exploring new applications in both the long- and short-wavelength operating regimes. For long-wavelength scenarios, cylindrical heterogeneous dielectric resonator antennas (DRAs) with radially and vertically varying permittivity profiles are investigated. Experimental results demonstrate that spatial modulation enhances both the impedance and axial ratio bandwidth compared to homogeneous DRAs. Furthermore, heterogeneous dielectric slabs within rectangular waveguides are explored, demonstrating practical control over transmission and reflection characteristics, exemplified through the realization of a third-order Chebyshev bandpass filter. Regarding short-wavelength applications, this research explores 3D periodic dielectric bandgap materials. A thorough numerical and experimental verification of the bandgap properties of woodpile structures is conducted, culminating in a novel dielectric rod antenna that significantly suppresses third harmonic radiation through combined long- and short-wavelength concepts. Collectively, these examples demonstrate the vast potential for innovative device performance enabled by spatially modulated periodic dielectric structures.

Fifth, integrating conductive and dielectric materials in a single AM process is highly advantageous yet underutilized, primarily due to the prohibitive cost of specialized equipment. Addressing this limitation, the thesis introduces an accessible, open-source inspired approach to hybrid AM. A custom-built AM system incorporating a micro-dispensing head for conductive ink deposition is successfully demonstrated through the fabrication of a fully additive-manufactured dielectric resonator phased array antenna operating at 20GHz. This practical demonstration confirms the viability and effectiveness of hybrid AM technology for advanced antenna applications.

In summary, this research underscores the transformative potential and enables new opportunities of additive manufacturing in EM device engineering. While recognizing the ongoing challenges related to material and equipment limitations, the thesis illustrates that these can be effectively managed through careful selection of homogenization, characterization, and design methodologies. Promising future directions identified include further exploration of hybrid AM for high-frequency EM applications, innovations in communications, radar, and sensing technologies, and continued advancements in integrated material processes. Ultimately, this work significantly advances additive manufacturing for electromagnetic applications, laying a strong foundation for future innovations in communication, radar, and sensing technologies.

Samenvatting

Vandaag de dag wordt de productie van de nieuwste apparaten voor hoogfrequente (HF) elektromagnetische (EM) toepassingen vooral gedaan met subtractieve technieken, zoals frezen, lasersnijden, vonkverspaning en chemisch etsen. Hoewel deze methoden goed werken en supernauwkeurig zijn, zijn ze nogal beperkt in de geometrische complexiteit die ze kunnen bereiken. De groeiende vraag naar compactere, efficiëntere en breedbandige EM-apparaten daagt deze beperkingen uit. Daarom zijn er steeds meer alternatieve productietechnieken die gebruikmaken van driedimensionale ruimte om extra ontwerpvrijheid te creëren. Dit onderzoek verkent de unieke mogelijkheden van extrusie gebaseerde additieve productie (AM) voor het realiseren van complexe periodieke diëlektrische structuren voor moderne hoogfrequente EM-toepassingen. Deze scriptie onderzoekt specifiek de homogenisatie, karakterisering en praktische implementatie van periodieke diëlektrische structuren – ook wel diëlektrische kristallen genoemd – voor geavanceerde EM-toepassingen bij microgolf- en millimetergolf frequenties.
De scriptie begint met een uitgebreid overzicht van AM-toepassingen in HF-elektromagnetisme, benadrukt het aanzienlijke potentieel en tegelijkertijd kritieke hiaten in de huidige stand van de techniek worden geïdentificeerd. Deze hiaten vormen de leidraad voor de originele bijdragen van het gepresenteerde onderzoek, die hieronder wordt samengevat.

Eerst wordt een uitgebreid overzicht en vergelijking gegeven van homogenisatie technieken en experimentele karakteriserings technieken voor het evalueren van diëlektrische materiaaleigenschappen. Hoewel de literatuur tal van analytische, numerieke en experimentele methoden behandelt, ontbreekt een systematische vergelijking die specifiek is toegesneden op AM-periodieke diëlektrische structuren. Dit proefschrift vult die leemte door geselecteerde homogenisatie methoden uitgebreid te vergelijken met experimentele karakteriseringsresultaten. Het biedt een analyse van de voordelen en beperkingen van elke benadering en identificeert hun geschiktheid voor het analyseren van AM-periodieke diëlektrica.

Ten tweede wordt de impact van additieve fabricage op de anisotropie van diëlektrische materiaaleigenschappen bestudeerd. Het fenomeen van mechanische anisotropie als gevolg van de additieve fabricagemethode waarbij laag voor laag wordt opgebouwd, is goed gedocumenteerd in de literatuur, maar de implicaties ervan voor diëlektrische eigenschappen zijn nog niet onderzocht. Dit onderzoek vult deze kritieke leemte op door de effectieve permittiviteitstensor grondig te onderzoeken. Hiervoor wordt een analytisch model gepresenteerd en worden de voorspellingen ervan gevalideerd door middel van numerieke simulaties en experimentele karakterisering met behulp van verschillende materialen en printparameters. De resultaten bevestigen een significante anisotropie met negatieve dubbele breking, wat goed overeenkomt met de theoretische voorspellingen.

Ten derde hebben eerdere studies weliswaar gebruik gemaakt van volumetrische invulvariaties om de effectieve diëlektrische eigenschappen van periodieke structuren te

beïnvloeden, maar is het fundamentele verband tussen de kristallografische theorie en het diëlektrische gedrag grotendeels ononderzocht gebleven. Dit proefschrift onderzoekt systematisch hoe roostersymmetrieën de effectieve permittiviteitstensor beïnvloeden. Er wordt een gedetailleerde parametrische studie uitgevoerd van geselecteerde Bravais-roosters en kristal centreringen, waaruit een nauwkeurige controle over diëlektrische anisotropie blijkt. Deze bevindingen worden experimenteel bevestigd door zorgvuldige karakterisering van verschillende roosterstructuren met duidelijke uniaxiale en biaxiale anisotrope eigenschappen.

Ten vierde zijn ruimtelijk gemoduleerde diëlektrische structuren voornamelijk gebruikt in gradiëntindexlenzen (GRIN) voor toepassingen met lange golflengten. Dit werk gaat veel verder dan dit toepassingsgebied en onderzoekt nieuwe toepassingen in zowel het lange- als het korte-golfgebied. Voor lange golflengten worden cilindrische heterogene diëlektrische resonatorantennes (DRA's) met radiaal en verticaal variërende permittiviteits profielen onderzocht. Experimentele resultaten laten zien dat ruimtelijke modulatie zowel de impedantie als de axiale verhouding bandbreedte verbetert in vergelijking met homogene DRA's. Verder worden heterogene diëlektrische platen in rechthoekige golfgeleiders onderzocht, waarmee praktische controle over transmissie- en reflectie-eigenschappen wordt aangetoond, bijvoorbeeld door de realisatie van een derde-orde Chebyshev-banddoorlaatfilter. Wat betreft korte golflengten, dit onderzoek verkent 3D-periodieke diëlektrische bandkloofmaterialen. Er wordt een grondige numerieke en experimentele verificatie uitgevoerd van de bandkloof-eigenschappen van woodpile-structuren, wat resulteert in een nieuwe diëlektrische staafantenne die derde harmonische straling aanzienlijk onderdrukt door een combinatie van lange en korte golflengteconcepten. Samen laten deze voorbeelden het enorme potentieel zien voor innovatieve apparaat prestaties die mogelijk worden gemaakt door ruimtelijk gemoduleerde periodieke diëlektrische structuren.

Ten vijfde is het integreren van geleidende en diëlektrische materialen in één AM-proces super handig, maar wordt het nog niet veel gebruikt, vooral omdat de speciale apparatuur erg duur is. Om dit op te lossen, laat het proefschrift een toegankelijke, open-source-geïnspireerde aanpak voor hybride AM zien. Een op maat gemaakt AM-systeem met een micro-doseerkop voor het aanbrengen van geleidende inkt is met succes gedemonstreerd door de fabricage van een volledig additief vervaardigde diëlektrische resonator-fase-array-antenne die werkt op 20 GHz. Deze praktische demonstratie bevestigt de haalbaarheid en effectiviteit van hybride AM-technologie voor geavanceerde antennetoepassingen.

Samenvattend onderstreept dit onderzoek het transformatieve potentieel en biedt het nieuwe mogelijkheden voor hybride additieve productie in de engineering van EM-apparatuur. Hoewel de voortdurende uitdagingen in verband met materiaal- en apparatuur beperkingen worden erkend, laat het proefschrift zien dat deze effectief kunnen worden beheerd door een zorgvuldige selectie van homogenisatie-, karakteriserings- en ontwerpmethodologieën. Veelbelovende toekomstige richtingen zijn aangegeven, waaronder verder onderzoek naar hybride AM voor hoogfrequente EM-toepassingen, innovaties in communicatie-, radar- en sensortechnologieën en verdere verbeteringen in geïntegreerde materiaalprocessen. Uiteindelijk betekent dit werk een belangrijke stap voorwaarts voor additieve fabricage voor elektromagnetische toepassingen en legt het een stevige basis voor toekomstige innovaties in communicatie-, radar- en sensortechnologieën.

Preface

The beauty of high-frequency electromagnetic systems lies in their ability to connect people, reveal hidden structures and material properties through radar and sensing technologies, and in their applications for medical and energy transmission. These systems profoundly shape nearly every aspect of our modern life and captured my curiosity already at the beginning of my tertiary education. Now, approaching the end thereof, my understanding of this important technological field has not only developed and matured but grown sufficiently to contribute in pushing their boundaries and adapt them to new applications. I am fortunate to have been presented with numerous amazing opportunities to learn, publish, travel, and network with a global community within the framework of my doctoral education.

The work presented here was carried out over four years while I was enrolled as an external PhD student at TU Delft in the Netherlands and employed at the Institute of Communication and Navigation of the German Aerospace Center. The purpose of the project was to explore the potential of low-cost, extrusion-based additive manufacturing for implementing novel design concepts in high-frequency electromagnetic devices.

Author Simon Philipp Hehenberger
Munich, July 2025

Acknowledgements

The successful conclusion of this work required dedication, discipline, and significant sacrifices in terms of personal time, sanity, hobbies, and relationships. Such sacrifices strike a remarking resemblance with the complaints I hear from young parents, and indeed, in my mind I often referred to my PhD project as my baby, which might seem preposterous to actual parents. Nevertheless, I nursed my ideas despite of them draining my energy and disrupting my sleep only for them to often turn out just as valuable as the contents of a heavy diaper. Despite the challenges and sacrifices, I love the work I did and continue doing and am proud of the presented ideas and results, proud that they are my original work, proud that I accepted and completed this academic challenge. However, I also realize that I did not raise this proverbial 'baby' on my own. I came across this old African proverb, "*It takes a village to raise a child*", which applies quite well to the circumstances of my (and probably any) PhD research project. And here I would like to seize the opportunity to express my sincere gratitude to the numerous people who have contributed and supported me both directly and indirectly.

Foremost, to my supervisory team. To my promoter Prof. Alexander Yarovoy, in whom I not only found an excellent academic advisor, but also a generally pleasant and trusted mentor. Thank you for encouraging my creativity, for your support in getting me enrolled at TU Delft, for your constructive criticism, and most importantly for your empathy and compassion. To my daily supervisor, Dr. Stefano Caizzone, thank you for your tolerance towards my chaotic and deadline-driven work style, for the trust you placed in me by letting me explore my ideas freely, and for the support you provided along the way. Additionally, I am thankful to the independent members of the committee for providing their expert opinions about the presented content. Your feedback and suggestions helped to improve the quality of the work. Additionally, I would like to acknowledge the efforts of Fred Boiten who generously contributed his personal time in translating the summary of this thesis into Dutch.

I would also like to thank former and current colleagues at the German Aerospace Center, including Federico, Ernest, Veenu, Aparna, Wahid, and Korbinian, for providing valuable insights, encouragement, and an enjoyable atmosphere to work in. Furthermore, I am indebted to Stefan Thurner and Prof. Dr. Thomas Jagdhuber of the German Aerospace Center's Institute for Microwaves and Radar for the experimental analysis of several specimens discussed in this work. Their insights into the intricacies of electromagnetic material characterization contributed significantly to the high quality of the results presented in the fundamental chapters of this work. Additionally, I would like to express my gratitude to the colleagues of the Microwave Sensing, Signals and Systems group at TU Delft, who, although I visited only once a year, always made me feel welcome and part of the group.

I am deeply grateful to my mother, Karin, for her unconditional love and support of my sister, Miriam, and me. You have given yourself unreservedly, devoting your life so that we could become educated, honest, and lovable adults. Each of my achievements in life is as much yours as it is mine! Similar to my adoptive father, Thomas, who taught me the value of hard work, taking responsibility, and a do-it-yourself attitude, which was invaluable for the successful completion of this thesis. The gratitude extends beyond my core family to my aunts, Regina and Elisabeth, my cousin Jan, and my friends, Marius, Jakob, Paul and Gierli. All of whom never failed to make me feel appreciated and provided open ears for my complaints about my self-inflicted suffering. The same is true for the most recent extension of loving people in my live, Manfred and Siegrun, who welcomed me into their home and family with open arms.

Last but not least I need to acknowledge a debt of gratitude to my lovely partner, Katja. We made it! Thank you for uprooting your life for me. Thank you for being my anchor to the real world. Thank you for every back rub, late-night snack, word of encouragement, and silly nonsense conversation (muuh). I love you and am happy to share my life with you.

1

Introduction

I do not think that the radio waves I have discovered will have any practical application. – Heinrich Hertz

1

1.1. Background

Since Heinrich Hertz experimentally verified the existence of electromagnetic (EM) waves, as predicted by James Clerk Maxwell's equations of electromagnetism, the field of electromagnetics has evolved dramatically. Applications of high-frequency EM waves, including communications, radar, sensing, and satellite navigation, have profoundly shaped nearly every aspect of modern life.

Evolution of Electromagnetic Devices and their Manufacturing

The earliest devices engineered to interact with EM waves were simple constructs made from wires and rods, such as the dipole and monopole antennas, used primarily for basic radio communication [1]. As the understanding of electromagnetic waves advanced, these devices evolved into various shapes and configurations to improve performance. This led to the development of loop antennas, Yagi-Uda arrays, and parabolic reflectors, each offering enhancements in directionality, gain, and bandwidth. The Yagi-Uda antenna, for instance, became a staple for television reception due to its high gain and directional properties [2]. The mid-20th century ushered in significant advancements driven by growing needs in broadcasting, radar systems, and early satellite communications. The introduction of horn antennas and the refinement of parabolic dishes allowed for better signal focusing and reception over longer distances [3]. Antenna arrays became more sophisticated, incorporating multiple elements to form phased arrays capable of electronic beam steering without physical movement [4].

The advent of printed circuit board (PCB) technology marked a pivotal point in antenna manufacturing. Techniques like photolithography enabled the mass production of planar antennas—such as microstrip and patch antennas—which could be easily integrated into electronic circuits [5]. Microstrip antennas offer the benefits of low profile, lightweight, and ease of fabrication, making them ideal for aerospace and satellite applications as well. Advancements in materials science further propelled antenna technology. The use of dielectric substrates with low-loss tangents improved efficiency, while the exploration of new conductive materials like graphene opened possibilities for antennas operating at terahertz frequencies [6]. Metamaterials emerged as a revolutionary concept, allowing engineers to design antennas with properties not found in natural materials, such as negative refractive index, leading to superlensing and cloaking applications [7].

Today, state-of-the-art device manufacturing for high-frequency applications is dominated by subtractive techniques such as milling, photolithography, and etching. While these methods enable remarkable accuracy, they are fundamentally constrained in terms of the geometric complexity they can achieve. The growing demand for more compact, efficient, and high-bandwidth EM devices challenges these limitations. Consequently, there has been a surge in exploring alternative manufacturing techniques that leverage three-dimensional space to unlock additional design freedoms, helping to overcome these limitations.

The Rise of Additive Manufacturing

Additive manufacturing (AM), a concept first imagined in science fiction during the mid-20th century, describes various processes in which a three-dimensional (3D) object is created via material deposition, typically layer by layer. This concept first became a reality in the 1980s when Charles Hull developed stereolithography (SLA), the first 3D printing tech-

nology. Over the years, AM matured, with methods like fused deposition modeling (FDM) and selective laser sintering (SLS), transforming it into a technology for rapid prototyping and the production of complex, customized parts across various industries.

AM has rapidly advanced in recent years, with significant developments across various domains. Material innovations have expanded the range of printable substances to include high-performance polymers, metals, ceramics, and composites. Improvements in resolution, printing speed, and multi-material capabilities have made AM viable for producing complex parts in low to mid-volume quantities. Hybrid additive manufacturing, integrating AM technologies with subtractive techniques, has further enhanced the precision and complexity of manufactured parts. Topology optimization and generative design have enabled the creation of lightweight and efficient structures. AM has revolutionized custom medical implants and prosthetics in healthcare, while bioprinting advances hold promise for future organ printing. Improved quality control, sustainability efforts, and integration of artificial intelligence (AI) for process optimization have made AM more efficient and reliable. These developments, combined with cost reductions and greater accessibility, have established AM as a key technology in aerospace, medical, automotive, electronics, and construction industries.

1.2. Motivation

This work is driven by several key factors:

1. **Limitations of Traditional Planar Design and Subtractive Manufacturing**
   A primary motivation for this research is to move beyond the constraints of traditional planar designs and subtractive manufacturing methods. The potential of AM allows for the creation of novel electromagnetic devices by utilizing three-dimensional space. This approach can be exploited to meet the ambitious efficiency and bandwidth requirements of modern communication, radar, sensing, and navigation systems.

2. **Engineering Dielectric Material Properties**
   One of the key visions of this research is to establish dielectric crystals as a design concept for enabling novel microwave components through additive manufacturing. The ability to control and manipulate the dielectric properties of materials—such as their homogeneity and isotropy—opens up new avenues for device design and optimization. By focusing on dielectric materials, this research aims to minimize or eliminate the need for metallic components, which often introduce complexity and cost.

3. **Hybrid Manufacturing Techniques**
   In addition to dielectric materials, there is growing interest in hybrid manufacturing techniques that combine dielectric and conductive materials. This approach has the potential to create fully integrated, high-performance electromagnetic devices that are both compact and cost-effective. Furthermore, hybrid techniques offer the opportunity to blend traditional design methods with modern manufacturing, combining the best of both worlds.

4. **COVID-19, Supply Chain Security, and IP Protection**

During the conception of this work, the COVID-19 pandemic was in full swing. Beyond its severe public health implications, the global economy experienced heavily strained supply chains due to the shutdown of factories and trade infrastructure. This posed a significant problem for many businesses and research facilities as lead times and prices for components and materials surged unexpectedly. A major motivation for this research was to develop in-house manufacturing and rapid prototyping capabilities to advance the work as independently as possible. Although pandemic-related disruptions have since been mitigated, supply chain security remains a critical issue today.

1.3. Objectives and Scope of the Thesis

Objectives

The primary objective of this thesis is to explore and expand the potential of extrusion-based hybrid AM for the design and fabrication of advanced EM devices. In this context, hybrid is defined as providing multi-material capabilities, combining multiple different dielectric and conductive materials in the same process. Specifically, the focus is on the development and application of periodic dielectric structures, also referred to dielectric crystals in the microwave and millimeter-wave frequency ranges. A review regarding research and state of the art about relevant topics is provided in Chapter 2. Based on this review, the following objectives for this work are identified:

1. **Understand the Challenges of AM in Terms of Material Properties:**
   To develop a systematic approach for modeling, simulating, and experimentally verifying the dielectric material properties in extrusion-based AM parts. This includes understanding the effect of the inherent manufacturing impurities and imperfections introduced by the layer-by-layer nature and the specific print settings of extrusion-based AM processes.

2. **Material Parameter Engineering via Periodic Structures:**
   To design, simulate, and fabricate dielectric crystals - 3D periodic dielectric structures - that can be engineered to exhibit specific anisotropic or inhomogeneous properties. This objective involves leveraging the unique capabilities of AM to create intricate 3D periodic lattices.

3. **Application of Dielectric Crystals in Electromagnetic Devices:**
   To apply the engineered dielectric crystals in practical electromagnetic devices, such as antennas, lenses and filters, demonstrating their effectiveness in real-world scenarios. This includes optimizing device performance through the control of material properties and validating the designs through experimental measurements.

4. **Development of Hybrid Printing Techniques:**
   To explore the integration of conductive inks with dielectric materials, enabling the creation of fully functional, compact, and high-performance electromagnetic devices, such as antennas and filters, that utilize both dielectric and conductive properties.

Scope

Addressing the objectives mentioned above requires a broad scope of topics, which are briefly summarized as:

1. **Additive Manufacturing Technologies:**
   The research is centered around extrusion-based additive manufacturing techniques, particularly fused deposition modeling (FDM), also referred to as fused filament fabrication (FFF). The main focus is on the use of polymer-based materials that can be printed with these technologies to create complex dielectric structures. Additionally the potential of hybrid methods, as in combining different dielectrics as well as conductive materials is addressed in this work.

2. **Dielectric Materials and Structures:**
   The thesis investigates dielectric materials and their properties, with an emphasis on engineering the effective permittivity tensor. The scope includes both theoretical modeling and practical fabrication of dielectric crystals, as well as the analysis of their anisotropic and inhomogeneous characteristics.

3. **Simulation and Experimental Verification:**
   A significant portion of the work involves the use of simulation techniques, including parallel plate capacitor models, eigenmode analysis, and Floquet port scattering methods, to predict the behavior of dielectric crystals. These simulations are complemented by experimental verification using a variety of measurement methods based on resonance and traveling wave techniques.

4. **Applications in Electromagnetic Devices:**
   The thesis explores the application of the developed dielectric crystals and hybrid printing techniques in practical electromagnetic devices. This includes designing and fabricating antennas, waveguide filters, and bandgap structures that operate in the microwave and millimeter-wave frequency ranges.

5. **Interdisciplinary Approach:**
   The research is inherently interdisciplinary, bridging the fields of materials science, high-frequency electromagnetic applications, and manufacturing technology. The scope includes both the fundamental study of material properties and the practical application of these findings in the design and fabrication of electromagnetic devices.

1.4. Structure of this Work

After the previous description of the background, motivation, objectives, and scope, the remaining thesis is structured as follows:

State of the Art and Methodology

- *Chapter 2,* provides a review of literature and the state of the art about topics relevant to this thesis. A brief overview of relevant literature for AM in general is provided, but the chapter focuses on the applications of AM for high-frequency electromagnetic applications grouped into metal, dielectric, and hybrid processes. Furthermore, a review of literature relevant to engineered materials, as well as material simulation and

characterization techniques, is provided. The review concludes with the identification of gaps in the literature and the formulation of respective research questions.

- *Chapter 3,* introduces the key theoretical concepts necessary to appreciate the research results by discussing the basic physics of dielectric material properties and how they are related to fundamental concepts in crystallography. Furthermore, Chapter 3 presents the methodology applied throughout the thesis. It provides an overview of the simulation methods and techniques utilized for experimental verification of manufactured prototypes. Additionally, the custom-built manufacturing setup and corresponding errors and uncertainties are explained.

Results

The research results are split into two parts. The first part contains the core research results concerning dielectric crystal engineering, synthesis, and characterization. The second part deals with the application scenarios of said dielectric crystals and the utilization of hybrid AM techniques to create fully 3D-printed antenna systems. Each Chapter of the research results presents an individual topic that was also published or is currently considered for publication.

Core Research Results - Effective Permittivity Tensor and Anisotropy

- *Chapter 4,* provides an in-depth investigation of the capabilities and tradeoffs between different material parameter simulation and experimental characterization techniques. It especially focuses on the shortcomings of effective media theories in predicting the dispersion characteristics of dielectric crystals. Its conclusions have been published in the IEEE Transaction of Microwave Theory and Techniques.

- *Chapter 5,* explains that extrusion-based additive manufacturing introduces an inherent uniaxial anisotropy into the dielectric material properties of printed parts. It provides a model based on an equivalent parallel plate capacitor to predict the effective permittivity tensor of printed parts as a function of the extrusion parameters and the size of air inclusions due to the imperfections of the print process. Predictions from this model are compared against experimental results and agree reasonably well. The conclusions have been published in the Elsevier Material Research Bulletin.

- *Chapter 6,* discusses the possibility of engineering the permittivity tensor via exploiting different crystal symmetries and inclusions. The approach is demonstrated by engineering dielectric crystal samples with uniaxial and biaxial anisotropic characteristics in different symmetries and in different centerings. A publication about theses results is currently prepared for submission in the IEEE Transactions of Microwave Theory and Techniques. Furthermore, an algorithm for the synthesis of arbitrary permittivity tensor values is introduced.

Application-Oriented Research Results

- *Chapter 7,* demonstrates the engineering of spatially modulated dielectric crystal lattices for several different applications. First, Dielectric Resonator Antennas (DRA) with heterogeneous resonating bodies for GNSS applications are discussed, simulated, and experimentally verified. The results show that heterogeneous resonating

bodies can provide improved impedance- and axial ratio bandwidth in DRAs and have been published in the IEEE Open Journal of Antennas and Propagation. A second application example of spatially modulated dielectric crystals is presented via a dielectric filter for a standard WR90 metallic rectangular waveguide. Experimental results verify the design but also show that the selection of crystal symmetry is important for this specific type of application. The study is currently considered for publication in the IEEE Transactions of Components, Packaging, and Manufacturing.

- *Chapter 8,* demonstrates the potential of short-wavelength dielectric crystals via the investigation, manufacturing, and experimental characterization of full 3D bandgaps. Additionally, an application example of a waveguide-fed dielectric rod antenna that incorporates 3rd harmonic suppression capabilities via a 3D bandgap is presented. This design exploits the fact that dielectric crystals act as effective materials at lower frequencies but can exhibit exotic properties at higher frequencies. The results of this work have been published in the IEEE Transactions of Antennas and Propagation.

- *Chapter 9,* deals with the potential of hybrid additive manufacturing to create fully 3D-printed antenna systems. This combined AM of different dielectrics and conductive ink is used to manufacture a dielectric resonator linear phased array antenna operating at K Band for satellite communication applications.

Conclusions

Detailed conclusions on the results are presented after each corresponding chapter. Additionally, Chapter 10. provides a summary of the core messages of this work, puts them in context with each other, and provides an overall conclusion to this thesis. Furthermore, an overview of the remaining open topics and possible future research directions are explored.

2

Review - Research and State of the Art

Facts are not science—as the dictionary is not literature. – Martin H. Fischer

2.1. Opening Remarks

AM offers the potential to revolutionize key industries today by changing how engineers design, produce, improve, and customize. In contrast to traditionally employed subtractive manufacturing methods, where selected regions are removed from a body of bulk material by milling or etching, additive manufacturing selectively deposits materials to create parts from 3D model data. The selective deposition of the material allows the creation of highly complex geometries that are impossible to manufacture with conventional subtractive techniques. The full potential and vision of what additive manufacturing might accomplish and how it will develop is still a topic of inspiring discussion [8]. Potential applications include but are not limited to

- **Aerospace**: Production of lightweight components with complex geometries. [9]
- **Medical and Dental**: Custom prosthetics, implants, and dental devices tailored to individual patients. [10], [11]
- **Automotive**: Rapid prototyping and production of specialized parts. [12]
- **Electronics**: Three-dimensional circuits allow for flexible and highly integrated designs. [13], [14]
- **Construction**: 3D printing components or or eveb entire buildings. [15]

2.1.1. Additive Manufacturing (AM) Process Technologies

In general, AM processes are classified into seven categories [16]:

- **Material extrusion** (polymers, metal-embedded polymers, metals, ceramics), where the material is selectively dispensed through a nozzle or orifice
- **Powder bed fusion** (polymers, metals, ceramics), where thermal energy selectively fuses regions of a powder bed
- **Directed energy deposition** (metals), where focused thermal energy fuses materials by melting them as they are being deposited
- **Material jetting** (polymers), where droplets of build material are selectively deposited
- **Binder jetting** (polymers, metals, ceramics), where liquid bonding agent is selectively deposited to join powder materials
- **Vat photopolymerization** (polymers), where liquid photopolymer in a vat is selectively cured by light-activated polymerization
- **Sheet lamination** (paper, polymers, metals), where sheets of material are bonded to form an object

Each of these seven processes has significant differences in their capabilities, e.g., accuracy, materials they can handle, build volume, required proficiency of operators, operating cost, etc., and [17] provides an excellent summary of their capabilities.

2.1.2. Research regarding AM

Currently, research is advancing AM in several fields. A huge drive is the combination of AM methods with Industry 4.0 to save time and cost while gaining flexibility [18] [19] [20] and shrinking supply chains. A major topic is the research of advanced methods and materials with applications in aerospace, biomedical, and electronics [21], [22]. Furthermore, the effect of the AM process and applicable post-processing methods on the effective material properties of the final part is an important field of research both in terms of predicting material properties through simulations to improve the manufacturing process and characterizing material properties of printed parts. Additionally, an important topic is the reduction of the environmental impact posed by AM technologies [23].
The research topics are all fascinating, but the work proposed here deals with the possibilities that AM offers for designing new electromagnetic devices for high-frequency applications.

2.1.3. AM in Electronics and Electromagnetics

The challenges and research activities regarding AM applied to electronics and electromagnetics (EM) are diverse, and a full literature review of all processes and their respective applications in the field of electronics and electromagnetics is out of scope here. It suffices to say that AM unlocks the potential of highly integrated devices like motors, sensors, circuits, batteries, etc., providing massive potential for future improvements in all respective areas [24] [25] [13]. In recent years, microwave community researchers have been investigating AM techniques' unique capabilities to create novel antenna and metamaterial structures [14] [24]. This work primarily concerns the homogenization, characterization, and application of dielectric structures with a secondary focus on combined dielectric and conductive techniques. For this purpose, a detailed review of techniques and applications is provided below.

In terms of commercialization, several companies are already trying to capitalize on AM's unique capabilities for EM applications. The currently prominent business model offers combined multi-material printing machines with a focus on electronic systems, each offering unique capabilities. Systems, such as nScrypt's 3Dn Series and Neotech AMT's 15X machine, combine several extrusion-based printheads, offering high-precision capabilities for printing complex multi-material parts with the capability of printing fine conductive traces and also providing the capability to utilize pick-and-place for embedding discrete components. Notable non-extrusion-based solutions include Nano Dimension's DragonFly LDM and ChemCubed's ElectroJet machines, which use inkjet technology to print high-resolution multi-layer electronic components. Furthermore, Optomec's Aerosol Jet Printers have been successfully used in NASA projects to produce space-grade materials. However, the initial investment for these machines, as well as the resources required, both monetarily and required technical expertise, for operating them, make these machines quite prohibitive. Nevertheless, as the field develops, its processes get more efficient, machines and materials cheaper, and designers become aware of the unique capabilities these initial roadblocks are likely to dissipate.

2.1.4. Scope of the Following Review

This work concerns itself primarily with the possibility provided by dielectric materials. Readers interested in full-metal AM techniques for the purposes of waveguide components,

horn antennas, and other metallic components are referred to the excellent review provided in [26]. Dielectric AM for high-frequency EM applications is primarily approached via two techniques: extrusion-based processes, commonly referred to as fused filament fabrication (FFF), and vat-photopolymerization, also known as stereolithography (SLA). While FFF exhibits inferior accuracy compared to SLA, FFF is the more accessible and versatile one with respect to the variety of different print materials as well as the possibility of combining different materials in the same print process. Furthermore, SLA printing requires extensive post-processing of prints in washing and thermal and ultra-violet (UV) curing. Despite that, the main appeal of SLA is its accuracy and smooth surface finish of SLA which makes it a popular candidate for post-print metallization via (electro-)chemical plating techniques, producing low-cost, lightweight, fully metalized parts. However, extrusion-based technology technology is preferred for this work due to its accessibility, material versatility, and capability to utilize multiple different materials in the same process.

A key area of research on this technology in the context of high-frequency EM is the development of periodic dielectric structures, which enable engineered dielectric responses through spatially varying permittivity distributions. The ability to precisely control the effective permittivity tensor of these structures opens pathways for designing components such as graded-index (GRIN) lenses, dielectric resonator antennas (DRAs), and electromagnetic bandgap materials. However, the accurate prediction of dielectric properties in additive manufactured structures and the respective implications in the design of devices remains a challenge due to inherent process-induced anisotropy and material inhomogeneities.

To address these challenges, the subsequent analysis will delve into the homogenization techniques employed to model and characterize the effective permittivity tensor of printed periodic structures. Additionally, different experimental characterization methods used to validate these models will be reviewed. Finally, the discussion will extend to the practical applications of periodic dielectric structures in high-frequency electromagnetic devices, with a secondary emphasis on hybrid AM approaches that integrate conductive and dielectric materials for enhanced performance.

2.2. Homogenization and Characterization of Dielectric Materials

The characterization of effective dielectric material properties, both from a predictive and experimental perspective, plays an important role in the contents of this thesis. Although it is out of scope to give a detailed review of all relevant dielectric characterization methods, it is valuable to give an overview of the general techniques and their most important trade-offs. The first Section about modeling discusses the most common effective media theories and the difficulty in applying them for modeling the effective permittivity tensor of non-resonant materials. The modeling of photonic crystals (PhC) is more cumbersome since the effective media approach is not valid anymore. Therefore, techniques for numerical simulation, focusing on the Plane Wave Expansion Method (PWEM) and Finite Element (FEM) simulations are discussed in Section two. The last Section deals with the experimental verification of the predicted material behavior. Again, different techniques have to be utilized to characterize non-resonant and wavelength structures.

2.2.1. Effective Media Theories

Modeling of dielectric composites where the particle size is much less than the wavelength is usually done by mixing rules and effective media theories. However, it has to be said that the application of one specific method relies heavily on a number of factors like particle size, shape, and distribution. Additionally, the frequency range, material phase, and expected loss of the composite further complicate selecting a suitable method.

Dielectric mixing rules are algebraic formulas with which the effective permittivity of the mixture can be calculated as a function of the constituent complex permittivities, their fractional volumes, and possibly some other parameters characterizing the properties of the mixture. This effective view of media is not exact because by using em waves of ever-higher frequencies, one can see more structural details of the media. Therefore, an effective quantity is usually only valid in the long-wavelength regime, and indeed, most mixing rules are derived using static approximations. It is not easy to predict an upper-frequency limit to the validity of effective media theorems as the exact response for an arbitrary heterogeneous composite is beyond analysis [27]. Often, the rule of thumb is that the size of inclusion in the mixture must not exceed a tenth of the wavelength in the effective media. However, works have shown [27] that this estimate is more on the conservative side for some composites. The first basic dielectric mixing rules can be traced back to big names like Clausius Mosotti, Maxwell, Lorentz, Rayleigh, and Garnett. Researchers incorporated shape and distribution effects into the models as soon as experimental data for effective media became available. Soon, it became clear that no one theory was capable of predicting effective dielectric properties significantly since different formulas predicted values different from others for the same material. This ambiguity forced the formulation of upper and lower bounds for the effective permittivity of a mixture in [28], [29]. Present-day research of effective media focuses on much more complex phenomena, like bi-anisotropy and non-linearity.

One specific effective media theory that is very popular in current research about additive manufactured structures in electromagnetic applications is the Maxwell-Garnett approximation (MGA) . Although it represents the idealized case of a two-component mixture with spherical inclusions, it is well suited for approximating the effective permittivity of graded infill materials commonly produced in additive manufacturing processes [30]. The basic MGA effective media theory lacks accuracy at higher volume fractions and fails to predict anisotropic behavior despite its success. Recently, an extension to the basic MGA approximation was introduced in [31], which is capable of predicting anisotropic behavior. No matter how good the effective material model is, it will always fail to predict broadband behavior like upper cut-off frequencies or bandgaps since these properties arise from the geometry of the material, which effective media theories try to omit from the model. Numerical techniques have to be used to predict cut-off frequencies and dispersion properties of dielectric crystals. An introduction to the numerical simulation of dielectric crystals is given in the next Section.

2.2.2. Numerical Techniques

A prevalent method of simulating the infinite lattice is to solve for the eigenmodes and corresponding eigenvalues via a Fourier space method called the plane wave expansion method (PWEM) [32]. This method expands the electric or magnetic fields for each field compo-

nent in terms of Fourier series components along the principal lattice vectors of the unit-cell. Similarly, the permittivity of the unit cell is also expanded through the Fourier series. For an exact model, the number of Fourier coefficients shall be infinite, but for practical modeling, this is reduced to some finite number satisfying some convergence limit [33]. The plane wave expansion technique has been successfully used to model photonic band structures of one-dimensional (1D), two-dimensional (2D), and three-dimensional (3D) photonic crystals. Since it can calculate the full band-structure of the dielectric crystal, it is capable of predicting effective material properties, cut-off frequencies, bandgaps, and dispersion characteristics.

Although the PWEM is robust and exceptionally well suited for the modal solution problem, it is not a tool to solve all problems concerning dielectric crystals. It is not well equipped to handle high index contrasts or metals in the unit cell. Furthermore, it is not capable of performing scattering analysis or transient phenomena. Generally, as soon as one is interested in the performance of a finite lattice, the PWEM is no longer the best choice for analysis. Problems like modeling the effects of a defect in the lattice or computing the scattering on an interface between free space and the crystal lattice are important for real-world applications. These problems are usually tackled with the finite element method (FEM) or finite-difference time-domain (FDTD) method, as has been done in [34] and [35]. A commonly used commercial approach employed in [36] is to use the Floquet-port simulation feature in the high-frequency-structure-simulator (HFSS) solver from Ansys. The Floquet-port method simulates the scattering of a single unit cell in a 2D periodic arrangement, thus allowing the simulation of scattering parameters with a variable number of stacked elements.

Of course, all the numerical techniques mentioned above can be utilized to model non-resonant and wavelength structures. They are capable of extracting the effective media properties of sub-wavelength structures at low frequencies, where the assumption of a linear dispersion relationship is locally true, as well as the complex dispersion characteristics of structures with periodicity in the wavelength regime.

2.2.3. Experimental Characterization

In general, RF and MW dielectric measurements prove to be very difficult. The field encompasses a large number of measurement techniques and material types. There are several trade-offs to consider when selecting a measurement approach and an excellent and extensive overview of the topic is given in [37] and [38]. Dielectric measurement methods and measurement cells broadly fall into two broad classes:

- Dielectric properties, measured as impedance or admittance. Collectively labeled as lumped impedance methods, which are primarily used at low frequencies up to 1GHz

- Dielectric properties, measured while the material in question is interacting with traveling and standing electromagnetic waves, collectively labeled as 'wave methods', which are usually employed above 1GHz.

The only overlap between these two classes is the resonator technique, which can be applied at both low and high frequencies. This work focuses on RF and MW frequencies; therefore, only resonator techniques and 'wave methods' will be further discussed.

Resonator methods

Resonance methods are generally used for measuring the loss of low-loss dielectrics. They work by placing a material in a resonator cavity and comparing the measurements of the empty and filled cavity. The material parameters are extracted based on the shift in resonance frequency and quality factor. Several different types of resonator material characterization setups have been introduced and discussed in the literature. Resonative methods are well suited to resolve small changes in the dielectric loss of a material. However, they deliver results only at one frequency point in contrast to broadband measurement techniques [37].

Traveling wave techniques

In the case of traveling wave techniques, one can further distinguish between guided and free space methods. Both methods rely on the measurement of scattering parameters but differ in the environment the waves are propagating. Traveling wave methods require high-quality calibration and are not as well equipped to measure materials with low-loss as resonative methods, but provide the main benefit of delivering broadband measurement results and straight-forward comparison to simulation data.

- *Guided waves* For guided wave methods, precisely machined material under test (MUT) samples are usually introduced to a guided wave structure like a coaxial cable or a rectangular waveguide. The benefit of this approach is the possibility of characterizing the MUT in terms of permittivity and permeability over a wide frequency band. Furthermore, it is possible to extract the anisotropic behavior of MUTs by inserting the sample in different orientations. These benefits are contrasted by the precise machining requirements of the sample since flat faces perpendicular to the waveguide axis are required, and minor gaps from the sample to the guided wave structure can have significant impacts on the accuracy of extracted material parameters. Furthermore, this measurement is more difficult for higher frequencies since the guided wave structures get smaller while machining tolerances stay the same. An additional drawback is the limited low-loss resolution, as it depends mainly on the thickness of the sample and the high calibration requirement of the measurement equipment [37]. Guided wave techniques have been implemented for coaxial and rectangular waveguides to characterize bulk material and even layered composites with high accuracy [39]. Furthermore, planar transmission lines methods like microstrips and coplanar waveguides have been increasingly utilized to create low-cost, broadband material characterization setups [40].

- *Free space waves* The application of free space waves for material characterization has much in common with guided wave characterization, as it works on the same principle to calculate back to material parameters based on scattered and transmitted complex amplitudes. However, free space methods come with unique problems like diverging and converging beams, beam polarisation, the use of lenses, and issues caused by diffraction [37]. Generally, one distinguishes between focused and unfocused methods depending on whether lenses are used to focus diverging beams toward the sample. In such methods, the real part of the permittivity is usually measured by the phase change of the transmitted signal, while the loss in the transmission

path determines the attenuation after inserting the specimen. The benefit of free space methods are that samples are rather easy to handle as they do not need to be precisely machined and fitted into the waveguide structure. However, care must be taken to ensure that the sample is big enough with respect to the wavelength so that diffraction effects are minimized. Therefore, free space methods are not well suited for lower frequencies and are usually applied for frequencies above several tens of GHz.

2.3. AM for High Frequency Electromagnetic Applications

2.3.1. Materials

Dielectric materials commonly employed in FFF processes include polylactic acid (PLA), acrylonitrile butadiene styrene (ABS), and high-performance polymers like polyether ether ketone (PEEK), all of which provide essential insulating properties [14]. Usually, these printing materials are optimized for their mechanical or optical (appeal) properties. However, recent developments also include materials specialized in terms of their dielectric properties [41], [42], including commercially available materials with high permittivity and low loss from Avient or Zetamix, which will be deployed heavily in this work.

2.3.2. Applications

Lenses

Probably the most popular application of dielectric 3D printing in antenna design is the manufacturing of GRIN lenses. Several GRIN lenses for gain enhancement and static beamforming have been discussed in the literature. Most of these early designs are based on single-material approaches, and proof-of-concepts have been demonstrated using the commonly known Luneburg lens. Advanced design approaches include the use of transformation optics (TO) to modify the Luneburg lens into a planar geometry. Additionally, other designs, such as the Gutman lens and Eaton lens, are gaining traction. These profiles can be easily realized using AM techniques. Additionally, with the advancement of multi-material printing, more sophisticated designs have emerged, incorporating high-permittivity materials for the lens cores and low-permittivity matching layers. An excellent overview of this topic is provided in [43].

Dielectric Resonator Antennas

Dielectric resonator antennas (DRA) have long been recognized as promising candidates for front-end antenna solutions in various applications to replace traditional radiating elements at high frequencies [44]: An excellent overview of the DRA is given in [45]. With respect to this research, the main benefit, however, is that they are ideally suited to be manufactured with dielectric AM methods. DRAs, typically made using ceramic parts, face challenges due to their manufacturing complexity, cost, and difficulty in integration with PCB technology. AM can address these challenges by making the production of complex DRA geometries more affordable. By leveraging AM, it becomes possible to create unconventional shapes that enhance bandwidth, gain, or radiation characteristics [46]. Several unique DRA designs have been demonstrated. A common theme is the deployment of non-regular shaped DRAs, difficult or impossible to machine with traditional subtractive techniques, to obtain

wide impedance bandwidth. [47] presents a tranpezoidal DRA compatible with 3D printing with 20% bandwidth. [48] demonstrates a fully FFF printed hemispherical DRA for C band applications achieving a 10% impedance bandwidth. [49] demonstrates a fully 3D printed design of a cylindrical DRA and utilizes a parasitic dielectric helix to achieve circular polarization. The utilization of Super-Shapes [50] for DRAs as discussed in [51] is realized in [52] and achieves an impedance bandwidth of about 10% while achieving an 80% volume reduction of the antenna compared to regular DRA shapes. Another popular DRA design method that leverages AM is the use of periodic dielectric and functionally graded materials in order to obtain larger bandwidths, improve axial ratios, or achieve circular polarization. [53] studies the impact of different infill patterns on AM DRAs. [36] demonstrates a DRA design, printed with a ceramic SLA process, with an effectively anisotropic periodic dielectric structure to achieve circular polarization. [54] present a rectangular DRA with multiple sections of homogeneous permittivity to obtain a large impedance bandwidth of 60% while [55] uses a similar concept with multiple rings of different effective permittivities to create a wideband DRA. [56] uses an AM ceramic DRA with two sections of different effective permittivities to achieve a dual-band DRA for global navigation satellite systems (GNSS) applications fit for space environments.

Non-effective Material Devices

In the examples above concerning dielectric resonators and lenses, periodic dielectric structures are generally used in their long-wavelength operational regime, meaning the periodicity of the lattice is much smaller than the wavelength of the applied EM field. In contrast to lattices operating in the short-wavelength regime, this allows the treatment of the periodic lattice as an effective material, leading to the term non-effective material, or short-wavelength, devices. One of the most popular applications of short-wavelength crystals is the creation of band gaps, which prohibits EM propagation in a finite frequency band. Several research works have already discussed the utilization of AM to create band gap structures in the mmWave regime with a full 3D bandgap. Ederra et al. created woodpile structures with 3D bandgaps using ceramic stereolithography to manufacture a bandgap waveguide [57]. Furthermore, stereolithography has been successfully employed in combination with gel casting to create structured diamond lattices with complete bandgaps [58]. Y. Chen et al. utilized fused deposition of multiple materials to create a woodpile structure with full band gaps [59]. However, previous works on this topic utilized materials that rely on high-temperature burnout and sinter processes to create the final structure after the additive manufacturing step, which adds complexity and cost. So far, there has been no investigation into utilizing low-cost and low-complexity methods like FFF to engineer bandgap materials. Another application of such non-effective materials is the exploitation of spatial dispersion for example, to create self-collimating materials. This is successfully demonstrated in [60] by implementing an unguided 90-degree bend.

2.3.3. Extrusion-Based Hybrid AM

The most versatile AM techniques for electronics and electromagnetic devices allow for the combined use of dielectric and conductive materials in the same process, enabling the production of fully integrated circuits and antenna systems. This capability eliminates separate fabrication steps, reducing potential points of failure and improving manufacturing

efficiency. In this regard especially extrusion-based hybrid AM is attractive due to its compatibility with a wide range of materials. Extrusion based hybrid AM allows the combination of dielectric and conductive materials within a single build process and recent developments have showcased the successful use of multi-material printing for antennas, offering innovative solutions for creating complex geometries and embedding active components [61].

Conductive Materials

Conductive materials compatible with AM can be broadly categorized into conductive filaments and conductive inks, each offering distinct advantages and challenges. On the one hand, conductive filaments, such as those made from carbon-doped polymers or PLA and ABS material with metallic fillers, are compatible with standard extrusion AM processes [62], [63]. However, the electrical conductivity of such polymers is significantly lower than that of bulk metals, limiting their effectiveness in high-performance or high-frequency applications [64]. For instance, carbon nanostructure-filled ABS filaments demonstrate decent conductivity but face challenges with heat dissipation and mechanical strength [65]. Considering antenna applications, the use of conductive filaments implies a severely reduced radiation efficiency due to the high conductor losses. Nevertheless, several studies successfully used conductive filament in 3D-printed antenna structures [66]. Conductive inks—often based on silver or copper nanoparticles—offer superior electrical performance with properties closer to bulk metals. These inks are ideal for printed circuit boards and flexible electronics, excelling in applications requiring intricate electrical patterns. However, they usually require a post-processing step like thermal curing or sintering with ultraviolet light, and their integration presents challenges [67]. The need for specialized printing equipment and higher-temperature post-processing can complicate their use with thermoplastic substrates. When designing integrated antenna systems or structural electronics in complex parts, choosing between conductive filaments and inks is crucial and depends on application-specific requirements, balancing electrical performance, manufacturing complexity, and cost efficiency. Commercial solutions vary, with filaments from companies like Multi 3D and Proto-pasta offering conductive options, while inks from DuPont, Elantas, or Henkel provide highly conductive nanoparticle-based products. Each option involves specific trade offs between cost, conductivity, and mechanical properties, making the selection process pivotal for the success of the intended application.

Integration of Components and Technical Challenges

A key challenge in the development of 3D-printed antennas and electronics, in general, is the integration of third-party passive and active components. Although the functionality of passives like resistors, capacitors, hybrids, etc., could be achieved with simple printed geometries of conductive and dielectric materials, integrating active components like diodes, mixers, amplifiers, etc., is much more challenging. A major challenge in integrating such third-party components is the necessity to do so without using traditional soldering, which can damage thermoplastic substrates due to high temperatures [68] necessary. Alternatives such as using conductive adhesives or embedding components directly during the printing process have shown promise in overcoming these limitations [69]. Process optimization, particularly in terms of extrusion parameters and thermal management, is crucial for ensuring the quality of printed parts while preventing warping and nozzle clogging. A promising method to ensure the quality of the print process is the real-time monitoring and model

predictive control of manufacturing equipment enabled by machine learning and artificial intelligence[70].

2.4. Engineered Materials

For the purposes of this thesis, it is worthwhile to discuss the use of engineered materials, as they are an important concept in modern high-frequency EM engineering. The term engineered material encompasses all materials specifically tailored to exhibit interesting, practical, and enabling electromagnetic properties [71] [72]. They exist in contrast to ordinary materials, which are solely characterized by their atomic-scale phenomena. For example, metals like copper, silver, and gold are commonly used in electromagnetic applications for their high conductivity, or iron and nickel for their magnetic behavior.

2.4.1. Classification

A classification of engineered materials in terms of their feature size concerning the wavelength λ of the applied electromagnetic wave is discussed below.

- ***Mixtures*** are composites of ordinary materials that provide averaged properties based on the mixing relationship and conditions. This is usually done to create dielectric, magnetic, and absorbing materials with desired electromagnetic properties. The theory of these materials is well established. An abundance of so-called ”mixing rules” can be found in the literature that model the resulting effective material parameters based on mixing relations, particle shape and size, etc., and [27] provides an excellent overview.

- ***Metamaterials*** have attracted a lot of research attention in the past two decades. However, there is no universally accepted definition. In the broadest definition, they are basically engineered composites structured in a periodic lattice, where the material's properties are more derived from its structure and geometry than from its chemistry. Metamaterials usually exhibit properties that are not observed in nature, and properties that emerge are not observed in their constituent materials. This makes them very interesting but also challenging to model. Generally, they exist as both 3D and 2D implementations, and notable reviews covering the history, types, and applications are given in [11] and [72]. Generally, one is able to distinguish between two types of meta-materials, resonant and non-resonant, with the focus of current research and applications clearly concentrating on the resonant type.

  Resonant Metamaterials

  In a resonant metamaterial lattice, the periodicity of the lattice is still sub-wavelength enough for electromagnetic waves not to be scattered around between individual features and, at the same time, large enough for the wave to interact with particular features of the lattice. The interaction of the wave with these periodically arranged features gives rise to very unusual effects, like negative index materials [73], [74], zero index materials [75], and single negative materials. Resonant metamaterials are used for various applications like cloaking [76], anti-reflection coatings [75], mutual coupling suppression [77], super-lensing [78], gain-enhancement, etc. They usually have small periodic metallic features in the order of $\approx \lambda/5$ where the mutual inter-

ference between the meta-atoms causes extreme material parameters. The drawback of resonant metamaterials is that they exhibit relatively large losses, are generally narrow-band, and obtain a limited field of view (FOV). Research in this area primarily focuses on increasing bandwidth [79], the field of view, and ways to incorporate gain to overcome losses [80].

Non-Resonant Metamaterials
In contrast to resonant metamaterials, non-resonant variations obtain periodicity far smaller than the applied wavelength. In fact, they usually have no lower cut-off frequency, meaning they work from static EM fields (0Hz) to some upper cut-off frequency. Therefore, they have great potential for broadband and wide FOV devices. Furthermore, they are robust to structural deformations. However, they usually do not obtain the same extreme properties that can be achieved with resonant metamaterials. Notable implementations of such non-resonant metamaterials are artificial dielectric layers as utilized in [81] for wideband impedance transformations or in [82] for the engineering of the uniaxial anisotropy in periodic dielectrics.

- ***Photonic Crystals*** Photonic crystals are periodic structures where the periodicity of the crystal is the same order of magnitude as the applied wavelength, resulting in a behavior analogous to electrons in semiconductors. By engineering the crystal geometry, one can design complete and partial bandgaps and engineer the dispersion to achieve the self-collimating or hyper-dispersive behavior of the material.

2.4.2. Realization

All of the above-identified materials classes are periodic in some sense, be it the periodicity of atomic lattices in ordinary materials, the stochastic distribution of the particles in mixtures, or the engineered periodicity of metamaterials and photonic crystals. The periodicity of engineered materials is generally challenging to engineer or realize with traditional means of manufacturing in more than two dimensions. Notable 3D realizations of metamaterials with traditional manufacturing techniques is the cloaking device engineered by Pendry et.al [83] with complicated nested PCBs and the implementation of the first photonic crystal by Yablonovich [84], who used oblique drilling in different directions through a block of dielectric material to proof the existence of 3D bandgaps. This limitation in traditional manufacturing can be effectively mitigated by utilizing AM. With additive techniques, the engineering of intricate 3D periodic lattices and the tailoring of their EM properties can be easily achieved, unlocking tremendous potential via the application of 3D metamaterials and photonic crystals [14].

2.4.3. Dielectric Crystals

In the framework of this thesis, engineered materials are relevant in terms of periodic dielectric structures for which the term dielectric crystal is used synonymous. One of the objectives of this research is to establish dielectric crystals as a design concept that enables novel microwave components with the help of additive manufacturing.

The term dielectric crystal encompasses all devices with periodic modulation of the realtive permittivity index, with 1D, 2D, and 3D periodicity as depicted in Figure 2.1 [85]. A few examples from literature, classified according to their periodicity are listed below.

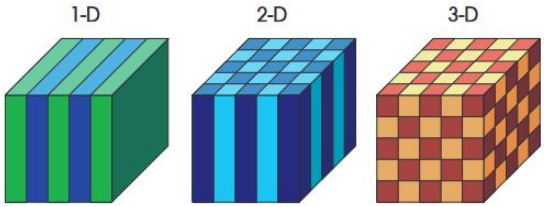

Figure 2.1: Classification of photonic crystals by the dimension of their periodicity [85].

Classification by Periodicity

- ***1D*** - Examples for 1D Photonic Crystals are Bragg mirrors, where the refractive index is modulated periodically along one axis to create a narrow-band reflector, commonly used in lasers and photonic integrated circuits [86]. Defects in 1D PhCs are used to create cavities with high quality factor values [87].
- ***2D*** - Two-dimensional modulation of the refractive index has been employed to create bandgap-waveguides in silicon [88], [89]. Several works performed studies investigating the properties of 2D PhCs as a function of their crystal geometry and air-filling fraction [90].
- ***3D*** - Photonic crystals with three-dimensional periodicity have been rarely used because they are very complex to create with traditional manufacturing methods. A lot of research in 3D PhCs has been done to find structures that exhibit a full bandgap [84] [91]. One particularly exciting possibility to utilize 3D photonic crystals is to engineer the dispersion of the crystal for higher order propagating modes as explained in [92]. This creates exciting possibilities; one example is self-collimating crystals, where the dispersion is engineered such that a non-diverging beam propagates within the lattice. The same concept of self-collimating crystals has also been applied with spatial variation to create an unguided 90-degree bend in the crystal structure [60], which has also been utilized in [93] to create the world tightest unguided bend.

This work distinguishes between two modes of operation in dielectric crystals, further referred to as long- and short-wavelength. These two modes of operation are further explained below with help of Figure 2.2 for a 1D periodic crystal comprised of two dielectric material with permittivities $\varepsilon_{r,1}$ and $\varepsilon_{r,2}$ for an applied field with a wave vector □.

One mode, called long-wavelength crystal, describes the scenario where the wavelength of the applied field is much larger than the crystal periodicity $\Lambda \ll \lambda$, thus the crystal behaves as an effective homogeneous material with approximately linear dispersion. The crystal in this case is engineered to exhibit some desired material parameters, efficiently described with an effective material tensor and thus falls into the category of a non-resonant metamaterial as explained above in Section 2.4.1. The engineering of effective properties is achieved via an appropriate choice of the relative permittivity values $\varepsilon_{r,1}$ and $\varepsilon_{r,2}$. This concept of effective permittivity has been employed in literature to engineer the permittivity of substrates [94], dielectric resonator antennas [95] [96], and lenses [43]. A more detailed review of such applications is provided in Section 2.3 in the context of dielectric AM techniques.

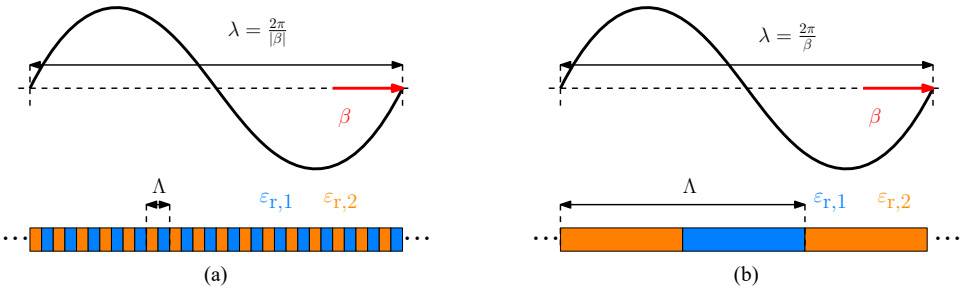

Figure 2.2: Visualization of a 1D periodic dielectric crystal comprised of two materials with relative permittivities $\varepsilon_{r,1}$ and $\varepsilon_{r,2}$, with periodicity Λ and an applied field with wave vector β. (a) Long wavelength mode $\Lambda \ll \lambda$ and (b) Short wavelength mode $\Lambda \approx \lambda$.

The second mode, further called short-wavelength crystal, describes the scenario where the applied field wavelength is the same order of magnitude as the crystal periodicity $\Lambda \approx \lambda$. This implies that the crystal cannot be described as an effective homogeneous material anymore, and non-linear effects dominate the dispersion relationship. The crystal, in this case, can be engineered to exhibit desired dispersion properties, including bandgaps or self-collimating behavior, and therefore falls into the category of a photonic crystal as explained in Section 2.4.1. Again, a more detailed review of these applications is provided in Section 2.3.

Spatial Modulation of Dielectric crystals

The concept of introducing spatial variation to create inhomogeneity for design purposes is not well established. Traditionally, this is achieved by creating perforated structures with subtractive techniques such as milling and drilling. With the advent of AM, this concept can now be easily extended to 3D. A commonly applied concept is to use space-filling curves with modulated trace thicknesses to achieve spatial-dependent material responses [97]. They are usually employed for planar designs and are difficult to adapt to 3D designs. 3D spatial variation has been introduced with voxel approaches, where unit cells are treated like individual voxels, and each of them is assigned an effective permittivity value. Another popular method is to create regions in a lattice that will be printed with different materials or different infill fractions, as done in [98] to create a flat graded index (GRIN) lens. One powerful algorithm for spatial modulation is introduced in [99], which allows not only to modulate the volumetric infill spatially but also to change the crystal symmetry and periodicity while obtaining minimal deformations to the individual unit cell. The latter is employed throughout the application oriented reseach presented in this thesis and discussed in more detail in Section 3.2.3.

2.5. Gaps and Corresponding Research Questions

Based on the review of research and the state of the art presented in this chapter, the work in this thesis is focused at the intersection of manufacturing technology, material science,

and high-frequency EM engineering. Specifically, the following gaps and corresponding research questions are identified.

1. What are the critical factors to consider when studying the effective dielectric material properties of additive manufactured periodic lattices, and what are suitable methods for homogenization and characterization?
2. How does the layer-by-layer build approach of extrusion-based AM affect the dielectric properties of printed parts?
3. How do lattice symmetries affect the effective anisotropy of periodic dielectric structures, and can this effect be exploited to engineer the effective permittivity tensor of AM dielectric crystals systematically?
4. Besides GRIN lenses, how can controlled dielectric heterogeneity via spatially modulated dielectric crystals improve existing or enable novel high-frequency EM devices?
5. What are suitable geometries to implement dielectric bandgap materials, and how can such materials be applied in high-frequency EM devices?
6. Is it possible to deploy cost-effective AM systems, capable of printing both dielectric and conductive materials, for the purpose of manufacturing high-frequency EM devices?

Compared to previous studies, which focus primarily on the rapid prototyping capabilities of AM, this work aims to advance the field by bridging the gap between theoretical design and practical implementation. By exploring both long- and short-wavelength regimes of dielectric crystals, it showcases their potential as both effective materials and photonic bandgap structures. The application of hybrid AM techniques, which combine dielectric and conductive materials, represents a significant step toward the realization of fully integrated EM devices. In essence, this thesis establishes AM not merely as a tool for rapid prototyping but as a transformative approach to engineering novel EM devices with customized material properties. Addressing both the fundamental challenges and practical applications of AM periodic dielectrics sets a new benchmark for the integration of AM with advanced EM device design, paving the way for future innovations in communication, sensing, and radar systems.

3

Theoretical Framework and Methodology

If we knew what it was we were doing, it would not be called research, would it? – Albert Einstein

In general, this thesis concerns itself with the potential of additive manufacturing for antenna applications. However, at its core, it deals with the capabilities to engineer and characterize dielectric material properties of periodic dielectric structures, also referred to as dielectric crystals. This Chapter first gives a general introduction to these properties and their nuances as they are relevant to the contents discussed in subsequent chapters. Furthermore, basic concepts from the fields of crystallography and how they relate to the dielectric material properties are explained. Additionally, in this work, employed manufacturing tools and utilized materials are presented together with a brief analysis of the achievable accuracy and tolerances of manufactured geometries.

3.1. Dielectric Material Properties

Starting with the foundation of the discipline, Maxwell's equations, which are in their differential form for time harmonic fields with frequency ω [100],

$$\nabla \times \mathbf{E}(\mathbf{r}) = -\jmath\omega\mathbf{B}(\mathbf{r}) - \mathbf{M}(\mathbf{r}) \tag{3.1}$$
$$\nabla \times \mathbf{H}(\mathbf{r}) = \jmath\omega\mathbf{D}(\mathbf{r}) + \mathbf{J}(\mathbf{r}) \tag{3.2}$$
$$\nabla \cdot \mathbf{D}(\mathbf{r}) = \rho(\mathbf{r}) \tag{3.3}$$
$$\nabla \cdot \mathbf{B}(\mathbf{r}) = 0 \tag{3.4}$$

with $\jmath^2 = -1$ representing the imaginary unit, $\mathbf{r}$ symbolizing 3D spatial coordinates, $\mathbf{E}$, $\mathbf{H}$ denoting the electric and magnetic fields and $\mathbf{D}$, $\mathbf{B}$ the electric and magnetic flux densities respectively, while $\mathbf{J}$ and $\mathbf{M}$ represent the electric and magnetic current densities. Furthermore, also the constitutive relationships

$$\mathbf{D}(\mathbf{r}) = [\varepsilon(\mathbf{r})]\,\mathbf{E} = \varepsilon_0\,[\varepsilon_\mathrm{r}(\mathbf{r})]\,\mathbf{E} \tag{3.5}$$
$$\mathbf{B}(\mathbf{r}) = [\mu(\mathbf{r})]\,\mathbf{H} = \mu_0\,[\mu_\mathrm{r}(\mathbf{r})]\,\mathbf{H} \tag{3.6}$$
$$\mathbf{J}(\mathbf{r}) = [\sigma(\mathbf{r})]\,\mathbf{E}(\mathbf{r}) \tag{3.7}$$

need to be considered, with $[\sigma]$ denoting the conductivity tensor, and $[\varepsilon_\mathrm{r}]$, $[\mu_\mathrm{r}]$ symbolizing the relative permittivity and permeability tensors respectively and ε_0, μ_0 denoting the vacuum permittivity and permeability[1].

This work is restricted to the discussion of a non-conductive ($[\sigma] = [0]$) and non-magnetic ($[\mu] = \mu_0\,[\mathbf{I}]$) material. Furthermore, it is imposed that the dielectric material response is linear and time-independent, implying $\frac{\partial}{\partial t}\,[\varepsilon] = 0$, and with no sources present $\rho = 0$, $\mathbf{J} = 0$, and $\mathbf{M} = 0$. The assumptions discussed above give rise to a simplified form of equations (3.1) - (3.4)

$$\nabla \times \mathbf{E}(\mathbf{r}) = -\jmath\omega\mu_0\mathbf{H}(\mathbf{r}) \tag{3.8}$$
$$\nabla \times \mathbf{H}(\mathbf{r}) = \jmath\omega\varepsilon_0\,[\varepsilon(\mathbf{r})]\,\mathbf{E}(\mathbf{r}) \tag{3.9}$$
$$\nabla \cdot ([\varepsilon(\mathbf{r})]\,\mathbf{E}(\mathbf{r})) = 0 \tag{3.10}$$
$$\nabla \cdot \mathbf{H}(\mathbf{r}) = 0 \tag{3.11}$$

[1] The square bracket notation $[\cdot]$ is employed to emphasize the tensor nature of the respective material property.

The relative permittivity $[\varepsilon_{\mathrm{r}}(\mathbf{r})]$ in general is a complex quantity

$$[\varepsilon_{\mathrm{r}}(\mathbf{r})] = [\varepsilon'_{\mathrm{r}}(\mathbf{r})] - \jmath\,[\varepsilon''_{\mathrm{r}}(\mathbf{r})] \tag{3.12}$$

where the imaginary part $[\varepsilon''_{\mathrm{r}}(\mathbf{r})]$ is associated with dielectric losses and the real part $[\varepsilon'_{\mathrm{r}}(\mathbf{r})]$ indicating the degree of polarization in the material. For the most part of this work the permittivity is treated to be lossless and in cases where the treatment of loss is necessary, perturbation theory is used to address the effects of the complex permittivity. Throughout the thesis three properties of the dielectric response are of special interest:

- (An)Isotropy, referring to the dependence of the material response on the direction of the applied field,
- (In)Homogeneity, referring to the dependence of the material response on spatial coordinates,
- Frequency dispersion, referring to the dependence of the material response on the frequency of the applied field $[\varepsilon_{\mathrm{r}}(\omega)]$.

which are further explained below.

3.1.1. (An)Isotropy

As mentioned above the permittivity is generally described as a tensor of rank 2, implying the dielectric flux density and electric field in an Cartesian coordinate system are related via

$$\begin{bmatrix} D_{\mathrm{x}} \\ D_{\mathrm{y}} \\ D_{\mathrm{z}} \end{bmatrix} = \varepsilon_0\,[\varepsilon_{\mathrm{r}}] \begin{bmatrix} E_{\mathrm{x}} \\ E_{\mathrm{y}} \\ E_{\mathrm{z}} \end{bmatrix} = \varepsilon_0 \begin{bmatrix} \varepsilon_{\mathrm{r,xx}} & \varepsilon_{\mathrm{r,xy}} & \varepsilon_{\mathrm{r,xz}} \\ \varepsilon_{\mathrm{r,yx}} & \varepsilon_{\mathrm{r,yy}} & \varepsilon_{\mathrm{r,yz}} \\ \varepsilon_{\mathrm{r,zx}} & \varepsilon_{\mathrm{r,zy}} & \varepsilon_{\mathrm{r,zz}} \end{bmatrix} \begin{bmatrix} E_{\mathrm{x}} \\ E_{\mathrm{y}} \\ E_{\mathrm{z}} \end{bmatrix}. \tag{3.13}$$

For most dielectric media, the electric permittivity tensor is symmetric, i.e. $\varepsilon_{\mathrm{ij}} = \varepsilon_{\mathrm{ji}}$, meaning the relationship in equation (3.13) is reciprocal. This symmetry is obeyed for non-magnetic materials that do not exhibit optical activity [101]. Given this symmetry the medium is characterized via six independent numbers in an arbitrary coordinate system. However a coordinate system can always be found such that the off-diagonal elements of $[\varepsilon]$ vanish and individual components of the dielectric flux density and the electric field are decoupled

$$\begin{bmatrix} D_1 \\ D_2 \\ D_3 \end{bmatrix} = \varepsilon_0 \begin{bmatrix} \varepsilon_{\mathrm{r},11} & 0 & 0 \\ 0 & \varepsilon_{\mathrm{r},22} & 0 \\ 0 & 0 & \varepsilon_{\mathrm{r},33} \end{bmatrix} \begin{bmatrix} E_1 \\ E_2 \\ E_3 \end{bmatrix}. \tag{3.14}$$

Tensor configuration

Assuming a permittivity tensor representation according to equation (3.14), three general cases of tensor component configurations can be identified:

- *Isotropic* case for which the tensor components satisfy $\varepsilon_{\mathrm{r},11} = \varepsilon_{\mathrm{r},22} = \varepsilon_{\mathrm{r},33}$. Implying the constitutive relationship between the dielectric flux density and the electric field reduces to a scalar form.

- *Uniaxial anisotropic* case for which the tensor components satisfy $\varepsilon_{\mathrm{r},11} = \varepsilon_{\mathrm{r},22} \neq \varepsilon_{\mathrm{r},33}$. In this case the individual permittivities are often denoted as $\varepsilon_{\mathrm{r},11} = \varepsilon_{\mathrm{r},22} = \varepsilon_{\mathrm{O}}$ and $\varepsilon_{\mathrm{r},33} = \varepsilon_{\mathrm{E}}$, also known as the ordinary and extraordinary permittivities respectively.

- *Biaxial anisotropic* the most general case where all tensor components are different from each other $\varepsilon_{\mathrm{r},11} \neq \varepsilon_{\mathrm{r},22} \neq \varepsilon_{\mathrm{r},33}$

3

3.1.2. (In)Homogeneity

The study of dielectric inhomogeneity, meaning a spatially dependent permittivity $[\varepsilon(\mathbf{r})]$, is challenging because a closed-form solution to equations (3.8) - (3.11) is only available for simple geometries like stratified media, materials with special symmetries, or materials with small inhomogeneities that allow the application of perturbation theory. In most cases, however, the treatment of dielectric inhomogeneity requires the utilization of computationally demanding numerical methods.

Homogenization

A significant simplification in the treatment of dielectric inhomogeneities can be achieved via homogenization techniques, which aim to replace the complex description of the spatially dependent permittivity with an equivalent homogeneous effective medium. A review of applicable techniques is provided in the previous Chapter in Section 2.2, and suitable methods are discussed and compared in detail in Chapter 4. However, the validity of such techniques hinges on several key requirements, primarily the scale separation between inhomogeneities and the operating wavelength. Furthermore, limitations arise when dealing with significant material contrasts, non-linear responses, or when detailed microstructural effects play a critical role in the material's electromagnetic behavior. Careful consideration of these factors is essential when applying homogenization techniques to ensure accurate and meaningful results.

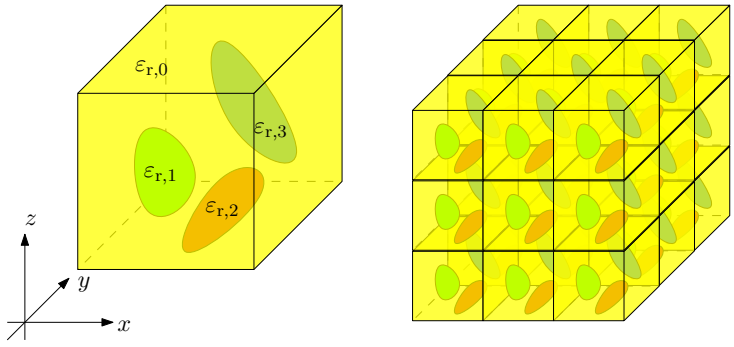

Figure 3.1: Inhomogeneous dielectric material comprised of individual homogeneous sections (left). 3D periodic arrangement of inhomogeneous unit cells (right).

3.1.3. Frequency Dispersion

Considering the simple case of a plane EM wave propagating through a linear, homogeneous, isotropic, and lossless material with homogeneous and isotropic permittivity ε and permeability μ, the magnetic field is written as

$$\mathbf{H} = \mathbf{H_0} e^{j(\mathbf{k}\cdot\mathbf{r}-\omega t)} \tag{3.15}$$

with ω representing the angular frequency, $\mathbf{k} = k\hat{\mathbf{k}}$ denoting the wave vector and $\mathbf{H_0}$ is some constant vector in the plane orthogonal to $\mathbf{k}$. Solving Maxwell's equations (3.8) - (3.11) with (3.15), one obtains a linear relationship between frequency and wave vector [100]

$$k = \frac{\omega}{c_0} = \omega\sqrt{\varepsilon\mu} \tag{3.16}$$

called the dispersion relation. Dielectric frequency dispersion generally occurs when the permittivity of a material depends on the frequency of the applied EM field. This happens naturally with increasing frequency due to the different polarization mechanisms failing to follow the oscillations of the applied electric field [102]. A special case that is especially relevant with respect to this thesis is the dispersion in periodic structures. In the case of an EM wave traveling through a periodic dielectric, the field can, according to the Bloch theorem, generally be written as [85]

$$\mathbf{H} = \mathbf{S}(\mathbf{r}) e^{j(\beta\cdot\mathbf{r}-\omega t)} \tag{3.17}$$

where $\mathbf{S}(\mathbf{r})$ is a periodic function with the same periodicity as the crystal and β is the Bloch vector (equivalent to the wave vector $\mathbf{k}$ as in equation (3.15)). Due to the now periodic (inhomogeneous) nature of the propagation medium, there is no simple solution for the dispersion relationship as for the homogeneous media in equation (3.16). Solutions need to be found by solving the wave equation

$$\nabla \times \left(\frac{1}{[\varepsilon(\mathbf{r})]} \nabla \times \mathbf{H}(\mathbf{r}) \right) = \left(\frac{\omega}{c_0} \right)^2 \mathbf{H}(\mathbf{r}). \tag{3.18}$$

Most works dealing with additive manufactured dielectric crystals do not consider the complex nature of the dispersion in periodic media but assume that the material can be modeled as a homogeneous effective media with linear dispersion according to equation (3.16). However, this assumption does only hold for sufficiently large wavelengths as indicated in equation (3.21). This is also indicated by the term *long-wavelength* as introduced in Section 2.4.3. As the frequency of the propagating fundamental mode in the lattice increases and its wavelength shrinks with respect to the lattice constant, this assumption is rendered invalid, giving rise to the *short-wavelength* operating regime of dielectric crystals where non-linear dispersion effects dominate the propagation behavior.

3.2. Dielectric Crystals

A special case of inhomogeneity is that of periodic dielectric structures, or dielectric crystals, for which the permittivity can be expressed via

$$[\varepsilon_r(\mathbf{r})] = [\varepsilon_r(\mathbf{r} + \mathbf{R})] \tag{3.19}$$

as a function of spatial coordinates $\mathbf{r} = [x, y, z]^{\mathrm{T}}$, with a translation vector

$$\mathbf{R} = n_1\mathbf{a} + n_2\mathbf{b} + n_3\mathbf{c},\ n_{\mathrm{i}} \in \mathbb{Z},\ i \in \{1,\ 2,\ 3\} \tag{3.20}$$

where **a**, **b**, and **c** denote the primitive lattice vectors of the corresponding crystal system.

In the long wavelength limit, where the wavelength of the applied electromagnetic wave λ is much larger than the size of the periodic unit cell, the behavior of the lattice can be described by a homogenized effective permittivity tensor

$$\lim_{\lambda\to\infty} [\varepsilon_{\mathrm{r}}(\mathbf{r})] = [\tilde{\varepsilon_{\mathrm{r}}}]. \tag{3.21}$$

A dielectric crystal can be arbitrarily complex, consisting of multiple materials with different relative permittivities as indicated in Figure 3.1. The discussion in this work is limited to the simplified case of a crystal comprised of two materials, a manufacturing material $[\varepsilon_{\mathrm{r,m}}]$ and a background material $[\varepsilon_{\mathrm{r,b}}]$. The manufacturing material is assumed to be produced via extrusion-based additive manufacturing and the background material is generally considered to be free space $[\varepsilon_{\mathrm{r,b}}] = [\mathbf{I}]$.

3.2.1. Crystals and Material Properties

A fundamental concept in crystallography and materials science is that the symmetry of physical properties relates to the symmetry of the crystal structure. Neumann's principle states [101] *"The symmetry of any physical property of a crystal must include the symmetry elements of the point group of the crystal."*. In simpler terms, this means that the symmetry of any physical property of a crystal (such as electrical conductivity, permittivity, elasticity, etc.) cannot be higher than the symmetry of the crystal's structure itself. The physical properties reflect the symmetry of the crystal system. This means that the principal form of the dielectric crystal's effective permittivity tensor can be concluded from the crystal symmetry in which the dielectric crystal is posed.

A crystal system is characterized by a set of reference vectors, labeled **a**, **b** and **c**, as depicted in Figure 3.2. The reference vectors span a parallelpiped with lengths $\|\mathbf{a}\|$, $\|\mathbf{b}\|$ and $\|\mathbf{c}\|$, and angles between the sides given by α, β, γ. Together, the lengths and angles of the parallelepiped are usually called lattice constants or lattice parameters. The seven crystal systems and the restrictions on their respective lattice parameters are given in Table 3.1. Furthermore, Table 3.1 displays the general form for the dielectric tensor for the various crystal systems. In summary, as the crystal's symmetry decreases, the dielectric tensor complexity increases, moving from a simple isotropic form in cubic crystals to a fully populated tensor in triclinic crystals. This complexity reflects the fact that lower symmetry allows for more directional dependence in the material's response to an electric field.

3.2.2. Unit Cell Design

As mentioned above, this work considers the simplified case of dielectric crystals comprised of a manufacturing material $[\varepsilon_{\mathrm{r,m}}]$ contrasted against free space (background material $[\varepsilon_{\mathrm{r,b}}] = 1\,[\mathbf{I}]$). In order to manufacture such crystals, the manufacturing material needs to be connected throughout neighboring cells. A plethora of methods exist with varying degrees of complexity to engineer such periodic dielectric structures. This work utilizes two different approaches, which are explained below.

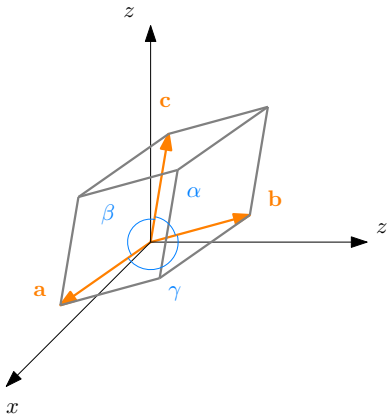

Figure 3.2: Characterization of crystal systems via a set of reference vectors **a**, **b** and **c**.

Table 3.1: The seven crystal systems and their respective dielectric tensors

Crystal system	Lengths	Angles	Tensor Form
cubic	$\|\mathbf{a}\| = \|\mathbf{b}\| = \|\mathbf{c}\|$	$\alpha = \beta = \gamma = 90°$	$\begin{bmatrix} \varepsilon_{11} & 0 & 0 \\ 0 & \varepsilon_{11} & 0 \\ 0 & 0 & \varepsilon_{11} \end{bmatrix}$
trigonal	$\|\mathbf{a}\| = \|\mathbf{b}\| = \|\mathbf{c}\|$	$\alpha = \beta = \gamma \leq 120°, \neq 90°$	$\begin{bmatrix} \varepsilon_{11} & 0 & 0 \\ 0 & \varepsilon_{11} & 0 \\ 0 & 0 & \varepsilon_{33} \end{bmatrix}$
hexagonal	$\|\mathbf{a}\| = \|\mathbf{b}\| \neq \|\mathbf{c}\|$	$\alpha = \beta = 90°, \gamma = 120°$	$\begin{bmatrix} \varepsilon_{11} & 0 & 0 \\ 0 & \varepsilon_{11} & 0 \\ 0 & 0 & \varepsilon_{33} \end{bmatrix}$
tetragonal	$\|\mathbf{a}\| = \|\mathbf{b}\| \neq \|\mathbf{c}\|$	$\alpha = \beta = \gamma = 90°$	$\begin{bmatrix} \varepsilon_{11} & 0 & 0 \\ 0 & \varepsilon_{11} & 0 \\ 0 & 0 & \varepsilon_{33} \end{bmatrix}$
orthorhombic	$\|\mathbf{a}\| \neq \|\mathbf{b}\| \neq \|\mathbf{c}\|$	$\alpha = \beta = \gamma = 90°$	$\begin{bmatrix} \varepsilon_{11} & 0 & 0 \\ 0 & \varepsilon_{22} & 0 \\ 0 & 0 & \varepsilon_{33} \end{bmatrix}$
monoclinic	$\|\mathbf{a}\| \neq \|\mathbf{b}\| \neq \|\mathbf{c}\|$	$\alpha = \beta = 90°, \gamma \neq 90°$	$\begin{bmatrix} \varepsilon_{11} & 0 & \varepsilon_{13} \\ 0 & \varepsilon_{22} & 0 \\ \varepsilon_{31} & 0 & \varepsilon_{33} \end{bmatrix}$
triclinic	$\|\mathbf{a}\| \neq \|\mathbf{b}\| \neq \|\mathbf{c}\|$	$\alpha \neq \beta \neq \gamma$	$\begin{bmatrix} \varepsilon_{11} & \varepsilon_{12} & \varepsilon_{13} \\ \varepsilon_{21} & \varepsilon_{22} & \varepsilon_{23} \\ \varepsilon_{31} & \varepsilon_{32} & \varepsilon_{33} \end{bmatrix}$

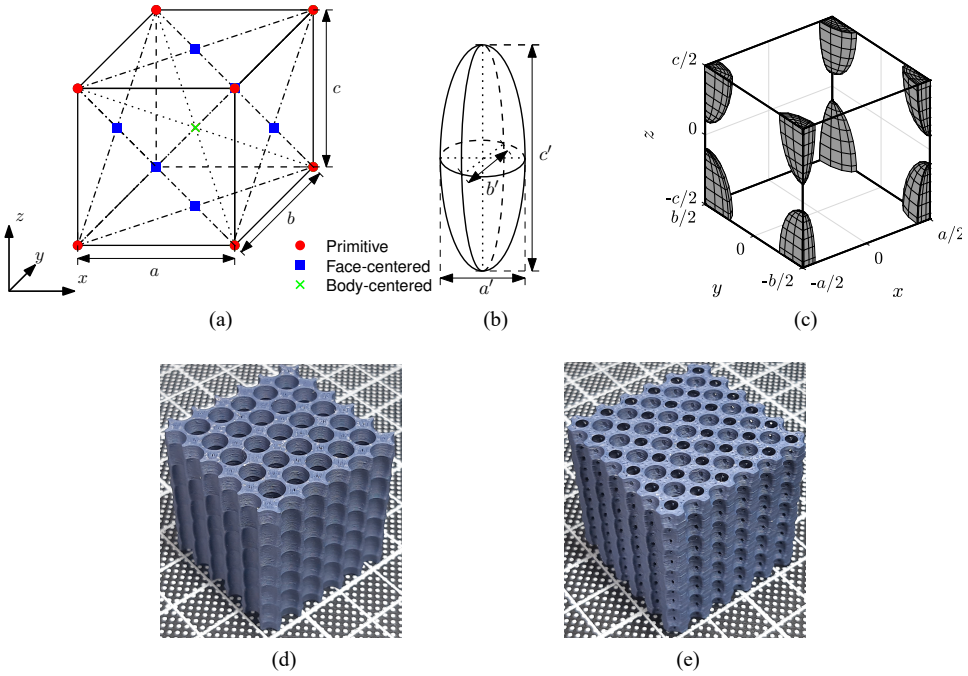

Figure 3.3: (a) Visualization of a parameterized orthogonal unit cell ($\alpha = \beta = \gamma = 90°$) with lattice parameters a, b, and c, with colorized node positions of different centerings. (b) Ellipsoidal inclusions with inclusion parameters a', b', and c'. (c) Cubic unit cell with primitive centering and ellipsoidal inclusion highlighted in grey with inclusion parameters $a' = 0.2a$, $b' = 0.5b$, $c' = 0.8c$. (d,e) Examples of manufactured lattices with ellipsoidal inclusions with (d) primitive and (e) body-centered centering.

Parametrically Defined

The most popular option for defining the unit cell of dielectric crystals is to utilize some kind of parametric definition based on geometric bodies. Their main benefit is that they can be easily modeled in commonly employed numerical simulation tools, which allows the extraction of their effective properties as a function of geometric parameters. This allows a straightforward extraction of their effective permittivities as a function of geometric parameters with effective media approximations and numerical homogenization methods.

In the following, the scope of this work is restricted to crystal systems with orthogonal angles, e.g., the cubic, tetragonal, and orthorhombic systems in their primitive, body-centered, and face-centered forms. Generally, one can consider a unit cell as depicted in Figure 3.3a with lateral dimensions a, b, and c, further referred to as lattice parameters. The unit cell is considered to be made up of a homogeneous and isotropic manufacturing materials material with ellipsoidal inclusions of free space with dimensions a', b', and c', further referred to as inclusion parameters, as depicted in Figure 3.3b, at the positions of the considered centering.

Parametrically defined unit cells are especially relevant in Chapter 6, which discusses the effective permittivity tensor engineering and synthesis via dielectric crystals. Manufac-

tured examples of periodic lattices comprised of such parametrically defined unit cells are depicted in Figures 3.3d and 3.3e. However, they can be quite cumbersome considering the implementation of spatial modulation of the effective effective properties of the lattice. For this reason, a more complicated but efficient method to define unit cells in different Bravais lattices is introduced in the following Section.

Spatial Harmonic Superposition

The method is introduced by the example of simple cubic (SC) and face-centered cubic (FCC) Bravais lattices in the cubic crystal structure. These are defined by their lattice constant a and their respective primitive lattice vectors $\mathbf{t}_1$, $\mathbf{t}_2$ and $\mathbf{t}_3$ which point from the current lattice node to its three nearest neighbors. For each set of two primitive lattice vectors, a perpendicular reciprocal lattice vector vector, can be found via

$$\mathbf{T}_1 = 2\pi \frac{\mathbf{t}_2 \times \mathbf{t}_3}{\mathbf{t}_1 \cdot (\mathbf{t}_2 \times \mathbf{t}_3)} \tag{3.22}$$

$$\mathbf{T}_2 = 2\pi \frac{\mathbf{t}_3 \times \mathbf{t}_1}{\mathbf{t}_1 \cdot (\mathbf{t}_2 \times \mathbf{t}_3)} \tag{3.23}$$

$$\mathbf{T}_3 = 2\pi \frac{\mathbf{t}_1 \times \mathbf{t}_2}{\mathbf{t}_1 \cdot (\mathbf{t}_2 \times \mathbf{t}_3)} \tag{3.24}$$

where the magnitude describes the periodicity of the lattice.

Lattice generation via spatial harmonics

The lattice geometry in the respective Bravais lattice is now created by calculating a superposition of N_H spatial harmonics

$$\Psi(\mathbf{r}) = \sum_{i=1}^{N_\mathrm{H}} \psi_\mathrm{i} e^{\jmath\left(g_\mathrm{i,x} x + g_\mathrm{i,y} y + g_\mathrm{i,z} z\right)} \tag{3.25}$$

with ψ_i denoting the complex weights of individual harmonics and $\mathbf{g}_\mathrm{i}$ representing individual grating vectors $i = 1 \ldots N_\mathrm{H}$.

By choosing the individual grating vectors $\mathbf{g}_\mathrm{i} = \left(g_\mathrm{i,x}\ g_\mathrm{i,y}\ g_\mathrm{i,z}\right)^\mathrm{T}$ such that they are oriented along the reciprocal lattice vectors $\mathbf{T}_\mathrm{i}$ as defined in (3.24) and their magnitude as an integer multiple of the lattice periodicity, the superposition of spatial harmonics obtains the respective crystal symmetry and periodicity. The overall lattice L is computed, for some threshold $th \in [0\ 1]$, on the min-max feature scaled real part of the superimposed spatial harmonics Ψ

$$\tilde{\Psi}(\mathbf{r}) = \frac{Re\{\Psi\} - \min(Re\{\Psi\})}{\max(Re\{\Psi\}) - \min(Re\{\Psi\})} \tag{3.26}$$

$$L: = \tilde{\Psi} \geq th. \tag{3.27}$$

The resulting geometry is converted into a 3D mesh which can easily be exported to a standard tessellation (STL) which in turn is commonly utilized file format for the purposes of additive manufacturing.

The unit cell design is further visualized with help of Figure 3.4. The normalized spatial harmonic superposition $\tilde{\Psi}(\mathbf{r})$ for $\mathbf{t}_1 = [1\ 0\ 0]^{\mathrm{T}}$, $\mathbf{t}_2 = [0\ 1\ 0]^{\mathrm{T}}$, and $\mathbf{t}_3 = [0\ 0\ 1]^{\mathrm{T}}$, corresponding to a cubic symmetry with primitive centering, together with contours for discrete values thereof are depicted in Figure 3.4a. For these discrete values, corresponding to threshold values th, individual unit cells are extracted and depicted in Figures 3.4c-3.4f. Similarly, unit cells in a cubic symmetry but with face-centered centering, $\mathbf{t}_1 = [0\ 1\ 1]^{\mathrm{T}}$, $\mathbf{t}_2 = [1\ 0\ 1]^{\mathrm{T}}$, and $\mathbf{t}_3 = [1\ 1\ 0]^{\mathrm{T}}$, are depicted in Figure 3.4g-3.4j. Additionally, manufactured lattice samples for the SC and FCC centerings are depicted in Figures 3.4k and 3.4l respectively. The reason for utilizing spatial harmonics to create a periodic lattice is that one can easily vary the fill fraction by changing the threshold value throughout the lattice or even within one unit cell. Therefore, provides better resolution for index-graded devices than unit cells that are parametrically defined. Furthermore, any unit cell geometry in any crystal system can be decomposed and represented by a discrete set of spatial harmonics with complex weights. This bears the benefit that the described approach is much more general and effective for handling 3D lattices. Furthermore, the utilization of spatial harmonics to represent periodic structures makes the applications of algorithms to vary the lattice, as proposed in [99], more accessible and computationally efficient.

3.2.3. Spatial Modulation

The idea of utilizing a spatial variation of dielectric infill to introduce inhomogeneous effective permittivity for design purposes is not new. A common planar design approach is utilizing space-filling curves with modulated trace thickness [97] to achieve spatial-dependent material responses. However, space-filling curves are challenging to adapt to 3D geometries. 3D spatial variation has been introduced with voxelated approaches where parametrically defined unit cells are treated like individual voxels, which have a practical permittivity value assigned that is engineered by changing the geometric parameters of the unit cell. Another popular method is to create sections in a lattice that will be printed with different materials or infill fractions, as shown in [98]. In this work, the less known but robust algorithm to synthesize spatially variant lattices (SVL) as introduced in [99] is used. The details of the SVL algorithm are not repeated here. The approach decomposes a given unit cell into spatial harmonics and applies spatial variations like rotations or changes in the lattice period onto these individual harmonics. Later, the whole lattice is assembled by the superposition of the individual harmonics, which results in a continuous and smooth structure with minimum deformation of individual unit cells. The SVL algorithm, although computationally expensive, offers a powerful tool to influence dielectric crystal lattices in numerous ways. Due to the computationally demanding nature of the SVL algorithm, the spatial harmonics approach is used to engineer a unit cell rather than decomposing an arbitrary unit-cell geometry in a large number of spatial harmonics. The spatial harmonics design approach as utilized in this work utilizes the unit cell definition via $N = 3$ spatial harmonics, as explained above in Section 3.2.2, resulting in a manageable computation time when applying the SVL algorithm. A full lattice is generated by computing $\tilde{\Psi}$ for the desired volume and applying a spatially dependent threshold value $th(\mathbf{r})$. This approach is visualized in Figure 3.5 by generating lattices with linearly varying volumetric infill ratio as a function of x. Manufactured spatially modulated lattices based on SC and FCC unit cells are depicted

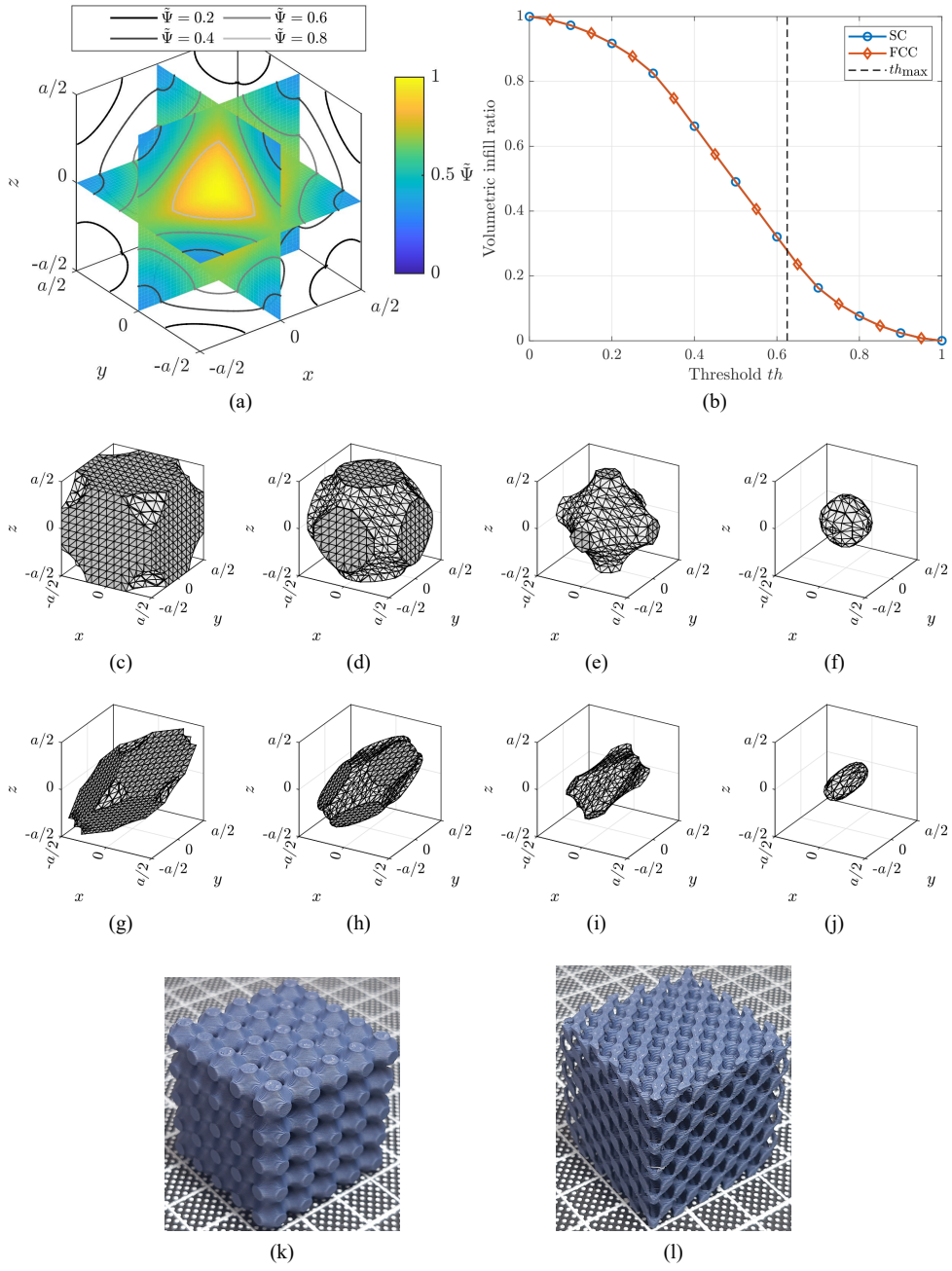

Figure 3.4: (a) Superimposed spatial harmonics $\tilde{\Psi}$ for SC symmetry, (b) volumetric infill ratio of SC and FCC symmetries as function of the threshold parameter and indication of the maximal threshold $th_{\max}$ for a connected lattice. Unit cells created by imposing a threshold th on $\tilde{\Psi}$ of the respective SC and FCC symmetries. (c) SC $th = 0.2$, (d) SC $th = 0.4$, (e) SC $th = 0.6$, and FCC unit cells (f) SC $th = 0.8$, (g) FCC $th = 0.2$, (h) FCC $th = 0.4$ and (i) FCC $th = 0.6$, (j) FCC $th = 0.8$. (k,l) Examples of manufactured lattices based on harmonic superposition (k) SC and (l) FCC symmetry.

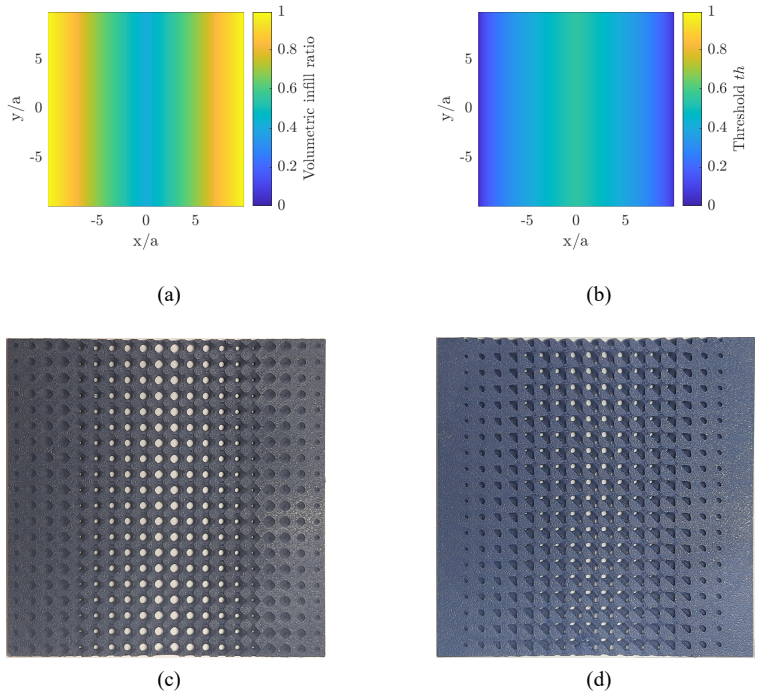

Figure 3.5: Demonstration of the SVL algorithm to create spatially modulated periodic lattices. (a) Volumetric infill, and (b) threshold parameter as a function of spatial coordinates and corresponding implementations of a $10 \times 10 \times 1$ lattice with a unit cell size of $a = 5$ mm with (c) SC and (d) FCC symmetry.

in Figures 3.5c and 3.5d, respectively. This concept is utilized heavily in the application oriented research presented in Chapters 7, and 9.

3.3. Manufacturing

3.3.1. Equipment

As mentioned in Section 2.1.3, commercially available additive manufacturing tools that can handle multiple different materials and even both dielectric and conductive materials in the same process are prohibitively expensive[2]. For this reason, an additive manufacturing setup with basic hybrid capabilities was put together for the purposes of this work. The manufacturing setup is based on a *core-XY* tool-changing concept based on the E3D motion system platform equipped with four independent tools that can be switched during the print process, allowing for flexible multi-material printing. In this case, the system is equipped

[2] While this was indeed the case at the time of conception of this thesis, low-cost hardware for semi-professional extrusion based additive manufacturing has been rapidly evolving over the last decade leading to sufficiently advanced commercially available machines with the necessary capabilities at a moderate price tag.

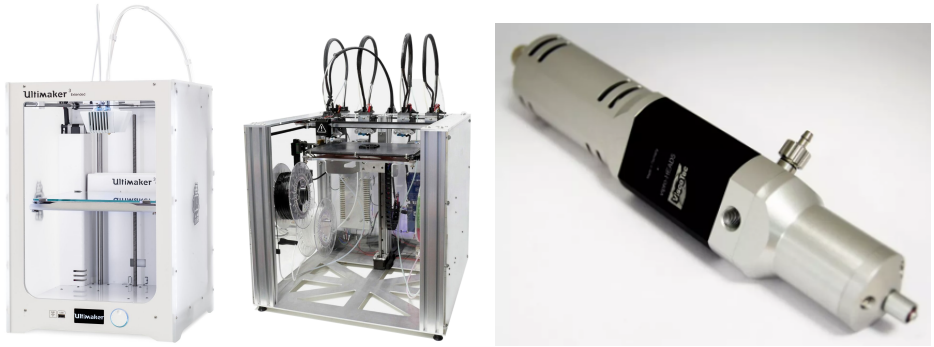

(a) (b) (c)

Figure 3.6: Manufacturing equipment utilized in this work. (a) Ultimaker 3, (b) custom built printing system based on the E3D Toolchanger concept with four independent tools, (c) ViproHead micro-dispensing print head for dispensing viscous inks and pastes.

Table 3.2: Overview of some properties of the thermoplastic print materials utilized throughout this work

Material	Manufacturer	Density	Cost	Permittivity	Loss Tangent
PLA	Ulitmaker	1.24 $\mathrm{g\,cm^{-3}}$	56 $\mathrm{€kg^{-1}}$	2.66	6.0E-2
ABS	Sunlu	1.05 $\mathrm{g\,cm^{-3}}$	17 $\mathrm{€kg^{-1}}$	2.3	2.0E-2
HIPS	FormFutura	1.03 $\mathrm{g\,cm^{-3}}$	33 $\mathrm{€kg^{-1}}$	2.25	4.0E-4
ABS300	Avient	1.12 $\mathrm{g\,cm^{-3}}$	180 $\mathrm{€kg^{-1}}$	3 ± 0.1	4.6E-3
ABS500	Avient	1.56 $\mathrm{g\,cm^{-3}}$	340 $\mathrm{€kg^{-1}}$	5 ± 0.15	3.6E-3
ABS650	Avient	1.80 $\mathrm{g\,cm^{-3}}$	420 $\mathrm{€kg^{-1}}$	6.5 ± 0.2	3.4E-3
ABS1500	Avient	2.85 $\mathrm{g\,cm^{-3}}$	654 $\mathrm{€kg^{-1}}$	15 ± 0.7	1.8E-3
COC	Ceramelt	1.01 $\mathrm{g\,cm^{-3}}$	151 $\mathrm{€kg^{-1}}$	2.45	2.0E-4

with three E3D Hemera filament extruders to enable the processing of up to three dielectrics and a third-party print-head, Vipro-HEAD 3 from VisoTec GmbH, for silver ink dispensing. The ViproHead print-head is selected due to its precise dispensing capabilities and stepper motor interface, which allows straightforward integration into the existing print hardware. The manufacturing setup is controlled via industry standard G-Code machine instructions prepared with the open-source slicer software *Prusa Slicer*.

3.3.2. Materials

Throughout the individual chapters of this thesis, a range of different thermoplastic print materials are utilized, and their properties are summarized in Table 3.2. Print settings for individual parts depend primarily on the utilized office diameters and whether or not multiple materials are used throughout the print. Settings pertaining to individual prints are therefore reported throughout the text at appropriate places. For hybrid prints that require conductive material, the silver ink Bectron CP6662 from Elantas is used. This ink provides low surface resistivity and the capability of curing with moderate temperatures of about 110°C, making it suitable to work with most of the thermoplastics listed in Table 3.2.

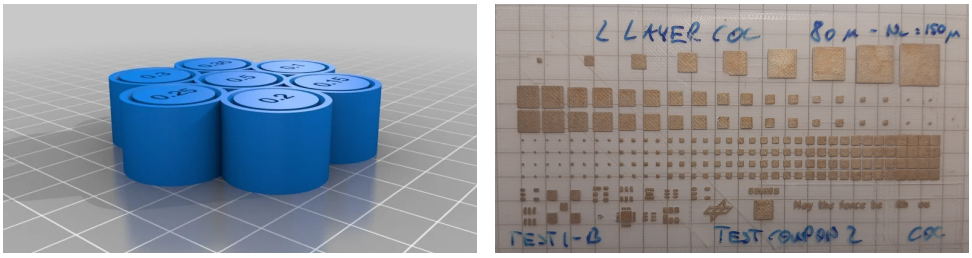

(a) (b)

Figure 3.7: Test coupon showing the capabilities of the custom-built extrusion-based hybrid AM system. Quadratic test shapes with different sizes and clearances as well as commonly used PCB component footprints created with dispensed, highly conductive silver ink Bectron CP6662 on printed transparent low-loss substrate material cyclo olefin copolymer (COC).

3.3.3. Accuracy and Tolerances

Several test prints are carried out to judge the system's repeatability and tolerance. For dielectric parts, test according the fashion of [103], as depicted in Figure 3.7a, are performed and showed that the system is able to produce parts with about $\pm 90\mu m$ for a print orifice with a diameter of $0.2mm$, $\pm 150\mu m$ for a print orifice with a diameter of $0.4mm$. Another test print to study the ink dispensation via quadratic test shapes with different sizes and clearances as well as commonly used PCB component footprints printed on transparent low-loss substrate material COC accuracy is visible in Figure 3.7b. From which tolerances of about $\pm 120\mu m$ in the lateral dimensions are extracted via measurement through a digital microscope for the conductive shapes dispensed with a print orifice diameter of $150\mu m$ and a layer height of $40\mu m$.

4

Homogenization and Characterization of Dielectric Crystals

Abstract
This chapter serves to judge the suitability of dielectric material parameter homogenization and characterization techniques, as reviewed in Section 2.2, for the purposes of this thesis. To this end several techniques for the homogenization and experimental characterization for dielectric properties of periodic structures are explained, their trade-offs discussed and individual results compared. Numerically obtained results from the eigenmode method and Floquet port scattering are compared with traveling wave measurements in both guided and free-space setups. Furthermore, the shortcomings of effective media theories and resonance measurement methods are addressed and contrasted against broadband methods. Additionally an electrostatic method based on an equivalent parallel plate capacitor method is introduced. Individual homogenization methods and measurement setups are reviewed with respect to dielectric crystals with simple cubic (SC) and face-centered cubic (FCC) symmetry, with different unit cell sizes and volumetric infill fractions. Extracted effective permittivity values from plane wave expansion method (PWEM) and Floquet scattering simulations show excellent agreement with traveling wave measurements in both guided and free-space scenarios. Furthermore, the discussed broadband methods predict and measure frequency-dependent effects that are not covered by effective media theories and resonance measurement setups, highlighting the necessity to adopt more sophisticated simulation tools for the design of graded-index devices. It is shown that the effective media bandwidth of dielectric crystals depends on the respective unit cell symmetry and that FCC symmetry obtains a significantly increased bandwidth compared to SC symmetry.

4.1. Motivation and Structure

The ability of additive manufacturing (AM) to create intricate periodic structures with different volumetric fill fractions of some base materials is especially well suited to engineer the effective properties of said periodic structures. This allows to introduce additional degrees of freedom in the design of high-frequency electromagnetic (EM) devices as reviewed in Section 2.3. The successful design of dielectric crystals graded-index (GRIN) devices requires solid knowledge of the constituent materials' permittivities, both as bulk medium and as a function of volumetric infill fraction. Furthermore, it is necessary to ensure that the periodic structure behaves like an effective material over the desired bandwidth of operation. Due to the periodic nature of dielectric crystals, a natural cut-off frequency arises where the propagating wave will experience internal scattering, resulting in non-linear dispersion. A commonly utilized approximation is that the unit cell should be ten times smaller than the smallest applied wavelength [96]. However, a more detailed study of this upper cut-off frequency is missing in the relevant literature. Generally, homogenization and characterization techniques employed to analyze dielectric crystals often rely on effective media theories (EMT) and resonance measurement setups which are ill suited to study frequency dispersion of EM waves in periodic media. Individual works have employed more sophisticated methods to model the broadband effective permittivity of dielectric crystals. For example, the plane wave expansion method (PWEM) is employed in [82] to predict the permittivity tensor of a uniaxial anisotropic periodic dielectric. Furthermore, Floquet port scattering simulations in combination with the Nicholson-Ross-Weir method is utilized in [36] to model anisotropic permittivity. However, there appears no comprehensive discussion of the different relevant techniques in the literature yet.

The work presented in this chapter intends to address this gap and investigates frequency-dependent effective material parameters of additive-manufactured dielectric crystal lattices via several independent computational and experimental techniques. The effect of unit-cell geometry, symmetry, and material on the effective permittivity is studied over a large frequency range up to effective media cut-off and beyond. Special attention is given to the effective media upper cut-off frequency of the studied periodic structures. It is worth highlighting that, although the discussed techniques have been employed and reported on independently, no comprehensive comparison of their respective predictions and discussion of their limitations and trade-offs have been published yet. The presented techniques can be applied to study effects of different crystal symmetries, effective material bandwidths, and dispersion characteristics of dielectric crystals and GRIN devices. To this end different unit cells sizes, volumetric infills, and crystal symmetries are considered based on the spatial harmonic superposition method explained in Section 3.2.2 and depicted in Figure 3.4. As discussed in Section 3.2 the discussion presented in this thesis is limited to dielectric crystals that are comprised of two materials, a manufacturing material with relative permittivity $[\varepsilon_{\mathrm{r,m}}]$ and a background material $[\varepsilon_{\mathrm{r,b}}]$. For the purposes of this chapter it is assumed that both the manufacturing and background materials are isotropic $[\varepsilon_{\mathrm{r,m}}] = \varepsilon_{\mathrm{r,m}}, [\varepsilon_{\mathrm{r,b}}] = \varepsilon_{\mathrm{r,b}}$.

The remainder of this chapter is structured as follows. Section 2 explains a range of homogenization methods in detail, compares results obtained for a variety of dielectric crystals, and provides a discussion of their respective trade-offs. Section 3, similar to Section two, provides insights resonant, waveguide, and free space characterization methods. Represen-

tative setups for each measurement method are used to extract the effective permittivity of dielectric crystals with different properties. The results obtained are compared to results extracted via the various homogenization techniques presented in Section 2. Section 4 discusses the presented work and results, while Section 5 provides conclusions to the chapter.

4.2. Homogenization Techniques

4.2.1. Effective Media Approximation

As a representative of effective media theories, as reviewed in Section 2.2.1, this thesis considers the Maxwell-Garnett approximation (MGA), which is commonly employed in literature for modeling the effective permittivity of additive-manufactured structured dielectrics. It regards the idealized case of a two-component mixture of isotropic dielectrics with spherical inclusions of relative permittivity $\varepsilon_{\mathrm{r,MGA,i}}$ and volume fraction δ_{i}, in a host medium with relative permittivity $\varepsilon_{\mathrm{r,MGA,m}}$. The MGA gives the algebraic relationship for the effective permittivity $\tilde{\varepsilon}_{\mathrm{r,MGA,eff}}$ of the mixture as [30]

$$\frac{\tilde{\varepsilon}_{\mathrm{r,MGA,eff}} - \varepsilon_{\mathrm{r,MGA,m}}}{\left(\tilde{\varepsilon}_{\mathrm{r,MGA,eff}} + 2\varepsilon_{\mathrm{r,MGA,m}}\right)} = \delta_{\mathrm{i}} \frac{\varepsilon_{\mathrm{r,i}} - \varepsilon_{\mathrm{r,MGA,m}}}{\left(\varepsilon_{\mathrm{r,MGA,i}} + 2\varepsilon_{\mathrm{r,MGA,m}}\right)}. \tag{4.1}$$

Despite reports that the MG rule lacks accuracy at higher volume fractions [104], it has been used successfully to predict effective permittivities of periodic dielectrics [105] and for the design of GRIN devices [106], even when the simplified assumption of perfectly spherical inclusions does not apply. Therefore, equation (4.1) can be used to estimate the effective permittivity of the dielectric crystals $\tilde{\varepsilon}_{\mathrm{r,eff}}$ assuming the manufacturing material $\varepsilon_{\mathrm{r,m}} = \varepsilon_{\mathrm{r,MGA,m}}$ as host and the background material $\varepsilon_{\mathrm{r,b}} = \varepsilon_{\mathrm{r,MGA,i}}$ as inclusion.

Figure 4.1 displays the computed effective permittivity $\tilde{\varepsilon}_{\mathrm{r,eff}}$ for an SC and FCC unit cell as a function of the threshold th, as defined in Section 3.2.2, as a function of the threshold parameter th. The MGA, as it is based on electrostatic assumptions, is not suitable to predict any frequency dependent effects nor is it capable to study anisotropic effective permittivity. Numerical values for the computed effective permittivity values are listed and compared to results obtained from an Eigenmode method and Floquet port scattering simulations in Table 4.1.

4.2.2. Equivalent Parallel Plate Capacitor Model

The parallel plate capacitor, as depicted in Figure 4.2 with perfectly conducting plates of area A, separated by some dielectric with permittivity ε_{r} and thickness D, is one of the simplest electrostatic devices and its capacitance C is expressed as

$$C = \varepsilon_0 \varepsilon_{\mathrm{r}} \frac{A}{D} \tag{4.2}$$

with ε_0, corresponding to the permittivity of free space. In case of an anisotropic permittivity, the direction of the electric field in the dielectric needs to be taken into account, resulting on different capacitance values C_{x}, C_{y} and C_{z} depending on the orientation of the substrate between the parallel plates, as indicated in Figure 4.2. If the capacitances C_{x}, C_{y} and C_{z} are

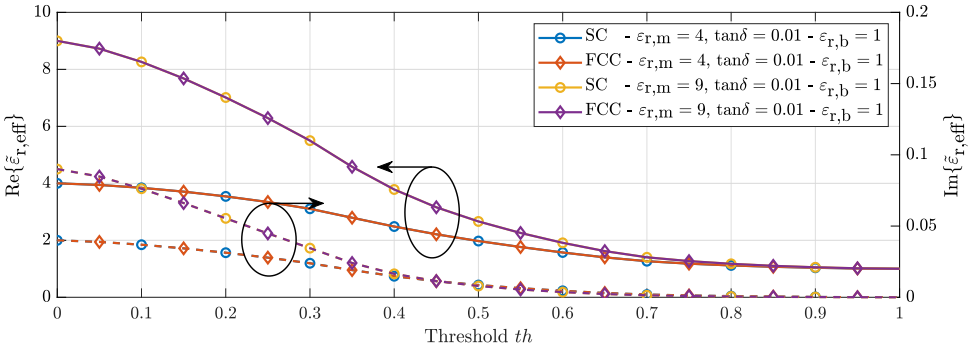

Figure 4.1: Effective relative permittivity of simple cubic (SC) and face-centered cubic (FCC) dielectric crystals with $\varepsilon_{r,i} \in [4, 9]$ and loss tangent $\tan\delta = 0.01$ as a function of th obtained via the Maxwell-Garnett approximation.

known, the corresponding effective permittivity tensor components can be calculated

$$\varepsilon_{r,xx} = \frac{C_x D}{\varepsilon_0 A} \tag{4.3}$$

$$\varepsilon_{r,yy} = \frac{C_y D}{\varepsilon_0 A} \tag{4.4}$$

$$\varepsilon_{r,zz} = \frac{C_z D}{\varepsilon_0 A}. \tag{4.5}$$

Generally an exact solution of the capacitance with a heterogeneous and/or anisotropic permittivity requires the solution of Laplace's equation which is difficult to obtain in closed form for complex structured geometries. This work proposes a simplified semi-analytical method to compute these capacitances derive the equivalent permittivity tensor components.

It is well known that equation (4.2) does not account for fringing fields on the edges of the plates and, therefore, only produces reasonably accurate results for $D << A$. However, in this work, a 2D-infinite periodic media between the virtual parallel PEC plates is assumed, which allows to limit the investigation to the volume of the unit cell itself and neglect the influence of fringing fields on the outer plate edges due to the periodic nature of the fields.

Semi-analytical Solution

In this approach the permittivity tensor in the unit cell, as described by equation (3.19), is discretized into individual homogeneous volumes via a regular grid

$$[\varepsilon_r]_{i,j,k} = \begin{bmatrix} \varepsilon_{r,xx,i,j,k} & 0 & 0 \\ 0 & \varepsilon_{r,yy,i,j,k} & 0 \\ 0 & 0 & \varepsilon_{r,zz,i,j,k} \end{bmatrix}, \; i = 1 \cdots N_x, \; j = 1 \cdots N_y, \; k = 1 \cdots N_z \tag{4.6}$$

with N_x, N_y and N_z elements in the corresponding directions.

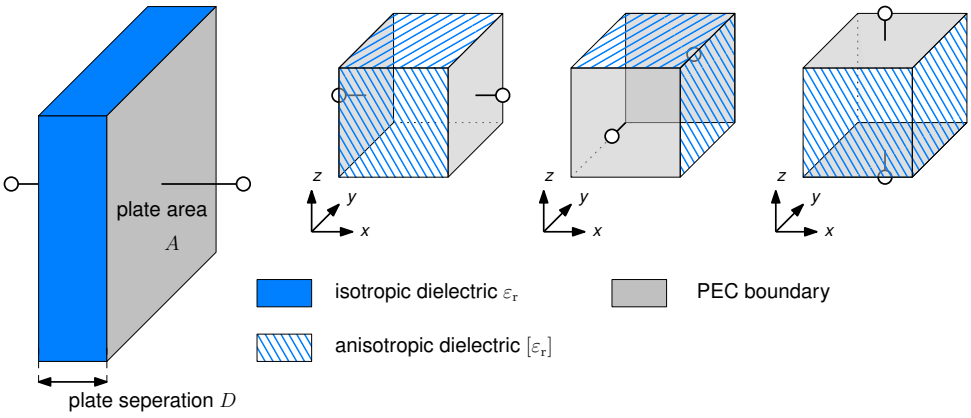

Figure 4.2: Schematic representation of the parallel plate capacitor with an isotropic dielectric and an anisotropic dielectric where the resulting capacitance depends on the axis in which the parallel plates are applied.

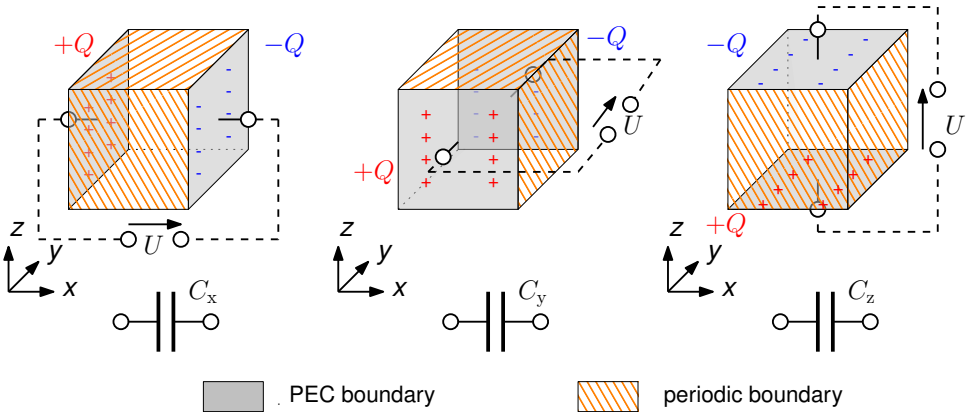

Figure 4.3: Schematic representation of simulation concept applied for the equivalent parallel plate capacitor model to extract the main diagonal components of the effective permittivity tensor.

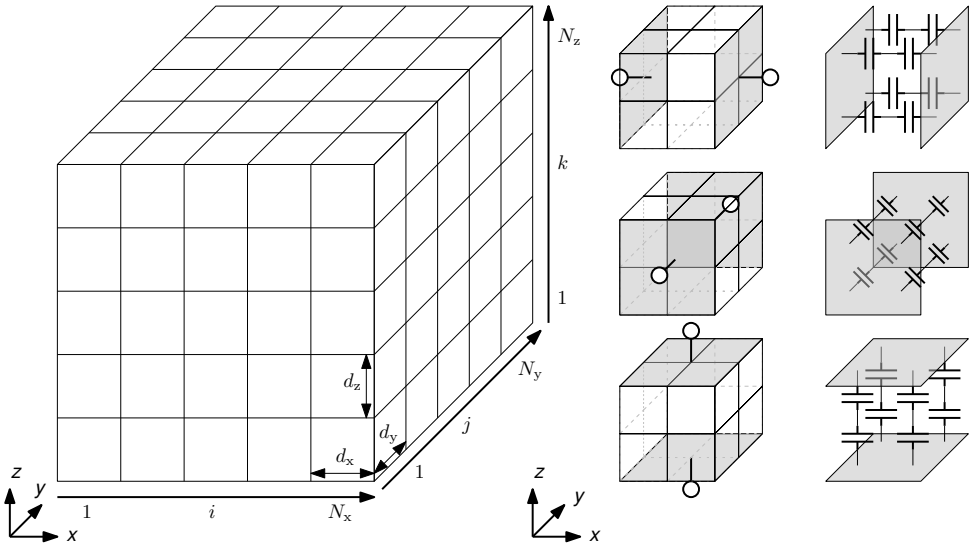

Figure 4.4: Unit cell discretized via a regular grid with N_x, N_y and N_z sections (left) and the representation of equivalent capacitance networks for computations of the equivalent capacitance along x, y and z.

For each section and direction one can compute an equivalent capacitance according to

$$C_{\mathrm{x,i,j,k}} = \varepsilon_0 \varepsilon_{\mathrm{r,xx,i,j,k}} \frac{d_\mathrm{y} d_\mathrm{z}}{d_\mathrm{x}} \tag{4.7}$$

$$C_{\mathrm{y,i,j,k}} = \varepsilon_0 \varepsilon_{\mathrm{r,yy,i,j,k}} \frac{d_\mathrm{x} d_\mathrm{z}}{d_\mathrm{y}} \tag{4.8}$$

$$C_{\mathrm{z,i,j,k}} = \varepsilon_0 \varepsilon_{\mathrm{r,zz,i,j,k}} \frac{d_\mathrm{x} d_\mathrm{y}}{d_\mathrm{z}} \tag{4.9}$$

The capacitance for the whole unit cell can then be easily computed via the equivalent network of series and parallel capacitances

$$C_\mathrm{x} = \sum_{k=1}^{N_z} \sum_{j=1}^{N_y} \left[\sum_{i=1}^{N_x} \frac{1}{C_{\mathrm{x,i,j,k}}} \right]^{-1} \tag{4.10}$$

$$C_\mathrm{y} = \sum_{k=1}^{N_z} \sum_{i=1}^{N_x} \left[\sum_{j=1}^{N_y} \frac{1}{C_{\mathrm{y,i,j,k}}} \right]^{-1} \tag{4.11}$$

$$C_\mathrm{z} = \sum_{i=1}^{N_x} \sum_{j=1}^{N_y} \left[\sum_{k=1}^{N_k} \frac{1}{C_{\mathrm{z,i,j,k}}} \right]^{-1} \tag{4.12}$$

Once the equivalent capacitances are known, the effective permittivity tensor components can be calculated via equations (4.3) - (4.5).

Of course this method relies on the approximation that the electric field and the dielectric displacement within the individual permittivity sections are perfectly perpendicular to the applied virtual perfectly conducting plates and ignores the contribution of fringing fields at the interfaces between different dielectric media. The contribution of fringing fields are increasingly significant for large contrasts in the permittivities of the two materials and expected to introduce a significant error in this model for such cases.

Numerical Solution

To account for the fringing fields at the interfaces between different dielectrics in the unit cell, one is able to utilize a numeric electrostatic solver. In the context of this work the commercial numerical software package CST is utilized. The computation is set up with a constant potential U between perfectly electrically conducting (PEC) boundary conditions along the principal axis for which the capacitance shall be computed and periodic boundary conditions perpendicular to it. The solver is set up to calculate the charge Q accumulating on the PEC boundaries, and the equivalent capacitance is simply found via

$$C = Q/U. \tag{4.13}$$

Performing this computation for PEC boundaries along the x,y, and z directions, provides the capacitances C_x, C_y and C_z. As already mentioned above, once the equivalent capacitances are known, the corresponding equivalent permittivity tensor components can be computed via equations (4.3) - (4.5). The homogenization is carried out using the following procedure:

1. **Simulation Setup**: The geometry under investigation is enclosed within a cubic envelope. Three separate simulations are conducted to determine the diagonal components of the permittivity tensor

2. **Boundary Conditions**: For each diagonal component, specific boundary conditions are applied:

   - To compute ($\varepsilon_{\mathrm{xx}}$), perfect electric boundary conditions are imposed on the faces of the cube perpendicular to the x-axis, effectively creating an equivalent parallel plate capacitor along this axis.
   - Periodic boundary conditions are applied on the faces perpendicular to the y- and z-axes to simulate an infinite periodic structure in the transverse directions.

3. **Excitation**: A constant potential difference U is applied between the perfect electric boundaries along the x-axis.

4. **Capacitance Calculation**: The simulation calculates the charge Q that accumulates on the boundaries as a result of the applied potential difference.

5. **Effective Permittivity Extraction**: From the computed charge, the capacitance of the geometry along the x-axis C_x is determined via

$$C_\mathrm{x} = \frac{Q}{U}. \tag{4.14}$$

The effective permittivity tensor component ε_{xx} is then calculated using the relationship between the capacitance, geometry, and permittivity of the parallel plate capacitor

$$C_x = \varepsilon_0 \varepsilon_{r,xx} \frac{A}{d} \tag{4.15}$$

where A denotes the area of the perfectly conducting plate and d the plate seperation.

6. **Repetition for Other Components**: The procedure is repeated with appropriate boundary conditions aligned along the y-axis and z-axis to determine $\varepsilon_{r,yy}$ and $\varepsilon_{r,zz}$ respectively.

Although the electrostatic method supported by numerical simulations is accurate in determining the components of the effective permittivity tensor, it lacks the capability to make prediction about dispersion in the lattice. The eigenmode and full-wave scattering techniques discussed in the following two sections address this issue.

Semi-analytical vs. Numeric

While the semi-analytical method to calculate the effective permittivity tensor components is computationally simple, it also introduces an error in the calculation due to the neglect of fringing fields at dielectric interfaces in the unit cell. This effect gets more pronounced with increasing contrast in relative permittivity between the two dielectrics.

4.2.3. Eigenmode Method

As explained in Section 3.1.3, EM waves propagating in periodic dielectric media experience frequency dispersion. The frequency dispersion for given propagation vectors in the lattice can be obtained by solving the wave equation (3.18) The Eigenmode method computes the eigenvectors in the infinite 3D lattice that fit the phase boundary condition imposed by a given Bloch wave vector β and its corresponding eigenvalue (angular frequency ω). The PWEM is an efficient Fourier space technique to solve the eigenvalue problem [107]. A complete analysis of the crystal with this method requires a dense sampling of Bloch vectors in the Brillouin zone of the crystal, which is computationally demanding. Therefore, the PWEM is usually evaluated for Bloch vectors on a path between the key points of symmetry, around the boundary of the irreducible Brillouin zone (IBZ) of the crystal as depicted in Figures 4.5b and 4.5d. [108]. The results of this reduced analysis are usually presented via band diagrams that display the eigenfrequencies of the individual modes as a function of the Bloch vector around the IBZ. The band diagram with the first ten modes for a unit cell with SC and FCC symmetry, created via $N = 3$ spatial harmonics and a threshold of $th = 0.5$, is depicted in Figure 4.5e and 4.5f respectively together with the light line of the fundamental mode. The light line represents the dispersion of the crystal if it is made from homogeneous material with the effective material parameters exhibited by the periodic crystal geometry.

The fundamental modes for both the SC and FCC lattice show a linear dispersion characteristic for low-magnitude Bloch vectors (around the Γ key point of symmetry) as assumed by effective media theories. However, for increasing Bloch vector magnitudes and wavelengths approaching the size of the unit cell, the assumption of linear dispersion for the dielectric crystal does not hold. In the band diagram, this is visible via the divergence of the bands from the light line. A normalized cut-off frequency $\omega_{n,c}$ is defined, for which the

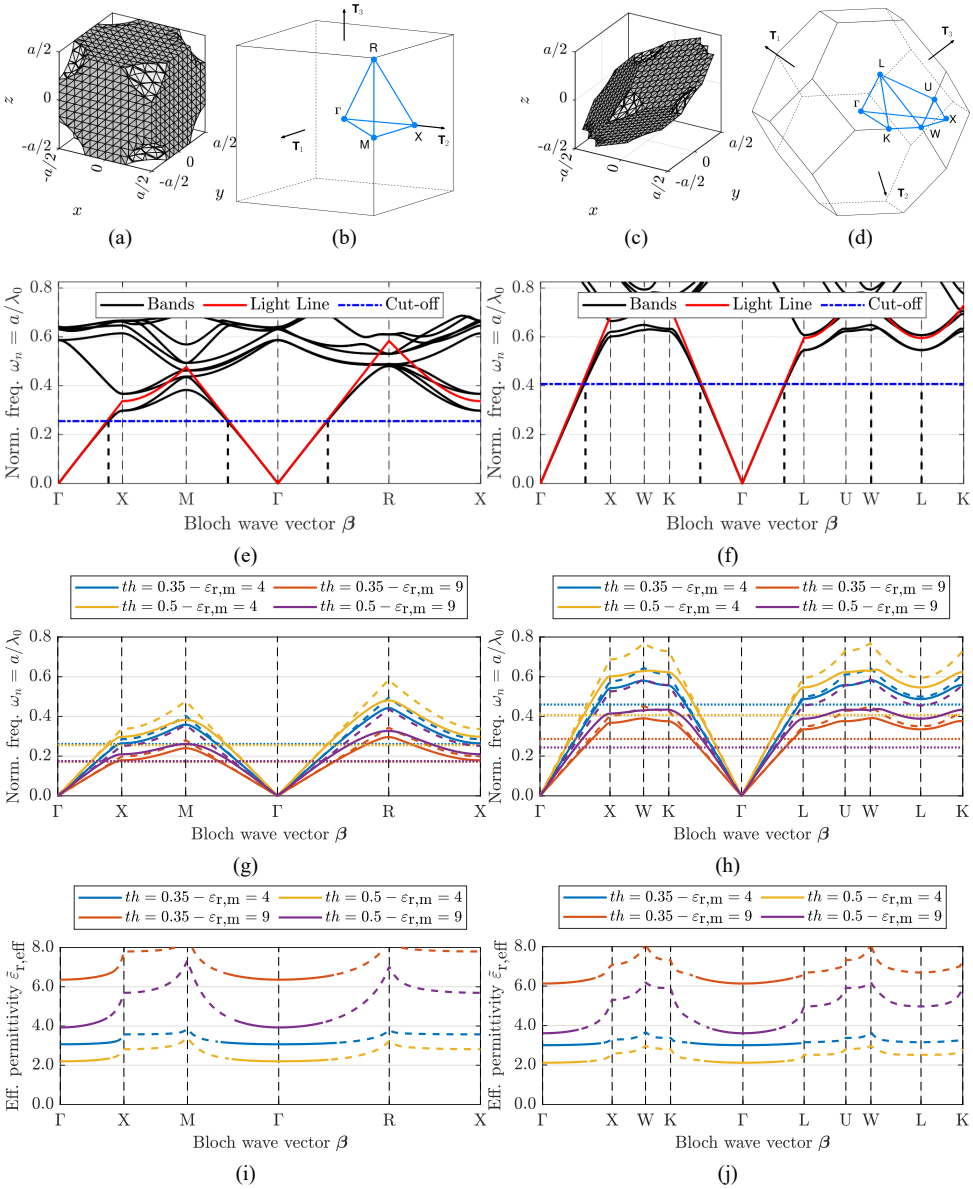

Figure 4.5: Unit cell geometries and corresponding irreducible Brillouin zones and their respective key points of symmetry of (a,b) simple cubic (SC) and (c,d) face centered cubic (FCC) crystals. The respective band diagrams of the SC (e) and FCC (f) unit cells via the PWEM method). Extracted fundamental modes of the SC (g) and FCC(h) dielectric crystals with different $\varepsilon_{r,i}$ and volumetric infill fractions th, and the further computed effective relative permittivities of the SC (i) and FCC (j) lattice.

divergence with respect to the light line is less than 1%, indicated by the dashed blue line in Figures 4.5e and 4.5f respectively. For the case of linear dispersion, the effective material refractive index n_{eff} can be extracted from the slope of the dispersion curve via

$$n_{\text{eff}} = \frac{|\beta|}{k_0} = \sqrt{\varepsilon_{\text{r,eff}}\mu_{\text{r}}} \tag{4.16}$$

which for purely dielectric media ($\mu_{\text{r}} = 1$), is the square root of the effective relative permittivity. The effect of crystal permittivity and the threshold is studied via the fundamental modes of SC and FCC dielectric crystals with thresholds $th \in [0.35, 0.5]$ and $\varepsilon_{\text{r,i}} \in [4, 9]$ together with their respective light lines (dashed lines), and normalized cut-off frequencies (dotted lines) that are plotted in Figures 4.5g and 4.5h respectively. Furthermore, their effective permittivities, computed via equation (4.16) are displayed in Figures 4.5i and 4.5j respectively and effective permittivity values represented with solid lines indicate values where the linear dispersion approximation gives less than 1% error. Already within the arbitrarily defined effective media theory cut-off of 1% divergence from the light line, one can observe a drastic change in the effective permittivity values. An interesting observation is the increased cut-off frequency of the linear dispersion in the FCC crystal at $\omega_{\text{n,c}} \approx 0.4$, compared to the SC crystal where the cut-off already appears at $\omega_{\text{n,c}} \approx 0.25$. Generally, the cut-off is shifted to lower normalized frequencies for increasing values of the dielectric crystal material permittivity $\varepsilon_{\text{r,m}}$ and decreasing thresholds th (increasing volumetric infill fraction). This observation can be explained by the higher effective permittivity of the dielectric crystal $\tilde{\varepsilon}_{\text{r,eff}}$ for increasing $\varepsilon_{\text{r,m}}$ and decreasing th, and the resulting shorter wavelength of a wave propagating in the crystal. The unit cell size does not influence the shape and behavior of the bands with respect to the normalized frequency. Numerical values for the estimated cut-off frequency and extracted effective permittivity for a normalized frequency corresponding to 2 GHz are listed and compared to results obtained from MGA and Floquet port simulation in Table 4.1.

4.2.4. Floquet Scattering

While the PWEM is a useful tool, 3D infinite lattices and plane waves are difficult to approximate in experimental setups. A widely employed method to circumvent this problem when dealing with the characterization of periodic structures is to compute the scattering of a 2D infinite slab via a Floquet port simulation. Modeling the material in terms of reflection and transmission parameters is favorable because these quantities are relatively easy to obtain with real-world measurement setups. For the simulation, the unit cell is set up with periodic boundary conditions along two axes and Floquet excitation along the third, as depicted in Figure 4.6. This setup allows the simulation of scattering of a semi-infinite slab of the material under test (MUT) with variable angles of incident and polarization. Based on the scattering parameters S_{11} and S_{21} one is able to extract effective parameters based on the Nicholson-Ross-Weir (NRW) method [109][110]. Although the NRW method can extract both complex permittivity and permeability of a MUT, the extraction of both complex quantities causes ill-behavior of the procedure at frequencies corresponding to one-half wavelength in the sample [111]. As this work only deals with dielectric materials, the assumption $\mu_r = 1$ is generally imposed on the utilized NRW procedure. The definition of all-dielectric materials leads to a more accurate and stable computation of the MUT's com-

plex permittivity [111]. Floquet port simulations have been carried out for SC and FCC crystals with $\varepsilon_{\mathrm{r,m}} \in [4,\ 9]$ and loss tangent $\tan\delta = 0.01$, thresholds $th \in [0.35,\ 0.5]$ and unit-cells sizes $a \in [7.5\mathrm{mm},\ 10\mathrm{mm}]$. The unit cells in simulations are oriented such that the wave is propagating along the $\Gamma - X$ direction. The scattering parameters from simulations are used to compute the effective material permittivity $\tilde{\varepsilon}_{\mathrm{r,eff}}$ which are displayed for the different crystal symmetries and unit cell sizes in Figure 4.7. For all simulations, a constant effective permittivity is observed for lower frequencies. However, at higher frequencies, resonances start to appear in the extracted effective permittivity values, corresponding to the cut-off frequency where the effective media approximation breaks down. Generally, one is able to observe a much-increased cut-off for FCC crystals which is in accordance with the observations in the previous section, where the behavior of the crystal was studied via the PWEM method. Furthermore, the same conclusions as from the PWEM investigation about the effect of crystal permittivity $\varepsilon_{\mathrm{r,m}}$ and threshold th can be drawn from the Floquet port simulations. The cut-off shifts to lower frequencies for higher $\varepsilon_{\mathrm{r,m}}$ and lower th (higher volumetric infill). Additionally, the effect of the unit cell size is clearly visible as it does not change the values or behavior of the extracted material parameters but only shifts them in frequency. Numerical values for the estimated cut-off frequency and computed effective permittivity are listed and compared to results obtained from MGA and the PWEM method in Table 4.1. Extracting anisotropic material parameters with this method

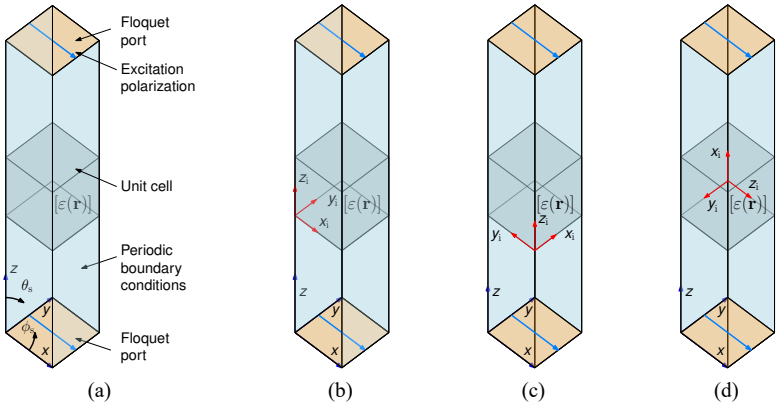

Figure 4.6: Schematic representation the Floquet port scattering method to numerically characterize materials. (left) general description. (right) rotated internal coordinate systems of the unit cell to align individual tensor components with the excitation polarization.

can be achieved using two different approaches. On the one hand, it is possible to subject the unit cell to normal incident plane waves while being oriented such that the polarization of the incident plane wave aligns with the desired material properties of tensor components. On the other hand, extracting the material property tensor components while keeping the unit cell orientation fixed and simulating the plane wave illumination with several different incident angles as described in. Although the latter method is more general, it is also more challenging to implement, while the first method is sufficient for this work. Therefore, scattering simulations in this work are carried out as schematically depicted in Figure 4.6, with

Table 4.1: Comparison of simulation results for the effective permittivity $\tilde{\varepsilon}_{\mathrm{r,eff}}$ and effective media cut-off frequency f_{c} for dielectric crystals with different lattice constants a thresholds th and manufacturing material permittivity $\varepsilon_{\mathrm{r,m\ m}}$ obtained with the Maxwell-Garnett approximation (MGA), plane wave expansion method (PWEM) and Floquet scattering simulations.

Crystal parameters				**MGA**	**PWEM**			**Floquet port**	
-	a in mm	th	$\varepsilon_{\mathrm{r,m}}$	$\tilde{\varepsilon}_{\mathrm{r,eff}}$	$\tilde{\varepsilon}_{\mathrm{r,eff}}$ at ω_{n}	ω_{n}	f_{c} in GHz	$\varepsilon_{\mathrm{r,eff}}$ at 2 GHz	f_{c} in GHz
SC	10	0.35	4	$2.80 + \jmath 0.019$	3.07	0.067	7.82	$3.15 + \jmath 0.021$	8.34
SC	10	0.35	9	$4.61 + \jmath 0.025$	6.36	0.067	5.17	$6.53 + \jmath 0.046$	5.75
SC	10	0.5	4	$1.98 + \jmath 0.009$	2.20	0.067	7.64	$2.28 + \jmath 0.011$	9.73
SC	10	0.5	9	$2.68 + \jmath 0.008$	3.93	0.067	5.23	$4.12 + \jmath 0.024$	6.99
SC	7.5	0.35	4	$2.80 + \jmath 0.019$	3.07	0.05	10.43	$3.15 + \jmath 0.021$	11.12
SC	7.5	0.35	9	$4.61 + \jmath 0.025$	6.36	0.05	6.89	$6.53 + \jmath 0.046$	7.59
SC	7.5	0.5	4	$1.98 + \jmath 0.009$	2.20	0.05	10.19	$2.28 + \jmath 0.011$	12.88
SC	7.5	0.5	9	$2.68 + \jmath 0.008$	3.93	0.05	6.98	$4.16 + \jmath 0.024$	9.39
FCC	10	0.35	4	$2.68 + \jmath 0.018$	3.01	0.067	11.21	$3.15 + \jmath 0.021$	16.69
FCC	10	0.35	9	$4.29 + \jmath 0.021$	6.13	0.067	7.30	$6.49 + \jmath 0.047$	11.34
FCC	10	0.5	4	$1.98 + \jmath 0.009$	2.12	0.067	13.78	$2.21 + \jmath 0.011$	22.00
FCC	10	0.5	9	$2.68 + \jmath 0.008$	3.61	0.067	8.60	$3.89 + \jmath 0.027$	15.54
FCC	7.5	0.35	4	$2.68 + \jmath 0.018$	3.01	0.05	16.27	$3.15 + \jmath 0.021$	22.24
FCC	7.5	0.35	9	$4.29 + \jmath 0.021$	6.13	0.05	9.74	$6.49 + \jmath 0.047$	15.24
FCC	7.5	0.5	4	$1.98 + \jmath 0.009$	2.12	0.05	18.38	$2.21 + \jmath 0.011$	29.14
FCC	7.5	0.5	9	$2.68 + \jmath 0.008$	3.61	0.05	11.46	$3.89 + \jmath 0.027$	20.71

differently oriented unit cells to align tensor components of interest with the excitation polarization. The corresponding effective permittivity tensor components are extracted using the traditional NRW method.

4.2.5. Comparison of Homogenization Methods

To give a better overview of the results of the individual simulation methods, the results with respect to computed permittivity and estimated effective media theory cut-off frequency are summarized in Table 4.1. Effective permittivity values obtained from Floquet port simulations are displayed for the lowest simulation frequency of 2 GHz. In order to compare effective permittivity values obtained via the PWEM to the results extracted from Floquet port simulations, the values are computed at normalized frequencies ω_{n} corresponding to 2 GHz. The effective media cut-off frequency f_{c} is computed from PWEM results with the 1% divergence point from the light line. For the Floquet port results the effective media cut-off frequency is determined via the local maximum of the imaginary part of the effective permittivity at the first visible resonance.

While the results obtained via the PWEM and Floquet port simulations agree reasonably well with each other, one can observe a rather large discrepancy with respect to the results obtained via the MGA method. The error in the results obtained with the MGA method seems to be worse with decreasing threshold th or increasing volumetric fill-fraction, which is an effect also observed in [104]. The obtained cut-off frequencies agree reasonably well with each other for the SC crystals. However, they show significant disagreement for FCC

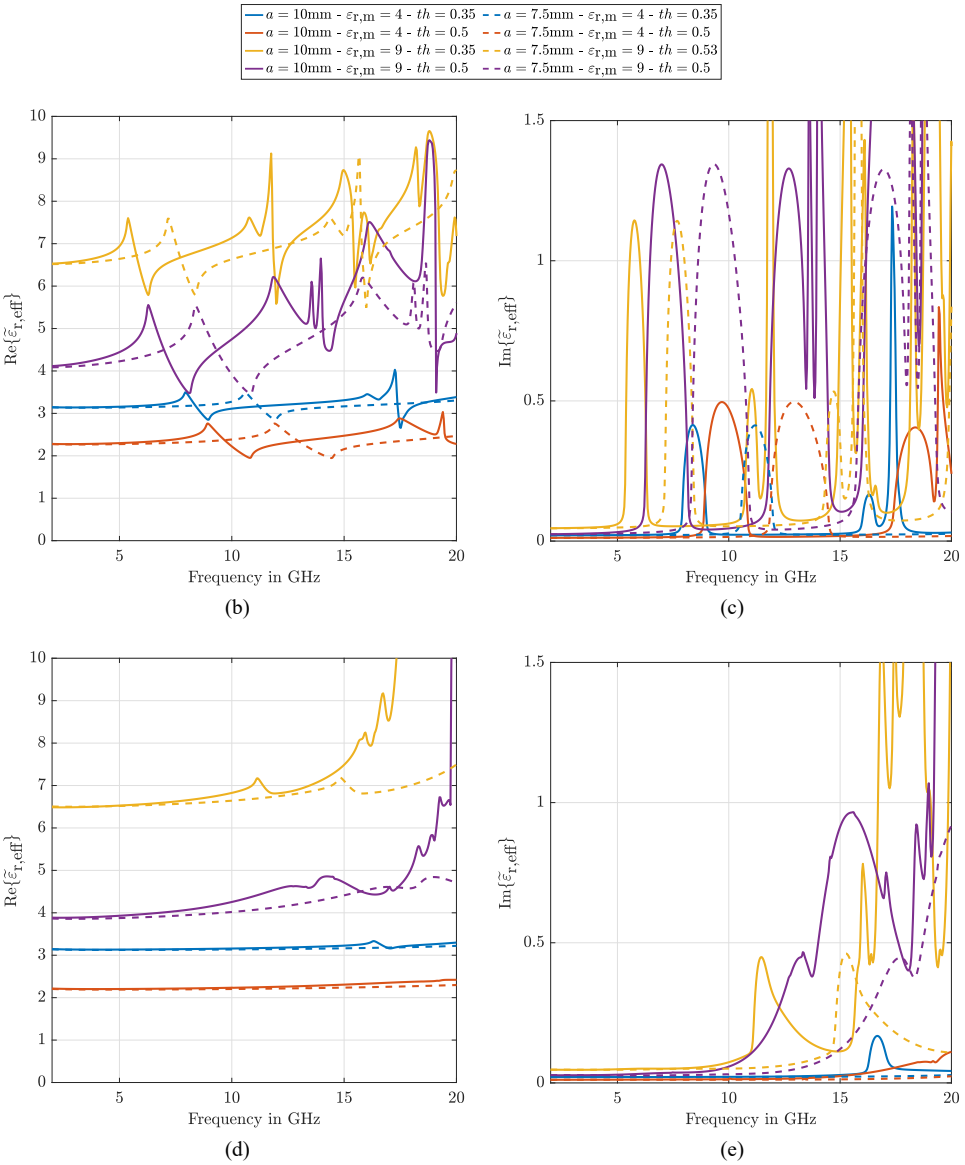

Figure 4.7: Complex effective relative permittivity $\tilde{\varepsilon}_{\mathrm{r,eff}}$ values of (b - real, c - imaginary) simple cubic and (d - real, e - imaginary) face-centered cubic dielectric crystals with different manufacturing material permittivities $\varepsilon_{\mathrm{r,m}}$ and thresholds th for unit cell sizes $a = 10$mm (solid lines) $a = 7.5$mm (dashed lines), computed from Floquet scattering simulations with the Nicholson-Ross-Weir method adapted for non-magnetic materials.

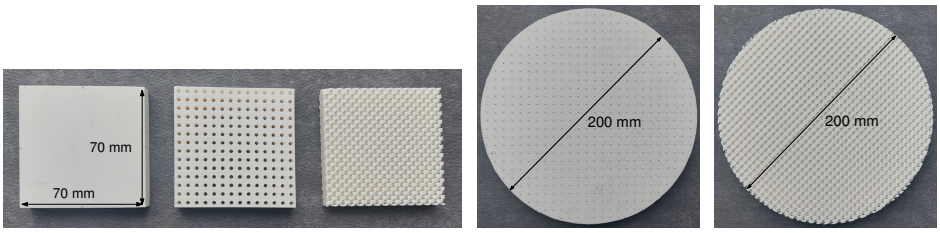

(a) (b) (c)

Figure 4.8: Additive manufactured dielectric crystal samples for material characterization. (a) Sample for measurement in a suspended microstrip measurement system, from left to right: bulk sample, simple cubic sample, face-centered cubic sample. (b) Simple cubic sample and (c) face-centered cubic sample for characterization in a free space traveling wave setup.

crystals where the Floquet port simulation shows very high cut-off frequencies. However, this issue can be explained by the ill-suited definition of the cut-off frequency in Floquet port simulations via the local maxima of the effective permittivities imaginary part. This definition was chosen for simplicity because these are easily identifiable. A more suitable definition of the cut-off shall be investigated in future work.

4.3. Characterization Methods

One experimental setup is considered for each of the characterization methods reviewed in Section 2.2.3, to characterize SC and FCC dielectric crystals with different threshold th and unit cell size a. The results are compared to predictions from the different simulation techniques discussed in the previous section.

Manufacturing of measurement samples for all methods is done with an Ultimaker 3 FDM additive manufacturing machine as described in Section 3.3.1 using the Ultimaker white polylactic (PLA) filament with properties listed in Table 3.2. All samples are manufactured with identical material and printing parameters[1] to ensure consistency of bulk material properties throughout the measurements. Prior to measurements of dielectric crystal samples, printed bulk samples of the selected material are subjected to measurements with the resonative setup, and it was found that it obtained a relative permittivity of $\varepsilon_{\mathrm{r,p}} = 2.66$ and a loss tangent of $\tan\delta_{\mathrm{p}} = 0.016$. Examples of the bulk, SC, and FCC samples used in the resonance and free space traveling wave setup are depicted in Figure 4.8. Measurements are carried out with samples oriented such that propagating waves through the samples would travel along the $\Gamma - X$ path of the crystal. In the resonance measurement setup the sample was oriented with the $\Gamma - X$ path normal to the microstrip ring resonator.

4.3.1. Resonant

The resonance measurement setup utilized in this work is based on a suspended microstrip ring resonator which has already been introduced in [112] and utilized for the characterization of 3D-printed dielectric crystals in [105]. Here a resonant setup to test predictions about

[1] Layer height 0.15mm; Nozzle diameter: 0.4mm; Nozzle temperature: 195°C; Bed temperature: 60°C; Max. printing speed: 50mm/s

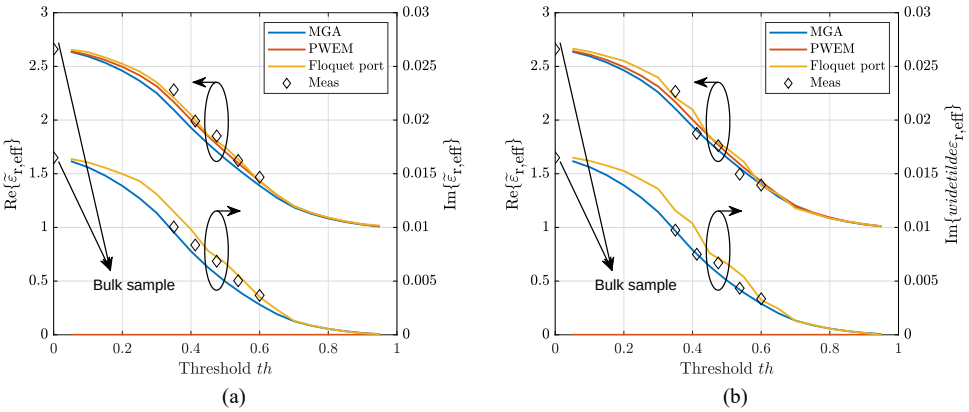

Figure 4.9: Extracted effective permittivities of (a) simple cubic and (b) face-centered cubic dielectric crystals with different thresholds obtained with a suspended microstrip resonator compared to results obtained via the Maxwell-Garnett approximation (MGA), plane wave expansion method (PWEM) and Floquet port simulations.

the effective permittivity obtained from MGA theory, PWEM, and Floquet port simulations. For this multiple lattices in SC and FCC with a range of different thresholds are manufactured with a lattice constant of $a = 5$ mm in a cubic volume of $70 \times 70 \times 10$ mm^3. The extracted effective permittivity results for the individual samples at the resonance frequency of the system f_{res} are listed in Table 4.2 as well as plotted together with simulation results as a function of th in Figure 4.9 for SC and FCC samples respectively. Care was taken that simulations results obtained via PWEM and Floquet port simulations are represented at frequency points corresponding to f_{res} of the measurements. Obviously, for PWEM data, no imaginary part of the effective permittivity is reported. While PWEM and Floquet port results show a better agreement with respect to the real part of the measured effective permittivity the MGA theory produces more accurate results concerning the measured imaginary part. For the SC samples, the predictions by PWEM and Floquet port simulations agree with the measurements well while the relative permittivity values obtained with the MGA produce a larger error. For the FCC no favorable simulation technique can be identified from the presented data.

4.3.2. Rectangular Waveguide

One option to circumvent the shortcomings of a resonance approach is to employ a traveling guided wave measurement system, where a MUT sample is fit into a waveguide and subjected to reflection and transmission measurements. This work utilizes a measurement system based on rectangular waveguides as depicted in Figure 4.10. Prior to the measurement of material samples, the setup is calibrated using a Through-Reflect-Line approach. The measurement is performed by inserting a MUT sample into the waveguide sample holder and recording transmission and reflection coefficients via a VNA. The effective material parameters are computed in post-processing via the NRW method. Although traveling-guided wave setups are considered broadband, they are usually only employed in the fundamental mode of the utilized waveguide. Therefore, this work makes use of several consecutive

Table 4.2: Characterization of additive manufactured dielectric crystals with simple cubic (SC) and face-centered cubic (FCC) geometries in terms of their dielectric permittivity and loss tangent via a resonant measurement setup compared to predictions obtained via the Maxwell-Garnett approximation (MGA), the plane wave expansion method (PWEM) and Floquet port scattering.

Sample		MGA		PWEM	Floquet Port		Measurement		
Crystal	th	$\tilde{\varepsilon}_{\mathrm{r,eff}}$	$\tan\delta$	$\tilde{\varepsilon}_{\mathrm{r,eff}}$ at f_{res}	$\tilde{\varepsilon}_{\mathrm{r,eff}}$ at f_{res}	$\tan\delta$	f_{res} in GHz	$\tilde{\varepsilon}_{\mathrm{r,eff}}$	$\tan\delta$
BULK	-	-	-	-	-	-	1.441	2.66	6.2E-3
SC	0.35	2.17	4.6E-3	2.17	2.21	5.2E-3	1.515	2.28	4.4E-3
SC	0.4125	1.98	3.9E-3	1.96	2.00	4.7E-3	1.581	1.99	4.2E-3
SC	0.475	1.79	3.3E-3	1.77	1.80	4.0E-3	1.616	1.85	3.7E-3
SC	0.5375	1.62	2.7E-3	1.60	1.63	3.4E-3	1.680	1.62	3.1E-3
SC	0.6	1.45	2.0E-3	1.43	1.43	2.5E-3	1.729	1.47	2.5E-3
FCC	0.35	2.17	4.6E-3	2.14	2.21	5.2E-3	1.518	2.27	4.3E-3
FCC	0.4125	1.98	4.0E-3	1.93	2.03	4.8E-3	1.609	1.88	4.0E-3
FCC	0.475	1.79	3.3E-3	1.75	1.79	4.0E-3	1.640	1.76	3.8E-3
FCC	0.5375	1.62	2.7E-3	1.56	1.64	3.5E-3	1.720	1.50	2.9E-3
FCC	0.6	1.45	2.1E-3	1.40	1.39	2.3E-3	1.754	1.39	2.4E-3

Table 4.3: Rectangular waveguide standards utilized in this work for effective permittivity measurement of additive manufactured dielectric crystals.

WG	Frequency in GHz	Width in mm	Height in mm
WR430	1.70 - 2.60	109.22	54.61
WR284	2.60 - 3.95	72.14	36.09
WR187	3.95 - 5.85	47.50	23.75
WR137	5.85 - 8.20	34.79	17.40
WR90	8.20 - 12.4	22.86	10.16

rectangular waveguide standards, as listed in Table 4.3, to cover a wide frequency range. This implies a high effort as many different-sized samples needed to be machined with high precision, and individual calibrations for consecutive waveguide standards had to be carried out before measurement. The individual waveguide and calibration pieces for the consecutive frequency bands are off the shelf components made from Brass. Machining tolerances and surface roughness of individual pieces can be extracted from the data sheets which are available upon request from the manufacturer Flann Microwave Inc.

SC and FCC dielectric crystal samples are manufactured with two different thresholds $th \in [0.35,\ 0.5]$ and unit cell sizes $a \in [7.5\mathrm{mm},\ 10\mathrm{mm}]$. The initial samples are printed in the dimensions of the WR284 waveguide standard with a thickness of two unit cells. Samples for measurements in consecutively smaller waveguide standards, as listed in Table 4.3, are cut from the original sample to reduce errors produced over multiple print jobs. Accurate machining of the MUT samples is essential since gaps between the sample and waveguide walls can cause significant errors in the extracted material parameters [113]. The precise machining is an error source that gets more significant with increasing frequency as the waveguide dimensions get consecutively smaller, but machining tolerances stay the same. Therefore, waveguide measurements are carried out up to 12.4 GHz and the resulting extracted complex effective relative permittivities are plotted as a function of frequency in

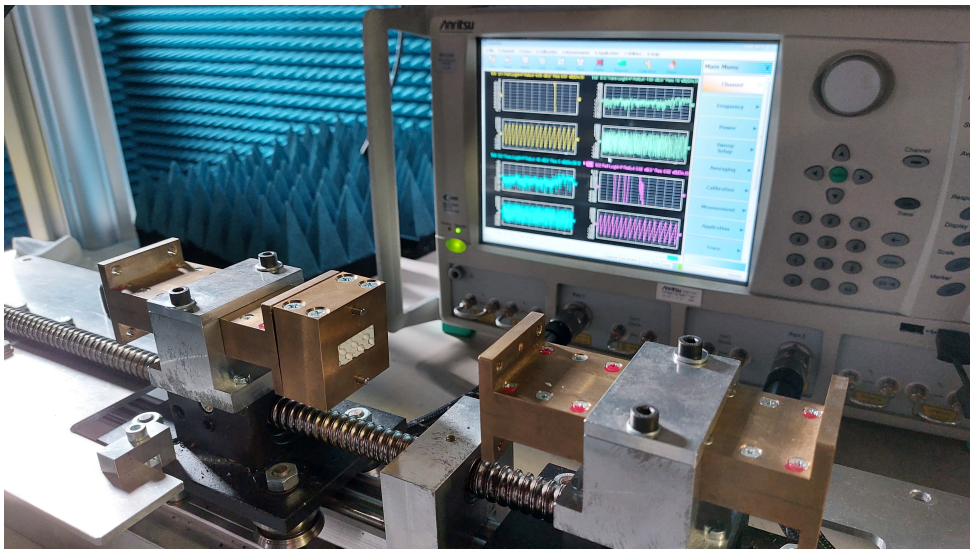

Figure 4.10: Measurement setup for reflection and transmission measurements in rectangular waveguides.

Figure 4.11. Extracted permittivity values across consecutive waveguide standards show excellent agreement with each other and with results obtained via HFSS Floquet port simulations. The measurement of the SC sample with unit cell size $a = 10\text{mm}$ in Figure 4.11a is especially interesting since the measurement frequency range covers the first resonance of the crystal lattice. Although the simulated and measured resonance peak shows a slight offset of about 1 GHz, the simulation accurately predicts the shape and size of the resonance peak in the measurement. One is able to observe several sharp peaks in the extracted imaginary part of the effective permittivity that are not predicted by simulations which are most likely caused by non-optimal calibration and slight misalignment of the individual waveguide pieces.

4.3.3. Free Space

Another option to measure broadband material parameters is to employ a free space wave measurement system, where a MUT sample is placed between two directive antennas and subjected to reflection and transmission measurements. The experimental setup utilized in this work, as depicted in Figure 4.12, consists of two horn antennas with wideband focusing lenses on opposite sides of a probe iris, surrounded by absorbing materials to avoid measurement artifacts due to scattering off of foreign objects. The system is calibrated via a line-reflect-line approach prior to measurements to compensate for the lens-spillover loss and other system errors. For measurement, the sample is fixed within the probe iris and is illuminated by EM radiation. The reflection and transmission parameters are recorded by a vector network analyzer and stored for post-processing. Measurements in the Cx-, X-, Ku-, K-, and Ka-band with different feed horns are carried out to cover a wide frequency range from 6 to 40 GHz. Four different dielectric crystal samples in SC and FCC geometry with two different thresholds $th \in [0.35,\ 0.5]$, unit cell sizes $a \in [7.5\text{mm},\ 10\text{mm}]$ are man-

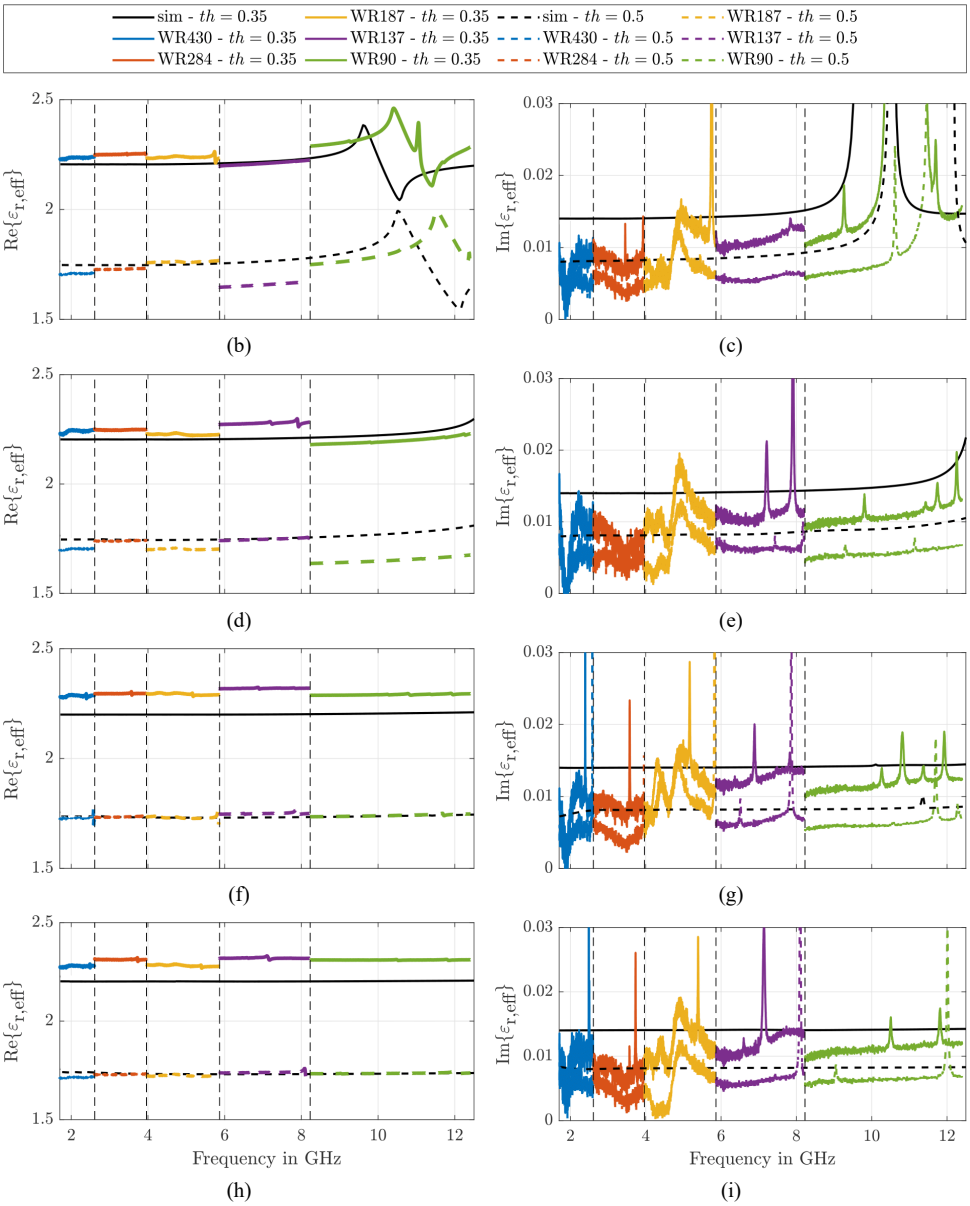

Figure 4.11: Complex effective relative permittivities of dielectric crystal samples with simple cubic (SC) (b,c,d,e), and face-centered cubic (FCC) (f,g,h,i) symmetry, unit cell sizes $a = 10\text{mm}$ (b,c,f,g) and $a = 7.5\text{mm}$ (d,e,h,i), and volumetric infills $th = 0.35$ (solid lines), and $th = 0.5$ (dashed lines) extracted from Floquet port simulations and measurements in consecutive rectangular waveguide standards, computed with the Nicholson-Ross-Weir method adapted for non-magnetic materials.

ufactured as cylindrical disks with a diameter of 200mm and a thickness of two unit cells. The individual samples, fixed in the probe iris, are subjected to reflection and transmission measurements, and the resulting extracted effective permittivities are depicted as a function of frequency in Figure 4.13a and 4.13b respectively. Measurements across consecutive frequency bands show excellent agreement with each other and with simulation results obtained from HFSS Floquet port simulations. Oscillations in the extracted permittivity values in the Cx-band are due to the measurement setup reaching a lower frequency limit. As the wavelength gets too large with respect to the utilized sample size, the diffraction effects around the sample start to play a significant role and distort the measurement. For SC samples, the first resonance's position, shape, and magnitude are accurately predicted by the HFSS Floquet port simulations. However, for frequencies above 25 GHz, some simulation artifacts are visible, especially in the data for the SC dielectric crystal with a unit cell size of $a = 10\text{mm}$. The measurement of FCC crystals shows some minor deviations from simulated behavior; most notably, the FCC crystal with $a = 7.5\text{mm}$ exhibits a relatively strong resonance at around 30 GHz, which is not well predicted by simulations.

4.4. Discussion

It has been demonstrated that effective media theories like the Maxwell-Garnett approximation provide good results for lower volumetric fill fractions and lower permittivity contrasts. However, they lack accuracy for high relative infill and moderate to high permittivity values. Additionally, they lack the capability to predict any broadband or anisotropic behavior of periodic dielectrics. Similar restrictions apply to dielectric characterization via resonance measurement setups. To address the limitations of EMTs and resonance measurement methods, two alternatives for both modeling and experimental verification are discussed in this work. For homogenizing dielectric crystals, the PWEM and Floquet port simulations have been shown to be powerful tools for predicting the effective material parameters and broadband effects like cut-off frequencies in the graded materials. The PWEM gives insight into the electromagnetic behavior of an infinite lattice via computing the dispersion for a given wave vector through the lattice. However, the PWEM can be computationally demanding depending on the complexity of the unit cell and the number of wave vectors considered in the analysis. Furthermore, as a Fourier space technique, it suffers from the Gibbs phenomenon, which limits its accuracy for unit cells with high permittivity contrast. However, the insights provided by the PWEM are of tremendous value, not only for predicting the effective permittivity values of graded dielectrics but also to study bandgaps and exotic dispersion effects like self-collimation. Floquet port simulations have the main benefit of not considering the infinite lattice but modeling the scattering of a semi-finite slab of the material under test. The results of this scattering analysis are more easily comparable to quantities obtained with real-world traveling wave measurement equipment. For experimental verification, traveling wave techniques in both a guided and a free space setup have been utilized to confirm predictions on the broadband effective permittivity obtained from PWEM and Floquet port simulations. While both methods delivered results in satisfying agreement to simulations, several trade-offs between the methods can be identified that are worth considering when selecting a measurement approach. The main drawback of the guided wave method is that the MUT samples need to be precisely machined to fit the cross-section of the utilized waveguide, as small air gaps between the sample and waveguide walls can already

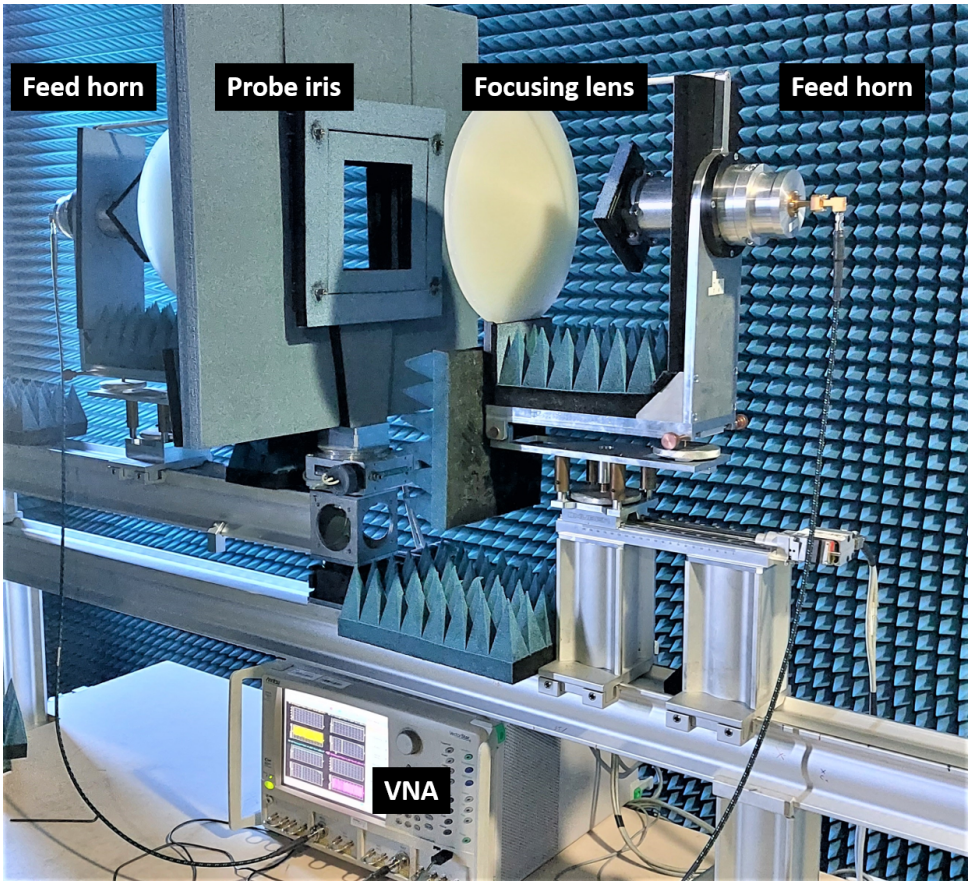

Figure 4.12: Measurement setup for reflection and transmission measurements consisting of feed horn antennas with focusing lenses, connected to vector network analyzer, on opposite sides of a probe iris.

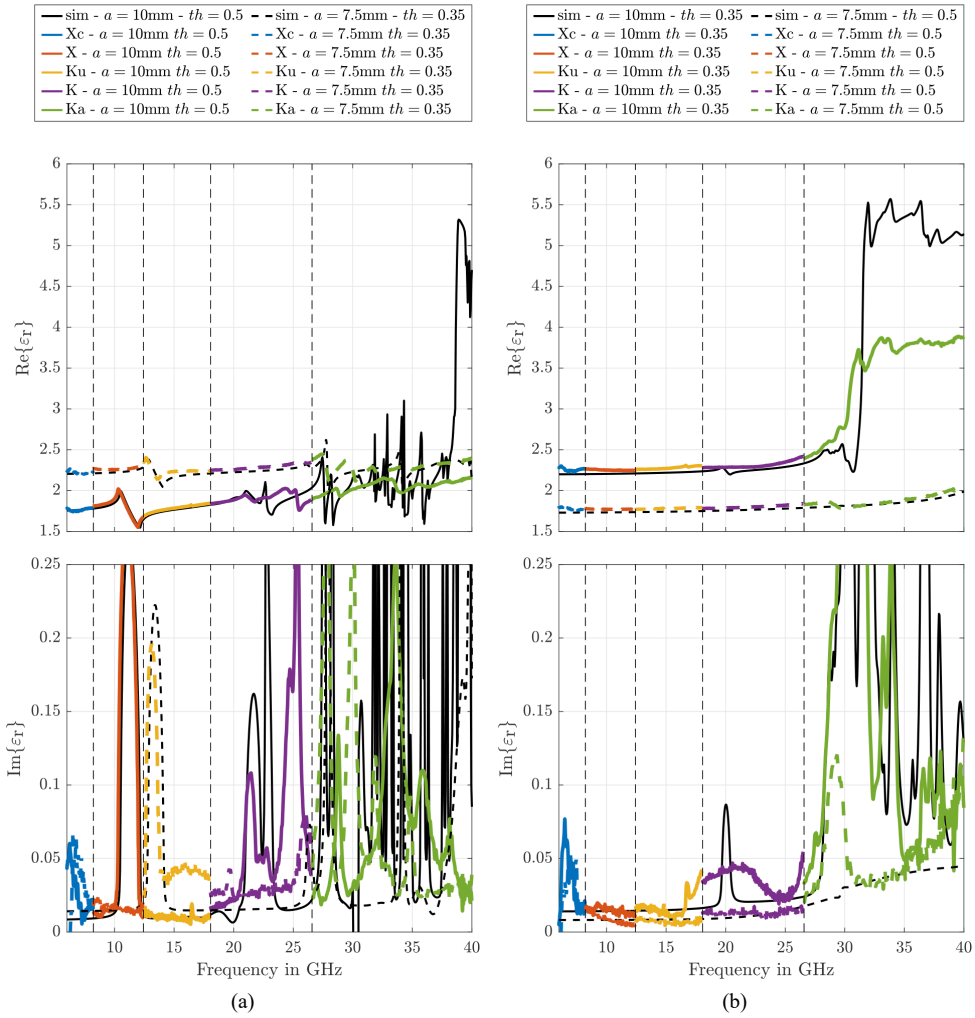

Figure 4.13: Complex effective relative permittivity (top - real), and (bottom - imaginary) extracted from free space traveling wave measurements of (a) simple cubic and (b) face-centered cubic dielectric crystals with different unit cell size a and threshold th.

cause significant errors in the retrieved material parameters. This issue of precise machining gets more significant with increasing frequency as the MUT sample size gets smaller while machining tolerances stay the same. A further drawback of guided wave methods is the inability to measure the same sample in different polarization's. The advantage, on the other hand, is the small sample size (with respect to the wavelength) necessary, which is especially beneficial for measurements at larger wavelengths (below 10 GHz). In contrast to the guided wave setup, the free space method has the drawback that the sample needs to be quite large compared to the wavelength in order to limit the influence of diffraction effects in the measurement. Furthermore, a free space measurement setup is more difficult to calibrate and needs more careful consideration of its environment, as radio sources or reflections from objects in the near vicinity can cause significant errors in the recorded scattering parameters. However, the free space method bears the advantage that one sample of the MUT is sufficient to measure a wide frequency band as well as arbitrary polarization planes.

4.5. Conclusion

This chapter presents novel insights into periodic dielectric structures (dielectric crystals), which are usually employed to synthesize a wide range of relative permittivity values with varied volumetric infill in the design of GRIN devices. An investigation of the effect of different unit cell sizes, base material permittivity, volumetric infill, and crystal symmetry on the effective permittivity and upper cut-off frequency of the effective material bandwidth is presented. This is done by reviewing and applying different computational and experimental methods to extract frequency-dependent effective permittivity values over a wide range of samples and frequencies. It is worth emphasizing that, although the discussed techniques have been employed and reported on independently, no comprehensive comparison of results on comparable samples and discussion of their limitations and trade-offs have been published yet. Predictions from the considered numerical methods agree excellently with extracted permittivities obtained via independent measurement methods. It is demonstrated that the periodic nature of the engineered dielectric crystals results in an upper cut-off frequency above which the assumption of an effective media is not applicable. Furthermore, it is shown that this upper cut-off depends on the crystal's periodicity, volumetric infill, symmetry, and constituent materials. One is able to conclude that the commonly utilized approximation, that unit cell size should be ten times smaller than the applied wavelength, is severely lacking. Generally, it is difficult to give a straightforward unit cell size to wavelength ratio as a design limit because such a limit depends on the employed unit cell symmetry and the permissible dispersion in the desired material properties.

5

Dielectric Anisotropy In Extrusion Based Additive Manufacturing

Abstract
Due to the layer-by-layer build approach employed by most AM techniques, internal periodic patterns are introduced to printed parts, which cause an effective anisotropy in their material parameters. An electrostatic model inspired by parallel plate capacitors, describing the dielectric anisotropy of materials manufactured with fused filament fabrication (FFF) AM techniques is proposed in this work. The accuracy of the model's predictions about the permittivity tensor of printed materials is investigated via numerical simulations. Furthermore, permittivity tensor measurements are carried out for samples printed with various materials and print settings. Measurement data is fitted to the model via a least squares approach, and excellent agreement is observed. Novel conclusions about the impact of material and print parameters on the effective permittivity of additive manufactured materials, improving the accuracy in modeling and designing additive manufactured microwave devices are drawn.

The contents and conclusions of this chapter have been published in the Science Direct Material Research Bulletin under the title *Modeling and measurement of dielectric anisotropy in materials manufactured via fused filament fabrication processes*, identified via the Digital Object Identifier: 10.1016/j.materresbull.2024.112938

5.1. Motivation and Structure

As concluded in section 2.3 AM is increasingly recognized as an enabling technology for novel microwave devices with increased functionality and bandwidth. While traditional subtractive manufacturing methods are well suited to process surfaces and achieve unparalleled tolerances, they cannot create intricate geometries throughout the volume of some material. Fused filament fabrication (FFF) is especially attractive among the various AM processes due to its capability of producing complex multi-material parts with readily available and inexpensive machines and materials with little to no post-processing. In the FFF process, molten thermoplastic polymer material is extruded through a heated nozzle and deposited layer-by-layer to create the desired geometry. One of the significant drawbacks of FFF in general is that, due to inconsistent extrusion and air inclusions between the parallel lines and layers, it is impossible to achieve a 100 percent dense part. Furthermore, the volume of air inclusions and therefore, the realized relative permittivity and loss-tangent, is heavily influenced by the utilized print parameters, such as the nozzle diameter, layer height, extrusion speed, and temperatures. A recently published study considers the effect of manufacturing parameters like nozzle diameter, layer height, and print temperature on the effective permittivity of additive manufactured substrates [114]. However, the aforementioned study considers the effect of print and design parameters on the realized permittivity only in an isotropic manner. Upon closer inspection, however, the assumption of dielectric isotropy in FFF additive manufactured parts does not hold. Due to the internal structure of parallel lines and layers, the FFF fabricated material will exhibit some anisotropy in its mechanical, electrical, and thermal material parameters [115]. While mechanical, thermal, and electrical conductivity anisotropy in FFF printed parts is well reported in the literature, no such study has yet been conducted with respect to the the dielectric material properties. This chapter intends to address this gap by investigating the effect of the utilized material and manufacturing parameters like nozzle size and layer height on the permittivity tensor of FFF-manufactured materials. The rest of the article is structured as follows. In section 2, a model for predicting the dielectric tensor of 3D printed materials is derived and its predictions compared to results obtained from a numerical technique. Section 3 provides insights into the manufacturing and post-processing of samples and details the waveguide measurement setup utilized to extract the permittivity tensor of said samples. Section 4, presents measurement results of different samples manufactured from various materials with a wide range of permittivities and different print settings and investigate the model's applicability to predict measured permittivity tensor components.

5.2. Modeling via Equivalent Capacitance

Geometries manufactured via extrusion methods are generally built layer by layer with parallel extruded lines where individual layers are rotated 90 degrees with respect to each other, as indicated in Figure 5.1 where x and y denote line directions and z the layer stack axis. This geometry can be modeled via a 3D periodic unit cell consisting of two stacked and 90° rotated lines of material with relative permittivity $\varepsilon_{\mathrm{r,p}}$, with layer height h, and an extrusion width d, as depicted in Figure 5.1. A 100% dense part is generally impossible to achieve, and this effect is accounted for by introducing inclusions made from a background material $\varepsilon_{\mathrm{r,b}}$. The print material is considered to be homogeneous and isotropic with a permittivity

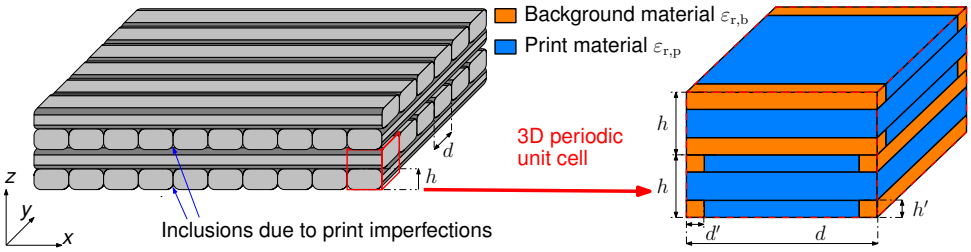

Figure 5.1: FFF additive manufacturing layer buildup comprised of parallel extruded lines with line width d and 90° stacked layers with layer height h (left) with emphasis on printing imperfections that introduce inclusions in the part. Proposed model of said imperfections as a 3D periodic unit cell comprised of a print (blue) and a background material (orange), which is modeled via rectangular inclusions with dimensions h' and d'.

of $\varepsilon_{r,p}$ and the background material to be empty space $\varepsilon_{r,b} = 1$. For simplicity's sake, the inclusions are modeled to be rectangular in shape with dimensions h' and d' at the edges of each extruded line. As explained in Section 3.2.1, from the symmetry of the unit cell, one can already infer that the permittivity tensor $[\varepsilon_r]$ will obtain a uniaxial anisotropic shape

$$[\varepsilon_r] = \begin{bmatrix} \varepsilon_{r,xx} & 0 & 0 \\ 0 & \varepsilon_{r,yy} & 0 \\ 0 & 0 & \varepsilon_{r,zz} \end{bmatrix} = \begin{bmatrix} \varepsilon_O & 0 & 0 \\ 0 & \varepsilon_O & 0 \\ 0 & 0 & \varepsilon_E \end{bmatrix} \tag{5.1}$$

with ordinary permittivity $\varepsilon_O = \varepsilon_{xx} = \varepsilon_{yy}$ and extraordinary permittivity $\varepsilon_E = \varepsilon_{zz}$. In the following, the permittivity tensor of the uniaxial unit cell is modeled via an electrostatic approach based on the well-known parallel plate capacitor and compare the model to results obtained from numerical finite element simulations.

5.2.1. Derivation

One can model the effective permittivity values of the permittivity tensor's main diagonal of the unit cell depicted in Figure 5.1 via assuming virtual parallel perfectly conducting plates on the individual axes, as explained in Section 4.2.2 and depicted in Figure 5.2. By computing the capacitance for each of the geometries and rearranging equation 4.2, one can compute the effective capacitance of the unit cell along a given axis via

$$\varepsilon_r = \frac{CD}{\varepsilon_0 A}. \tag{5.2}$$

An exact solution for the capacitance of a structure with inhomogeneous dielectric requires the solution of the Laplace equation, which is difficult to obtain in a closed form for complex structured unit cells with different materials, as considered in this chapter. In order to obtain a closed-form solution for the permittivity tensor components, the electric field and the electric displacement field in the material is approximated to be perfectly perpendicular to the parallel plates, thus ignoring fringing fields along or between dielectric interfaces. This approach is very similar to the semi-analytical approach described in Section 4.2.2, however, in this case the unit cell geometry is simple enough to compute the resulting effective permittivity tensor components in a closed form. With this assumption, one is able

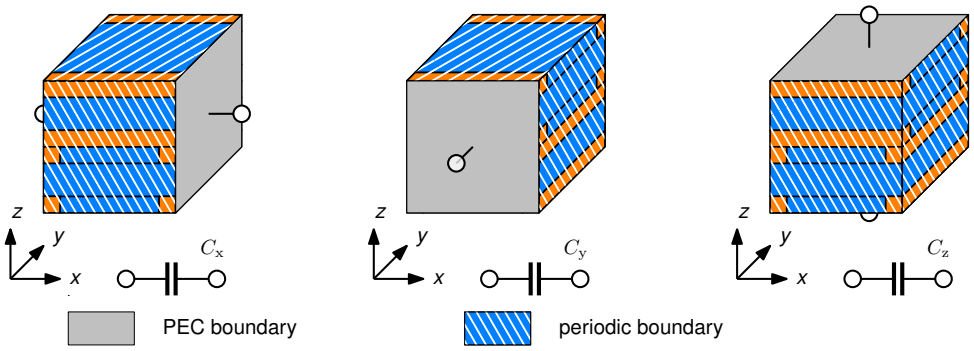

Figure 5.2: Schematic representation of the equivalent parallel plate capacitor method applied to the proposed 3D periodic unit cell to model the effect of print imperfections introduced by extrusion based additive manufacturing.

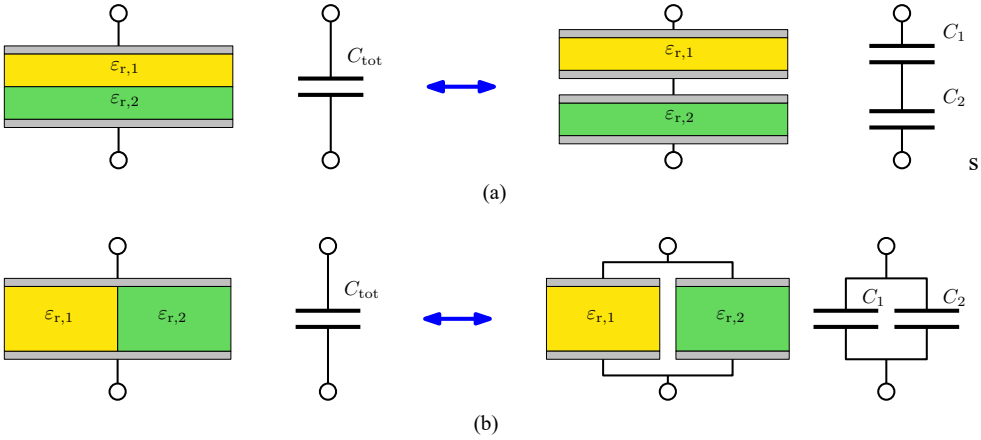

Figure 5.3: Representation of the series and parallel equivalent capacitor circuits for inhomogeneous parallel plate capacitors, assuming the electric and displacement fields are perfectly perpendicular to the PEC plates throughout the dielectric material.

to separate the complex unit cell into an equivalent circuit of series and parallel capacitances representing the individual homogeneous material sections as depicted in Figure 5.3.

This method of computing the capacitance is applied to the unit cell in Figure 5.1 along its x/y and z axis below.

Capacitance along x/y - Ordinary Axis

To compute the capacitance of the unit cell depicted in Figure 5.1, virtual perfectly conducting plates are applied as depicted in Figure 5.2. Splitting the unit cell into equivalent capacitances representing the homogeneous material sections in the unit cell along the x-axis, an equivalent circuit as depicted in Figure 5.4a is obtained. The equivalent circuit is split into two individual layers, which are parallel aligned. For layer a, the capacitances

$$C_{\mathrm{a},1} = C_{\mathrm{a},2} = C_{\mathrm{a},3} = C_{\mathrm{a},4} = \varepsilon_0 \frac{d'h'}{d} \tag{5.3}$$

are obtained for the inclusions and

$$C_{\mathrm{a},5} = \varepsilon_0 \varepsilon_{\mathrm{r,m}} \frac{dh - 4d'h'}{d} \tag{5.4}$$

for the material part. Since in layer a all homogeneous material sections are aligned parallel one can find the equivalent capacitance as

$$C_{\mathrm{a}} = 4C_{\mathrm{a},1} + C_{\mathrm{a},5}. \tag{5.5}$$

In layer b the capacitances

$$C_{\mathrm{b},1} = C_{\mathrm{b},3} = C_{\mathrm{b},5} = C_{\mathrm{b},7} = \varepsilon_0 \frac{dh'}{d'} \tag{5.6}$$

and

$$C_{\mathrm{b},2} = C_{\mathrm{b},6} = \varepsilon_0 \varepsilon_{\mathrm{r,m}} \frac{dh - 2dh'}{d'} \tag{5.7}$$

are found for the three homogeneous material sections adjacent to the virtual PEC plates. Furthermore, for the middle section the capacitance

$$C_{\mathrm{b},4} = \varepsilon_0 \varepsilon_{\mathrm{r,m}} \frac{dh}{d - 2d'} \tag{5.8}$$

is obtained. The capacitance of layer b can be expressed via

$$C_{\mathrm{b}} = \left(\frac{2}{2C_{\mathrm{b},1} + C_{\mathrm{b},2}} + \frac{1}{C_{\mathrm{b},4}} \right)^{-1}. \tag{5.9}$$

Due to the parallel alignment of layer a and b the total capacitance of the unit cell along the x axis can be expressed as

$$C_{\mathrm{x}} = C_{\mathrm{a}} + C_{\mathrm{b}} \tag{5.10}$$

and, as mentioned above, due to the symmetry of the unit cell,

$$C_{\mathrm{y}} = C_{\mathrm{x}}. \tag{5.11}$$

Capacitance along z - Extraordinary Axis

Investigating the capacitance of the unit cell along the z-axis, as depicted in Figure 5.2, the equivalent capacitance circuit, representing the individual homogeneous sections of the unit cell, in Figure 5.4b is obtained. As done above, the equivalent circuit is split into the individual layers, which are serially aligned this time. In layer a the capacitances

$$C_{\mathrm{a},1} = C_{\mathrm{a},3} = C_{\mathrm{a},5} = C_{\mathrm{a},7} = \varepsilon_0 \frac{dd'}{h'} \tag{5.12}$$

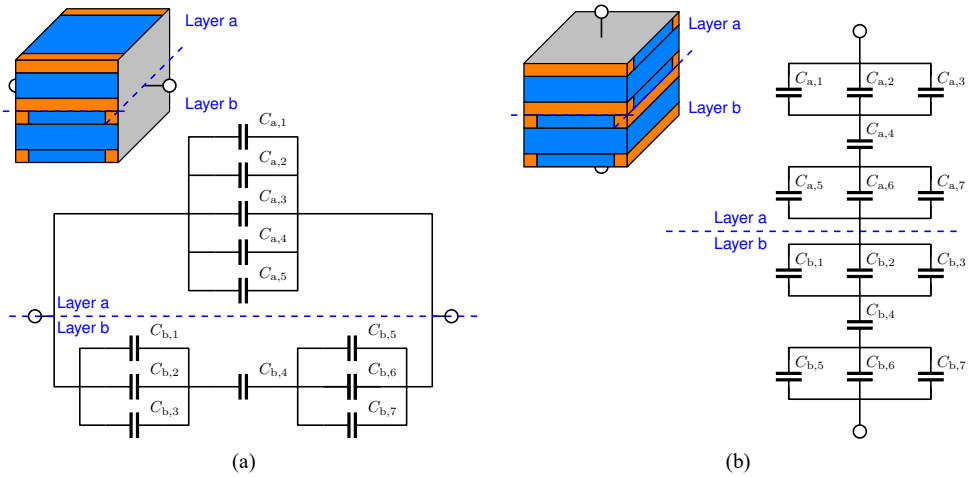

Figure 5.4: Representation of the equivalent capacitor circuits modeling the anisotropy of a material manufactured with fused filament fabrication additive technologies. Each capacitor represent a homogeneous section of material in the unit cell with virtual perfectly conducting plates along (a) the x/y axis and (b) the z axis.

and

$$C_{\mathrm{a},2} = C_{\mathrm{a},6} = \varepsilon_0 \varepsilon_{\mathrm{r,m}} \frac{d^2 - 2dd'}{h'} \tag{5.13}$$

are present for the parallel material sections adjacent to the virtual PEC plates and

$$C_{\mathrm{a},4} = \varepsilon_0 \varepsilon_{\mathrm{r,m}} \frac{d^2}{h - 2h'}. \tag{5.14}$$

Since layers a and b are 90° shifted with respect to each other but have the same geometry they obtain equal equivalent capacitances

$$C_{\mathrm{b}} = C_{\mathrm{a}}. \tag{5.15}$$

Finally, due to the series arrangement of the layers, the equivalent capacitance of the unit cell along the z axis can be expressed as

$$C_{\mathrm{z}} = \left(\frac{2}{C_{\mathrm{a}}} \right)^{-1}. \tag{5.16}$$

Effective permittivity tensor

With the capacitances of the unit cell computed for its principal axis above one can extract the effective permittivity tensor components for the main diagonal in 5.1, according to

equation 5.2, as

$$\varepsilon_{\mathrm{O}} = \varepsilon_{\mathrm{xx}} = \varepsilon_{\mathrm{yy}} = \frac{C_{\mathrm{x}} d}{\varepsilon_0 2hd} = \\ - \frac{\left(\left(8d'^2 - 4dd'\right)\varepsilon_{\mathrm{r,m}}^2 + \left(8dd' - 16d'^2\right)\varepsilon_{\mathrm{r,m}} + \left(8d'^2 - 4dd'\right)\right)h'^2}{\left(\left(4dd' - 2d^2\right)\varepsilon_{\mathrm{r,m}} + \left(2d^2 + 4dd'\right)\right)hh' + d^2h^2\varepsilon_{\mathrm{r,m}}} \\ - \frac{\left(2d^2\varepsilon_{\mathrm{r,m}}^2 - 2d^2\varepsilon_{\mathrm{r,m}}\right)hh' - d^2h^2\varepsilon_{\mathrm{r,m}}^2}{\left(\left(4dd' - 2d^2\right)\varepsilon_{\mathrm{r,m}} + \left(2d^2 + 4dd'\right)\right)hh' + d^2h^2\varepsilon_{\mathrm{r,m}}} \tag{5.17}$$

and

$$\varepsilon_{\mathrm{E}} = \varepsilon_{\mathrm{zz}} = \frac{C_z 2h}{\varepsilon_0 d^2} = -\frac{\left(\left(2d' - d\right)\varepsilon_{\mathrm{r,m}}^2 - 2d'\varepsilon_{\mathrm{r,m}}\right)h}{\left(4d'\varepsilon_{\mathrm{r,m}} - 4d'\right)h' + \left(\left(d - 2d'\right)\varepsilon_{\mathrm{r,m}} + 2d'\right)h} \tag{5.18}$$

While the values for h and d can be adjusted via the individual settings of the print, the values of h' and d' depend on the quality of the print setup. Uniaxial anisotropic material can be characterized by their birefringence η, which is the difference between the extraordinary and ordinary permittivities

$$\eta = \varepsilon_{\mathrm{E}} - \varepsilon_{\mathrm{O}}. \tag{5.19}$$

Figure 5.5 depicts the birefringence predicted from equations 5.17 and 5.18 for print material relative permittivities $\varepsilon_{\mathrm{r,m}} \in \{4,\ 8\}$ as function of h'/h and d'/d. One can observe both negative and positive birefringence depending on the values of h' and d'. While there is a negative birefringence for large values of d', a positive birefringence for large values of h' is observed. The larger the print material permittivity, the larger the resulting birefringence for equal h' and d'.

The investigation about the birefringence in the effective permittivity tensor of printed materials above has been carried out with respect to the real part of the tensor components. However, the model is not limited to lossless materials, and equally valid predictions can be made about the imaginary part by utilizing a complex value for the print material permittivity $\varepsilon_{\mathrm{r,m}}$ in equations (5.18) and (5.17) but are omitted here for brevity sake.

5.2.2. Numerical Investigation

In order to estimate the error due to the neglected fringing fields in the model derived above, the electrostatic solver in the CST software package and the approach as described in 4.2.2 is employed. The solver's mesh is refined iteratively until an energy variation threshold of below 1E-6 between consecutive iterations is reached. The permittivities from the CST simulation results are again extracted via equation (5.2). The error with respect to the parallel plate capacitor model is computed via

$$error_{\mathrm{O}} = \frac{\varepsilon_{\mathrm{O,CST}} - \varepsilon_{\mathrm{O}}}{\varepsilon_{\mathrm{O,CST}}} 100 \tag{5.20}$$

$$error_{\mathrm{E}} = \frac{\varepsilon_{\mathrm{E,CST}} - \varepsilon_{\mathrm{E}}}{\varepsilon_{\mathrm{E,CST}}} 100. \tag{5.21}$$

The error of the model with respect to the numerical simulations are depicted for different print material permittivities and layer heights with respect to the extrusion width in Figure

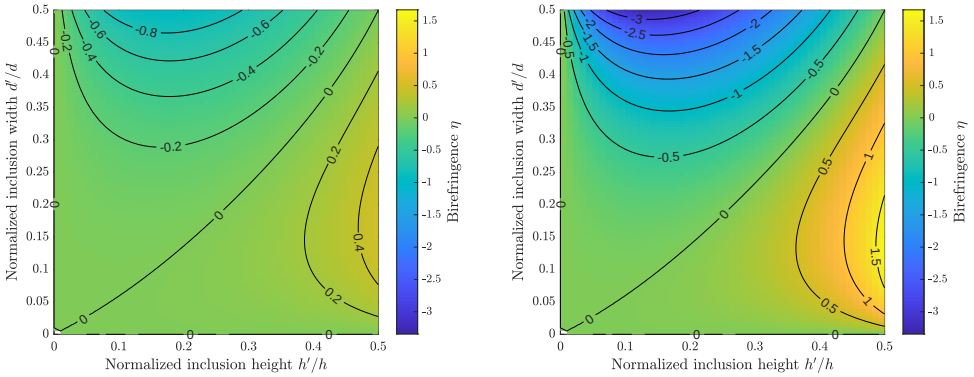

Figure 5.5: Birefringence values predicted by the equivalent parallel plate capacitor model for print material relative permittivity (a) $\varepsilon_{r,p} = 4$ and (b)$\varepsilon_{r,p} = 9$ as function of the normalized rectangular inclusion size parameters h'/h and d'/d.

5

5.6. One is able to observe that good predictions are achieved via the parallel plate capacitor model for low print material permittivities and that the error in the prediction of the extraordinary tensor component is always negative. Furthermore, the model error grows for small layer heights compared to the extrusion width. A similar conclusion is obtained for the error with respect to the imaginary part of the permittivity but omitted here for brevity sake.

5.3. Experimental Characterization

In order to test the model derived above against experimentally obtained data, several samples are manufactured from materials with a wide range of permittivities with different print settings. The utilized manufacturing equipment, materials, print settings, post-processing steps, and measurement hardware used to fabricate, prepare, and measure the individual samples are discussed below.

5.3.1. Quadratic Waveguide Setup

Due to variations in the printing process it is desirable to extract the material permittivity tensor from a single sample. Another significant factor is the sample size required. Small samples create issues with printing tolerances and repeatability, too large samples would require tremendous amount of material and printing time. To address this issue a dedicated X-band waveguide system, depicted in Figure 5.7, for anisotropic material parameter measurement requiring only a single cube shaped sample as introduced in [116] is devised. The system consists of common WR90 coaxial to waveguide transition but then utilizes a tapered waveguide section to transit from a rectangular to a quadratic aperture. This allows the measurement of a perfectly cube-shaped sample in six different orientations in the sample holder and thus enables extraction of the main diagonal components of the permittivity and permeability tensor via the Nicholson-Ross-Weir (NRW) method. As this work only deals with dielectric materials, the assumption of non-magnetic material $\mu_r = 1$ is generally imposed

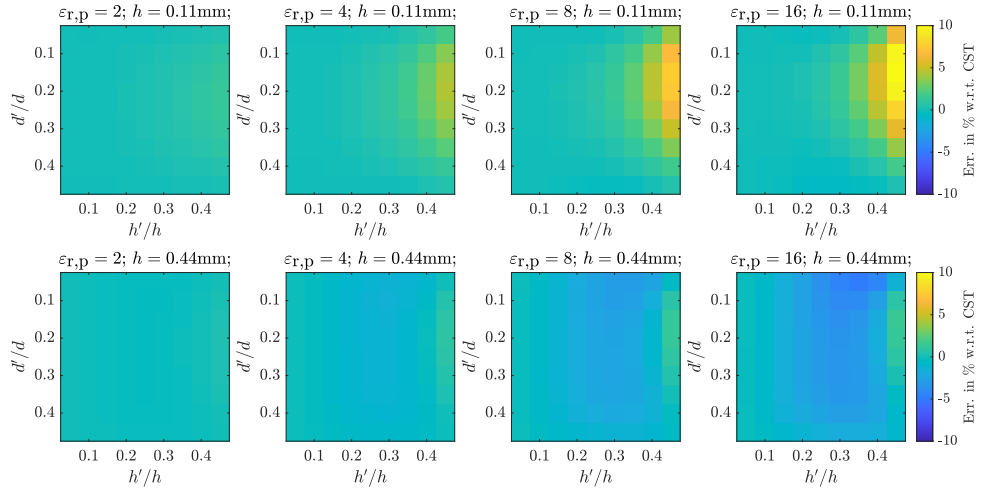

(a)

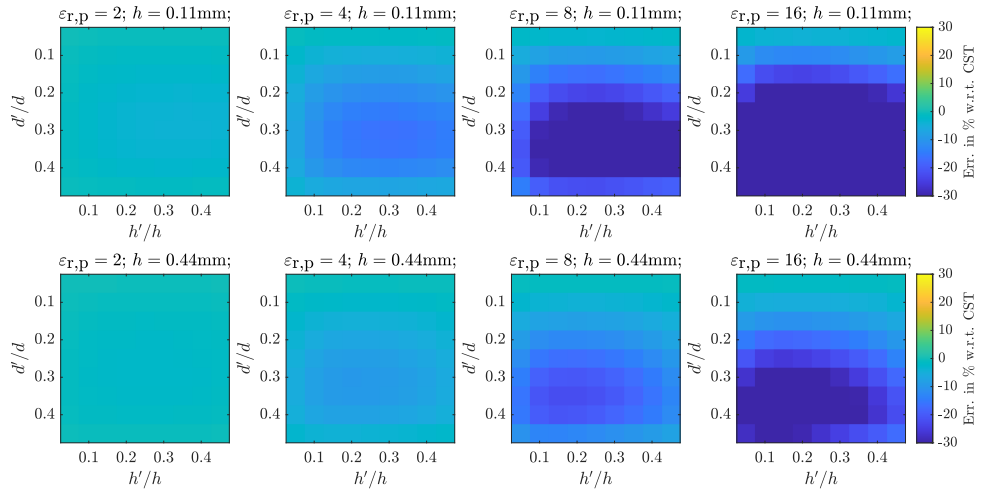

(b)

Figure 5.6: Error of the (a) ordinary and (b) extraordinary permittivities as a function of inclusion dimensions h' and d' of FFF 3D printed materials predicted via a parallel plate capacitor model with respect to values obtained from an electrostatic finite element simulation for constant line width of $d = 0.55$ mm. From left to right, increasing print material permittivities $\varepsilon_{r,p}$ and from top to bottom increasing layer height h with respect to the line width d.

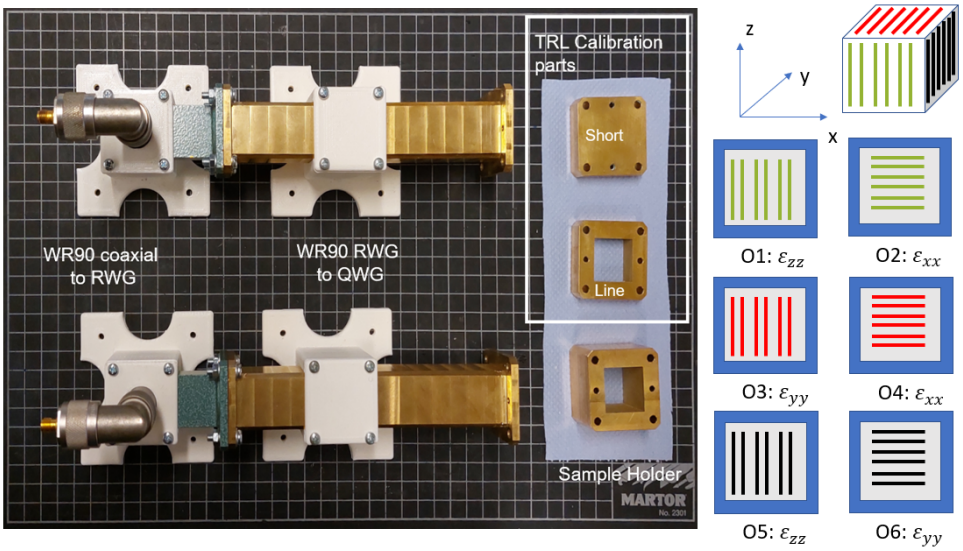

Figure 5.7: Left: WR90 waveguide measurement system for anisotropic material parameter measurement with TRL calibration parts and sample holder. Right: Sample orientations and corresponding permittivity tensor components measured.

on the utilized NRW procedure. This leads to a more accurate and stable computation of the material under test's complex permittivity [111]. Due to the tapering of the standard WR90 rectangular waveguide to a quadratic aperture, higher-order modes exhibit a lower cut-off frequency, thus reducing the upper limit of the measurement bandwidth from 12.4 GHz to $\approx$ 9.2 GHz. Prior to measurement, the system is calibrated via a through-reflect-line (TRL) calibration with reference planes at the end of the quadratic tapering section.

The different nozzle size and layer height combinations utilized during manufacturing of the individual samples imply different tolerances and surface qualities which affect the quality of measurements. In order to homogenize the dimensions and surface qualities, individual samples are printed slightly bigger than required and reduced in a post-processing step to precisely match the required dimensions of the waveguide measurement system utilizing a computerized numerically controlled (CNC) milling machine.

5.3.2. Sample Preparation

three materials are selected for testing, namely the ABS300, ABS650, and ABS1500 materials from Avient (former PREPERM) with properties listed in Table 3.2 in Section 3.3.2. Samples for measurement are printed with three different nozzle sizes (0.25mm, 0.4mm, and 0.6mm), as well as two different layer heights for each nozzle size. In order to present data with statistical significance, three individual samples for each material, nozzle size, and layer height combination are fabricated, resulting in 54 samples to be measured. Samples are printed with customized 3D printing hardware based on the E3D motion system with direct-drive Hemera extruders as presented in 3.3.1. Print settings for the individual material, nozzle size, and layer height combinations are listed in Table 5.1.

Table 5.1: Material print settings

Material	**ABS300**	**ABS650**	**ABS1500**
Nozzle temp.	225°C	235°C	285 °C
Bed temp.	85°C	90°C	105°C
Max. speed	$25\,\mathrm{mm\,s^{-1}}$	$20\,\mathrm{mm\,s^{-1}}$	$15\,\mathrm{mm\,s^{-1}}$
Max. acceleration	$400\,\mathrm{mm\,s^{-2}}$	$400\,\mathrm{mm\,s^{-2}}$	$150\,\mathrm{mm\,s^{-2}}$

The different nozzle size and layer height combinations utilized during manufacturing of the individual samples imply different tolerances and surface qualities which affect the quality of measurements. In order to homogenize the dimensions and surface qualities, individual samples are printed slightly bigger than the waveguide aperture and reduced in a post-processing step to precisely match the required dimensions of the waveguide measurement system utilizing a CNC milling machine.

5.3.3. Results

Measurement results for the real main-diagonal components of the permittivity tensor of individual samples of the three utilized materials are depicted in Figure 5.8 as a function of frequency respectively. One is able to observe uniaxial characteristics for each of the individual samples with measured values for $\varepsilon_{\mathrm{r,xx}}$ and $\varepsilon_{\mathrm{r,yy}}$ (extruder movement directions) aligning perfectly with each other and different measured values for $\varepsilon_{\mathrm{r,zz}}$ (layer stack direction). The small oscillations of the measured permittivity values as a function of frequency can be most likely attributed to an imperfect calibration of the setup. The observed anisotropy is especially prominent for samples printed from material with high relative permittivity, as can be observed in Figure 5.8g. For a given material and print settings d and h one can extract the values of the inclusion dimensions d' and h' by performing a least-squares fit of the real measured permittivity data to the model described by equations (5.17) and (5.18). The values for the inclusion dimensions d' and h' for the measurement data shown in Figures 5.8a, 5.8d, and 5.8g and the corresponding predicted tensor components ε_0 and ε_{E} are depicted in the same Figures. One is able to observe an excellent agreement between the predicted and measured tensor components. Detailed measurement results for all samples are listed in Table 5.2. Extracted values for d' and h' are visualized via bar plots in Figures 5.8b and 5.8c for the ABS300 material, in Figures 5.8e and 5.8f for the ABS650 material and in Figures 5.8h and 5.8i for the ABS1500 material respectively with error bars indicating the standard deviation of the extracted quantities.

The imaginary part of the permittivity tensor component values reported in Table 5.2 generally follow the same trend as the real part with respect to the different materials and print settings. However, loss measurements in traveling wave setups, and especially in waveguide setups, are less reliable due to the limited sample thickness and the additional losses due to the finite conductivity of the waveguide itself. For this reason, the investigation in this work has been carried out with emphasis on the real part of the permittivity tensor components.

Several observations can be made from the data presented in Figures 5.8 and Table 5.2 that support the applicability of the model:

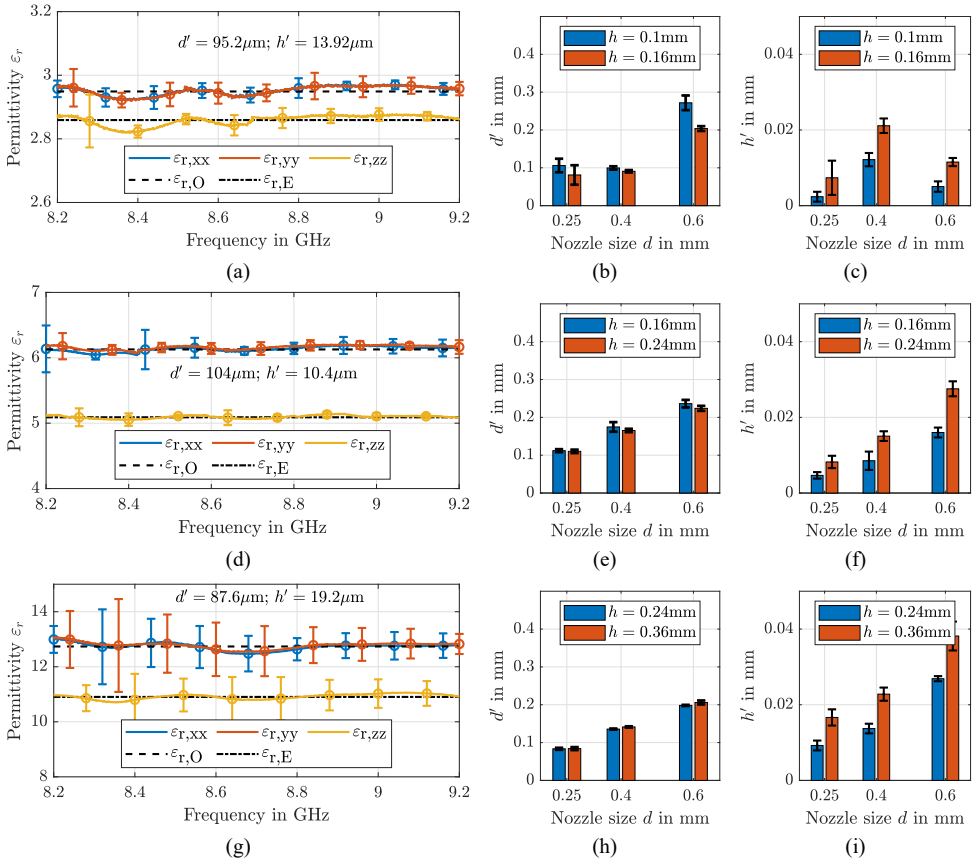

Figure 5.8: Permittivity tensor main-diagonal component measurements obtained from FFF 3D printed (a) ABS300 ($\varepsilon_{r,p} = 3$), (b) ABS650 ($\varepsilon_{r,p} = 6.5$), and (c) ABS1500 ($\varepsilon_{r,p} = 15$) samples (solid lines) and comparison to predicted values (dashed lines) from equivalent parallel plate capacitor model.

- Inclusion dimensions d' and h' increase with increasing nozzle diameter d
- The print layer height h seems to have a significant influence on the inclusion dimension h' but a rather negligible effect on the inclusion dimension d'
- Similar values for d' and h' are obtained for samples manufactured with different materials but the same print settings d and h
- Generally, the observed trends listed above are less clear for the measurements of samples manufactured with the ABS300 material. Due to the minuscule difference in the ordinary and extraordinary permittivities, measurement errors have a significant effect on the extracted inclusion dimensions

5.4. Conclusion

In this chapter, novel insights into the dielectric anisotropy of FFF 3D printed materials are presented. This has been done by introducing an approximate model inspired by a parallel plate capacitor to model the permittivity tensor of additive manufactured layer-by-layer geometries assuming an isotropic base material and rectangular-shaped free-space inclusions. Several assumptions are applied for the model to arrive at a closed-form expression for the permittivity tensor. The error of the derived model is estimated via electro-static finite element simulations. The investigation allows to conclude that the error is within reasonable bounds for low to moderate base material permittivities. The real-world applicability of the model is studied via experimental characterization of dielectric anisotropy in 3D printed samples made from different materials with a wide range of permittivities and a variety of different print parameters. The experiments are carried out using a custom waveguide measurement setup operating in the X band, capable of extracting a material permittivity tensor from a single cube shaped sample. The experimental data is fitted to the model via a least-squares approach to extract the dimensions of the modeled rectangular-shaped inclusions. Generally, good results are achieved. However, since the dimensions of the inclusions generally depend on the quality of the print setup, it is difficult to apply the model without prior knowledge of the inclusion dimension. Nevertheless, the model can be applied to estimate the permittivity tensor for a given material and print setting combination or check the quality of a given print hardware. Based on the presented work, several open topics of interest remain for future research. Optimization of print settings or adequate post-processing techniques for a minimization of the printed material birefringence may be of interest. Furthermore, this work is limited to materials manufactured with FFF additive manufacturing processes. Similar experiments with respect to other additive manufacturing techniques are of interest to the community. Additionally, the presented results are mostly limited to the real part of the permittivity tensor components due to the reliability issue of characterizing losses with waveguide measurement setups. A more precise investigation of the samples in terms of their losses, for example with resonance measurement methods could provide additional insights.

Table 5.2: Measurement results for all relative permittivity tensor components $\varepsilon_{r,xx}$, $\varepsilon_{r,yy}$ and $\varepsilon_{r,zz}$ for all print materials ABS300, ABS650 and ABS1500, and print settings h and d with extracted inclusion dimensions h' and d'.

Mat.	d in mm	h in mm	$\varepsilon_{r,xx}$	$\varepsilon_{r,yy}$	$\varepsilon_{r,zz}$	η	d' in µm	h' in µm
ABS 300	0.25	0.1	$2.928 - 0.022j$ ± 0.015	$2.943 - 0.019j$ ± 0.0156	$2.845 - 0.022j$ ± 0.016	0.090 ± 0.016	106 ± 18	2.4 ± 1.3
ABS 300	0.25	0.16	$2.901 - 0.021i$ ± 0.015	$2.915 - 0.019j$ ± 0.016	$2.841 - 0.022j$ ± 0.018	0.067 ± 0.018	81 ± 25	7.4 ± 4.5
ABS 300	0.4	0.16	$2.846 - 0.030j$ ± 0.010	$2.863 - 0.029j$ ± 0.010	$2.791 - 0.032j$ ± 0.009	0.064 ± 0.009	100 ± 4	12.2 ± 1.8
ABS 300	0.4	0.24	$2.834 - 0.026j$ ± 0.014	$2.879 - 0.029j$ ± 0.015	$2.786 - 0.030j$ ± 0.018	0.071 ± 0.018	91 ± 3	21.1 ± 1.9
ABS 300	0.6	0.24	$2.928 - 0.022j$ ± 0.015	$2.931 - 0.029j$ ± 0.017	$2.824 - 0.023j$ ± 0.013	0.106 ± 0.013	272 ± 19	5.0 ± 1.4
ABS 300	0.6	0.36	$2.913 - 0.025j$ ± 0.017	$2.902 - 0.025j$ ± 0.035	$2.850 - 0.040j$ ± 0.018	0.057 ± 0.018	204 ± 6	11.5 ± 1.1
ABS 650	0.25	0.1	$6.043 - 0.061j$ ± 0.062	$6.082 - 0.048j$ ± 0.052	$5.047 - 0.051j$ ± 0.035	1.016 ± 0.035	112 ± 4	4.7 ± 0.9
ABS 650	0.25	0.16	$6.002 - 0.061j$ ± 0.057	$6.035 - 0.051j$ ± 0.053	$5.100 - 0.052j$ ± 0.041	1.009 ± 0.041	102 ± 5	8.2 ± 1.6
ABS 650	0.4	0.16	$5.993 - 0.069j$ ± 0.055	$5.855 - 0.050j$ ± 0.191	$5.021 - 0.036j$ ± 0.033	0.903 ± 0.020	175 ± 13	8.5 ± 2.4
ABS 650	0.4	0.24	$5.927 - 0.093j$ ± 0.067	$5.926 - 0.084j$ ± 0.068	$5.033 - 0.072j$ ± 0.029	0.893 ± 0.029	165 ± 4	15.0 ± 1.3
ABS 650	0.6	0.24	$5.916 - 0.059j$ ± 0.071	$5.975 - 0.046j$ ± 0.054	$5.134 - 0.036j$ ± 0.033	0.811 ± 0.034	236 ± 9	16 ± 1.3
ABS 650	0.6	0.36	$5.862 - 0.074j$ ± 0.075	$5.917 - 0.055j$ ± 0.069	$5.153 - 0.047j$ ± 0.036	0.737 ± 0.036	224 ± 6	27.5 ± 2.0
ABS 1500	0.25	0.1	$13.225 - 0.742j$ ± 0.193	$13.113 - 0.806j$ ± 0.263	$11.505 - 0.514j$ ± 0.174	1.664 ± 0.158	84 ± 3	9.2 ± 1.3
ABS 1500	0.25	0.16	$12.984 - 0.696j$ ± 0.184	$12.945 - 0.709j$ ± 0.216	$11.123 - 0.506j$ ± 0.161	1.846 ± 0.154	84 ± 4	16.6 ± 2.1
ABS 1500	0.4	0.16	$13.328 - 0.651j$ ± 0.187	$13.274 - 0.703j$ ± 0.226	$11.585 - 0.538j$ ± 0.180	1.716 ± 0.172	136 ± 1	13.7 ± 1.3
ABS 1500	0.4	0.24	$13.066 - 0.728j$ ± 0.199	$13.096 - 0.725j$ ± 0.187	$10.976 - 0.449j$ ± 0.094	2.105 ± 0.097	141 ± 2	22.8 ± 1.7
ABS 1500	0.6	0.24	$12.849 - 0.622j$ ± 0.176	$12.781 - 0.744j$ ± 0.206	$11.022 - 0.383j$ ± 0.119	1.793 ± 0.114	198 ± 2	26.9 ± 7
ABS 1500	0.6	0.36	$12.895 - 0.629j$ ± 0.150	$12.369 - 0.713j$ ± 0.203	$10.893 - 0.383j$ ± 0.109	1.739 ± 0.100	206 ± 5	38.2 ± 3.8

6

Engineering Anisotropy in Long-Wavelength Dielectric Crystals

Abstract
The effect of different crystal symmetries and centerings on the effective permittivity tensor of long-wavelength periodic dielectric structures is discussed. A series of experiments to characterize dielectric crystals with uniaxial and biaxial anisotropy is carried out to confirm the predictions obtained from the equivalent parallel plate capacitance homogenization method with respect to the effective permittivity tensor. An algorithm for synthesizing dielectric crystals with a desired permittivity tensor is presented and experimentally verified. It is demonstrated that additive manufactured periodic dielectric structures are well suited to tailor the effective dielectric tensor of composite materials.

6.1. Motivation and Structure

The ability to tailor the effective permittivity tensor of a dielectric crystal opens up new degrees of freedom in the design and optimization of advanced electromagnetic devices like antennas, lenses, substrates, and filters. Traditionally, however, the design of dielectric crystals has been constrained by the limitations of subtractive manufacturing techniques. These methods allowed for the creation of relatively simple two-dimensional (2D) periodic structures but fell short when fabricating more complex three-dimensional (3D) geometries, which are crucial for optimizing dielectric properties in novel applications. With the capabilities of AM, it is feasible to efficiently engineer dielectric properties with desired effective anisotropic properties. Two major challenges can be identified in the engineering of dielectric crystals, as indicated in Figure 6.1. On the one hand, the homogenization of the effective permittivity tensor $[\tilde{\varepsilon_{\mathrm{r}}}]$ from the periodic permittivity definition of the unit cell. It is important to understand the effect of crystal symmetry and the crystal's shape and constituent materials for the successful engineering of its effective parameters. In the following, this is referred to as the forward problem. On the other hand, the inverse problem is how, given a desired effective permittivity tensor, a periodic dielectric structure can be synthesized that exhibits this desired permittivity tensor.

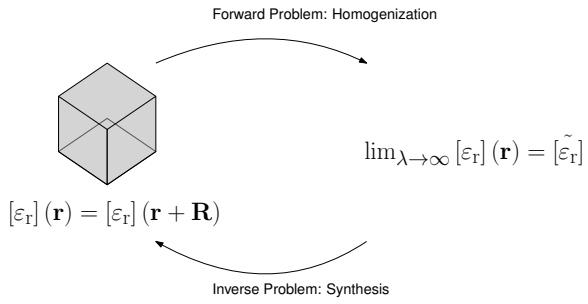

Figure 6.1: Dielectric Crystal Engineering.

The remainder of this chapter is structured as follows: In Section 2, the effect of crystal properties on the effective permittivity tensor is discussed. Section 3 deals with the homogenization of dielectric crystals and presents a parametric study and an experimental study to verify the results of the forward problem. Section 4 presents an algorithm implementing the inverse problem. Section 5 discusses and concludes the chapter.

6.2. Effect of Crystal Properties on the Effective Dielectric Tensor

As explained in Section 3.2.1, and indicated in Table 3.1, the shape of the effective permittivity tensor of dielectric crystals is fundamentally determined by the symmetry of the unit cell. Additionally, the shape of the inclusions and their respective centering in the lattice affect the individual permittivity tensor components. In the following, the scope of this chapter is restricted to crystal systems with orthogonal angles, e.g., the cubic, tetragonal, and orthorhombic systems in their primitive, body-centered, and face-centered forms with

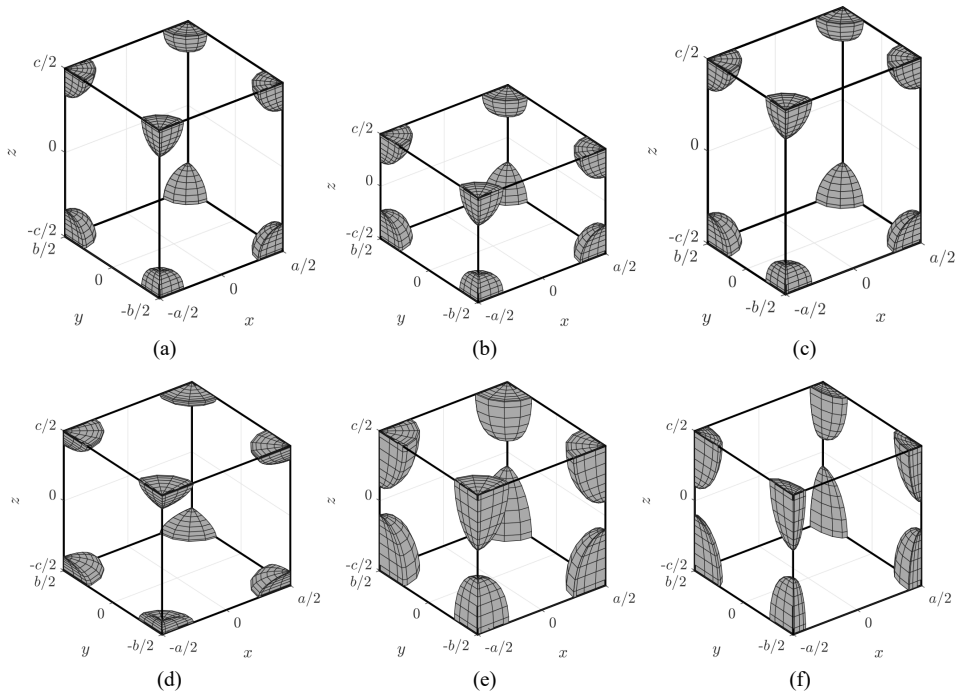

Figure 6.2: 3D periodic unit cells with inclusion volumes indicated in gray visualizing the breaking of cubic symmetry with (a,b,c) lattice parameters and (d,e,f) with inclusion parameters. Resulting in tetragonal symmetry, exhibiting uniaxial effective anisotropy with (a,d) negative birefringence, and with (b,e), positive birefringence, and orthogonal symmetry resulting in biaxial effective anisotropy (c,f).

ellipsoidal inclusion as introduced in Section 3.2.2.

6.2.1. Effect of Crystal Symmetry

Based on the information presented in Table 3.1 and the unit cell with inclusions as depicted in Figure 3.3, the approach to engineer the tensor form of a dielectric crystal is demonstrated. First, a unit cell which exhibits cubic symmetry is considered (lattice parameters $a = b = c$ and inclusion parameters $a' = b' = c'$), which results in an effectively isotropic dielectric crystal. Now, anisotropy is introduced into the dielectric crystal by breaking the cubic symmetry, which can be approached in two different ways, further elaborated in the following.

Breaking symmetry with the lattice parameters

As indicated in Table 3.1, the cubic symmetry can be broken by adjusting the dimension of the lattice parameters while keeping the inclusion parameters uniform, meaning the inclusion corresponds to a perfect sphere or perfect cube. Uniaxial anisotropy can be introduced by adjusting the length of one of the parameters, for example, $a = b \neq c$. Similarly, a biaxial anisotropy is introduced when imposing $a \neq b \neq c$ on the unit cell and keeping the inclusion parameters uniform. The different realizations in the context of ellipsoid inclu-

sions with primitive centering are depicted in Figure 6.2.

Breaking symmetry with the inclusion parameters

Similarly to breaking the symmetry by changing the lattice parameters while keeping the inclusion parameters uniform, as described above, one can break unit cell symmetry by keeping the lattice parameters uniform and adjusting the inclusion parameters. Based on this approach, one can introduce uniaxial anisotropy by imposing $a' = b' \neq c'$ or biaxial anisotropy by imposing $a' \neq b' \neq c'$. The different realizations in the context of ellipsoid inclusions and a primitive form are depicted in Figure 6.2.

The exact values of the tensor components depend on the specific values of the lattice and inclusion parameters, as well as the centering of the unit cell.

6.2.2. Effect Crystal Centering

The centering of a crystal system, whether primitive, body-centered, or face-centered, affects the distribution of material within the unit cell and, consequently, the effective permittivity of the crystal. In a primitive centered crystal, the unit cell contains lattice points only at the corners, which is the simplest form of crystal centering, resulting in a single lattice point per unit cell. In a body-centered crystal, in addition to the lattice points at the corners of the unit cell, there is an additional lattice point at the center of the cell, effectively doubling the number of lattice points in the unit cell w.r.t. to the primitive lattice. In a face-centered crystal system, there are lattice points at each corner of the unit cell, as well as at the center of each face of the unit cell, resulting in a total of four lattice points per unit cell. On the one hand, an increase in lattice points increases the sensitivity of the effective permittivity with respect to the lattice- and inclusion parameters because the ratio of the inclusion volume to the unit cell volume δ_V changes more dramatically for a higher number of lattice points as depicted in Figure 6.3 for uniform lattice and inclusion parameters.

6.3. Forward Problem: Tensor Homogenization

In this section, the possible approaches to manipulating the effective permittivity tensor form discussed in the previous section are validated. To this end, first, a parametric study of dielectric crystals over a range of lattice and inclusion parameters for an isotropic host material is carried out, and the results organized isotropic, uniaxial anisotropic, and biaxial anisotropic are presented. Additionally, the effect of an anisotropic host material is discussed due to the inherent anisotropy introduced during the manufacturing process, as discussed in Chapter 5. From this study, various crystals exhibiting uniaxial and biaxial anisotropy are manufactured and characterized. The measured effective permittivity tensor component values from these samples are compared to results obtained from the homogenization.

6.3.1. Parametric Study

The parametric study is carried out for two principal cases for unit cells with ellipsoidal inclusions in primitive, body-centered, and face-centered centering. The breaking of symmetry with inclusion parameters and the breaking of symmetry with lattice parameters is investigated using the numerical parallel plate capacitor method as presented in Section

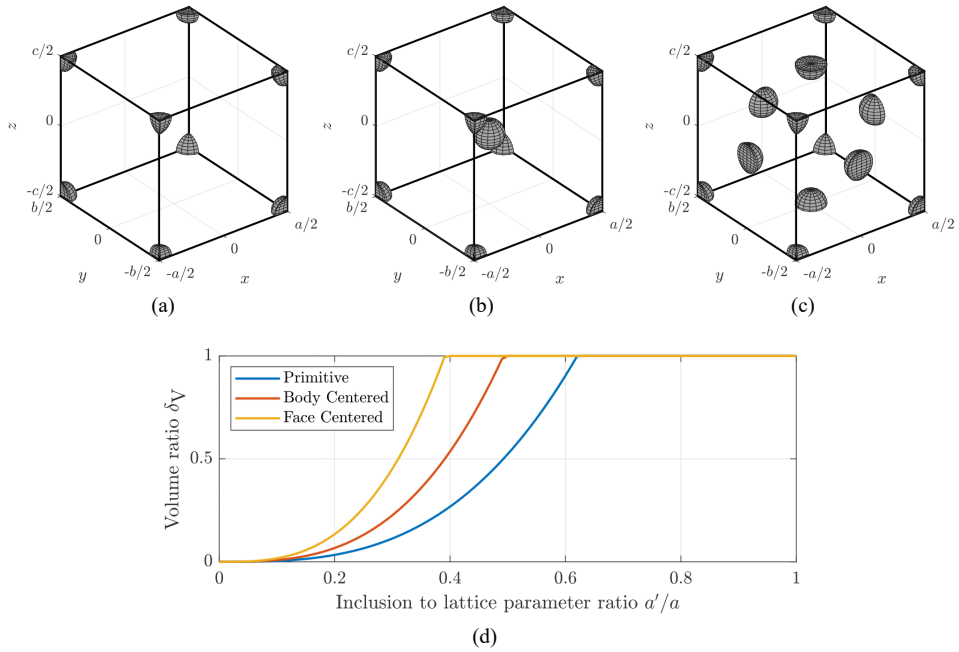

Figure 6.3: 3D periodic unit cells with inclusions (in gray) exhibiting cubic symmetry in (a) primitive, (b) body-centered, and (c) face-centered configurations and the respective (d) volumetric infill ratio.

4.2.2 to homogenize the effective permittivity tensor of the respective crystals. The results of the parametric study are split into isotropic, anisotropic uniaxial, and anisotropic biaxial cases below. Additionally, the effect of a uniaxial anisotropic host material due to the layer-by-layer manufacturing is discussed.

Isotropic

The effect of different isotropic base material permittivities $\varepsilon_{\mathrm{r,m}}$ and centerings on the effective permittivity tensor components is depicted in Figure 6.4. While Figure6.4a depicts the components as functions of lattice parameters $a = b = c$ for constant inclusion parameters, Figure 6.4b depicts the tensor components as functions of the inclusion parameters $a' = b' = c'$ for constant lattice parameters respectively. As expected, the dielectric crystal exhibits an isotropic effective permittivity tensor due to the cubic symmetry of the unit cells. In the case of the sweep regarding the lattice parameters, increased lattice parameters results in more material per unit cell, thus $\lim_{a=b=c\to\infty}[\tilde{\varepsilon_{\mathrm{r}}}] = \varepsilon_{\mathrm{r,m}}\mathbf{I}$ and $\lim_{a=b=c\to 0}[\tilde{\varepsilon_{\mathrm{r}}}] = \mathbf{I}$. In the case of the inclusion parameter sweeps, the relationship is reversed, and increasing inclusion parameters imply less material per unit cell, thus $\lim_{a'=b'=c'\to\infty}[\tilde{\varepsilon_{\mathrm{r}}}] = \mathbf{I}$ and $\lim_{a'=b'=c'\to 0}[\tilde{\varepsilon_{\mathrm{r}}}] = \varepsilon_{\mathrm{r,m}}\mathbf{I}$. Furthermore, the impact of different centerings is recognized in the higher sensitivity to changes in the inclusion parameters. This is due to the increased number of inclusions per unit cell; more material in the cell is removed in these configurations to increase inclusion dimensions.

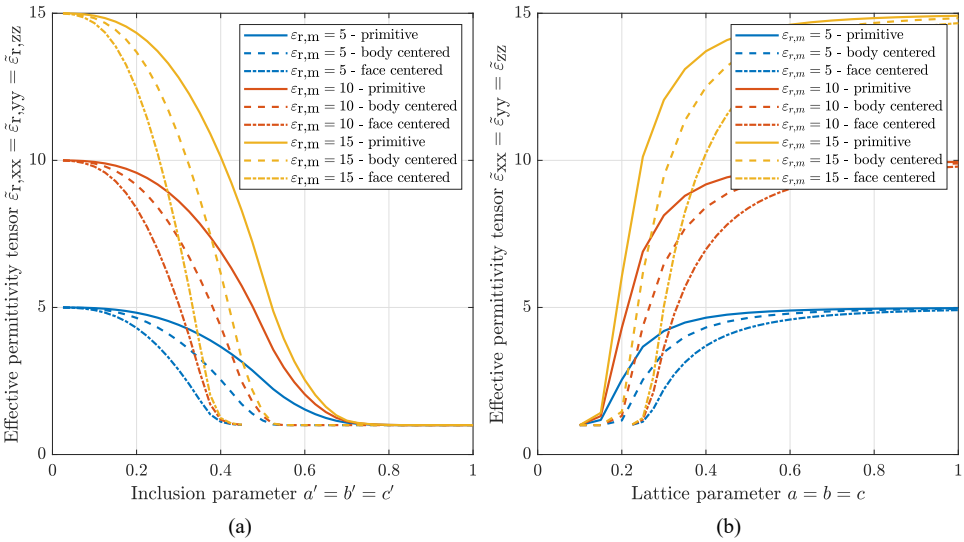

Figure 6.4: Effective permittivity tensor components of isotropic dielectric crystals with different base material permittivities and centerings as (a) a function of the lattice parameters $a = b = c$ for constant inclusion parameters $a' = b' = c' = 0.1$, and (b) a function of inclusion parameters $a' = b' = c'$ for constant lattice parameters $a = b = c = 1$.

6

Uniaxial Anisotropic

The effect of different isotropic base material permittivities $\varepsilon_{r,m}$ and centerings on the effective permittivity tensor components is depicted in Figure 6.5. While Figures 6.5a and 6.5b depict the components as functions of lattice parameters $a = b \neq c$ for constant inclusion parameters $a' = b' = c'$, Figures 6.5c and 6.5d depict the tensor components as function of the inclusion parameters $a' = b' \neq c'$ for constant lattice parameters $a = b = c$ respectively. For these two configurations, the unit cells obtain tetragonal symmetry and, thus, exhibit uniaxial anisotropy in their effective permittivity tensors. Concerning the sweep of lattice parameter, significant practical birefringence values $\tilde{\eta}$ are observed for low values of $a = b$, with low values for c providing positive and high values for c providing negative effective birefringence. The relationship is inverted for the sweep of inclusion parameters.

Biaxial Anisotropic

The effect of different isotropic base material permittivities $\varepsilon_{r,m}$ and centerings on the effective permittivity tensor components is depicted in Figure 6.6. While Figure 6.6a depicts the components for a sweep of the of lattice parameters $a \neq b \neq c$ for constant inclusion parameters $a' = b' = c'$, Figure 6.6b depicts the tensor components for a sweep of the inclusion parameters $a' = b' \neq c'$ for constant lattice parameters $a = b = c$ respectively. Due to the large amount of data concerned with the three practical permittivity tensor components as functions of three independent variables, a detailed discussion of the results is omitted. Instead, the results of the parameter sweeps presented in Figure 6.6 present the achievable parameter space of effective permittivity tensor component values.

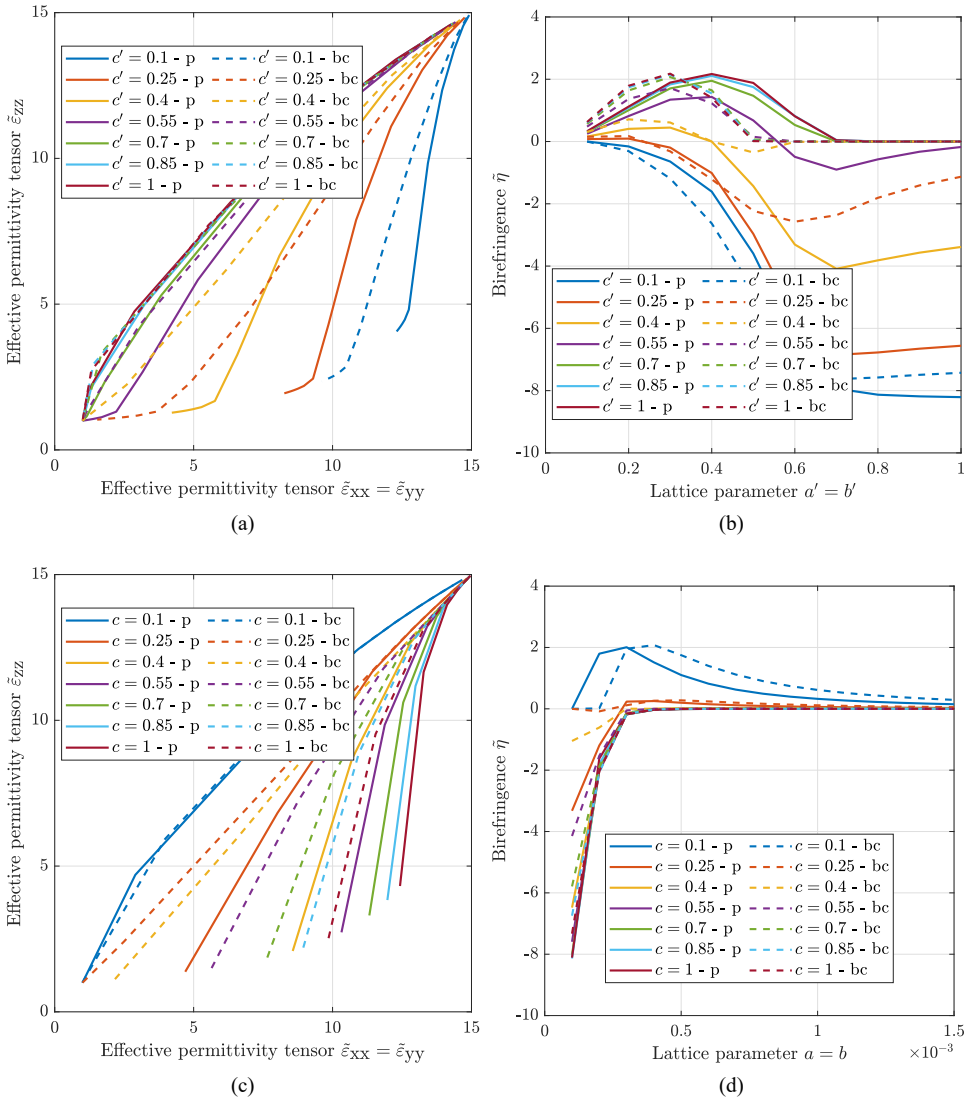

Figure 6.5: Effective permittivity tensor components of dielectric crystals exhibiting tetragonal symmetry with different base material permittivity $\varepsilon_{r,m} = 15$ and centerings as (a,b) a function of the lattice parameters $a = b \neq c$ for constant inclusion parameters $a' = b' = c' = 0.1$, and (c,d) a function of inclusion parameters $a' = b' \neq c'$ for constant lattice parameters $a = b = c = 1$.

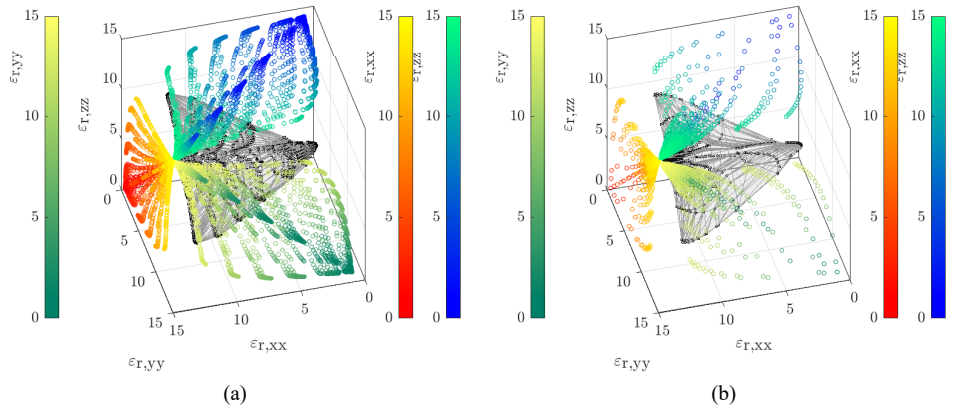

Figure 6.6: Visualization of possible values of individual effective relative permittivity tensor components (gray volume) with indications of numerical values as colored scatter plots for (a) manipulated lattice and (b) inclusion parameters of the dielectric crystal.

Uniaxial Anisotropic Host Material

The results regarding the parameter study of the effect of lattice and inclusion parameters presented in this chapter are considered an isotropic host material $\varepsilon_{\mathrm{r,m}}$. The results confirm the concept of engineering the effective permittivity of the dielectric crystal via manipulating the symmetry of the unit cell. However, as discussed in Chapter 5 the extrusion-based AM process introduces inherent anisotropy in the host material. This means that even for dielectric crystals that exhibit cubic symmetry in a geometric sense, the resulting effective permittivity tensor will exhibit some anisotropy because the symmetry is already broken due to the host material. This effect needs to be considered when engineering the effective permittivity tensor of dielectric crystals.

6.3.2. Experimental Validation

This section aims to provide an experimental verification of the parameter study above. To this end, dielectric crystals with biaxial and uniaxial effective permittivity tensors and both positive and negative birefringence are considered. Similar to the parametric study, the design of the dielectric crystals to exhibit the desired permittivity tensors is done via the engineering of either the lattice or the inclusion parameters for both primitive and body-centered configurations. The manufacturing material selected for this purpose is the ABS500 from Avient with a nominal permittivity of $\varepsilon_{\mathrm{r,ABS500}} = 5$ extruded with a $0.4\mathrm{mm}$ nozzle at a layer height of $0.16\mathrm{mm}$. As discussed in Chapter 5, the AM process introduces anisotropy in the host material of the crystal, which, as explained above, also affects the effective permittivity tensor. Therefore, a cubic sample of the ABS500 material printed with the above-mentioned print settings is characterized using the sample preparation process and measurement equipment as explained in 5.3.1. The extracted permittivity tensor for the

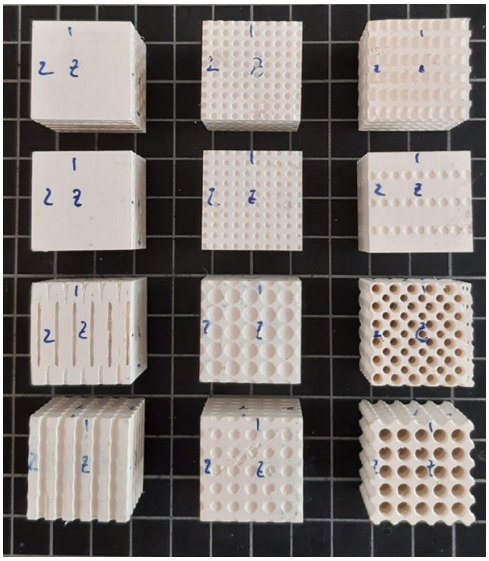

Figure 6.7: Anisotropic dielectric crystal samples for experimental characterization in a quadratic waveguide setup.

host material is

$$\left[\varepsilon_{\mathrm{r,m}}\right] = \begin{bmatrix} 4.62 & 0 & 0 \\ 0 & 4.58 & 0 \\ 0 & 0 & 4.25 \end{bmatrix}. \tag{6.1}$$

Similarly, each of the 12 dielectric crystal samples considered is manufactured and characterized three times to evaluate the statistics of the results. The manufactured samples are depicted in Figure 6.7. Furthermore, schematic plots of the individual unit cells and manufacturing samples in the quadratic waveguide sample fixture together with corresponding measurement results are depicted in Figures 6.8 and 6.9 for the samples with engineered inclusion and lattice parameters respectively. Additionally, numerical values for the lattice and inclusion parameters of individual samples together with homogenization and averaged measurement results are reported in Table 6.1. Generally, a good agreement between the homogenized and characterized values for the effective relative permittivity tensor components is observed. A continuous trend visible throughout all samples is that the homogenized values slightly under-predict the measured values, hinting at a systematic error in the procedure. The most reasonable explanation is a slight over-extrusion of material during the print process. Other potential errors include, an increased effect of manufacturing tolerances due to increased surface area of the dielectric lattice compared to a bulk sample, non-perfect sample preparation and inconsistencies in the repeated (dis-)assembly of the waveguide measurement equipment.

6.4. Inverse Problem: Dielectric Tensor Synthesis

After the treatment of the forward problem in the section above, this particular section demonstrates the inverse problem, as indicated in Figure 6.1, referring to the design of a

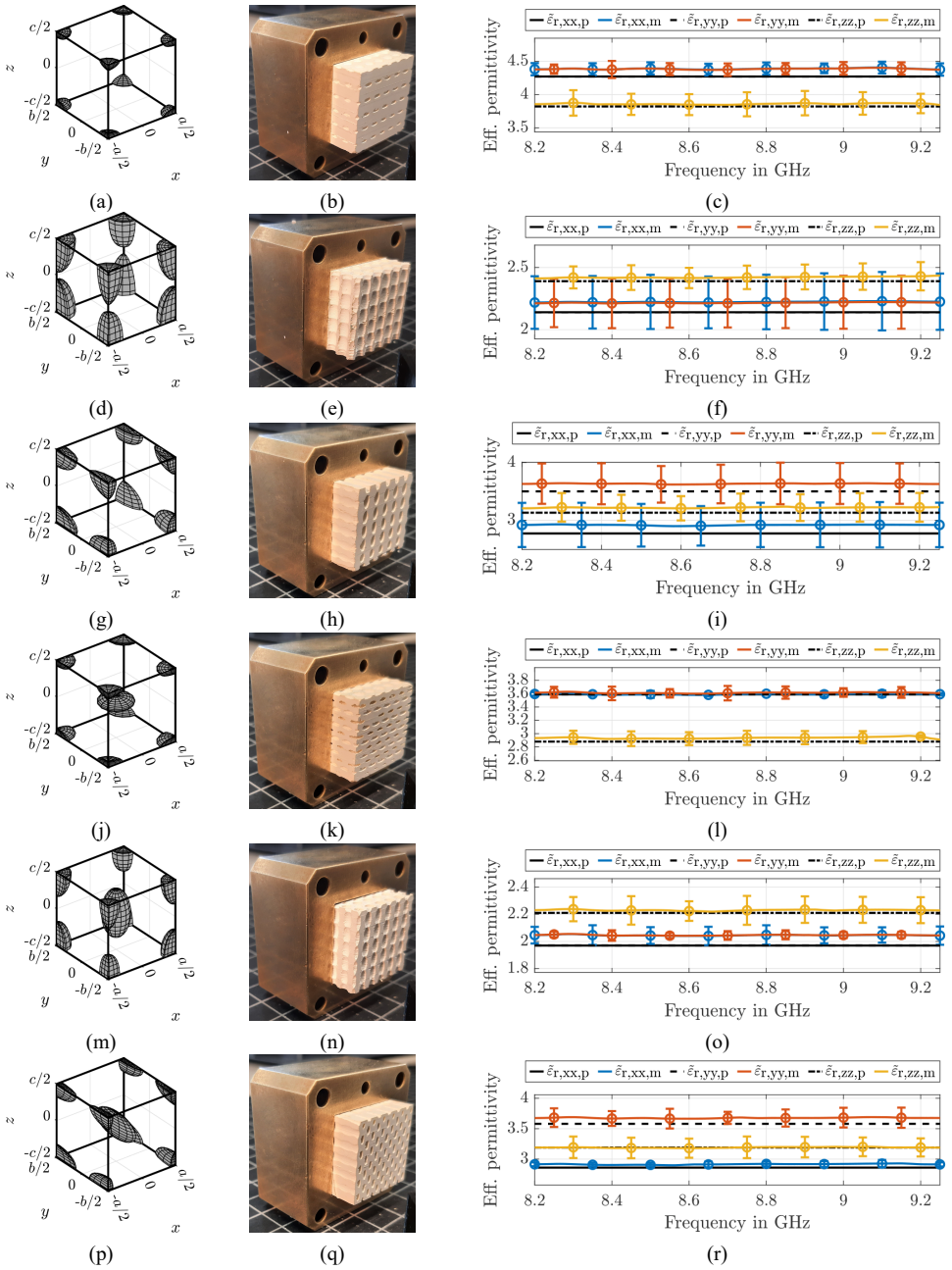

Figure 6.8: Experimental validation of effective relative permittivity tensor manipulation via the parameters of ellipsoidal inclusions in primitive (a-i) and body-centered(j-r) centering, with (a-c,j-l) uniaxial - negative birefringence, (d-f, m-o) uniaxial - positive birefringence, (g-i,p-r) biaxial tensor shape. Left: unit cells with inclusions highlighted in grey. Middle: manufactured samples placed in the waveguide fixture for characterization. Right: measured effective permittivity tensor components as a function of frequency, error-bars indicating the 99% confidence interval obtained via averaging over three independent samples.

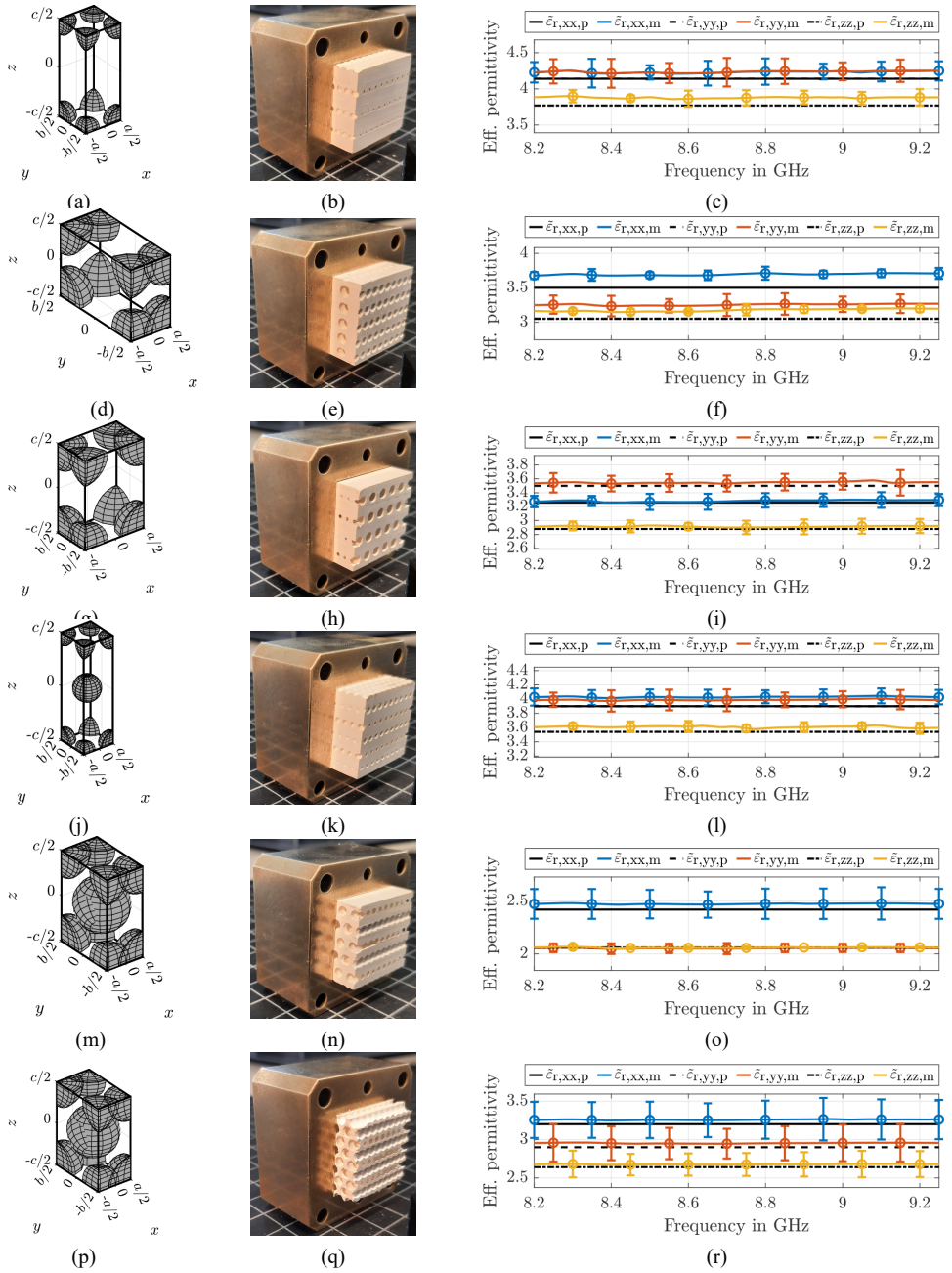

Figure 6.9: Experimental validation of effective relative permittivity tensor manipulation via the lateral dimensions of the lattice in primitive (a-i) and body-centered(j-r) centering, with (a-c,j-l) uniaxial - negative birefringence, (d-f, m-o) uniaxial - positive birefringence, (g-i,p-r) biaxial tensor shape. Left: unit cells with inclusions highlighted in gray. Middle: manufactured samples placed in the waveguide fixture for characterization. Right: measured effective permittivity tensor components as a function of frequency, error-bars indicating the 99% confidence interval obtained via averaging over three independent samples.

Table 6.1: Comparison of predicted and averaged experimental validation results of effective relative permittivity tensor components of different dielectric crystal samples with manipulated permittivity tensor components via lattice and ellipsoidal inclusion parameters in primitive and body-centered symmetries.

Shape	Cent.	Lattice in mm	Inclusion in mm	Prediction $[\varepsilon_{r,h}]$	Measurement $[\varepsilon_{r,m}]$	rel. Error $\Delta[\varepsilon_r]$
Manipulation of inclusion parameters ($a = b = c$)						
uni. $\eta-$	p	$a = 4$ $b = 4$ $c = 4$	$a' = 1.4$ $b' = 1.4$ $c' = 0.6$	$\varepsilon_{r,xx,h} = 4.27$ $\varepsilon_{r,yy,h} = 4.27$ $\varepsilon_{r,zz,h} = 3.82$	$\varepsilon_{r,xx,m} = 4.39 \pm 0.09$ $\varepsilon_{r,yy,m} = 4.38 \pm 0.08$ $\varepsilon_{r,zz,m} = 3.86 \pm 0.17$	2.73 % 2.65 % 0.98 %
uni. $\eta+$	p	$a = 4$ $b = 4$ $c = 4$	$a' = 1.8$ $b' = 1.8$ $c' = 3.4$	$\varepsilon_{r,xx,h} = 2.14$ $\varepsilon_{r,yy,h} = 2.14$ $\varepsilon_{r,zz,h} = 2.39$	$\varepsilon_{r,xx,m} = 2.22 \pm 0.22$ $\varepsilon_{r,yy,m} = 2.15 \pm 0.20$ $\varepsilon_{r,zz,m} = 2.42 \pm 0.10$	3.89 % 3.55 % 1.34 %
bi	p	$a = 4$ $b = 4$ $c = 4$	$a' = 1$ $b' = 3$ $c' = 1.8$	$\varepsilon_{r,xx,h} = 2.77$ $\varepsilon_{r,yy,h} = 3.50$ $\varepsilon_{r,zz,h} = 3.13$	$\varepsilon_{r,xx,m} = 2.92 \pm 0.38$ $\varepsilon_{r,yy,m} = 3.63 \pm 0.35$ $\varepsilon_{r,zz,m} = 3.22 \pm 0.23$	5.27 % 3.78 % 2.82 %
uni. $\eta-$	bc	$a = 4$ $b = 4$ $c = 4$	$a' = 1.8$ $b' = 1.8$ $c' = 0.6$	$\varepsilon_{r,xx,h} = 3.59$ $\varepsilon_{r,yy,h} = 3.59$ $\varepsilon_{r,zz,h} = 2.88$	$\varepsilon_{r,xx,m} = 3.59 \pm 0.03$ $\varepsilon_{r,yy,m} = 3.61 \pm 0.09$ $\varepsilon_{r,zz,m} = 2.93 \pm 0.10$	0.10 % 0.65 % 1.96 %
uni. $\eta+$	bc	$a = 4$ $b = 4$ $c = 4$	$a' = 1.4$ $b' = 1.4$ $c' = 2.6$	$\varepsilon_{r,xx,h} = 1.97$ $\varepsilon_{r,yy,h} = 1.97$ $\varepsilon_{r,zz,h} = 2.21$	$\varepsilon_{r,xx,m} = 2.05 \pm 0.06$ $\varepsilon_{r,yy,m} = 2.05 \pm 0.03$ $\varepsilon_{r,zz,m} = 2.23 \pm 0.10$	3.84 % 3.87 % 0.87 %
bi.	bc	$a = 4$ $b = 4$ $c = 4$	$a' = 0.6$ $b' = 3$ $c' = 1.4$	$\varepsilon_{r,xx,h} = 2.86$ $\varepsilon_{r,yy,h} = 3.58$ $\varepsilon_{r,zz,h} = 3.19$	$\varepsilon_{r,xx,m} = 2.92 \pm 0.04$ $\varepsilon_{r,yy,m} = 3.68 \pm 0.14$ $\varepsilon_{r,zz,m} = 3.19 \pm 0.16$	1.91 % 2.70 % 0.02 %
Manipulation of lattice parameters ($a' = b' = c'$)						
uni. $\eta-$	p	$a = 2.40$ $b = 2.40$ $c = 6.24$	$a' = 1.92$ $b' = 1.92$ $c' = 1.92$	$\varepsilon_{r,xx,h} = 4.14$ $\varepsilon_{r,yy,h} = 4.14$ $\varepsilon_{r,zz,h} = 3.77$	$\varepsilon_{r,xx,m} = 4.23 \pm 0.15$ $\varepsilon_{r,yy,m} = 4.24 \pm 0.16$ $\varepsilon_{r,zz,m} = 3.86 \pm 0.09$	2.22 % 2.30 % 2.91 %
uni. $\eta+$	p	$a = 2.67$ $b = 6.22$ $c = 4.44$	$a' = 3.56$ $b' = 3.56$ $c' = 3.56$	$\varepsilon_{r,xx,h} = 3.50$ $\varepsilon_{r,yy,h} = 3.05$ $\varepsilon_{r,zz,h} = 3.05$	$\varepsilon_{r,xx,m} = 3.70 \pm 0.16$ $\varepsilon_{r,yy,m} = 3.16 \pm 0.13$ $\varepsilon_{r,zz,m} = 3.18 \pm 0.09$	5.59 % 6.72 % 4.11 %
bi.	p	$a = 4.00$ $b = 2.40$ $c = 5.60$	$a' = 3.20$ $b' = 3.20$ $c' = 3.20$	$\varepsilon_{r,xx,h} = 3.26$ $\varepsilon_{r,yy,h} = 3.50$ $\varepsilon_{r,zz,h} = 2.88$	$\varepsilon_{r,xx,m} = 3.28 \pm 0.10$ $\varepsilon_{r,yy,m} = 3.55 \pm 0.12$ $\varepsilon_{r,zz,m} = 2.92 \pm 0.06$	0.74 % 1.35 % 1.22 %
uni. $\eta-$	bc	$a = 2.40$ $b = 2.40$ $c = 8.16$	$a' = 1.92$ $b' = 1.92$ $c' = 1.92$	$\varepsilon_{r,xx,h} = 3.90$ $\varepsilon_{r,yy,h} = 3.90$ $\varepsilon_{r,zz,h} = 3.54$	$\varepsilon_{r,xx,m} = 4.03 \pm 0.10$ $\varepsilon_{r,yy,m} = 3.99 \pm 0.13$ $\varepsilon_{r,zz,m} = 3.61 \pm 0.06$	3.34 % 2.28 % 1.92 %
uni. $\eta+$	bc	$a = 2.40$ $b = 4.00$ $c = 5.60$	$a' = 3.20$ $b' = 3.20$ $c' = 3.20$	$\varepsilon_{r,xx,h} = 2.42$ $\varepsilon_{r,yy,h} = 2.06$ $\varepsilon_{r,zz,h} = 2.06$	$\varepsilon_{r,xx,m} = 2.47 \pm 0.14$ $\varepsilon_{r,yy,m} = 2.06 \pm 0.04$ $\varepsilon_{r,zz,m} = 2.06 \pm 0.01$	2.20 % 0.26 % 0.02 %
bi.	bc	$a = 2.40$ $b = 4.00$ $c = 8.80$	$a' = 3.20$ $b' = 3.2.0$ $c' = 3.2.0$	$\varepsilon_{r,xx,h} = 3.20$ $\varepsilon_{r,yy,h} = 2.90$ $\varepsilon_{r,zz,h} = 2.64$	$\varepsilon_{r,xx,m} = 3.24 \pm 0.20$ $\varepsilon_{r,yy,m} = 2.94 \pm 0.18$ $\varepsilon_{r,zz,m} = 2.64 \pm 0.13$	1.20 % 1.22 % 0.93 %

dielectric crystal, exhibiting a desired effective permittivity tensor. This topic is much more sophisticated than the forward problem, and a full treatment is out of the scope of this work. The problem is simply demonstrated via the synthesis of an effectively isotropic dielectric crystal with a target effective permittivity tensor $[\varepsilon_{\mathrm{r,target}}] = 4\mathbf{I}$. The synthesis shall be carried out considering manufacturing from the ABS650 material with a nozzle diameter of $0.4\mathrm{mm}$ and a layer height $0.16\mathrm{mm}$. As reported in Table 5.2, this material and print settings combination exhibits a permittivity tensor

$$[\varepsilon_{\mathrm{r,m}}] = \begin{bmatrix} 5.93 & 0 & 0 \\ 0 & 5.93 & 0 \\ 0 & 0 & 5.03 \end{bmatrix}. \tag{6.2}$$

The synthesis is implemented as a two-stage optimization using a parametrically defined unit cell with ellipsoidal inclusion in a primitive centering configuration as a template, using the inclusion parameters as optimization variables. Since the synthesis concerns the design of an effectively isotropic dielectric crystal from a uniaxial anisotropic host material, the optimization variables can be limited to $a' = b'$ and c'. The optimization is implemented in Matlab using the *fmincon*[1] function. In the first optimization stage, the semi-analytical variant of the equivalent parallel plate capacitance model, as explained in Section 4.2.2, is utilized due to its superior computational efficiency. The outcome of this rough optimization is further utilized as an initial value in the second optimization step, which uses the numerical variant of the equivalent parallel plate capacitance model, as explained in Section 4.2.2, to arrive at final values for unit cell geometry. As last step the unit cell is scaled prior to manufacturing such that effects from manufacturing tolerances and frequency dispersion in the lattice to be negligible. Three samples of the synthesized dielectric crystal, as depicted in Figure are manufactured and characterized. The averaged measurement results for the individual permittivity tensors as a function of frequency are depicted in Figure 6.11, and the mean effective permittivity tensor is

$$[\varepsilon_{\mathrm{r,synth}}] = \begin{bmatrix} 3.99 \pm 0.12 & 0 & 0 \\ 0 & 3.96 \pm 0.11 & 0 \\ 0 & 0 & 3.93 \pm 0.08 \end{bmatrix} \tag{6.3}$$

with the ranges indicating the 99% confidence interval based on the standard deviation from three independently characterized samples.

6.5. Conclusion

This chapter presents novel insights into manipulating the effective permittivity tensor of periodic dielectric structures. It investigates the fundamental relationship between crystal symmetry and anisotropy in the effective permittivity tensor, as predicted by crystallographic principles. To this end, a parametrically defined unit cell consisting of an isotropic host material with ellipsoidal inclusions was considered. Using the simple example of a unit cell with cubic symmetry, the effect of symmetry breaking on the effective permittivity tensor was demonstrated. Cubic symmetry was disrupted in two distinct ways: by altering

[1] A more appropriate choice for the optimization algorithm might exist for this type of problem, but the in-depth analysis of the cost function is out of scope for this work.

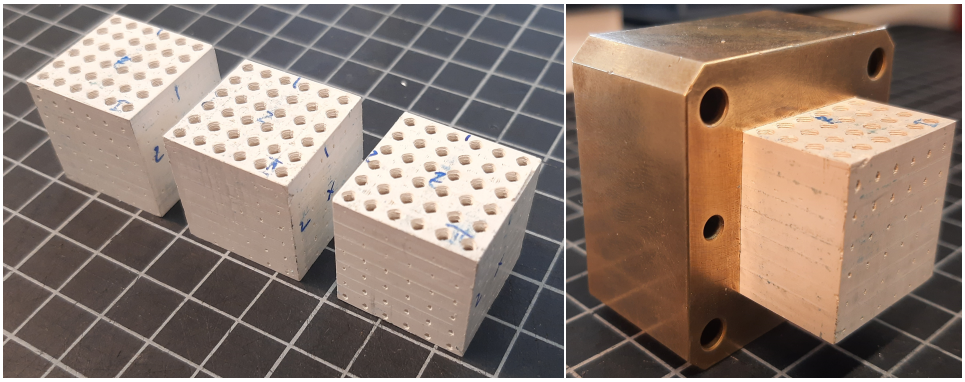

(a) (b)

Figure 6.10: (a) Three independently manufactured samples of the periodic dielectric lattice synthesized to exhibit an isotropic effective relative permittivity tensor $[\tilde{\varepsilon}_{\mathrm{r,target}}] = 4\mathbf{I}$. (b) Sample in quadratic waveguide fixture for experimental characterization of the effective relative permittivity tensor.

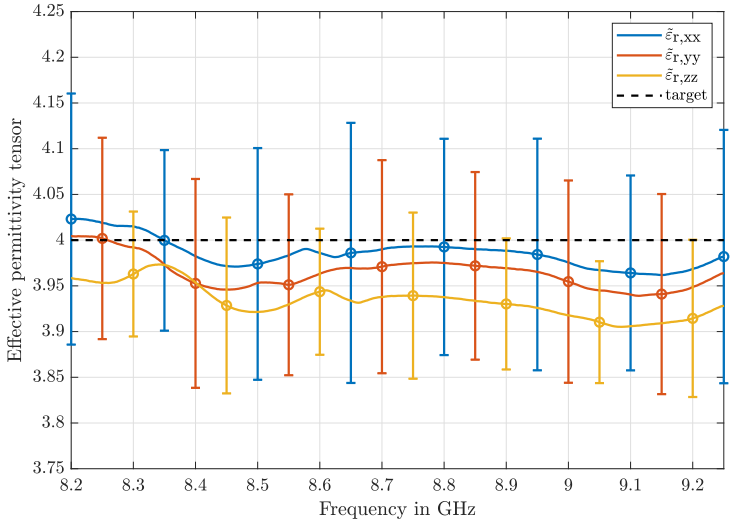

Figure 6.11: Effective permittivity tensor components of the synthesized dielectric crystal averaged over three samples. Error bars indicating the 99% confidence interval based on the standard deviation over three samples.

the spacing between uniform ellipsoidal (spherical) inclusions and by modifying the ellipsoidal inclusions' parameters. In both cases, it was shown that unit cells with tetragonal symmetry exhibit uniaxial anisotropy for isotropic host materials, whereas unit cells with orthorhombic symmetry exhibit biaxial anisotropy. The impact of an anisotropic host material introduced through extrusion-based additive manufacturing (AM) was also examined. The predictions derived from the parameter study were validated through experimental verification of the effective permittivity tensor for twelve dielectric crystals in both primitive and body-centered configurations, exhibiting uniaxial and biaxial anisotropy. The experimental results confirmed the feasibility of precisely manipulating the effective permittivity tensor components of periodic dielectric lattices. Furthermore, the inverse problem—designing a dielectric crystal with a desired effective permittivity tensor—was briefly considered. A dielectric crystal was synthesized to achieve an isotropic effective permittivity tensor using a two-stage optimization approach to address this. Experimental validation confirmed that the synthesized structure achieved the targeted isotropic effective permittivity tensor.

7

Spatially Modulated Long-Wavelength Dielectric Crystals

Abstract
The attention of the thesis now shifts to application oriented research. In the present chapter the concept of spatial modulation in long-wavelength dielectric crystals is applied in two novel ways. First the effect of controlled heterogeneity, specifically linearly varying relative permittivity profiles, on the performance of cylindrical dielectric resonator antennas is studied. From numerical simulation and experimental verification it is demonstrated that the introduction of such heterogeneity into the resonating body of the antennae provides improvements in terms of impedance and axial ratio bandwidth. Second the application of heterogeneous slabs in rectangular waveguides to engineer the transmission and reflection spectra is considered. Specifically a heterogeneous slab is engineered via an optimization approach to approximate the transfer function characteristics of a 3rd order Chebycheff bandpass filter.

7.1. L-Band Heterogeneous Dielectric Resonator Antennas

7.1.1. Motivation

Dielectric resonator antennas (DRAs), as reviewed in Section 2.3 are viable alternatives to traditionally employed radiating elements such as wire and patch antennas thanks to their high radiation efficiency due to the absence of conduction losses [117]. Multi-permittivity and inhomogeneous variations of the dielectric resonator are thought to be a proper way to achieve wideband operation [118][119][120], multi-band behavior [118] or increase the spurious-free window [121]. Several works successfully utilized AM of dielectrics to create bulk homogeneous DRAs with various materials and shapes[122][52][123]. Furthermore, the AM capabilities have been exploited to create complex periodic distributions of high-permittivity material to engineer the permittivity of a DRA [36]. Additionally, multi-permittivity (inhomogeneous) DRAs have been created for bandwidth improvement [55] [54] [124] [56]. However, so far, additive manufactured devices with inhomogeneous permittivity have only been manufactured with discrete sections of a specific permittivity. The potential of continuously swept permittivity distributions in the device has yet to be explored in literature. This Section aims to address this literature gap by utilizing spatial variant lattices (SVL), as introduced in Section 2.4.3, to create periodically structured geometries with continuously varied volumetric fill-fraction. The goal is to show the design, simulation, and manufacturing of swept permittivity profiles and investigate their effect on the performance of cylindrical DRAs. For this purpose, linearly swept profiles with increasing permittivity along the radial and vertical axis are studied. The DRAs discussed here are intended for application in the L-band and optimized for operation at the Galileo E1 band center frequency of 1.575 GHz. However, the proposed approach for creating continuously swept permittivity profiles can be scaled to any desired frequency band, given that the manufacturing process can produce structures sufficiently small with respect to the wavelength.

The rest of the Section is structured as follows. First the DRA concept and the selected permittivity profiles are introduced. Next, the optimization results to find the appropriate dimensions for DRAs with linearly swept effective permittivity profiles along their radial and vertical axis are presented and finally the measured results are discussed and compared to full wave simulations

7.1.2. Design

Antenna Geometry and Permittivity Range

The individual cylindrical DRAs with radius a_{DRA}, height h_{DRA} on a cylindrical ground plane with radius a_{GP}, as depicted in Figure 7.1a, are fed via two 50 Ω coaxial probes of length l_{feed} with an offset of a_{feed} from the DRA center. The probes are excited with 90° phase offset (Port 1: 0°; Port2: -90°) for right-hand circular polarization (RHCP). The antennas are manufactured via a fused deposition modeling (FDM) process utilizing the ABS1500 filament from Avient (former Preperm) with a nominal relative permittivity of $\varepsilon_{\mathrm{r,p}} = 15$. However, the relative permittivity of printed substrates heavily depends on the FDM process parameters like layer height, line width, extrusion multiplier, etc., as demonstrated in [114]. Therefore, the effect of the later utilized printing parameters on the relative permittivity of a printed bulk ABS1500 sample was investigated with a material character-

ization setup based on rectangular waveguides as described in Chapter 5. The experiment showed a reduction in relative permittivity from the nominal value to $\tilde{\varepsilon}_{\mathrm{r,max}} = 13.7$, which is further considered to be the maximum achievable permittivity in our design. The swept permittivity profiles are generated via the method introduced in [99], based on an FCC unit cell generated via spatial harmonics as described in [105]. The effective permittivity of the unit cell can be adjusted with the threshold values th, which controls the volumetric infill, as further explained below.

The dielectric crystal used to realize the effective permittivity distribution described in the following section is based on a spatial harmonic superposition based on the face-centered cubic lattice vectors, as described in Section 3.2.2 and the spatial modulation technique explained in Section 3.2.3.

Effective Permittivity

The relationship of the effective permittivity to the threshold parameter is studied with the eigenmode method as explained in Section 4.2.3. The effective permittivity as a function of the threshold th is depicted in Figure 7.1b. The lattice is connected to its neighboring unit cell up to a maximum threshold of $\tilde{th}_{\mathrm{max}} = 0.625$, and for convenient manufacturing, a maximum threshold of $th_{\mathrm{max}} = 0.6$ is chosen which corresponds to a minimum manufacturable effective relative permittivity of $\tilde{\varepsilon}_{\mathrm{r,min}} = 3$, which is further considered to be the minimum achievable permittivity in this design.

Permittivity Profiles

Three individual cylindrical DRA versions with different permittivity profiles $\varepsilon_{\mathrm{r}}(\mathbf{r})$, based on the geometry depicted in Figure 7.1a are considered in this work. A homogeneous DRA is manufactured with the maximum achievable relative permittivity while two inhomogeneous DRAs are engineered to obtain a linearly swept permittivity profile from $\tilde{\varepsilon}_{\mathrm{r,min}}$ to $\tilde{\varepsilon}_{\mathrm{r,max}}$. The individual DRAs will further be referred to as:

- *DRA-H* - Homogeneous DRA with $\varepsilon_{\mathrm{r}}(\mathbf{r}) = \tilde{\varepsilon}_{\mathrm{r,max}}$ for comparison purposes;
- *DRA-IHZ* - Inhomogeneous DRA with a linearly swept permittivity profile along the vertical (z)-axis, $\varepsilon_{\mathrm{r}}(\mathbf{r}) = k_z z + d_{\mathrm{IHR}}$;
- *DRA-IHR* - Inhomogeneous DRA with a linearly swept permittivity profile along the radial (r)-axis, $\varepsilon_{\mathrm{r}}(\mathbf{r}) = k_{\mathrm{r}} r + d_{\mathrm{IHR}} = k_{\mathrm{r}}\sqrt{x^2 + y^2} + d_{\mathrm{IHR}}$;

with

$$k_z = \frac{\tilde{\varepsilon}_{\mathrm{r,max}} - \tilde{\varepsilon}_{\mathrm{r,min}}}{h_{\mathrm{DRA}}} \tag{7.1}$$

$$k_{\mathrm{r}} = \frac{\tilde{\varepsilon}_{\mathrm{r,max}} - \tilde{\varepsilon}_{\mathrm{r,min}}}{a_{\mathrm{DRA}}} \tag{7.2}$$

$$d_{\mathrm{IHR}} = d_{\mathrm{IHZ}} = \tilde{\varepsilon}_{\mathrm{r,min}}. \tag{7.3}$$

The individual permittivity profiles of the three considered DRA configurations are depicted in Figure 7.1c.

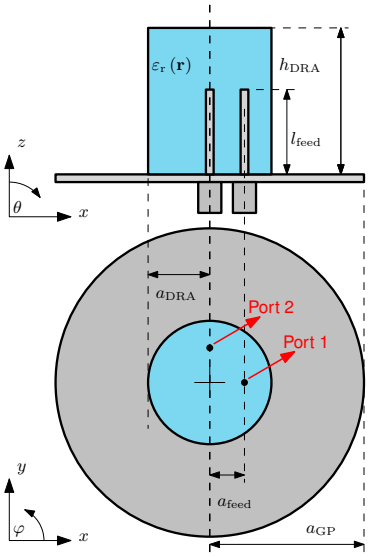

(a)

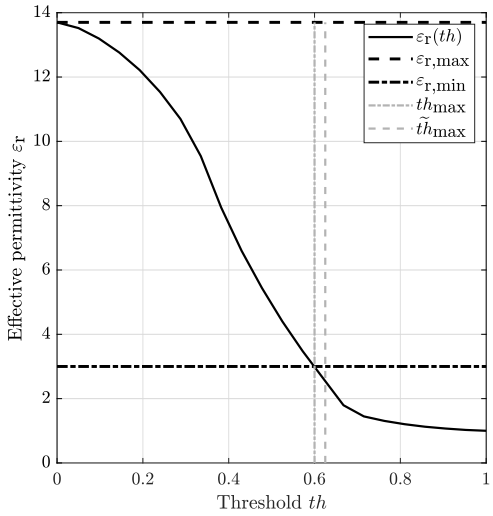

(b)

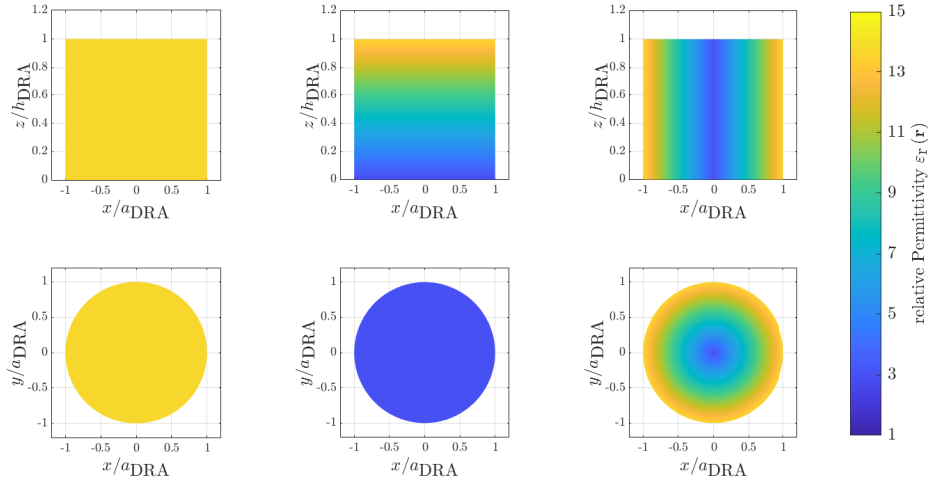

(c)

Figure 7.1: (a) Geometry of the cylindrical dielectric resonator antenna with two coaxial probe feeds mounted on a cylindrical ground plane. (b) Relationship between the unit cell threshold (th) and the effective permittivity for a face-centered cubic dielectric crystal created from a material with permittivity $\tilde{\varepsilon}_r = 13.7$. The lattice is fully connected up to a maximum threshold $\tilde{th}_{max}$ and is compatible to our manufacturing process up to th_{max}. (c) Permittivity profile cuts of the considered homogeneous (left), inhomogeneous along the vertical axis (middle) and inhomogeneous along the radial axis (right) DRAs in the xz plane at $y = 0$ (top) and in the xy plane at $z = 0$ (bottom)

Table 7.1: Geometric parameters of DRA antennas and permittivity function $\varepsilon_r(\mathbf{r})$ after optimization with the goal obtain a minimum in the reflection coefficient at the design frequency 1.575 GHz.

DRA (units in mm)	a	h	a_{feed}	l_{feed}	$\varepsilon_r(\mathbf{r})$
DRA - H	22.85	33.00	12.95	22.45	13.7
DRA - IHZ	27.75	38.85	16.15	20.10	$0.275z$+3
DRA - IHR	22.80	34.29	13.10	19.30	$0.469r$+3

Optimization

While the dimensions of a homogeneous DRA dimensions can be found quickly utilizing the design equations in [125], no such equations are available for inhomogeneous DRAs. Therefore, the dimensions of the two inhomogeneous antenna variations are found via optimization in the commercial EM solver package Ansys high-frequency structure simulation software (HFSS). Since HFSS does not allow the definition of inhomogeneous material, the model for the inhomogeneous DRAs is built with distinct layers or shells of homogeneous material to approximate the desired permittivity profile in the resonating body, as depicted in Figure 7.1c. While the range of the permittivity profile is fixed form $\varepsilon_r \in [3\ 13.7]$ as explained above, the model geometry is subject to an optimization problem to match the antenna to the center frequency of the E1 GNSS band (1.575 GHz). The optimization is set up to minimize the reflection S_{11} and transmission S_{21} at the E1 center frequency by changing the geometric parameters a_{DRA}, h_{DRA}, a_{feed} and $_{\text{feed}}$. It has been observed that the results obtained from the simulations sufficiently converged around 20 shells and layers. Therefore, the optimization routine was carried out with 20 individual shells/layers, and for the final simulations, this number was increased to 50. While Table 7.1 lists the optimized geometry parameters for each of the three antenna variations with their respective permittivity function $\varepsilon_r(\mathbf{r})$, the resulting reflection coefficients, realized gain, and the axial ratio at $\theta = 0°$ are plotted as a function of frequency in Figures 7.2a and 7.2b, respectively. In Figure 7.2a one can observe that the reflection coefficients show respective minima approximately at the E1 center frequency, as was the goal of the optimization. Furthermore, both inhomogeneous DRAs extend the impedance bandwidth with respect to the homogeneous one. An interesting observation is that the coupling between the two feed ports is reduced for the inhomogeneous DRAs at the design frequency, which implies improved realized gain and axial ratio values, which is confirmed by the plots in Figure 7.2b.

7.1.3. Results

The geometric mesh of the continuously varied lattice for the inhomogeneous DRAs is obtained directly from the SVL algorithm and saved as a standard tessellation (STL) file. Models are printed with 100% infill, employing the ABS1500 material. A 0.25mm nozzle is utilized at an extrusion temperature of 270° Celsius with a heated bed at 110° Celsius and a layer height of 0.15mm [1]. The produced antennas with installed coaxial probes and mounted on individual aluminum ground planes are depicted in Figure 7.3. Scattering parameters between the two feed-ports were measured with a vector network analyzer between 1 and 2 GHz and are compared to the simulation results in Figure 7.4a. For the measurement of

[1] The printing parameters are the same used for manufacturing the bulk sample which was measured to obtain a permittivity of $\varepsilon_{r,\max} = 13.7$, as explained in Section 7.1.2

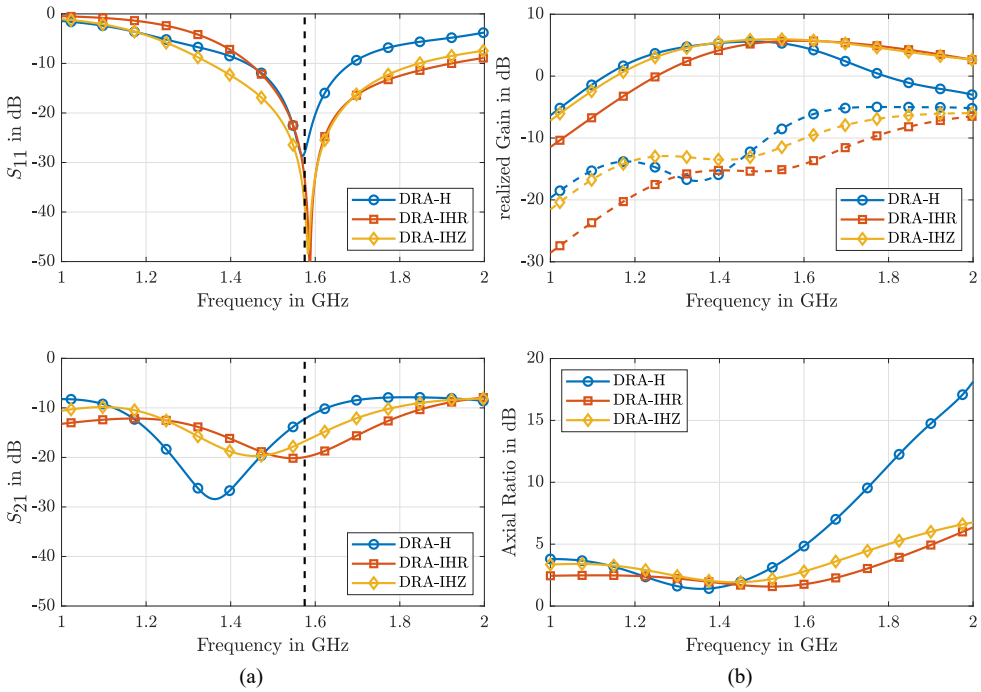

Figure 7.2: Simulated (a) S-parameters and (b) realized gain and axial ratio values of the homogeneous (blue), radial inhomogeneous (red), and vertical inhomogeneous (yellow) cylindrical dielectric resonator antennas between the two feeding probes. (top) S_{11}; (bottom) S_{21}.

7

the DRAs radiation patterns, the individual antennas are fed via a 90° hybrid (MiniCircuits ZX10Q-2-19+) for RHC polarization and placed in an MVG Starlab near-field chamber. Measured realized gain in RHC and LHC polarization values at $\theta = 0°$, as well as the axial ratio at $\theta = 0°$, are plotted as a function of frequency in Figure 7.4b and compared to simulated results. The simulated and measured realized gain and axial ratio patterns at the design frequency are compared for the DRA-H, DRA-IHR, and DRA-IHZ in Figures 7.5, 7.6 and 7.7 respectively. Simulated and measured numerical values of impedance bandwidth, axial ratio bandwidth, and realized gain are compared for each of the three antennae in Table 7.2. From Figure 7.4a one is able to observe some discrepancies between simulation and measurement. First of all, the homogeneous antenna obtains a broader impedance bandwidth than predicted from simulations. Furthermore, the reflection coefficients for the DRA-IHR and DRA-IHZ antennae do not obtain their respective minima at the design frequency but are shifted to higher frequencies. Although there are some shifts in the center frequency, the predicted effect of improved isolation between the feed ports is confirmed for both the DRA-IHR and DRA-IHZ antennas.

The measured RHC realized gains of the DRA-H, DRA-IHR, and DRA-IHZ antennas in Figure 7.4b show slightly reduced values compared to the simulated ones, which can be explained via the insertion loss of the utilized 90° hybrid that was employed to achieve RHC

Table 7.2: Comparison of simulated and measured results for the resonance frequency f_{res}, impedance bandwidth B_{Z}, axial ratio bandwidth B_{AR} and realized gain G_{r} of the DRA antennas.

DRA	source	f_{res} in GHz	B_{Z} ($S_{11} < -10$dB)		B_{AR} (3dB; $\theta = 0$)		G_{r} ($\theta = 0$; $f = 1.575$ GHz)	
			in MHz	in %	in MHz	in %	RHC in dBiC	LHC in dBiC
DRA-H	sim	1.575	245	15.7	353	26.3	5.0	-7.5
DRA-H	meas	1.591	457	28.7	425	29.8	4.3	-15.3
DRA-IHR	sim	1.582	475	28.2	790	58.7	5.71	-14.7
DRA-IHR	meas	1.794	513	28.6	549	32.1	4.1	-16.5
DRA-IHZ	sim	1.580	495	30.9	410	29.9	5.9	-10.8
DRA-IHZ	meas	1.631	384	23.5	355	21.4	4.8	-14.8

polarized radiation. Additionally, the realized gain of the DRA-IHR antenna shows a more significant reduction in realized Gain between 1.35 and 1.55 GHz compared to simulation which most probably due to the shifted resonance frequency of the DRA-IHR antenna. The predicted improvement of axial ratio values at $\theta = 0°$ is well observed in measurement in Figure 7.4b (bottom) for both inhomogeneous DRAs. However, the shape of the axial ratio curves is shifted to higher frequencies similar to the shift observed in the feed coupling $|S_{21}|$ in Figure 7.4a.

The realized gain and axial ratio patterns at 1.575 GHz depicted in Figures 7.5, 7.6, and 7.7 are not perfectly symmetric as the azimuth region $\varphi \in [0° \; 90°]$ experiences higher RHCP realized gain and improved axial ratio values. This effect is due to the position of the two coaxial feed probes at $\varphi = 0°$ and $\varphi = 90°$ as shown in the schematic of the antenna in Figure 7.1a. This distortion can be improved by further increasing the number of feed points of the individual antennas. Overall the shape of the realized gain and axial ratio patterns predicted by simulations is adequately reproduced in the measurement. The inhomogeneous DRAs show significantly improved axial ratio values, not only at $\theta = 0°$ but also over a larger angular area compared to the homogeneous DRA due to the reduced feed coupling in the inhomogeneous resonator bodies.

7.1.4. Discussion and Conclusion

Generally, the chosen simulation approaches deliver a reasonable agreement between simulations and measurements. This fact is essential to highlight due to two reasons. First, the modeling of the relationship between the volumetric fill-fraction and effective permittivity of the unit cell is done with the plane wave expansion method, which assumes a plane wave propagating through the infinite lattice, while the DRA feeding can be considered to be more of a point-like source. The point-like source excites a broad spectrum of homogeneous and inhomogeneous spectral harmonics of the electromagnetic field. Nevertheless, the results are in reasonable agreement confirming the validity of the PWEM modeling approach. Another reason is that the numerical simulation model of the DRA is not considered with the final geometry of the DRA but with individual layers and shells of homogeneous dielectrics. The layered/shelled approach was chosen because the spatial harmonic design approach cannot be replicated in HFSS. However, still, a high number of layers/shells is necessary for the model to adequately represent the intended permittivity profile, leading to a rather complex mesh and significantly increased simulation times. The observed improve-

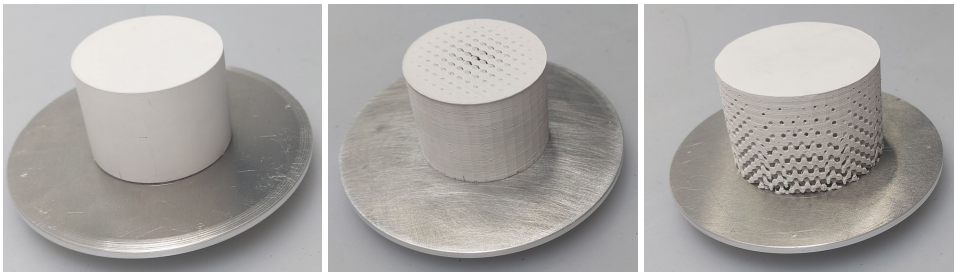

(a) (b) (c)

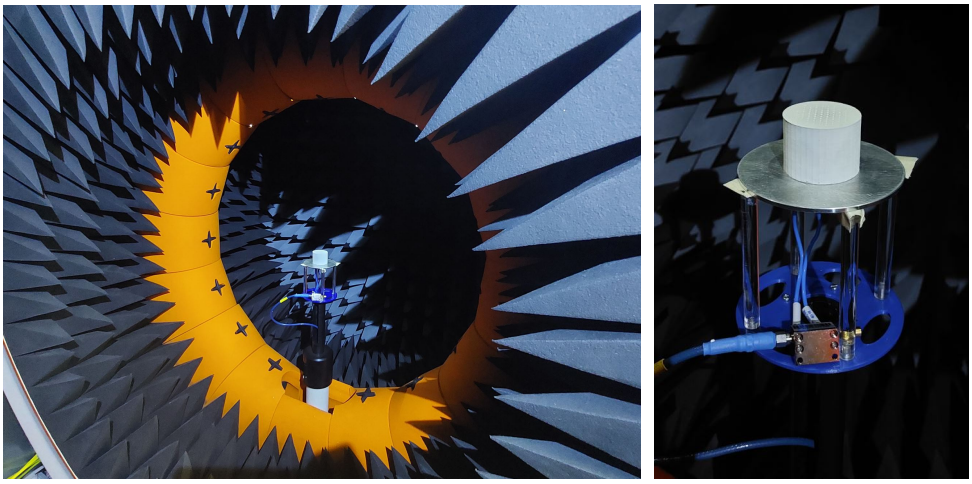

(d) (e)

Figure 7.3: Manufactured DRA antennas with different permittivity profiles (a) homogeneous (DRA-H); (b) linear permittivity profile, increasing in the radial direction (DRA-IHR); (c) linear permittivity profile, increasing along the vertical axis (DRA-IHZ).

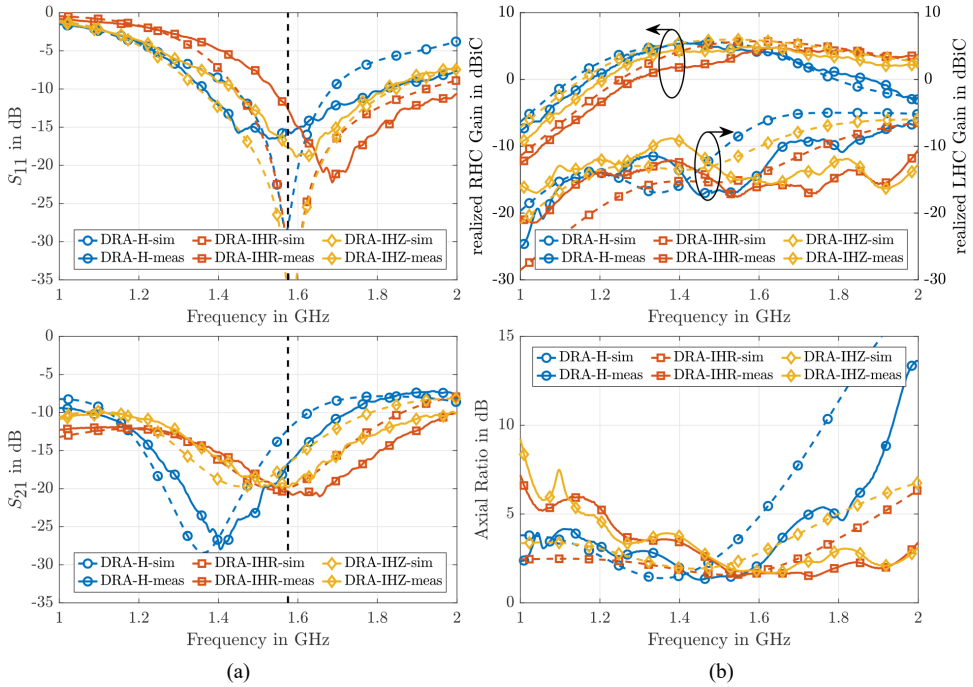

Figure 7.4: (a) Comparison of measured (solid) and simulated (dashed) S-parameters of the homogeneous (blue), radial inhomogeneous (red), and vertical inhomogeneous (yellow) cylindrical dielectric resonator antennas between the two feeding probes. (top) S11; (bottom) S21. (b)Comparison of measured (solid) and simulated (dashed) RHCP realized gain (top), LHCP realized gain (middle), and axial ratio (bottom) of the homogeneous (blue), radial inhomogeneous (red) and vertical inhomogeneous (yellow) cylindrical dielectric resonator.

ment in the operational bandwidth of DRAs with heterogeneous dielectric can be attributed to a decreased coupling between the two coaxial feeds of the DRAs. The physical reason for the mitigated feed-coupling seems to be a decreased dielectric permittivity in the DRAs resonating body between both feeding points. One drawback of the inhomogeneous DRAs is their increased complexity in manufacturing and, for the DRA-IHZ only, the increased volume compared to the homogeneous version. Another potential issue is that this approach is challenging to scale to higher frequencies. The unit-cell size needs to be small compared to the design wavelength for the resulting volume to act as an effective medium but at the same time big enough to be compatible with the employed manufacturing process.

This work accomplishes two goals. For the first time in literature, it describes the design and additive manufacturing of an artificial dielectric volume with a continuous linear variation of its relative permittivity and applies such permittivity profiles to improve the performance of probe-fed dielectric resonator antennas. This is achieved by utilizing a dielectric unit cell with face-centered cubic symmetry that is created via the superposition of spatial harmonics. The individual spatial harmonics are used in the powerful SVL algorithm to synthesize a volume with continuously changing volumetric fill-fraction that is then manufactured with a single high-permittivity material in a fused deposition modeling process.

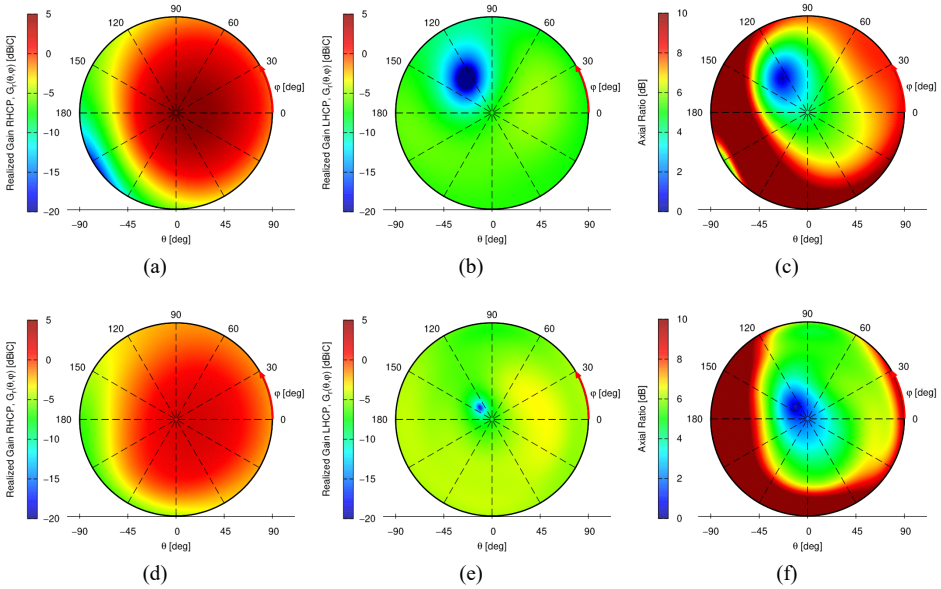

Figure 7.5: RHCP realized gain (a,d), LHCP realized Gain (b,e), and axial ratio (c,f), simulation (top) and measurement (bottom) results of the homogeneous DRA at E1 center frequency (1.575 GHz).

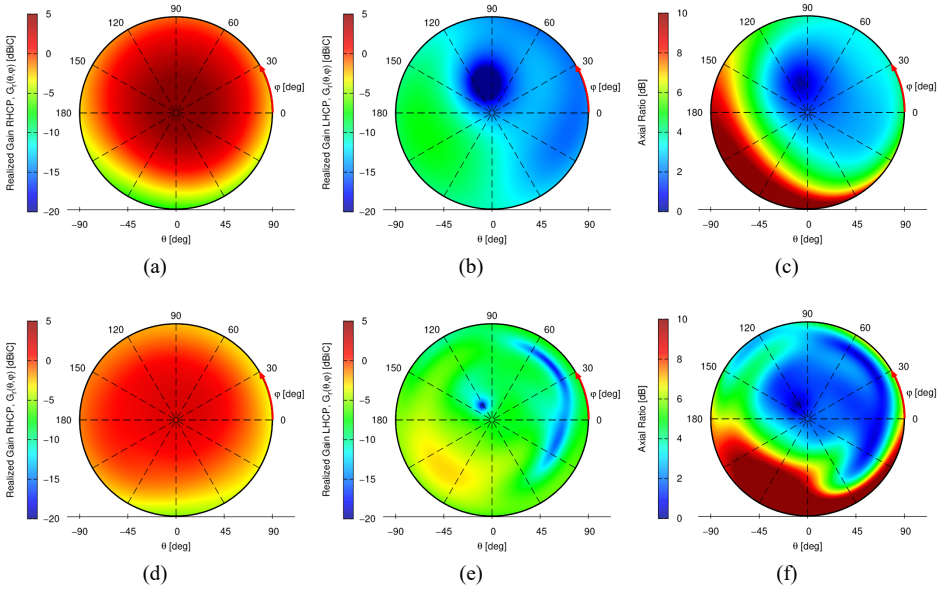

Figure 7.6: RHCP realized gain (a,d), LHCP realized Gain (b,e) and axial ratio (c,f), simulation (top) and measurement (bottom) results of the inhomogeneous DRA with a linear permittivity profile along the radial axis at E1 center frequency (1.575 GHz).

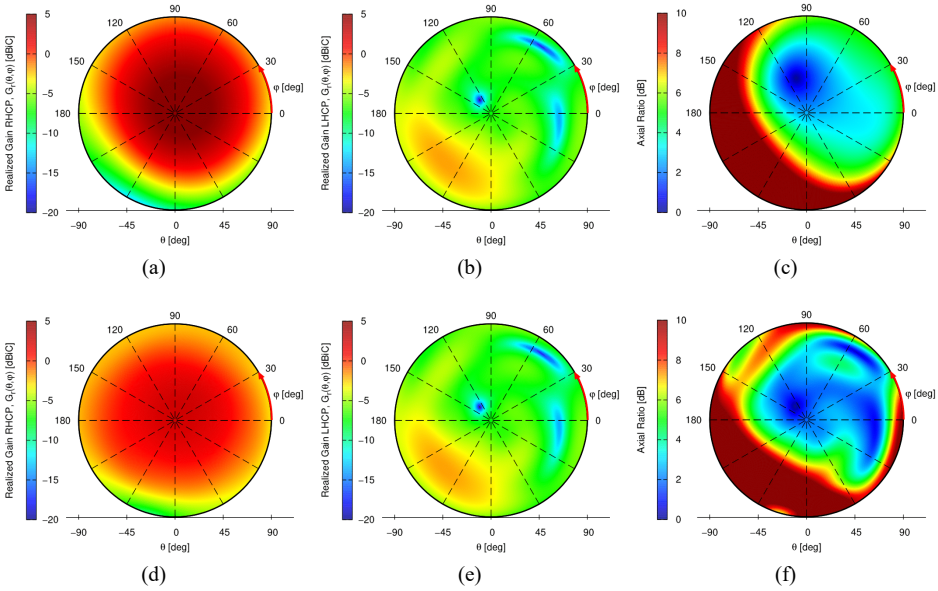

Figure 7.7: RHCP realized gain (a,c), LHCP realized Gain (b,e) and axial ratio (c,f), simulation (top) and measurement (bottom) results of the inhomogeneous DRA with a linear permittivity profile along the vertical axis at E1 center frequency (1.575 GHz).

Two inhomogeneous DRAs with linear varied permittivity profiles along their radial and vertical axis, and one homogeneous DRA for comparison. The choice of the manufactured permittivity profiles in this work was driven by simplicity in their description rather than optimization constraints. Nevertheless, both inhomogeneous DRAs show mitigated coupling between the feed ports leading to improved realized gain and axial ratio values at the design frequency. These benefits are demonstrated with both numerical simulations and measurements, validating the design and simulation approach proposed. The presented approach to continuously linearly sweep the permittivity profile of dielectric volumes is applicable to DRAs. However, the same technique can be applied to design DRAs with inverse linear or even non-linear profiles, which shall be addressed in future research. Furthermore, this approach can be applied in numerous other ways, for example, to engineer flat lenses or to introduce tapers in dielectric waveguides without changing their geometry.

7.2. X-Band Heterogeneous Dielectric Filter

7.2.1. Motivation

Filtering functionality in hollow waveguide structures is usually integrated via corrugating the walls [126] or inserting metal discontinuities into said waveguides [127]. The components are however bulky, heavy and, for high-frequency applications, these methods might introduce significant deviations from the desired performance due to the tolerances in the manufacturing process. Furthermore, the high-power handling of waveguide structures

might be compromised due to metallic discontinuities. A possible solution to overcome these issues in waveguide-based microwave devices is to fill their aperture with a heterogeneous dielectric where the desired functionality is implemented with the specific heterogeneity of the dielectric [128]. Up until now, this possibility has received little attention from researchers due to the challenges of manufacturing heterogeneous dielectrics with precisely defined characteristics. The design of inhomogeneous dielectrics for impedance matching and filters in rectangular waveguides has received some attention [128][129][130]. However, manufacturing the resulting arbitrary dielectric profile, proved to be cumbersome and limited due to the utilization of predefined materials with known relative permittivities. In this section, the capability of extrusion-based additive manufacturing technology to create a heterogeneous dielectric slab rectangular waveguide aperture is considered. The heterogeneity of the slab is engineered to approximate the behavior of a 3rd-order Chebycheff type 1 bandpass filter. The methodology to obtain the heterogeneity of the slab, which implements the filter characteristic, strongly resembles the work published in [130] while the focus of this work is to identify the challenges and provide solutions to arrive at a manufacturable design. To this end, we utilize periodic dielectric structures designed via the superposition of spatial harmonics manufactured with a thermoplastic filament, exhibiting moderate relative permittivity and low loss. We investigate the effect of print settings on the effective permittivity tensor of the material and study the influence of unit cell size and symmetry on the filter performance. Three filter prototypes with different unit cell sizes and symmetries are manufactured and experimentally verified, and measurement results are compared to numerical simulations.
The rest of this article is structured as follows. Section II explains the filter design methodology. Section III. considers the effect of the print settings on the structure's effective permittivity tensor and provides insight into how the unit cell symmetry affects the dispersion of the periodic structure. Furthermore, the design of the periodic dielectric structure via the spatial harmonic superposition method is explained. Section IV explains the numerical simulations carried out in CST, and Section V presents the manufacturing and experimental verification process. Finally, Section VI provides a conclusion to the presented work.

7.2.2. Filter Design

Fundamentals

In order to realize a desired transfer function $H(f)$, we consider a rectangular waveguide loaded with N_{slab} homogeneous dielectric slabs with relative permittivity ε_{n} and equal thickness d as depicted in Figure 7.8.

The transverse electric E_{y} and magnetic H_{x} fields at the interfaces of the individual dielectric sections can be expressed in terms of chain matrices as [130]

$$\begin{aligned}\begin{bmatrix} E_{\mathrm{y}}(z) \\ H_{\mathrm{x}}(z) \end{bmatrix} &= \begin{bmatrix} A_{\mathrm{n}} & B_{\mathrm{n}} \\ C_{\mathrm{n}} & D_{\mathrm{n}} \end{bmatrix} \begin{bmatrix} E_{\mathrm{y}}(z+d_{\mathrm{n}}) \\ H_{\mathrm{x}}(z+d) \end{bmatrix} \\ &= [ABCD]_{\mathrm{n}} \begin{bmatrix} E_{\mathrm{y}}(z+d) \\ H_{\mathrm{x}}(z+d) \end{bmatrix}\end{aligned} \tag{7.4}$$

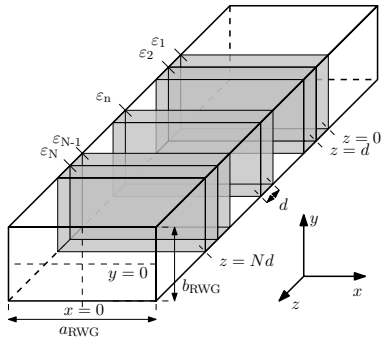

Figure 7.8: Schematic of a heterogeneous dielectric slab with N_{slab} sections of equal thickness d and locally homogeneous permittivity ε_n, $n = 1, \dots, N$ in a rectangular waveguide with lateral dimensions a_{RWG} and b_{RWG}.

$\varepsilon_{r,1}$	3.50	$\varepsilon_{r,2}$	5.99	$\varepsilon_{r,3}$	2.50
$\varepsilon_{r,4}$	5.99	$\varepsilon_{r,5}$	2.99	$\varepsilon_{r,6}$	3.73
$\varepsilon_{r,7}$	5.99	$\varepsilon_{r,8}$	2.50	$\varepsilon_{r,9}$	5.99
$\varepsilon_{r,10}$	2.50	$\varepsilon_{r,11}$	3.89	$\varepsilon_{r,12}$	5.99
$\varepsilon_{r,13}$	2.50	$\varepsilon_{r,14}$	5.99	$\varepsilon_{r,15}$	2.50
$\varepsilon_{r,16}$	3.67	$\varepsilon_{r,17}$	5.71	$\varepsilon_{r,18}$	2.50
$\varepsilon_{r,19}$	5.99	$\varepsilon_{r,20}$	2.91	d	3.96 mm

Table 7.3: Values of the optimized section permittivities $\varepsilon_{r,i}$, $i = 1 \cdots N_{\text{slab}}$ and thickness d

with

$$\begin{aligned} A_n = D_n &= \cos\left(\beta_{z,n} d\right) \\ B_n = \eta_{z,n}^2 C_n &= \sin\left(\beta_{z,n} d\right) \end{aligned} \tag{7.5}$$

and

$$\beta_{z,n} = \frac{2\pi f}{c_0} \sqrt{\varepsilon_{r,n} - \left(f_{c,\text{RWG}}/f\right)^2}, \tag{7.6}$$

$$\eta_{z,n} = -\frac{\eta_0}{\sqrt{\varepsilon_{r,n} - \left(f_{c,\text{RWG}}/f\right)^2}} \tag{7.7}$$

where $f_{c,\text{RWG}} = \frac{c_0}{2a_{\text{RWG}}}$ denotes the cutoff frequency of the waveguides fundamental TE_{10} mode, $\eta_0 = \sqrt{\mu_0/\varepsilon_0}$ is the wave impedance, and c_0 the speed of light in free space. Due to the definition of the chain matrix, the $ABCD$ parameters of the full heterogeneous slab can be obtained via

$$[ABCD]_{\text{slab}} = \prod_{n=1}^{N} [ABCD]_n \tag{7.8}$$

and conveniently transformed into its scattering parameters via

$$\begin{aligned} S_{11} &= \frac{A_{\text{slab}} Z_{\text{TE}} + B_{\text{slab}} - C_{\text{slab}} Z_{\text{TE}}^2 - D_{\text{slab}} Z_{\text{TE}}}{A_{\text{slab}} Z_{\text{TE}} + B_{\text{slab}} + C_{\text{slab}} Z_{\text{TE}}^2 + D_{\text{slab}} Z_{\text{TE}}} \\ S_{21} = S_{12} &= \frac{2Z_{\text{TE}}}{A_{\text{slab}} Z_{\text{TE}} + B_{\text{slab}} + C_{\text{slab}} Z_{\text{TE}}^2 + D_{\text{slab}} Z_{\text{TE}}} \\ S_{22} &= \frac{-A_{\text{slab}} Z_{\text{TE}} + B_{\text{slab}} - C_{\text{slab}} Z_{\text{TE}}^2 + D_{\text{slab}} Z_{\text{TE}}}{A_{\text{slab}} Z_{\text{TE}} + B_{\text{slab}} + C_{\text{slab}} Z_{\text{TE}}^2 + D_{\text{slab}} Z_{\text{TE}}} \end{aligned} \tag{7.9}$$

with

$$Z_{\mathrm{TE}} = -\frac{\eta_0}{\sqrt{1-(f_\mathrm{c}/f)^2}} \tag{7.10}$$

denoting the characteristic impedance of the in- and output of the filter. The desired filter transfer function $H(f)$ is now realized by optimizing the permittivity values $\varepsilon_{\mathrm{r,n}}$ of the individual homogeneous dielectric slabs and their thickness d. The optimization is carried out for a set of M discrete frequencies $f_\mathrm{m} > f_\mathrm{c}$ while minimizing the error function

$$\mathrm{err} = \left[\frac{1}{M}\sum_{m=1}^{M}\left|\frac{|S_{21}(f_\mathrm{m})| - |H(f_\mathrm{m})|}{|H(f_\mathrm{m})|}\right|^2 + \frac{1}{M}\sum_{m=1}^{M}\left|\frac{|S_{11}(f_\mathrm{m})| - \sqrt{1-|H(f_\mathrm{m})|^2}}{\sqrt{1-|H(f_\mathrm{m})|^2}}\right|^2\right]^{1/2} \tag{7.11}$$

Implementation

The procedure discussed above is demonstrated with a heterogeneous slab of $N = 20$ homogeneous sections in a WR90 standard rectangular waveguide optimized to approximate the characteristics of a third-order Chebyshev type 1 bandpass filter. The filter shall obtain a bandwidth of $B = 1$ GHz, centered around 10 GHz and exhibit a permissible passband ripple of 0.01 dB. The manufacturing circumstances drive the choice for the lower and upper bounds of the optimization variables, with two limitations that need to be considered in the design. First, the additive manufacturing setup's accuracy in this work limits the minimum unit cell size to about 1.5mm. The necessary thickness of at least one unit cell per filter section establishes a lower bound for the individual slab thickness d. Second, for manufacturing the material ABS650 with a nominal relative permittivity of $\varepsilon_{\mathrm{r,ABS650}} = 6.5$ is selected. The choice of material limits the range of values for the permittivity of the individual sections to $\varepsilon_{\mathrm{r,n}} \in [2.5\ 6]$. This limitation is further explained in Section III. The optimization task constitutes a non-linear, constrained multi-variable problem which is addressed with the help of the Matlab optimization algorithm *fmincon*[2]. The optimization for the specific design example in this work considers $M = 300$ frequency points within the recommended frequency range of the WR90 waveguide fundamental mode 8.2−12.4 GHz. Initial values for the individual slab permittivities are based on random variables with a uniform distribution constrained to the permittivity limits discussed above. The optimization results are depicted in Figures 7.9a and 7.9b, respectively. Furthermore, the final values of the individual optimization variables are reported in Table 7.3. The optimization routine is run on a Dell Latitude 9410 office notebook with an Intel Core i7 10610U processor with 1.8GHz and 16 GB memory. The desired transfer function and number of optimization variables $N + 1$ is chosen such that the routine converges in reasonable time, which for this specific design is ≈ 30 minutes. It is observed that a higher number of homogeneous dielectric sections N in the filter provides better convergence and is able to approximate filter

[2] A more appropriate choice for the optimization algorithm might exist for this type of problem, but the in-depth analysis of the cost function is out of scope for this work.

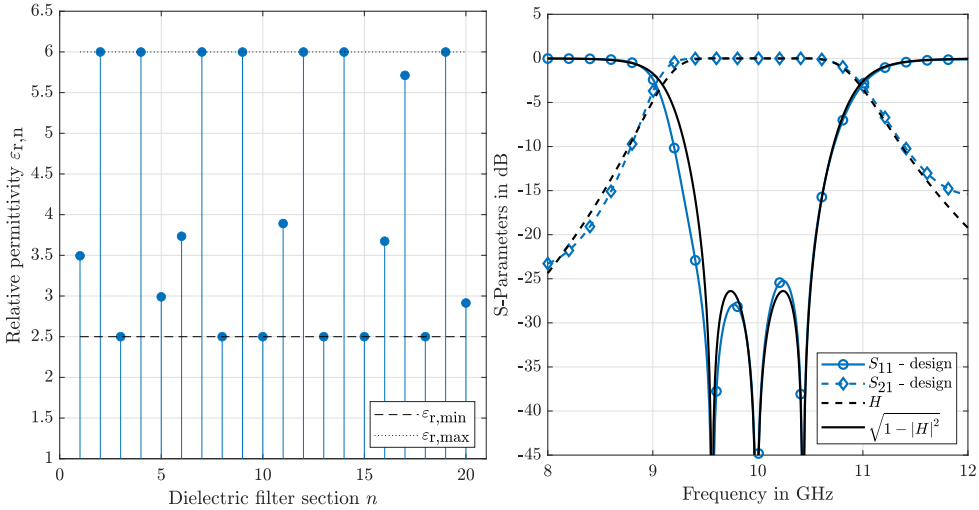

Figure 7.9: (a) Permittivity distribution of a heterogeneous dielectric slab with $N = 20$ individual homogeneous sections approximating a 3rd order Chebycheff type 1 bandpass filter. (b) Comparison between the target transfer function $H(f)$ corresponding to a 3rd order Chebycheff type 1 bandpass filter with 0.01dB ripple in the passband and results of the optimization routine targeting the goal function with a heterogeneous dielectric slab in a WR90 rectangular waveguide.

transfer functions with higher orders. However, as the focus of this work is the feasibility of manufacturing such structures, an in-depth analysis of the achievable filter performance as function of the number of optimization variables is out of scope.

7

7.2.3. Dielectric Crystal Design

In this work we utilize the thermoplastic material ABS650 from Avient, which exhibits a moderate nominal permittivity of $\varepsilon_{r,p} = 6.5$ and a low loss tangent of $\tan\delta_{ABS650} = 0.0034$[3]. The effective permittivity tensor of a solid part printed from the ABS650 material with an extrusion width of 0.2mm and a layer height of 0.12mm (as later utilized during the manufacturing) is characterized utilizing the same waveguide measurement setup as described in Section 5.3.1 and measured to be

$$[\varepsilon_{r,m}] = \begin{bmatrix} \varepsilon_{r,xx} & 0 & 0 \\ 0 & \varepsilon_{r,yy} & 0 \\ 0 & 0 & \varepsilon_{r,zz} \end{bmatrix} = \begin{bmatrix} 6.03 & 0 & 0 \\ 0 & 6.01 & 0 \\ 0 & 0 & 5.03 \end{bmatrix}. \tag{7.12}$$

In the following, the effectively uniaxial anisotropic material described by the permittivity tensor in equation (7.12) is considered to be the host material from which the heterogeneous slab, realizing the desired filter characteristic, will be manufactured. The dielectric crystal utilized for the filter is designed via the spatial harmonic superposition approach as described in Section 3.2.2 and its effective dielectric properties of the unit cells are extracted via Floquet port scattering simulations discussed in Section 4.2.4. The effective permittivity

[3]Material datasheet available from Avient upon request.

tensor components in non-dispersive frequency regimes are presented as a function of volumetric infill in Figure 7.10a. The effective permittivity tensor components are computed up to the maximum threshold value $\tilde{th}_{\max} = 0.625$ for which the lattices are still connected[4]. Although a lattice with such a threshold value is theoretically possible, it would be quite fragile. Therefore, a maximum threshold value of $th_{\max} = 0.6$ is used, which provides effective permittivity ranges of $\varepsilon_{\underline{xx}} = \varepsilon_{\underline{yy}} \in [2.5\ 6]$ and $\varepsilon_{\underline{zz}} \in [2.25\ 5]$. As explained above, a permittivity range of $[2.5\ 6]$ is considered during the design of the filter. This needs to be considered later during the manufacturing of the filter, which is further explained in Section 7.2.4.

Dispersion in the lattice

As reported in Table 7.3, the individual sections of the filter slab are $d = 3.96\ \mathrm{mm}$ wide and ought to be realized with an integer multiple of unit cells. As mentioned above, with the manufacturing setup employed in this work, a minimal unit cell size of $\approx 1.5\mathrm{mm}$ is feasible. Therefore, the filter can be realized with either one or two unit cells per individual section corresponding to possible lattice constants of $a = d$ and $a = d/2$ for the unit cells of the periodic structure. The frequency dispersion of the effective permittivity tensor components for a number of different volumetric infill fractions is depicted in Figure 7.10b. One can observe that the effective permittivity tensor components of the SC unit cell with a lattice constant $a = d$ already exhibit significant dispersion within the fundamental mode bandwidth of the WR90 waveguide while the dispersion for lattice constant $a = d/2$ is negligible.

Compiling the lattice

Periodic structures with SC symmetries and lattice constants $a = d$ and $a = d/2$ are also considered in the following discussion. The three filter geometries are designed via a Matlab script that computes the spatial harmonics of the selected unit cells over the whole filter volume and applies a spatially modulated threshold value corresponding to the locally desired effective permittivity. The resulting geometries are then exported into the commonly utilized *stl* file format to be used for both numerical simulations and manufacturing. This process is visualized in the following for the SC unit cell with $a = d$;

To engineer the periodic structure based on unit cells with SC symmetry and a lattice constant a, we superimpose spatial harmonics along the reciprocal lattice vectors $\mathbf{T}_\mathrm{i}$ throughout the volume of the filters, as introduced in Section 3.2.2. The harmonic superposition Ψ is computed in the volume $V = a_{\mathrm{RWG}} b_{\mathrm{RWG}} N d$ as

$$\Psi = \sum_{i=1}^{3} e^{j\mathbf{T}_\mathrm{i}\cdot\mathbf{r}}, \quad r \in V \tag{7.13}$$

and its real part normalized to values between 0 and 1

$$\tilde{\Psi} = \frac{Re\{\Psi\} - \min(Re\{\Psi\})}{\max(Re\{\Psi\}) - \min(Re\{\Psi\})}. \tag{7.14}$$

[4] A connected lattice is necessary to be manufactured from a single material.

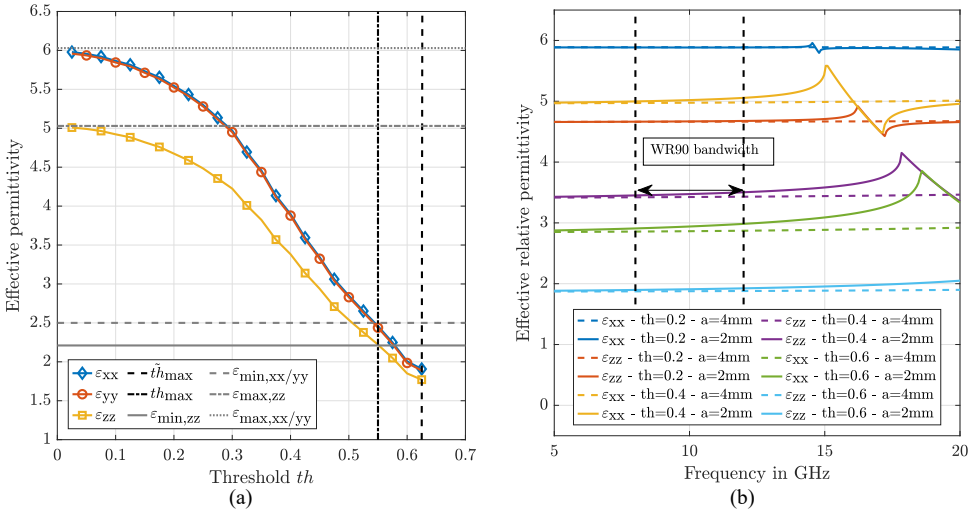

Figure 7.10: (a) Effective permittivity tensor components of the SC unit cells as a function of the threshold value with indication on the realizable values $\varepsilon_{\min}$ and $\varepsilon_{\max}$ and (b) the dispersion of the effective permittivity tensor components as a function of frequency with an indication of WR90 fundamental mode bandwidth.

Finally the heterogeneous dielectric slab S is created by thresholding $\tilde{A}$ with a spatially modulated threshold value $th\,(\mathbf{r})$ realizing the desired effective permittivity values according to the analysis carried above with the data presented in Figure 7.10a

$$S := \tilde{\Psi} \geq th\,(\mathbf{r})\,. \tag{7.15}$$

7

7.2.4. Results

Manufacturing of the three prototypes is carried with the E3D Toolchanger, as described in Section 3.3.1, with the ABS650 material as listed in Table 3.2. An extrusion width of 0.2mm, a layer height of 0.12mm, and a print speed of $15\text{mm}\,\text{s}^{-1}$ is chosen, and during the print, the models are oriented such that the y-axis of the slabs, as depicted in Figure 7.8, corresponds to the layer stack direction $\hat{z}$ of the printer. This orientation ensures that the electric field components of the fundamental TE_{10} mode in the WR90 waveguide are along the desired effective permittivity tensor component. Furthermore, the individual heterogeneous dielectric slabs are printed with slightly increased lateral dimensions, which serves two purposes. First, this accounts for the slight shrinkage of the printed model during the cool down after the print completion. Second, it allows for the milling of the surfaces of the dielectric slabs that face the waveguide walls via a CNC mill, providing a clean surface and enabling a precise fit into the waveguide aperture. The two manufactured prototypes are depicted in Figure 7.12. The individual samples are carefully inserted into a WR90 rectangular waveguide. The measured scattering parameter results for the $a = d$ and $a = d/2$ slabs are depicted in Figure 7.13 and compared to the design as well as their respective simulation result. The realization of the $a = d$ filter exhibits an excellent agreement with the results obtained from the CST simulation with only a slight shift ($\approx$ 100MHz) of the center

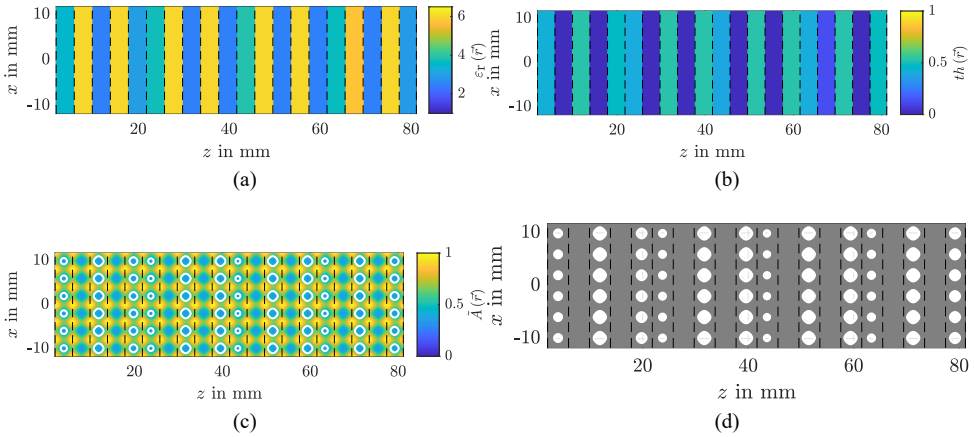

Figure 7.11: Visualization of the lattice compilation process for a plane ($y = 0$) through the volume of the dielectric slab. The (a) desired permittivity distribution $\varepsilon_r(\mathbf{r})$, and its (b) threshold value $th(\mathbf{r})$ realizing the desired permittivity distribution when applied to (c) the normalized spatial harmonic superposition $\tilde{A}(\mathbf{r})$ with the boundary established by the threshold value indicated in white and (d) the binary lattice S with print material in gray and free space in white.

frequency to larger values. A similarly good agreement is obtained for the $a = d/2$ realization, where a more significant shift of the center frequency ($\approx 350\text{MHz}$) to higher values is noticeable. Ironically, this more significant deviation from simulated results shifts the measured filter characteristic closer to the desired one. The more considerable discrepancy between simulated and measured results for the $a = d/2$ filter realization compared to the $a = d$ realization can be attributed to the increased effect of tolerances for the smaller unit cell. The measured insertion loss of the filters is $\approx 0.68\text{dB}$ and $\approx 0.71\text{dB}$ for the $a = d/2$ and $a = d$ realizations respectively which is slightly higher than predicted in simulations. However, this can be explained by the finite conductivity of the waveguide walls in the measurement setup which were assumed perfectly electrically conducting in the simulation setup.

7.2.5. Discussion and Conclusion

In this work, the design of a realizable heterogeneous dielectric slab fitted into a WR90 rectangular waveguide to approximate the transfer function of a 3rd-order Chebycheff type 1 bandpass filter with a permissible passband ripple of 0.01dB is demonstrated. To this end, we employ extrusion-based additive manufacturing to create a periodic dielectric structure with a spatially modulated infill fraction from a single material. The filter design is carried out assuming a dielectric slab with $N_{\text{slab}} = 20$ homogeneous sections with a thickness of d along the propagation axis of the waveguide. The permittivity distribution approximating the desired filter characteristic is found via a multi-variable optimization concerning the relative permittivities of the individual homogeneous sections and their respective thickness. Special attention is given to the engineering of the spatially modulated lattice and the particularities associated with extrusion-based additive manufacturing. The effect of the

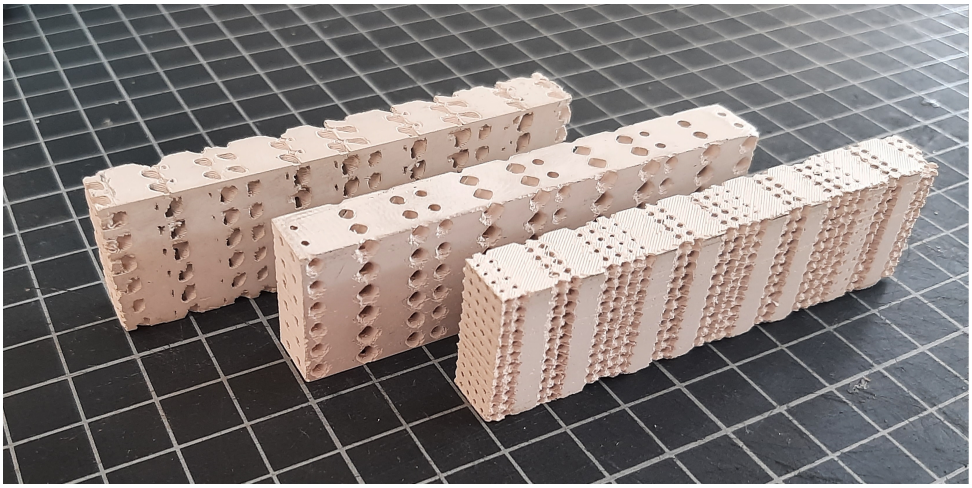

.

Figure 7.12: Manufactured waveguide filter prototypes based on heterogeneous dielectric slabs (front) SC $a = d$, (middle) SC $a = d/2$, and (back) FCC $a = d$.

print settings and the volumetric infill of the lattice onto the effective permittivity tensor is studied. Furthermore, the dispersion of different unit cell symmetries is considered. Additionally, the individual steps in compiling the lattice are presented. Three realizations of the same heterogeneous dielectric slab are selected, investigated via numerical simulations, manufactured, and experimentally verified. Good agreement for the realizations based on simple cubic symmetry is observed. It is demonstrated that the manufactured filter is compact, light and possesses low losses. At the same time, unexpected results are obtained for the realization based on face-centered cubic symmetry.

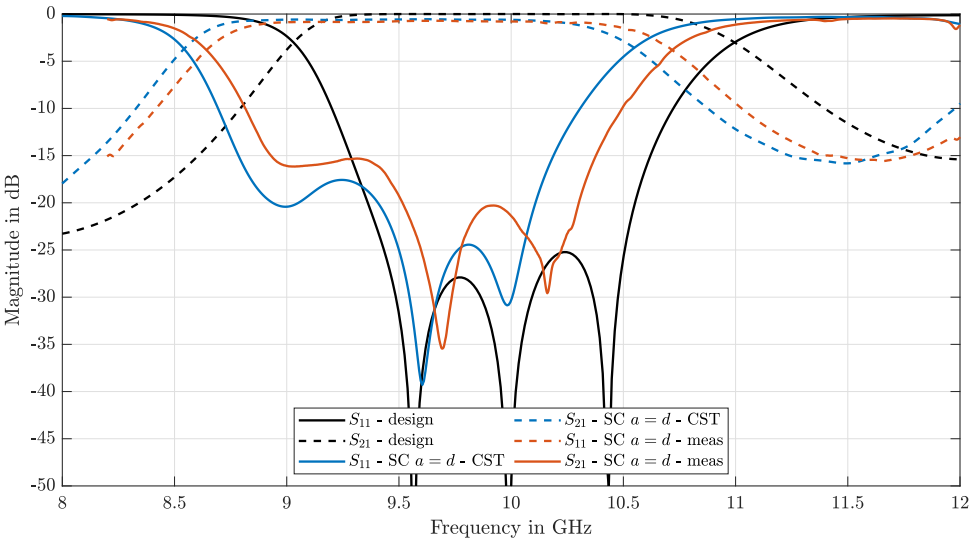

(a)

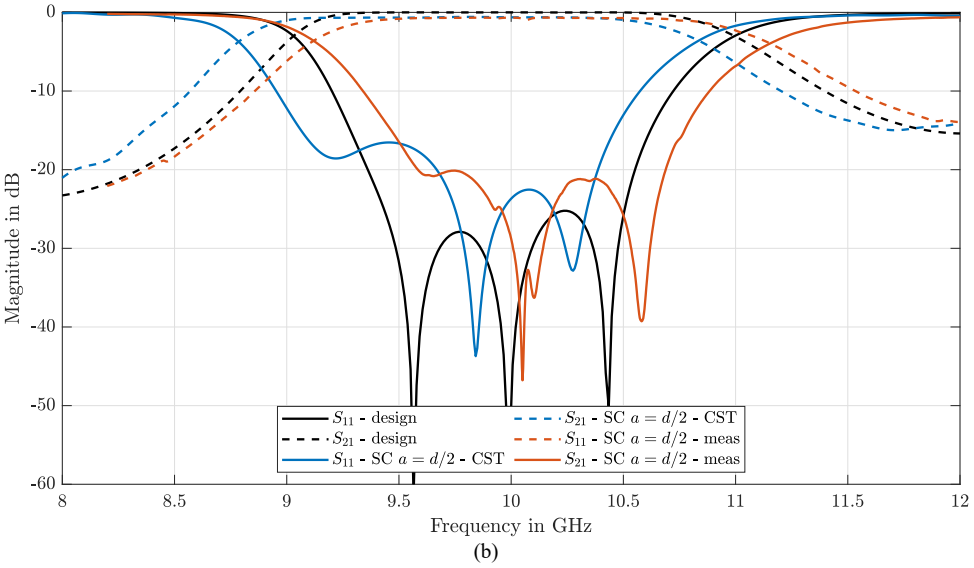

(b)

Figure 7.13: Comparison between the designed, simulated and measured scattering parameters for the three realized heterogeneous dielectric slabs (a) SC $a = d$, (b) SC $a = d/2$.

8

Short-Wavelength Dielectric Crystals

Abstract The properties of short-wavelength dielectric crystals in the context of 3D bandgap materials are studied. Two known periodic dielectric structures exhibiting 3D bandgaps, the woodpile and diamond lattice, are selected for investigation and their properties investigated via Eigenmode techniques. A woodpile slab is designed to exhibit a bandgap at 30 GHz and the existence of the bandgap verified in a free space measurement setup. The concept of a combining the functionality of a long- and short-wavelength dielectric crystal is demonstrated via the design, manufacturing and experimental verification of a dielectric rod antenna with integrated 3rd harmonic suppression capability.

8.1. Motivation and Structure

Photonic crystals are attractive optical materials for controlling and manipulating the flow of light. 1D, as well as 2D photonic crystals, are already widely used in the form of thin-film optics with applications ranging from low and high reflection coatings on lenses and mirrors to bandgap waveguides in optical integrated circuits. Up to now, the concept of photonic band gaps (PBG) in dielectric crystals has not been applied to problems in communication or radar engineering where PBG devices obtain physically large dimensions. Additionally, PBG materials are difficult to manufacture with traditional subtractive methods due to the complex 3D lattices. As already demonstrated in the context of this thesis AM is especially well suited to create complex periodic structures. Several research works have already discussed the utilization of AM to create band gap structures in the mmWave regime. However, previous works on this topic utilized materials that rely on high-temperature burnout and sinter processes to create the final structure after the additive manufacturing step, which adds complexity and cost. This chapter explores the possibility of utilizing low-cost FDM additive manufacturing with high-permittivity filaments to create complete 3D electromagnetic bandgap structures requiring no post-processing. In Section 2, dielectric bandgap structures are explained, and the woodpile and diamond lattices are chosen for further investigation. In Section 3, a simulation study is carried out to find bandgap frequencies and fractional bandwidths as a function of the lattices index contrast, and suitable materials for manufacturing are identified. Furthermore, the additive manufacturing and subsequent experimental verification of a woodpile bandgap material are presented in Section 4, and a conclusion is given in Section 5.

8.2. Dielectric Bandgap Structures

Dielectric crystals, as introduced in Section 3.2 can exhibit an omni-directional photonic bandgap, meaning that there is a band of frequencies for which electromagnetic waves obtain an imaginary propagation constant. As explained in 4.2.3 frequencies of propagating modes in the crystal can be found through solving the equation 3.18. Although the number of crystal geometries exhibiting a PBG is relatively tiny, a PBG can be identified in all Bravais lattices [131]. This preliminary investigation considers two PBG lattices, namely the Woodpile and Diamond lattice, which are compatible with low-cost additive manufacturing. The Woodpile structure, a simple-cubic geometry with stacked dielectric bars, as depicted in 8.1a, is a popular choice of a PBG material due to its apparent simple layout, making it possible to be manufactured with conventional subtractive methods. The Diamond lattice, consists of two interlaced face-centered-cubic lattices with spherical inclusions as depicted in Figure 8.1c. In contrast to the Woodpile lattice, the Diamond lattice is rarely discussed in literature due to the difficulty in manufacturing it with conventional subtractive methods. Both lattices are created with a single material with refractive index $n_{\mathrm{m}} = \sqrt{\varepsilon_{\mathrm{r,m}}}$, with $\varepsilon_{\mathrm{r,m}}$ denoting the relative permittivity of the manufacturing material, against the background material (free space) $n_{\mathrm{b}} = \sqrt{\varepsilon_{\mathrm{b}}} = 1$. The existence, position and width of a PBG in the Woodpile and Diamond lattice depends on the size of the unit cell a and index contrast between the manufacturing and background material $\Delta n = n_{\mathrm{m}} - n_{\mathrm{b}}$.

8.2.1. Numerical Investigation

Two different simulation techniques are employed in this work to analyze PBG material properties. First, a plane wave expansion method (PWEM) is used to identify the existence, position, and bandwidth of PBG in the Woodpile and Diamond lattice for different index contrasts Δn. Secondly, the commercial software package HFSS from Ansys is employed to compute the reflection and transmission spectra of a one unit-cell thick slab of woodpile and diamond PBG material.

Band diagram

The PWEM solves the eigenvalue problem posed by equation (3.18), and is used to find the frequencies of propagating modes in the infinite 3D lattice. For a given unit cell $\varepsilon(\mathbf{r})$ and Bloch vector β, the PWEM computes the eigenmodes and corresponding eigenfrequencies ω. Doing this for a set of Bloch vectors, on the boundary of the irreducible Brillouin zone of the unit-cell, and plotting the eigenfrequencies over the Bloch vectors gives the band-diagram of the cell. The band-diagrams of the Woodpile and Diamond unit-cells are shown in 8.1, for refractive indices $n_{\mathrm{m}} = 3$ and $n_{\mathrm{b}} = 1$, respectively. In order to identify suitable materials for creating PBGs with additive manufactured Woodpile and Diamond lattices, the band-diagram for both geometries, are computed using a custom 3D PWEM code. The band-diagrams are computed for index contrasts between 2 and 6 with a resolution 0.25. The lower ω_{L} and upper ω_{U} bandgap frequencies are extracted for each considered index contrast and plotted together with the obtained fractional bandwidth B for Woodpile and Diamond lattice in Figures 8.1g and 8.1h respectively. It can be observed that for the Woodpile lattice a PBG appears at lower frequencies and for slightly higher refractive index contrasts compared to the Diamond lattice. However, the fractional bandwidth of the Woodpile bandgap exceeds the one of the Diamond bandgap for high index contrasts, while the opposite is true for lower index contrasts. Furthermore, it can be seen that either geometry to exhibit a PBG requires a minimum refractive index of 2.5 corresponding to a minimum relative permittivity of 6.26.

In literature, several high permittivity filaments have been reported, as reviewed in Section 2.3. They are usually created by adding high-permittivity ceramic powders to stock plastics and processing them into filament form. However, at the inception of this work on Avient (former PREPERM) materials are easily commercially available and the material ABS1500 with nominal relative permittivity of 15 has been chosen for manufacturing.

Full Wave Simulation

Although results from the 3D PWEM provide valuable insight into the behavior of the lattice, the assumption of an infinite structure is not compatible with physical experiments. The easiest experimental way of verifying the existence of a bandgap is to perform reflection and transmission measurements as a function of frequency. However, simulation methods to compute the transmission and reflection from large finite lattices are computationally expensive. To overcome this, the transmission and reflection of a large finite PBG slab can be approximated by the simulation of a plane-wave incident on a single unit-cell with periodic boundary conditions. The simulated scattering parameters of the 2D infinite Woodpile and Diamond lattice are compared to finite PBG slab measurements in the section below.

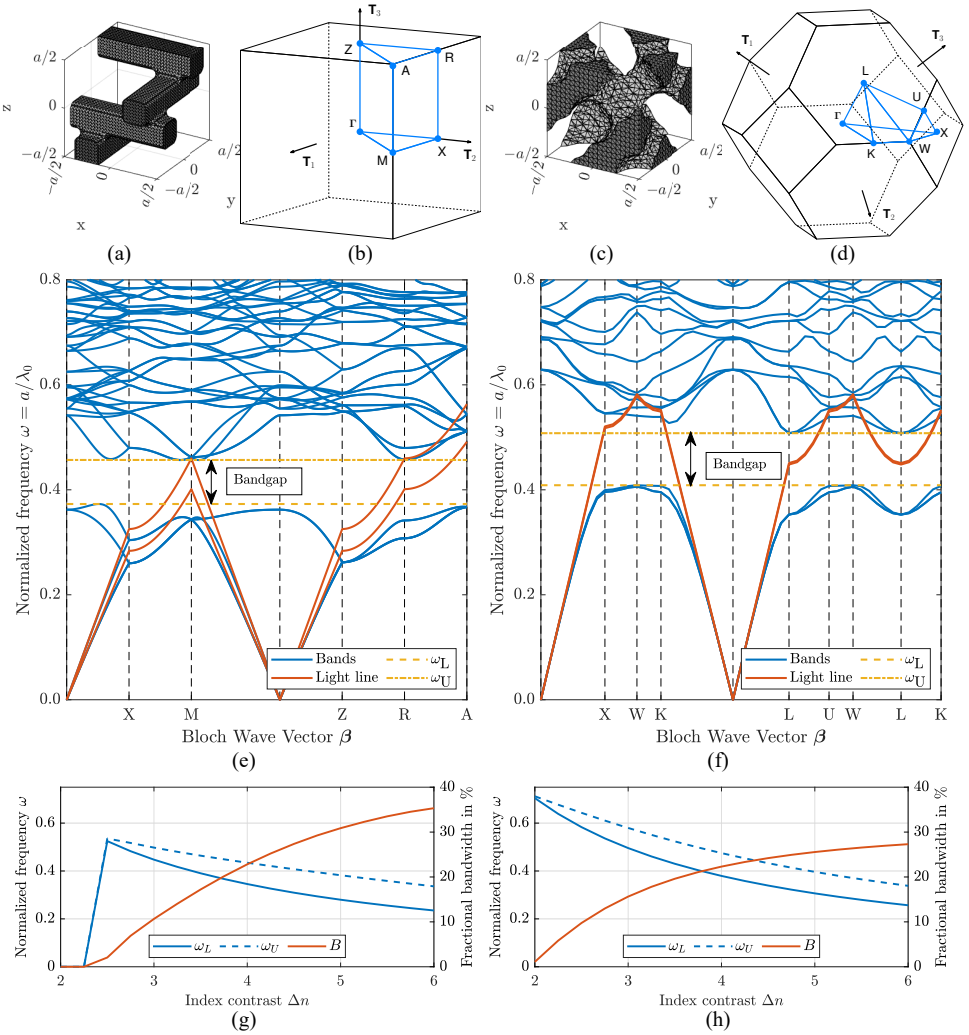

Figure 8.1: Unit cells of the (a) Woodpile and (b) Diamond lattice with lattice constant a. Dark areas are touching the boundary of the cell. Band-diagram computed from a 3D plane wave expansion method for the (a) Woodpile and (b) Diamond unit cell with a material refractive index contrast of $\Delta n = 3$ against free space. Simulation of upper ($\omega_{\mathrm{n,U}}$) and lower ($\omega_{\mathrm{n,U}}$) bandgap frequencies as well as the fractional bandwidth B as a function of the index contrast Δn for the (a) Woodpile, and (b) Diamond lattice.

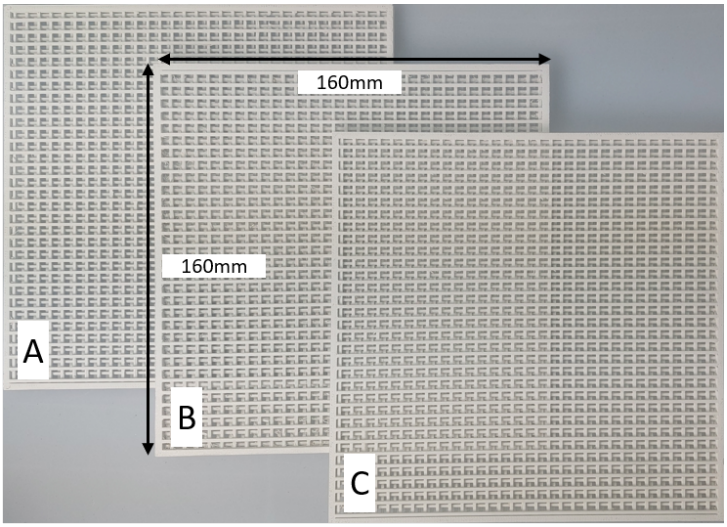

Figure 8.2: Three additive manufactured Woodpile lattices with a unit cell size of $a = 5$ mm and slab dimension of 160×160 mm^2.

8.2.2. Manufacturing and Measurement

Lattices were manufactured with a unit-cell size of $a = 5\text{mm}$ as $160 \times 160\text{mm}^2$ slabs with a height of one unit-cell. Due to reasons explained below, the manufacturing of the Diamond lattice failed. Therefore, experimental results are only discussed for the Woodpile lattice, for which three individual slabs are manufactured, distinguished in the following with labels A, B and C, as depicted in Figure 8.2. The measurements are carried out with a free-space measurement setup at the German Aerospace Centers Institute for Microwaves and Radar.

Individual transmission and reflection measurements in a free-space measurement setup have been performed with the three manufactured Woodpile PBG slabs. The experimental setup, as explained in section 4.3.3, consists of two horn antennas with wideband focusing lenses on opposite sides of a probe iris, surrounded by absorbing materials. The sample is fixed within the probe iris and is illuminated by focused beams of EM radiation. The reflection and transmission parameters are recorded by a vector network analyzer and stored for post-processing. Measurements in the Ku-, K- and Ka-band with three different feed horns are carried out to cover a wide frequency range from 12 to 40 GHz. The measurement results for the individual Woodpile PBG slabs are compared to simulated transmission and reflection scattering parameters from 2D infinite slabs in Figure 8.3 and the following observations can be made:

- Consecutive measurements in different frequency bands, obtained with different feed horns, agree well and only minor discontinuities are noticeable.
- A small shift of the center frequency (global minima of the transmission spectrum) between the individual samples can be identified, with samples A and C showing the best agreement, which is expected .

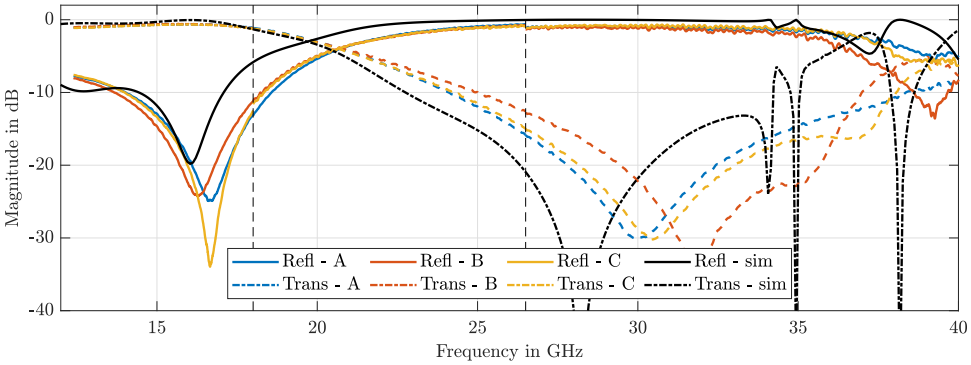

Figure 8.3: Reflection (solid lines - R) and transmission (dashed lines – T) spectra of the manufactured Woodpile lattices in the Ku, K and Ka band. Measured results for samples A, B and C in red, blue and green compared to simulation results in black.

- The reflection in the bandgap is a up to 1.5 dB lower than predicted. This can be attributed to the fact that not all reflected energy is captured by the feed horn. A further explanation might be that the sample slightly bends due to tension in the probe iris which would cause oblique reflection.

- The predicted center frequency differs from the measured one by about 2GHz. This is most likely due to a further reduction of the effective permittivity in the Woodpile lattice due to the "sagging" of the filament during the bridging of gaps in the print process. Figure 7 shows a detailed top and bottom view of the Woodpile PBG sample C. It can be seen that from the top side the structure looks very smooth and individual print lines cannot be recognized. However, from the bottom point of view we can see the effect of the bridging. This introduces air gaps between the individual extruded lines, which reduces the effective permittivity of the material and results in a rise of the bandgap frequencies.

- For high frequencies we observe small dips in the simulated reflection and transmission spectra which are not reproduced by measurements. The reason for this is currently under investigation, but one possible explanation is that these are due to higher order modes that start propagating in the infinite 2D lattice and are not present in the manufactured slabs.

8.3. Dielectric Rod Antenna with Bandgap for Harmonic Suppression

8.3.1. Dielectric Rod Antenna

Dielectric-rod antennas, also known as Polyrod antennas, are regarded as a type of surface-wave antenna. Their size and weight are very suitable for the millimeter-wave range, and their compatibility with dielectric waveguides opens a wide range of applications [132]. While a wide range of configurations of feeds and rod geometries are possible for the dielectric rod antenna, this work utilizes a simple rectangular-shaped rod with relative per-

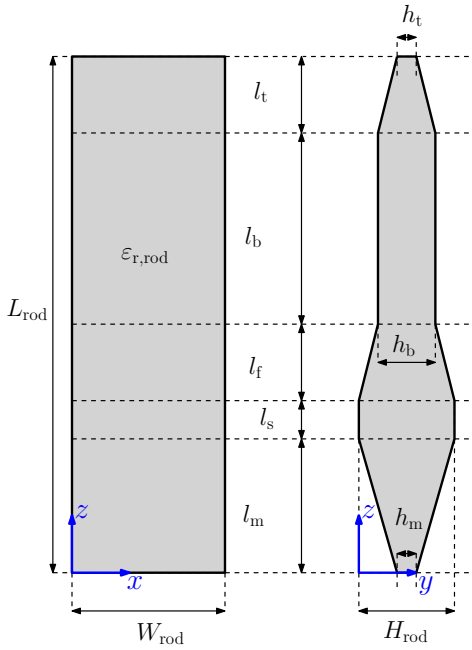

Figure 8.4: Schematic drawing indicating the geometric parameters of the proposed dielectric rod antenna.

L_{rod}	191,84 mm
l_s	10mm
$b_{RWG} = H_{rod}$	22,15 mm
$a_{RWG} = W_{rod}$	47,55 mm
l_f	36,54 mm
h_b	10,53 mm
h_m	2,54mm
l_b	55,30mm
h_t	5 mm
l_m	60 mm
l_t	30mm
$\varepsilon_{r,rod}$	2.66

Table 8.1: Geometric parameters of the proposed dielectric rod antenna.

mittivity $\varepsilon_{r,rod}$ and linear tapered sections, as shown in Figure 8.4. Impedance matching to the feed waveguide is improved via a tapered matching section leading up to the aperture of the feed waveguide. The taper gradually transforms the propagating mode in the waveguide to a surface wave in the dielectric. The feed taper increases the excitation efficiency and influences the feed pattern, while the termination taper reduces the reflected surface wave to negligible values. The efficiency of surface wave excitation is usually between 65 and 75 percent [133], and the feed aperture radiates power not coupled into the surface wave. The rod is designed with a relative permittivity of $\varepsilon_{r,rod} = 2.7$ to exhibit a gain of about 12 dBi at the design frequency $f_{d,rod} = 5$ GHz while minimizing the rod length and being fed via a standard WR187 rectangular waveguide (RWG) with lateral dimensions $a_{RWG} = W_{rod} = 47.55\text{mm}$ and $b_{RWG} = W_{rod} = 22.15\text{mm}$. Justification for the design permittivity is provided in the next section. Details about the design of the rod are not repeated here as they are not the focus of this work, and interested readers are referred to [132][133]. The geometric parameters of the rod antenna, referenced in Figure 8.4 are given in Table 8.1.

8.3.2. Bandgap Dielectric Crystal

As explained above, certain periodic geometries exhibit a full 3D bandgap. In this particular work, this effect is used to create a bandgap at the third harmonic of the design frequency of the dielectric rod antenna, resulting in effective attenuation of waves at said frequencies.

This is done by utilizing one of the most commonly employed photonic bandgap geometries, the woodpile structure as depicted with its Brillouin zone in Figures 8.1a and 8.1b. The woodpile geometry has primitive tetragonal lattice symmetry and consists of stacked dielectric bars with relative permittivity $\varepsilon_{\mathrm{r,w}}$ against free space. Here the plane wave expansion method (PWEM), as explained in Section 2.2.2, is utilized to solve equation (3.18) for the mode frequencies of a given Bloch-wave vector β, as explain in section 4.2.3. The band diagram corresponding to a woodpile lattice with $\varepsilon_{\mathrm{r,w}} = 13.7$ is depicted in Figure 8.5, and the justification for the choice of relative permittivity is further explained in Section 8.3.3. It is worth highlighting several key aspects of the band diagram. First, for low frequencies $\omega_{\mathrm{n}} < 0.2$ the fundamental mode closely follows the light line. This allows to approximate the behavior of the woodpile lattice as an effective medium with linear dispersion. Additionally in this effective region the propagating modes in the directions $\Gamma - \mathrm{X}$ (propagation along $\hat{\mathbf{x}}$ or $\hat{\mathbf{y}}$[1]) and $\Gamma - \mathrm{M}$ (propagation along $(\hat{\mathbf{x}} + \hat{\mathbf{y}})/\sqrt{2}$) two distinct bands are visible, which implies an effective anisotropy of the woodpile lattice and thus a dependency on the polarization of the wave propagating along these general directions. Second, although propagating modes are present at frequencies in the range of $0.2 < \omega_{\mathrm{n}} < 0.373$, these modes experience significant non-linear dispersion. And third, one is able to observe an absence of propagating modes between the normalized frequencies $\omega_{\mathrm{n,L}} = 0.373$ and $\omega_{\mathrm{n,U}} = 0.457$, indicating a full 3D bandgap with a center frequency $\omega_{\mathrm{n,m}}$. The unit cell size of the crystal a can be designed such that the bandgap center frequency $\omega_{\mathrm{n,m}}$ occurs at the third harmonic of the design frequency,

$$a = \omega_{\mathrm{n,m}} \lambda_{\mathrm{3HM}} = \frac{\omega_{\mathrm{n,L}} + \omega_{\mathrm{n,U}}}{2} \frac{c_0}{3 f_{\mathrm{d}}} = 8.3\mathrm{mm} \tag{8.1}$$

where λ_{3HM} denotes the free space wavelength at the 3rd harmonic of the design frequency f_{d}. A woodpile lattice with a lattice constant according to equation (8.1) exhibits a bandgap at 15GHz. The lattice simultaneously behaves as an effective material at the design frequency of 5GHz, the effective refractive index n_{eff} of the woodpile can be extracted from the banddiagram via the technique discussed in Section 2.2.2. Applying equation (4.16) gives a relative permittivity of $\varepsilon_{\mathrm{r,eff}} = 2.7$, which has been used as dielectric rod design permittivity in the previous section. To summarize, the dielectric rod antenna with geometry indicated in Figure 8.4 with dimensions given in Table 8.1, comprised of a woodpile lattice made from material with relative permittivity $\varepsilon_{\mathrm{r,w}} = 13.7$ and lattice constant $a = 8.3\mathrm{mm}$, should exhibit the same characteristics as one comprised of solid material with relative permittivity $\varepsilon_{\mathrm{r,rod}} = \varepsilon_{\mathrm{r,eff}} = 2.7$ at the fundamental design frequency $f_{\mathrm{d}} = 5\mathrm{GHz}$. However, the dielectric rod comprised of the woodpile lattice should prohibit any radiation at the third harmonic $3f_{\mathrm{d}} = 15\mathrm{GHz}$ due to the full 3D stopband exhibited by the woodpile lattice at these frequencies.

8.3.3. Manufacturing

Two materials are employed to manufacture two dielectric rod antennas, one solid and one comprised of a woodpile lattice. The solid dielectric rod is manufactured with white PLA from Ultimaker, exhibiting a measured[2] relative permittivity of $\varepsilon_{\mathrm{r,PLA}} = 2.66$ and a loss

[1] Bold letters with ˆ symbolizing unit-vectors

[2] No nominal permittivity is mentioned in the datasheet of this material.

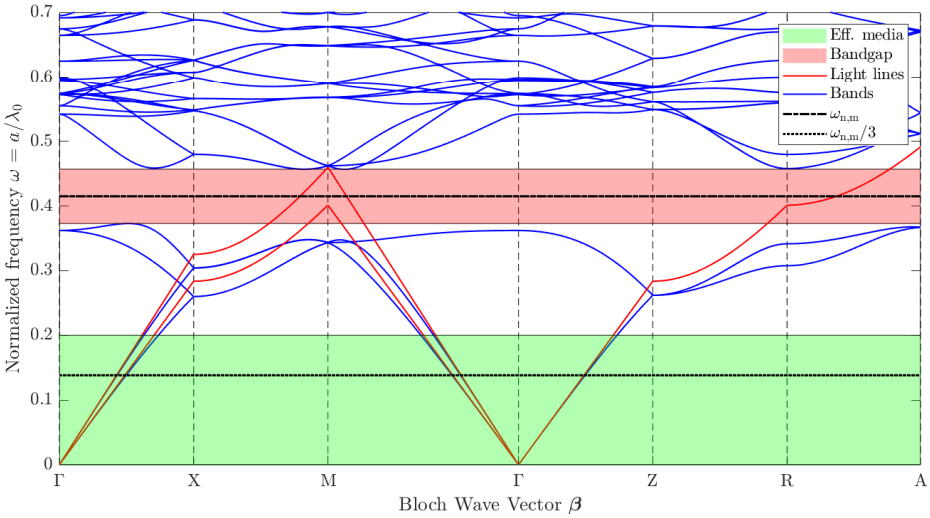

Figure 8.5: Banddiagram of the Woodpile unit cell with visualization of the effective media region (green), the bandgap (red).

tangent of $\tan\delta_{\mathrm{ABS1500}} = 0.062$ [134], which is considered sufficiently similar to the design permittivity of $\varepsilon_{\mathrm{r,rod}} = 2.7$ for the purposes of this proof of concept. The dielectric rod comprised of a woodpile lattice is manufactured via the ABS1500 material from Avient (former PREPERM), which exhibits a nominal relative permittivity of $\varepsilon_{\mathrm{r,p}} = 15$ and a loss tangent of $\tan\delta_{\mathrm{p}} = 0.018$, as mentioned in Table 3.2. In order to estimate the effect of the print process on the dielectric properties of the ABS1500 material, a printed bulk sample was characterized via the Nicholson-Ross-Weir method based on measured scattering parameters within a WR187 rectangular waveguide. The measured relative permittivity is $\varepsilon_{\mathrm{ABS1500,r}} = 13.7$ with a loss tangent $\tan\delta_{\mathrm{ABS1500}} = 0.02$, which is the effective permittivity utilized in the design of the woodpile lattice $\varepsilon_{\mathrm{r,w}}$ in the previous section. The manufactured prototypes of the solid and woodpile dielectric rod are depicted in Figure 8.6.

8.3.4. Simulation

To confirm the operational principle of the proposed antenna, numerical analysis of the rectangular waveguide-fed dielectric rod antenna is carried out with CST Microwave Studio for three individual cases. One for the standalone rectangular waveguide, one for the waveguide-fed dielectric rod antenna with dimensions given in Figure 8.4 and Table 8.1, and one for the waveguide fed dielectric rod antenna where the dielectric rod body is intersected with the woodpile lattice. The 3D models for the latter two cases are depicted in Figure 8.7.

The intended working principle of the woodpile dielectric rod can be well observed in the comparison of the electric fields inside the solid and woodpile dielectric rod antennas at 5 and 15GHz in Figures 8.7c-8.7f. The electric field distribution in the solid and woodpile rod

are similar at the design frequency at 5GHz, but the woodpile strongly attenuates the field at 15GHz due to the presence of a stopband. The radiated power and reflection coefficient as a function of frequency, as well as the realized gain patterns at the fundamental and third harmonic, are compared for the three individual cases for the excitation of the fundamental mode in the waveguide in Figure 8.8. From the reflection coefficient and the radiated power in Figures 8.8a and 8.8b it can be well observed that the woodpile dielectric rod is effective in suppressing radiation between 10 and 16GHz, compared to the solid rod and standalone waveguide. Furthermore, as intended, the woodpile rod mimics the characteristics of the solid rod at lower frequencies between 4 and 7GHz. This is also well observed with respect to the realized gain in Figures 8.8c and 8.8d, respectively. At 5 GHz, both the solid and woodpile rod exhibit the desired increase in gain of about 5dB compared to the standalone waveguide and have almost identical radiation patterns. However, at 15GHz the realized gain of the woodpile rod is $\approx$ 30dB lower at broadside compared to the solid rod and the standalone waveguide. Nevertheless, there is also a noticeable increase in realized gain for angles between 60 and 140 degrees off the broadside. While no difference in the front-to-back ratio between the solid and woodpile rod is observed at the design frequency, there is a degradation of $\approx$ 9dB of it at the third harmonic. Generally, it appears the bandgap does not center at the desired frequency of 15 GHz but around 13 GHz. The difference might be caused by an insufficient converged band diagram of the PWEM, resulting in small errors in the estimated bandgap frequencies and corresponding unit cell size in equation (8.1). Furthermore, some unexpected behavior is worth highlighting. There is an increase in the reflection coefficient and corresponding drop in radiated power between 8 and 9GHz for the woodpile rod compared to the solid rod, which does not seem to correspond to the stopband of the woodpile structure. Consulting the band diagram in Figure 8.5, one can observe that this frequency range falls between the bandgap and effective media frequency regimes,

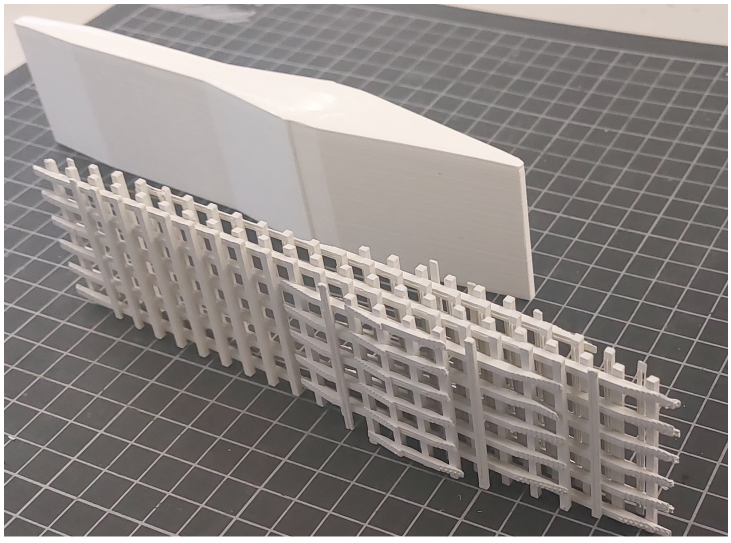

Figure 8.6: Manufactured solid (back) woodpile (front) dielectric rod antennas ready for measurement.

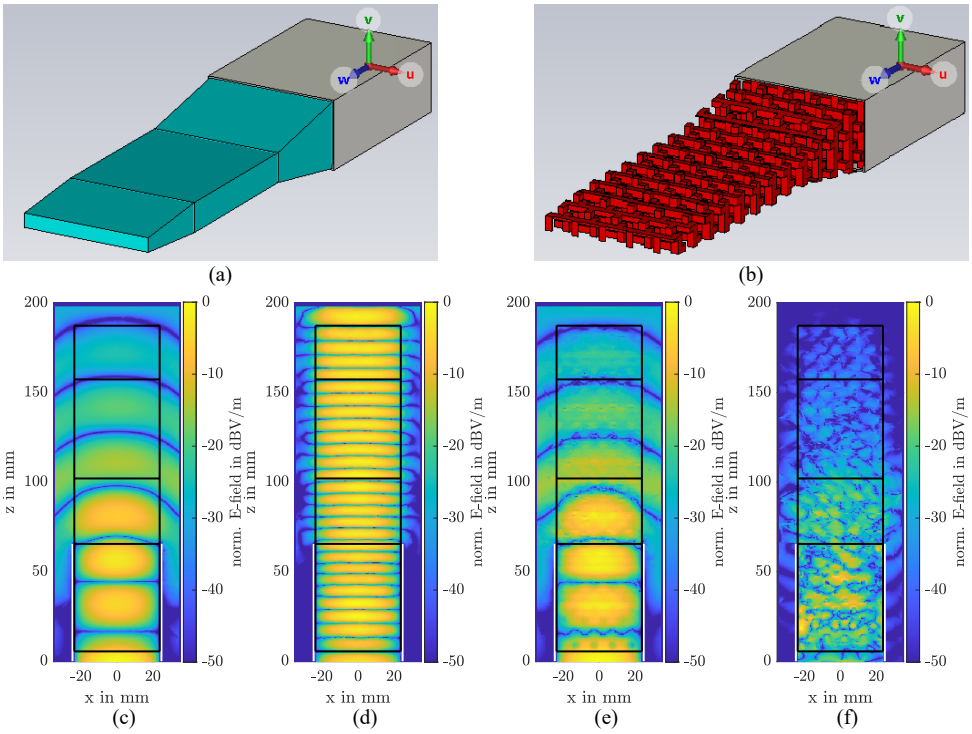

Figure 8.7: CST Microwave Studio models for the dielectric rod antenna with rectangular waveguide feed in (a) solid - material permittivity $\varepsilon_{\mathrm{r,rod}} = 2.7$, (b) woodpile - material permittivity $\varepsilon_{\mathrm{r,w}} = 13.7$ configurations and normalized simulated electric field values in the solid (c,d) and woodpile (e,f) rod antennas at (c,e) 5GHz and (d,f) 15GHz in the *xz*-plane where the waveguide dimensions and rod dimensions are indicated as white and black lines respectively.

where the fundamental mode in the woodpile lattice experiences non-linear dispersion and interaction with higher order modes in the woodpile lattice. To further study this behavior, a multi-mode simulation for the first ten propagating waveguide modes has been carried out, and the corresponding scattering parameters with respect to the fundamental mode are depicted in Figure 8.9 for the solid and woodpile dielectric rod respectively. One is able to observe an increased coupling into the higher order modes in the simulated scattering parameters of the woodpile dielectric rod compared to the solid rod. Already at the design frequency, an increased scattering to the TE11 and TM11 is noticeable. Furthermore, a significantly increased coupling to higher order modes is found at frequencies where the woodpile cannot be approximated as an effective medium with linear dispersion anymore. This phenomenon could explain well the unexpected rise in the reflection coefficient and corresponding drop in radiated power observed between 8 and 9 GHz in the single-mode simulations in Figures 8.8a and 8.8b.

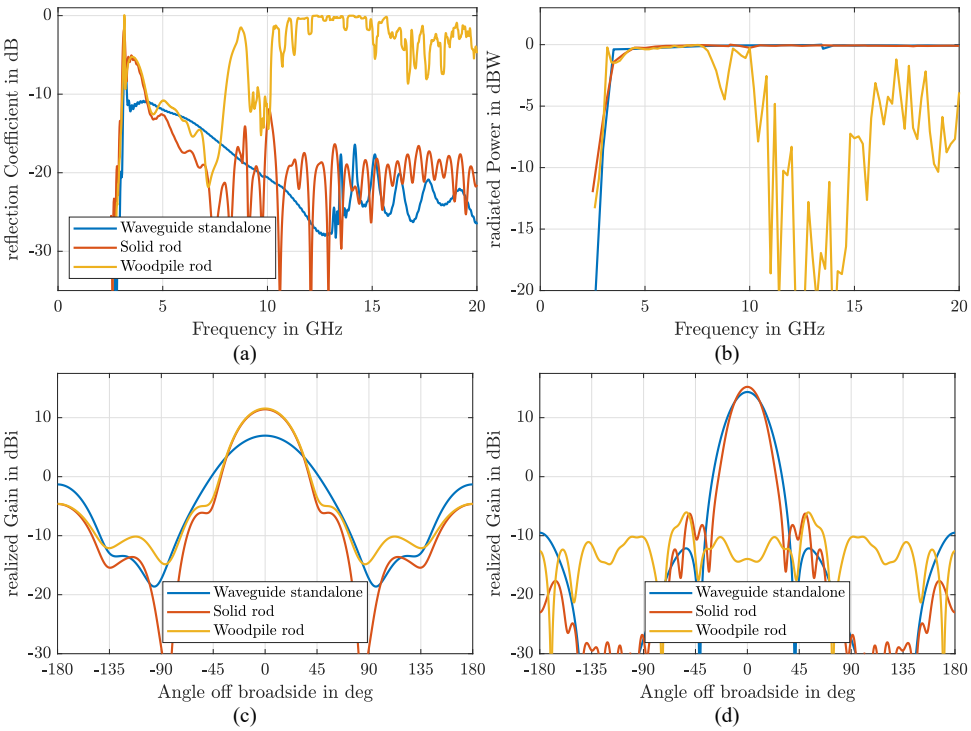

Figure 8.8: Simulation results of the different antenna configurations. Standalone waveguide (blue), the solid dielectric rod (red) and the woodpile dielectric rod(yellow) configurations. (a) Reflection coefficient of the rectangular waveguide waveport (b) Radiated power and co-polarized realized gain radiation patterns at (c) the design frequency (5 GHz) and (d) its third harmonic (15 GHz).

8

8.4. Measurement

The three antenna configurations discussed in the numerical simulations are now also considered in an experimental setup and characterized in terms of their input reflection coefficient and their far-field radiation patterns. The rectangular waveguide utilized for the measurement is a standard WR187 with a length of 150mm and fed via a coaxial transition with an N-type connector. The individual rod antenna prototypes are inserted into the waveguide aperture as depicted in Figure 8.10. Antenna measurements are carried out with the individual antennas in receiving configuration and under far-field conditions in the Delft University Chamber for Antenna Tests (DUCAT) for a frequency range of 2.5-20 GHz. The measured input reflection coefficients, as depicted in Figure 8.11, are dominated by the reflection of the coaxial to waveguide transition employed in the measurements. The coaxial transition primarily supports the fundamental TE_{10} mode, which explains the high reflections for frequencies above 7 GHz compared to the simulation result presented in Figure 8.8a, as the simulation only considers the fundamental mode.

Furthermore, compared to simulations presented in Figure 8.8a, the reflection coefficient for the woodpile dielectric rod at the third harmonic is not $\approx$ 0dB as predicted by simula-

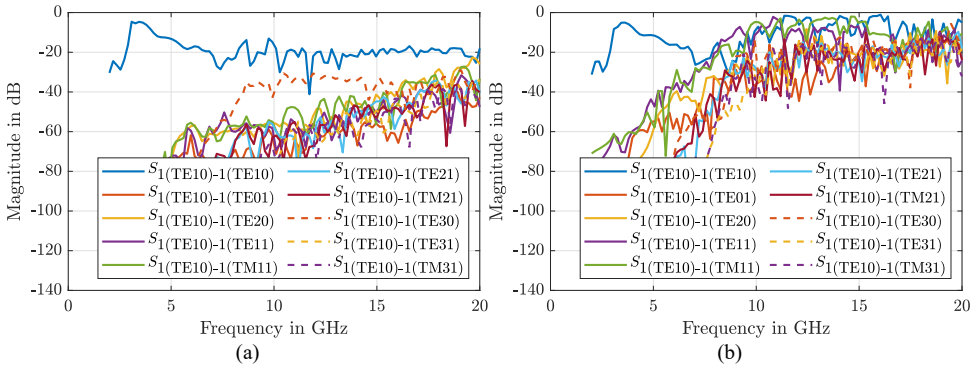

Figure 8.9: Multi-mode scattering parameters of the waveguide-fed dielectric rod antenna with respect to the fundamental mode in the waveguide (TE10) for the (a) solid and (b) woodpile rod, as a function of frequency.

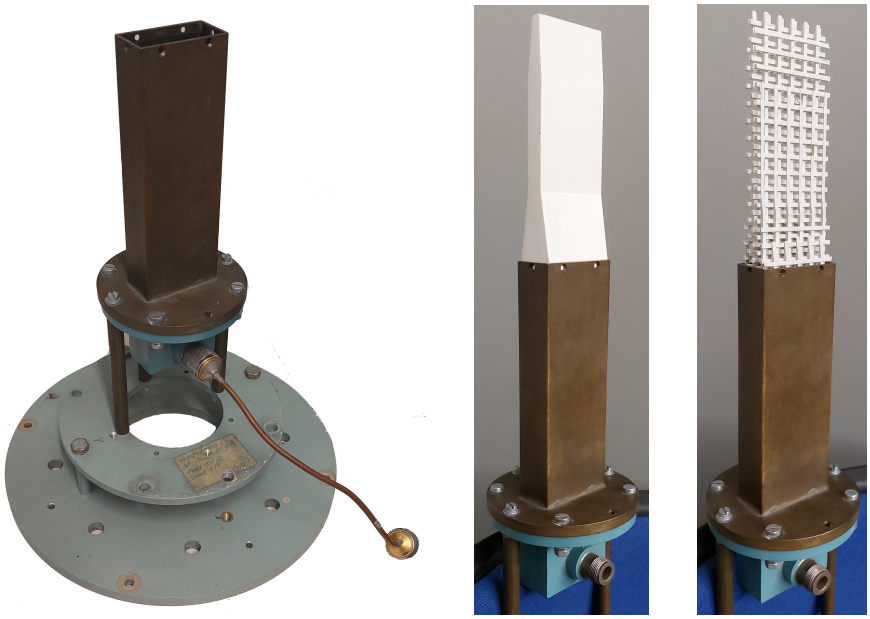

Figure 8.10: Measured antenna configurations. (a) Standalone rectangular waveguide with mounting plate. (b) Solid dielectric rod inserted into the waveguide aperture. (c) Woodpile dielectric rod inserted into the waveguide aperture.

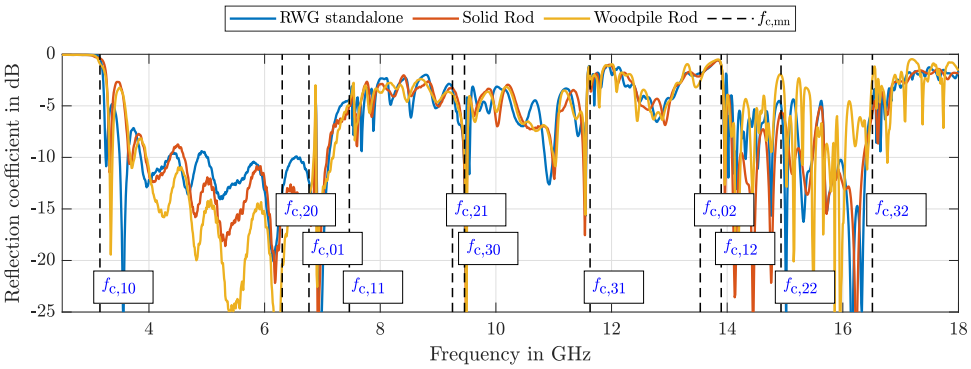

Figure 8.11: Measured input reflection coefficient of the rectangular waveguide standalone (blue), with the solid dielectric rod antenna (red) and with the woodpile dielectric rod antenna inserted into the waveguides aperture and cut-off frequencies f_{mn} of individual TE_{mn} modes in plotted in black dashed lines and labeled in blue.

tions. This can, again, be attributed to the feed primarily supporting the fundamental mode, as scattering from the woodpile excites a plethora of higher order modes as demonstrated with the multi-mode simulations in the previous section. This leads to a "ping-pong" of the energy contained in the higher order modes between the waveguide feed and the woodpile rod and a subsequent dissipation due to the conductive and dielectric losses. Due to the limitations of the waveguide feed, the effect of the solid dielectric rod compared to the woodpile rod can be best observed considering the realized gain measurements in the E- and H-plane as a function of frequency and the angle off broadside for all three antenna configurations presented in Figures 8.12 and 8.13. As expected at the design frequency 5 GHz, the solid rod and woodpile rod behave almost identically and increase the gain compared to the standalone rectangular waveguide. At the third harmonic frequency, the comparison between the solid and woodpile rod presents a drastic reduction in the realized gain of up to 35dBi corresponding again well to the expected results from the simulations. Although the presented experimental results confirm the antenna's operational principle, one can observe oscillations in the input reflection coefficient and realized gain values as a function of frequency. This phenomenon is present even in the standalone waveguide measurement. We attribute this effect to an issue with coaxial waveguide transition, which results in poor matching. An alternative explanation could be an interaction of the antenna under test with the mounting equipment in the an-echoic chamber.

8.5. Conclusion

Additive manufactured photonic band gap materials for mmWave applications have been shown. In contrast to other works, the structures presented here are compatible with low-cost processes and require no post-processing. The Woodpile and Diamond structures are selected to be investigated in this work. Two simulation methods to investigate the behavior of PBG materials are discussed, and simulations are performed to identify suitable high-permittivity filaments for low-cost manufacturing. Three individual Woodpile PBG slabs are manufactured and their reflection and transmission spectra are measured in a free-

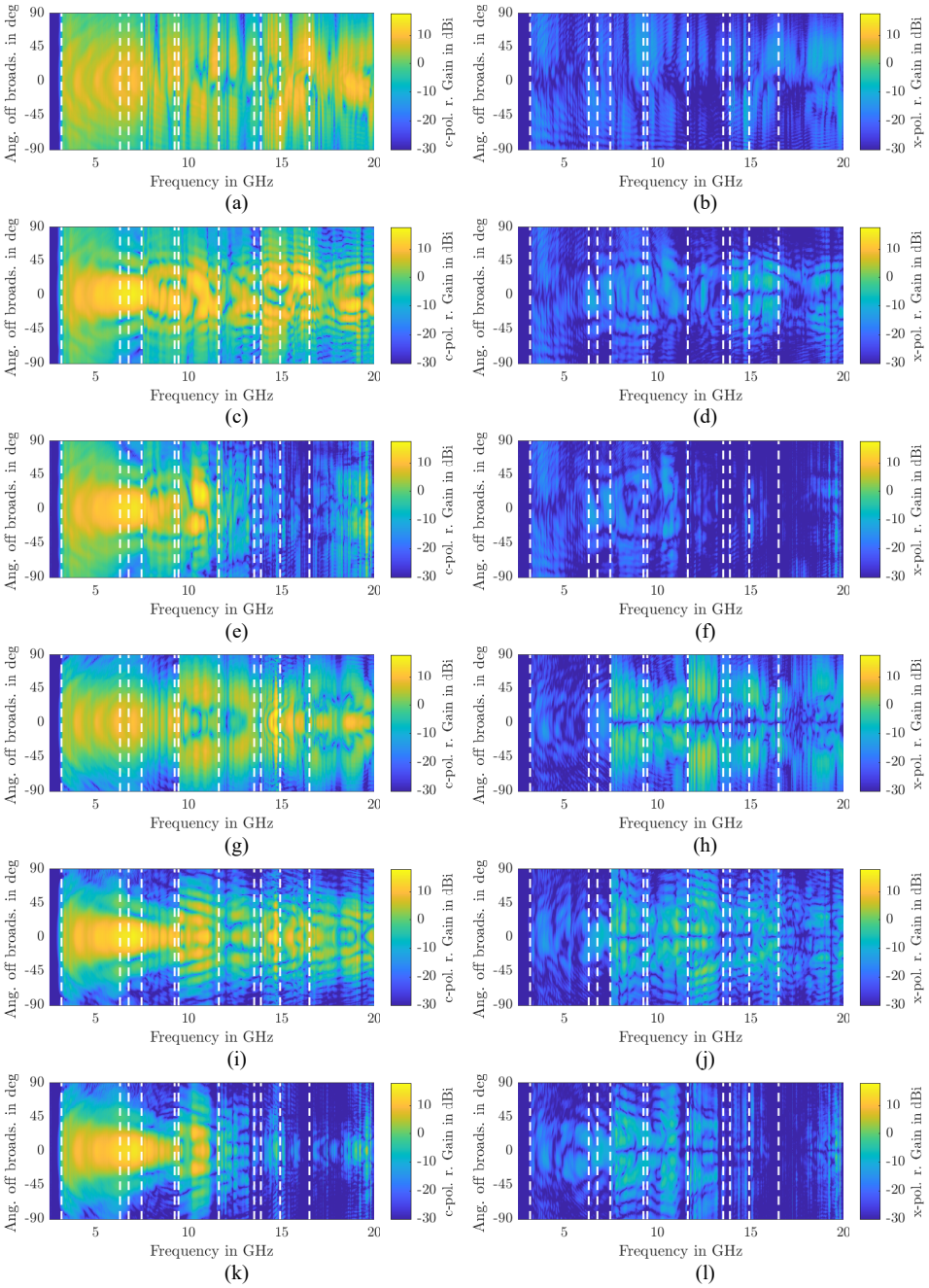

Figure 8.12: E-plane (a-f) and H-plane (g-l), co- (left) and cross-polarized (right), realized gain measurements as a function of frequency and angle of broadside for (a,b,g,h) standalone rectangular waveguide, (c,d,i,j) solid dielectric rod and (e,f,k,l) woodpile dielectric rod antenna with the cutoff frequencies of individual higher order modes in the waveguide plotted in dashed white lines.

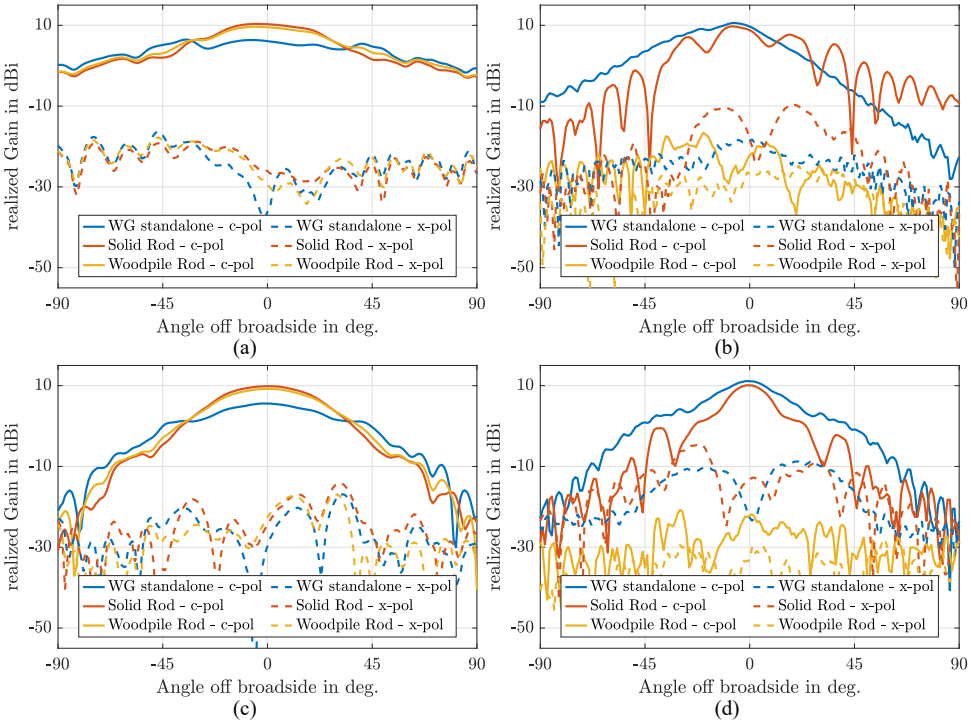

Figure 8.13: Comparison of measured co-(solid lines) and cross-polarized (dashed lines) realized gain values in the E- (a,b) and H-plane (c,d) for the standalone rectangular waveguide (blue), solid dielectric rod (red) and woodpile dielectric rod (yellow) antenna as a function of angle off broadside for 5 GHz (a,c) and 15 GHz (b,d).

space measurement setup. The measurements agreed reasonably well with predictions from simulations. Deviations from the predicted performance and probable causes have been discussed. It can be concluded that low-cost additive manufacturing is a viable method for producing PBG materials. However, there is much room for improvement. Different materials and bandgap geometries need to be investigated to find a good trade-off between performance and printability.

This work introduces a novel concept to mitigate the unintended transmission and reception of signals at the third harmonic of dielectric rod antennas without requiring additional components or complex feed networks. The presented antenna exploits the concept of a bandgap dielectric crystal with a woodpile unit cell that behaves like an effective material at the design frequency but exhibits a complete 3D bandgap at the third harmonic. Numerical simulations confirm the operational principle of the antenna and show a significant drop in the realized gain and overall radiated power at the third harmonic. Unexpected behavior of the bandgap rod antenna at intermediate frequencies between the fundamental and third harmonic are investigated and linked to the excitation of higher order modes in the waveguide due to scattering off the periodic structure. The operational principle of the antenna is confirmed in experiments via the characterization of the input reflection coefficients and far-field radiation patterns of a traditional rod antenna and its bandgap counterpart.

9

Hybrid AM of Phased Array Antenna at K-Band

Abstract This study explores the feasibility of using a hybrid, combined conductive and dielectric, additive manufacturing (AM) to design and produce low-cost, wideband phased array antennas for SatCom applications. We demonstrate the design, fabrication and experimental verification of an eight-element linear array comprised of multi-mode dielectric resonator antennas (DRAs) providing full coverage of the K-band SatCom downlink bandwidth (17.7-21.2 GHz). The impact of print settings on material properties is assessed and incorporated into the antenna design process. The manufactured prototype is experimentally verified via impedance and far-field measurements. Furthermore, beam steering capabilities are demonstrated using a commercially available integrated circuit and a simple calibration procedure. The phased array antenna achieves full coverage of the intended band with an input reflection coefficient below -10 dB. The averaged embedded element pattern demonstrates a realized gain of approximately 3 dB and a half-power beamwidth of 81 degrees. These results highlight the potential of combining hybrid AM and DRA technologies for future mmWave phased array development.

9.1. Motivation and Structure

Modern mmWave phased array antennas face challenges in providing sufficient bandwidth at a cost suitable for mass-market applications. As demonstrated in previous chapters, AM can be applied in pethora of ways to engineer novel devices. The primary utilized advantage of AM so far is its capability to engineer the effective dielectric permittivity of materials via non-resonant periodic structures, providing additional degrees of freedom in the design of novel RF and microwave devices.

However, single-material AM processes face limitations when developing advanced designs requiring multiple dielectrics and conductive materials or interfacing with conventional microwave equipment. Hybrid techniques[1], such as electroplating of printed parts [135] and copper foil deposition [136], can retain bulk metal conductivity but often require extensive post-processing, limiting their ability to fully exploit AM's potential.

Recently, AM technology has matured sufficiently to allow the combination of dielectric and conductive materials within the same process. Techniques like inkjet printing of dielectric and conductive inks [137], and the combination of extrusion-type AM with microdispensing of conductive inks [138], are particularly promising. While inkjet printing offers exceptional accuracy, extrusion-based methods are more accessible and compatible with a wide range of materials. Both methods trade bulk metal conductivity for the ability to manufacture complex parts in a single process, enabling the integration of dielectric materials with internal conductive traces or patches. This capability opens up tremendous possibilities in the design and manufacturing of novel antennas and complex metamaterial structures.

Extrusion-based hybrid AM has been used to create various antenna designs and RF components [139–141], though most applications have been limited to sub-10GHz frequencies and largely replicate designs already feasible with traditional methods. Regarding the utilization of AM for antenna applications, dielectric resonator antennas (DRAs) have emerged as a promising technology in the past decade, offering greater bandwidth and design flexibility for microwave and mmWave antennas compared to traditional microstrip patch antennas [44, 122]. The combination of hybrid AM and DRAs holds significant potential for developing low-cost, high-performance mmWave phased array antennas, yet this potential remains largely unexplored.

In this work, we demonstrate the feasibility of using hybrid AM and DRA technology to create wideband, low-cost phased array antennas for K-band receivers, covering the SatCom downlink band from 17.7 to 21.2 GHz. We introduce a novel DRA element design that utilizes two higher-order modes to achieve the desired bandwidth while enhancing directivity across the band. Additionally, we demonstrate the antenna's performance in an eight-element linear array configuration and its beam steering capabilities using a commercially available integrated circuit. The manufacturing process incorporates several innovative AM techniques: the DRA is printed using both low- and high-permittivity materials, with the high-permittivity material forming a periodic lattice to engineer the DRA's permittivity, and the low-permittivity material providing structural support. The ground plane and feedlines are fabricated using a low-loss dielectric and highly conductive silver ink. We also discuss the impact of print settings on material properties and experimentally characterize these effects to ensure accurate antenna performance prediction through full-wave

[1] the combination utilization of dielectric and conductive materials

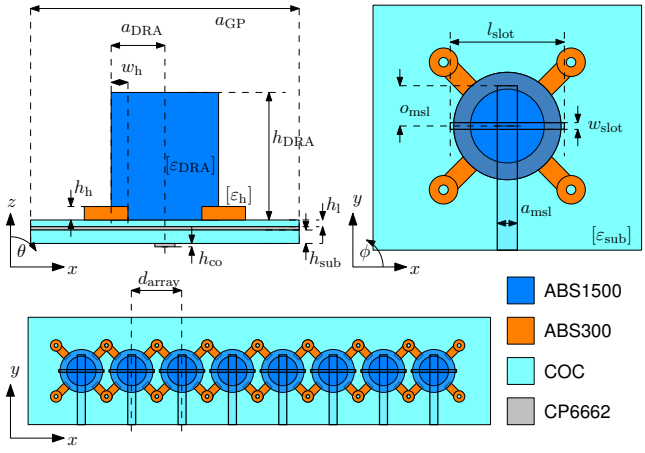

Figure 9.1: Schematic drawing of the dielectric resonator antenna element considered in this work and its extension to an eight element linear array with color-coding corresponding to the different utilized materials.

Variable	Value
a_{DRA}	3.15 mm
h_{DRA}	8 mm
a_{GP}	50 mm
h_{sub}	0.48 mm
w_{h}	0.8 mm
h_{h}	0.8 mm
a_{msl}	1.5 mm
o_{msl}	3.5 mm
l_{slot}	7 mm
w_{slot}	0.45 mm
h_{l}	0.24 mm
h_{co}	40 µm

Table 9.1: Geometric parameters of proposed dielectric resonator antenna design.

simulations.

This chapter is structured as follows: Section 1 details the antenna design, both standalone and within the linear array. Section 2 discusses the manufacturing setup and print settings, including inspection of the manufactured parts and identification of print artifacts. Section 3 presents the experimental verification of the antenna in both standalone and array configurations through impedance and far-field measurements. Furthermore, beam steering with an eight-channel integrated circuit is demonstrated. Finally, Section 4 discusses the measurement results, and Section 5 concludes the work.

9.2. Design

9.2.1. Single Element Design

A schematic drawing of the proposed antenna is depicted in Figure 9.1. The design process and individual steps are explained in detail below.

Design methodology

While DRAs reportedly exhibit larger bandwidths than traditionally employed microstrip patch antennas, their bandwidth is insufficient to cover the whole SatCom downlink band in the K band ($17.7-21.2$GHz). To address this, we employed a technique that places two resonant modes in close frequency proximity, resulting in overlapping radiating bands and thus a wider bandwidth[142]. The antenna design process is carried out as follows.

(i) *Material Parameter Simulation:* We first identify the appropriate lattice constant and crystal symmetry for the DRA body, selecting a lower effective permittivity to reduce the Q factors of the resonant modes.

(ii) *Eigenmode Simulation:* Using CST's eigenmode solver, we determine the DRA dimensions (a_{DRA} and h_{DRA}) that support the selected modes at the desired resonant

frequencies.

(iii) *Full-Wave Simulation:* Finally, we conduct full-wave simulations including the feed network to optimize the aperture dimensions and microstrip line termination, ensuring the antenna is well-matched.

Engineering the DRA permittivity

Given the available materials, the DRA is manufactured from high-permittivity ABS1500 thermoplastic, as listed in Table 3.2. Although high-permittivity materials are a great tool to achieve miniaturization, they also limit the bandwidth of the resulting antenna. The capability of AM to create complex structures is commonly exploited to engineer the permittivity of some dielectric material by manufacturing a periodic structure with a given volumetric infill. Here we utilize dielectric periodic structures, or dielectric crystals, created via the superposition of spatial harmonics as discussed in Section 3.2.2. Generally, there are two issues when engineering effective material parameters via AM periodic structures.

(i) *Printing Imperfections:* These introduce tiny air gaps, reducing permittivity [114] and causing effective uniaxial anisotropy due to the layer-by-layer construction as discussed in chapter 5.

(ii) *Frequency Dispersion:* Effective material parameters of periodic structures are inherently frequency-dispersive; thus, the lattice constant must be small enough to minimize this effect.

Both of these issues need to be taken into account for a successful design. The effective permittivity tensor of a solid part printed from the ABS1500 material with an extrusion width of $0.15\mathrm{mm}$ and a layer height of $0.1\mathrm{mm}$ is measured to be

$$[\varepsilon_{\mathrm{r,m}}] = \begin{bmatrix} 13.36 & 0 & 0 \\ 0 & 13.32 & 0 \\ 0 & 0 & 11.71 \end{bmatrix}. \tag{9.1}$$

which is now assumed to be the permittivity of the host material for manufacturing the DRA. We select a face-centered-cubic (FCC) symmetry for the dielectric crystal, as it offers lower dispersion across a larger frequency band as demonstrated in Section 4.3.3. Several FCC unit cells, created with the spatial harmonic superposition method, with lattice constant a and different threshold values th, are depicted in Figures 3.4g-3.4i. The relationship between the threshold value and the volumetric infill fraction is discussed in Chapter 3, Section 3.2.2. The effective material parameters are extracted via Floquet port scattering simulations as presented in Section 4.2.4. The effective permittivity tensor components in non-dispersive frequency regimes are presented as a function of volumetric infill in Figure 9.2a, and the effective permittivity tensor components as a function of frequency for different lattice constants and a specific volumetric infill are depicted in Figure 9.2b. In order to avoid significant dispersion for frequencies up to $30\mathrm{GHz}$, a lattice constant $a = 1.5\mathrm{mm}$ is selected for the further design. Although the permittivity tensor of the resonating body can be a powerful degree of freedom in the design of DRAs, as demonstrated in [143], the

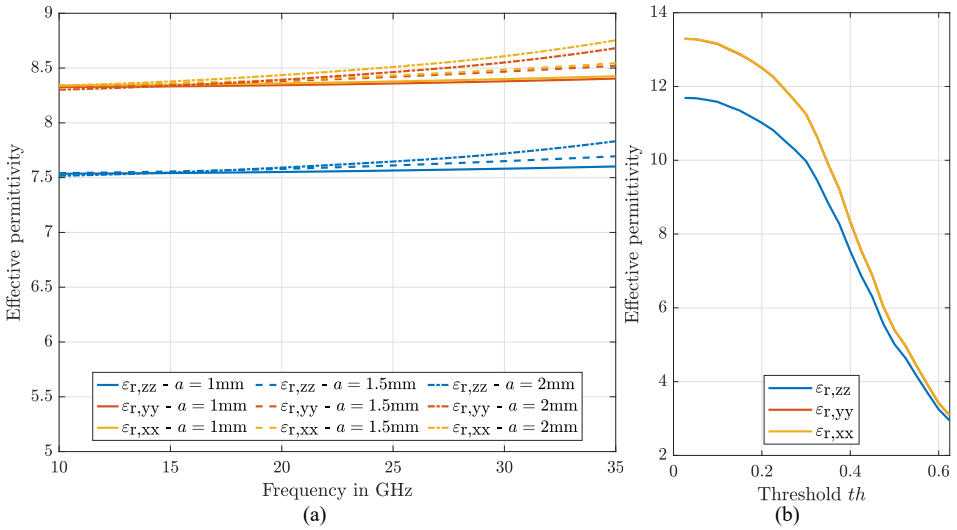

Figure 9.2: (a) Tensor components as a function of frequency for different lattice constants a for threshold $th = 0.4$. (b) Tensor components as a function of spatial harmonic threshold.

utilization of it is out of scope for this work. In this work, we specify the threshold of our periodic structure as 0.5, which provides a permittivity tensor for the DRA

$$[\varepsilon_{\mathrm{r,DRA}}] = \begin{bmatrix} 5.5 & 0 & 0 \\ 0 & 5.5 & 0 \\ 0 & 0 & 5.1 \end{bmatrix}. \tag{9.2}$$

DRA dimensions

In contrast to most DRA applications, we do not utilize the fundamental mode of the DRA, which usually provides a relatively broad beam, but rather opt for higher-order modes to increase the directivity of the antenna. Two different resonating DRA modes in close proximity are used to widen the bandwidth of the antenna. To this end, the $HEM_{11\delta}$ and $HEM_{12\delta}$ modes are selected, which both offer broadside radiation and relatively low Q factors. Furthermore, they both are compatible with feeding from a rectangular aperture in the ground plane due to the magnetic field distribution at the bottom of the DRAs. The DRA with permittivity tensor according to equation (9.2) is modeled together with the holding structure, as depicted in Figure 9.1, with parameters $w_{\mathrm{h}} = 0.8\mathrm{mm}$ and $h_{\mathrm{h}} = 0.8\mathrm{mm}$ in a CST eigenmode environment. The holding structure is printed from the ABS300 material from Avient which exhibits a nominal permittivity of $\varepsilon_{\mathrm{r,\ ABS300}} = 3$ and a loss tangent of $\tan_{\delta} = 4.6\mathrm{E}{-3}$. In the simulation the measured permittivity value of the ABS300 material, as reported in Section IV in equation (9.3), is utilized to model the holding structure. For DRA dimensions reported in Table 9.1 the desired modes exhibit resonance frequencies at 17.87 and 21.01GHz with corresponding Q factors 9.3 and 3.2, respectively. The electric W_{e} and magnetic W_{m} energy densities of the selected modes are depicted in Figure 9.3 in the $xz(y = 0)$-, $yz(x = 0)$- and $xy(z = 0)$-planes respectively.

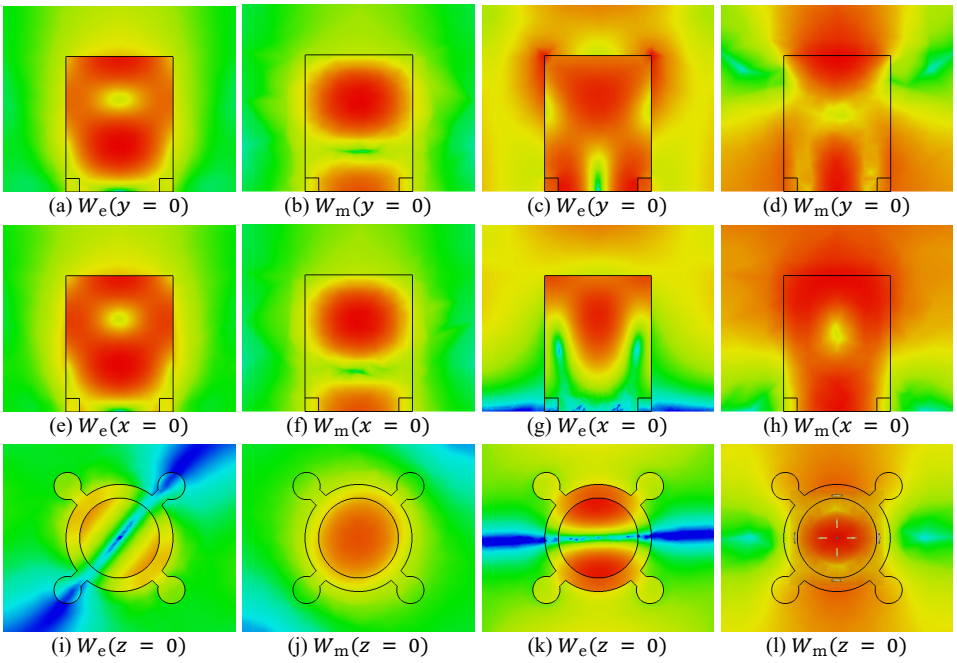

Figure 9.3: Simulated electric (column 1 and 3) and magnetic (column 2 and 4) energy densities of the $HEM_{11\delta}$ (a,b,e,f,i,j) and $HEM_{12\delta}$ (c,d,g,h,k,l) in the xz- (row 1), yz- (row 2) and xy(z=0)- (row 3) planes.

Element feed

The antenna is excited using a 50Ω microstrip transmission line on a substrate with height h_{sub} made from Cyclo-Olefin-Copolymer (COC) from Creamelt, a low-permittivity ($\varepsilon_{\mathrm{r,COC}} = 2.4$), low-loss ($\tan_\delta = 2\mathrm{E}{-}4$) material thermoplastic. The antenna and transmission line are coupled via a rectangular aperture directly below the dielectric resonator with dimensions l_{slot} and w_{slot}. The transmission line is terminated with an open at an offset of o_{msl} w.r.t. the center of the slot. The DRA is positioned centrally above the feed aperture and fixed in place via four M2 nylon screws. Since printing conductive ink directly to the heated print bed is not possible, an additional layer of substrate with height h_{l} between the ground plane and the DRA is considered in the design. For later manufacturing, a layer height of $0.12\mathrm{mm}$ is selected for the feed substrate. It is desired to extrude two and four layers for the spacer substrate and microstrip substrate, respectively, resulting in $h_{\mathrm{l}} = 0.24\mathrm{mm}$ and $h_{\mathrm{sub}} = 0.48\mathrm{mm}$. The microstrip substrate exhibits a permittivity of $\varepsilon_{\mathrm{r,sub}} = \varepsilon_{\mathrm{r,COC}}$, as reported in (9.4) in Section IV, and the conductive ink is dispensed with $0.04\mathrm{mm}$ layer height, which implies a line width of $a_{\mathrm{msl}} = 1.5\mathrm{mm}$ to realize a characteristic impedance of $Z_0 = 50\Omega$. The remaining parameters of the feed structure, namely the rectangular aperture dimensions l_{slot} and w_{slot} as well as the microstrip termination offset o_{msl}, are subject to an optimization routine in a full-wave simulation environment with the goal to minimize the input reflection coefficient at the resonance frequencies obtained via the eigenmode simulation explained above. The input reflection coefficient as a function of frequency and the co- and cross-polar far-field plots are depicted in Figure 9.5. The local

Table 9.2: Hardware configuration of the toolchanger additive manufacturing setup.

E3D Motion System - Toolchanger Configuration				
Tool	**1**	**2**	**3**	**4**
Device	E3D Hemera Extruder	E3D Hemera Extruder	ViscoTec vipro-HEAD 3	E3D Hemera Extruder
Material	Avient ABS1500	Avient ABS300	Elantas Bectron CP6662	Creamelt COC
Orifice diameter	0.15mm	0.15mm	0.2mm	0.6mm

Table 9.3: Material print settings

Setting - Material	**ABS1500**	**ABS300**	**CP6662**	**COC**
Extrusion width [mm]	0.15	0.15	0.2	0.6
Nozzle temp. [°C]	280	230	-	245
Bed temp. [°C]	105	105	55	75
Max. speed [$\mathrm{mm\,s^{-1}}$]	5	7.5	10	60
Max. acc. [$\mathrm{mm\,s^{-2}}$]	200	200	100	1500
Layer height [mm]	0.1	0.1	0.04	0.12

minima of the input reflection coefficient at 17.7 and 21.4 GHz correspond well to the predicted values from the eigenmode simulation. The full-wave simulations show realized gain values of 9.06 dBi and 7.6 dBi for $\theta = 0$, at the two resonance frequencies respectively. All geometric parameters are summarized in Table 9.1.

9.2.2. Array

The designed element, without further optimization is introduced into the eight element linear array geometry with a half-wavelength spacing at 19 GHz corresponding to an inter-element distance, as indicated in Figure 9.1, of $d_{\mathrm{array}} = 7.9\mathrm{mm}$. The arm-length of the holding structure is chosen such that the mounting holes of neighboring elements coincide.

9.3. Manufacturing

9.3.1. Hardware Setup and Print Parameters

The manufacturing setup is based on a *core-XY* tool changing concept based on the E3D motion system platform equipped with four independent tools that can be switched during the print process, allowing for flexible multi-material printing. In our case, the system is equipped with three E3D Hemera filament extruders for the three utilized dielectrics and a third-party print-head, Vipro-HEAD 3 from VisoTec GmbH, for silver ink dispensing. The ViproHead print-head is selected due to its precise dispensing capabilities and stepper motor interface, which allows straightforward integration into the existing print hardware. The hardware setup is summarized in Table 9.2, and the corresponding print settings are reported in Table 9.3.

9.3.2. RF interface

In order to support measurements of the manufactured antennas, an interface from the microstrip feed network to the measurement equipment needs to be established. In this work, we utilize a 2.92mm SMA connector (Amphenol SF1521-60061) that is screwed onto the substrate and establishes a reliable connection via compression. The choice of the connector is driven by the necessity to employ a low-temperature solution because the utilized substrate material has a comparably low glass-transition temperature of 80°C, which renders it incompatible with soldering techniques.

9.3.3. Visual inspection

Figure 9.4 depicts the manufactured single element and array antennas with mounted connectors. To provide sufficient space for the connectors, the feedlines of odd-numbered elements in the array are flipped around to the other side of the substrate, as opposed to the depiction in Figure 9.1. Although the print can be considered successful, several imperfections can be identified in the prints and are studied further in detail below.

Air gaps and warping in extruded dielectrics

Air gaps and layer lines can be seen in the dielectric parts in Figure 9.4. This effect has already been explained above in Section II-2 and is most obvious in the substrate material COC due to the large nozzle utilized during the print and the transparent nature of the thermoplastic. Furthermore, the ABS materials are prone to warping due to temperature differences in the material during manufacturing, which may result in slightly twisted geometries, as can be observed on the holding structure in Figure 9.4b.

Ink dispensing edges

The dispensing of silver ink onto the substrate material does not create perfect edges, as depicted in Figures 9.4c; this results in small variations in the thickness of the microstrip lines and a blurring of the edges in the rectangular feed aperture. Furthermore, ink dispensing inconsistencies result in areas with no ink coverage, as can be observed in Figure 9.4d.

Dimensions of printed parts

The tolerances of the manufacturing lead to slightly different values for the microstrip line widths, offsets, and slot dimensions as depicted in 9.4e and 9.4f, respectively. Furthermore, the ABS materials from Avient are prone to shrinkage during part cool down after the printing process, which results in slightly reduced dimensions of the printed parts as depicted in Figure 9.4b.

9.4. Simulation and Measurement Results

9.4.1. Material Parameters

Dielectric properties

To achieve an accurate simulation of the antenna, the anisotropic permittivity of both the ABS1500, ABS300 and COC, printed with settings provided in Table 9.3, are measured with a quadratic aperture waveguide system in the X-band as explained in Section 5.3.1,

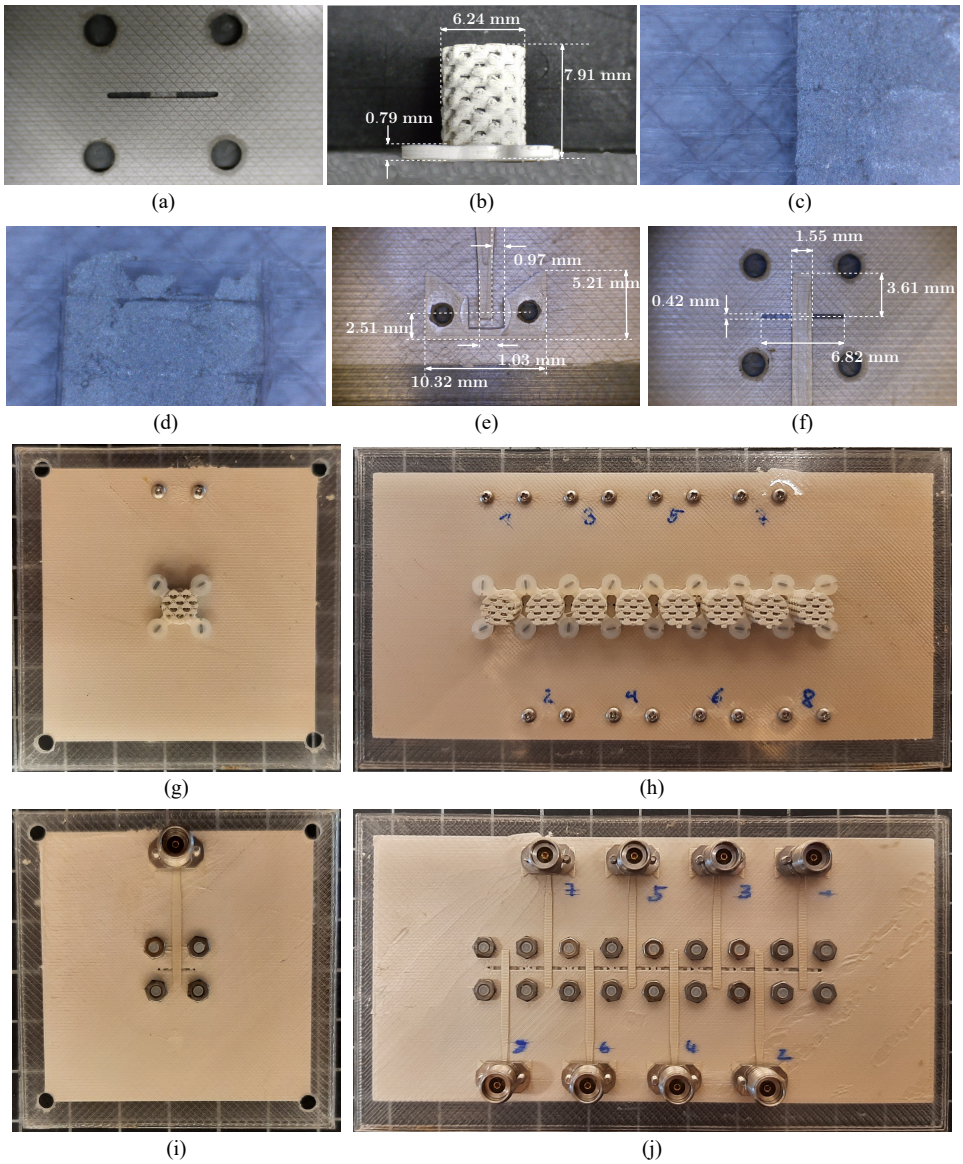

Figure 9.4: Visual inspection and identification of imperfections in the printed parts. (a) Gaps in the substrate material along the extruded lines and blurred corners of the rectangular slot. (b) Layer lines and 'blobs' of extruded materials on the DRA. (c) Microstrip line edge - blurry edge. (d) Microstrip line edge open termination - under extrusion. (e) Connector landing pad - dimensions. (f) Slot and microstrip line dimensions. Manufactured prototypes of the K band DRA antennas, manufactured via hybrid additive techniques. Single element (g) front, (h) back. Eight element linear array (i) front, (j) back.

and the averaged real-valued[2] permittivity tensors are

$$[\varepsilon_{\mathrm{r,ABS300}}] = \begin{bmatrix} 2.95 & 0 & 0 \\ 0 & 2.95 & 0 \\ 0 & 0 & 2.86 \end{bmatrix} \tag{9.3}$$

and,

$$[\varepsilon_{\mathrm{r,COC}}] = \begin{bmatrix} 2.25 & 0 & 0 \\ 0 & 2.25 & 0 \\ 0 & 0 & 2.20 \end{bmatrix}. \tag{9.4}$$

The measured permittivity value for the ABS1500 material has already been reported above in equation (9.1). Measurements of the extracted material permittivity tensor values in (9.1), (9.3) and (9.4), we can see that the layer-by-layer buildup results in a uniaxial anisotropic material with negative birefringence as demonstrated in Chapter 5.

Conductivity

After dispensing, the Bectron CP 6662 silver ink is thermally cured by pausing the print and setting the heated bed to the desired curing temperature (120 °C for 10 minutes). The surface resistivity ρ_s after thermal curing is measured with a four-point-probe system Jandel RM3-AR from Polytech GmbH to be about $\rho_s = 12$ mΩ/sq for a layer height of $40\mu m$, corresponding well to the value reported in the datasheet of the ink (10 mΩ/sq/mil).

9.4.2. Single Element

The single DRA element, as depicted in Figure 9.4, is characterized by input reflection coefficient and far-field radiation while being mounted in a bench-top anechoic chamber from Millibox. The input reflection coefficient and the co- and cross-polarized realized gain values obtained through measurement and full-wave simulation are compared in Figure 9.5a. Furthermore, the measured co- and cross-polarized realized gain patterns are displayed for orthogonal azimuth cuts for 19GHz in Figure 9.5b.

9.4.3. Embedded Element

The embedded elements are first measured in a passive configuration and then connected to the evaluation board of the Anokiwave AWMF-0197, a commercially available integrated circuit intended for satellite communication receivers operating in the desired frequency range. The mounting of the array together with the evaluation board is depicted in Figure 9.8.

Passive

Embedded input reflection coefficient measurements of each array element are depicted in Figure 9.6a. Furthermore, the measured cross- and co-polarized realized gain is plotted as a function of frequency in Figure 9.6c and at 20 GHz as a function of the angle θ for two orthogonal azimuth cuts in Figure 9.6d. Additionally, measured values for the impedance bandwidth and half-power beam widths are reported in Table 9.4.

[2] imaginary parts omitted for brevity sake

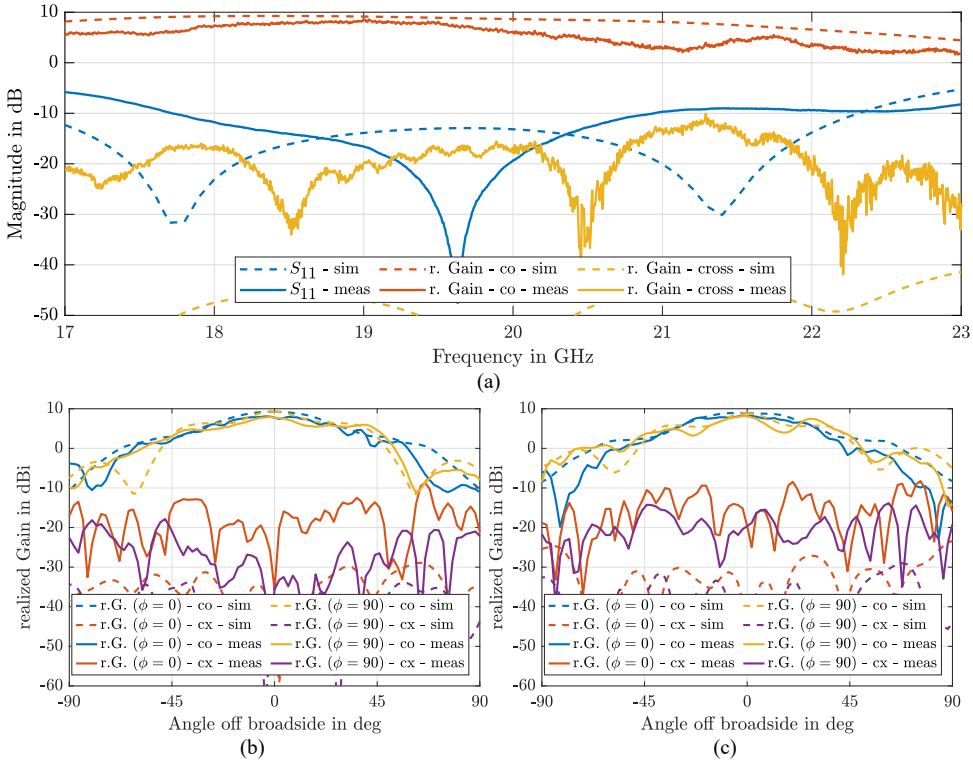

Figure 9.5: Measurement results of the single element antenna prototype compared to simulation results. (a) Input reflection coefficient and realized gain in cross- and co-polarization as a function of frequency. (b) Co- and cross-polarized realized gain values at 19 GHz.

Table 9.4: Impedance bandwidth and half power (HP) beamwidth measurement results of the single element and embedded antenna elements.

	Impedance Bandwidth			**HP beamwidth**		
	f_l GHz	f_u GHz	B GHz | %	θ_1 deg	θ_2 deg	θ_HPBW deg
Single Element	17.71	20.95	3.24 | 17.1	24	24	48
Ant. 1	17.06	23.72	6.66 | 35.1	−43	31	74
Ant. 2	17.13	22.13	5.00 | 26.3	−42	38	80
Ant. 3	17.40	23.59	6.20 | 32.6	−5	39	44
Ant. 4	17.71	23.34	5.62 | 29.6	−35	36	71
Ant. 5	17.01	21.48	4.47 | 23.5	−36	31	67
Ant. 6	18.09	20.93	3.00 | 15.8	−36	42	78
Ant. 7	17.84	20.26	2.42 | 12.7	−40	42	82
Ant. 8	19.20	20.69	1.49 | 7.8	−30	39	69
Avgd. Pattern	17.47	21.24	4.36 | 22.9	−41	40	81

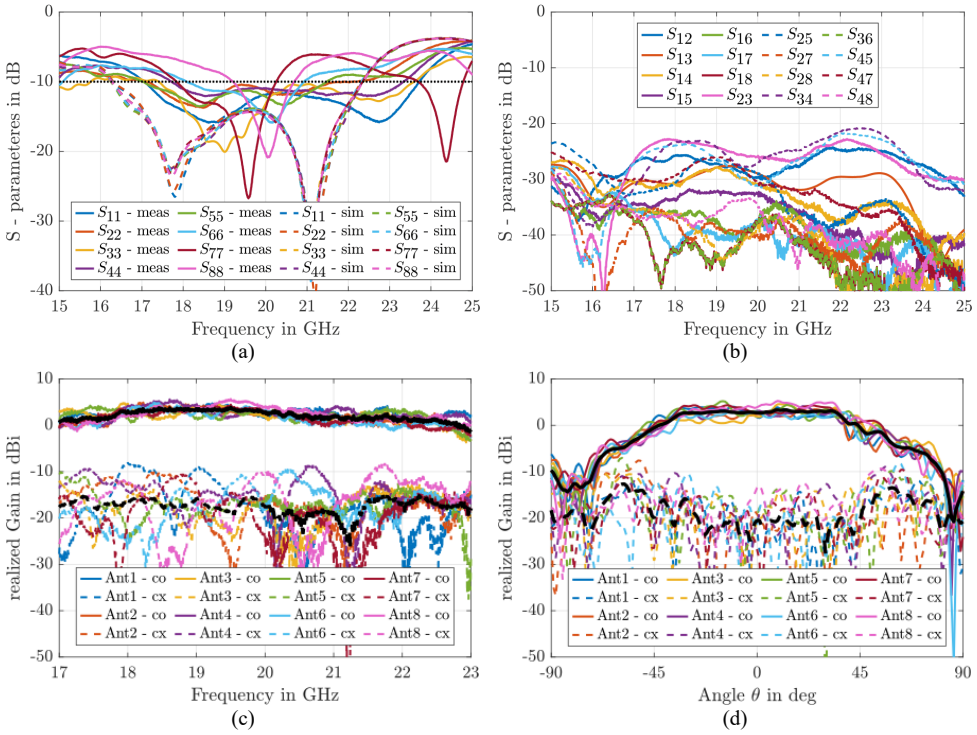

Figure 9.6: Measurement results of the passive embedded elements. (a) Input reflection coefficients as a function of frequency compared to simulation results. (b) Cross- and co-polarized realized gain values of the individual elements at $\theta = 0$ as a function of frequency. (c) Cross- and co-polarized realized gain values of the individual embedded antenna elements as a function of the angle θ for two orthogonal azimuth cuts. Bold black curves correspond to the averaged beampattern values over all elements.

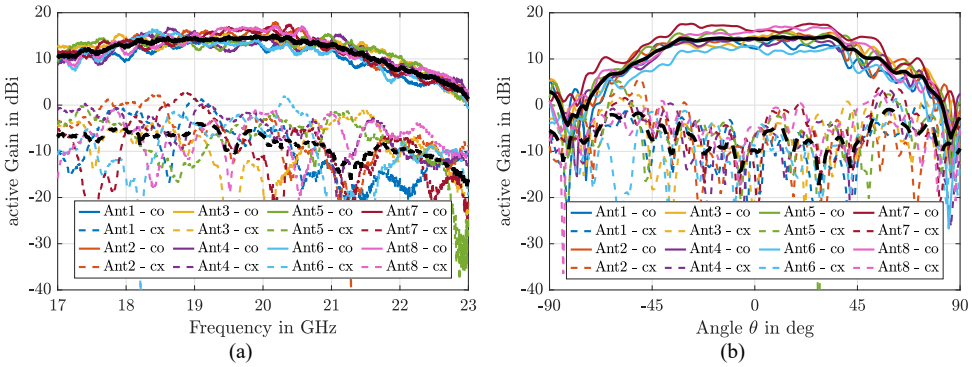

Figure 9.7: Measurement results of the active embedded elements. (a) Cross- and co-polarized realized gain values of the individual elements at $\theta = 0$ as a function of frequency. (b) Cross- and co-polarized realized gain values of the individual embedded antenna elements as a function of the angle θ for two orthogonal azimuth cuts. Bold black curves correspond to the averaged beampattern values over all elements.

Active via Anokiwave AWMF 0197 IC

The measured cross- and co-polarized realized gain is plotted as a function of frequency in Figure 9.7a and at 20 GHz as a function of the angle θ for two orthogonal azimuth cuts in Figure 9.7b.

9.4.4. Array measurements

A beamforming measurement with a uniform excitation is carried out. Calibration weights for the individual channels of the Anokiwave IC are simply extracted from the embedded element measurements at $\theta = 0$ and 20 GHz. The IC provides five- and six-bit digital control for attenuation and phase, respectively, on each channel, implying a discretization error in the individual channel weights. Optimal and configured individual channel gain values and phase shifts are depicted in Figure 9.9a. Furthermore, Figures 9.9d and 9.9e depict the resulting combined beampattern measurements for steering angles 0° and 30° respectively.

9.5. Discussion

9.5.1. Single element

The measurement results for the single element, presented in Figure 9.5, reveal a shift in the targeted mode resonance frequencies, indicated by two local minima in the measured S_{11} parameter—one at approximately 19.5 GHz and another at approximately 22.5 GHz. While the match for the first resonance is excellent, the matching for the upper mode is slightly sub-optimal. This resonance shift is likely caused by a slight under-extrusion during the printing of the DRA periodic structure, leading to a lower-than-targeted effective permittivity and, consequently, a shift to higher frequencies. This effect also impacts the feed network performance, which was optimized based on the targeted effective permittivity. Additionally, tolerances in the print process contribute to the observed deviations from the desired performance. The far-field results generally align well with the simulations, though increased

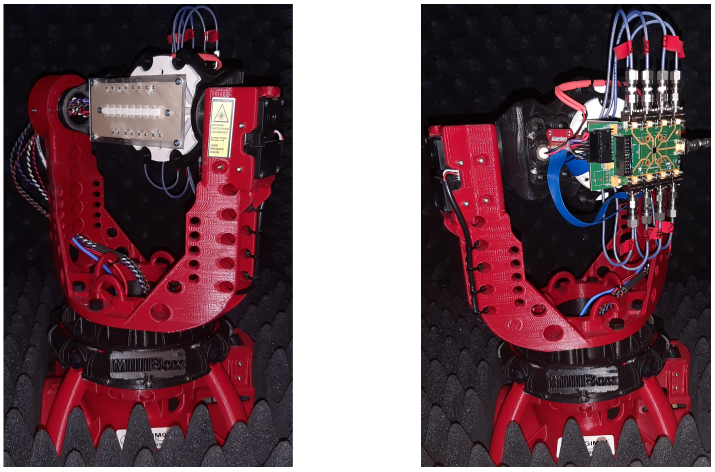

(a) (b)

Figure 9.8: The linear dielectric resonator phased array prototype is mounted on the Millibox positioner (a), with individual antenna elements connected to the inputs of the Anokiwave AWMF0197 beamformer IC (b).

deviations are noted at high θ angles, which can be attributed to interference from the millibox positioner at these angles. A slight reduction in realized gain, observed in Figure 9.5, is likely due to additional losses from the SMA connector, which were not accounted for in the simulations.

9.5.2. Embedded elements

The input reflection coefficient of the embedded elements, as shown in Figure 9.6, generally exhibits the same upward shift in resonances as observed with the single element. Notably, elements 7 and 8 show more significant deviations, with element 7 displaying a pronounced second resonance at approximately 24.5 GHz. For the purposes of this discussion, we focus on results at 20 GHz, where all elements exhibit an input reflection coefficient of less than -10 dB.

Realized gain values exhibit a mean of $\approx 3 \pm 1\text{dB}$ in co- and $\approx -20 \pm 5\text{dB}$ in cross-polarized components at $\theta = 0$, which is a significant reduction in the co-polarized component compared to the values obtained in the single element. The reason for the reduced gain at $\theta = 0$ is a broadening of the embedded beam pattern through mutual coupling compared to the single element from a half-power beamwidth (HPBW) of 48° in the single element to 82° in the averaged embedded pattern. Individual measured values of the impedance bandwidth and HPBW in Table 9.4 show a degrading performance for array elements with increasing index in the array. Although this artifact might be a coincidence, it may also indicate a degradation of print performance on one side of the array due to an uneven print surface.

Similar results are obtained via the measurements where the individual antenna elements are connected to the input ports of the Anokiwave AWMF0197 evaluation board. The main difference is the increased element gain of $\approx 15.2 \pm 1.5\text{dB}$ and corresponding variations

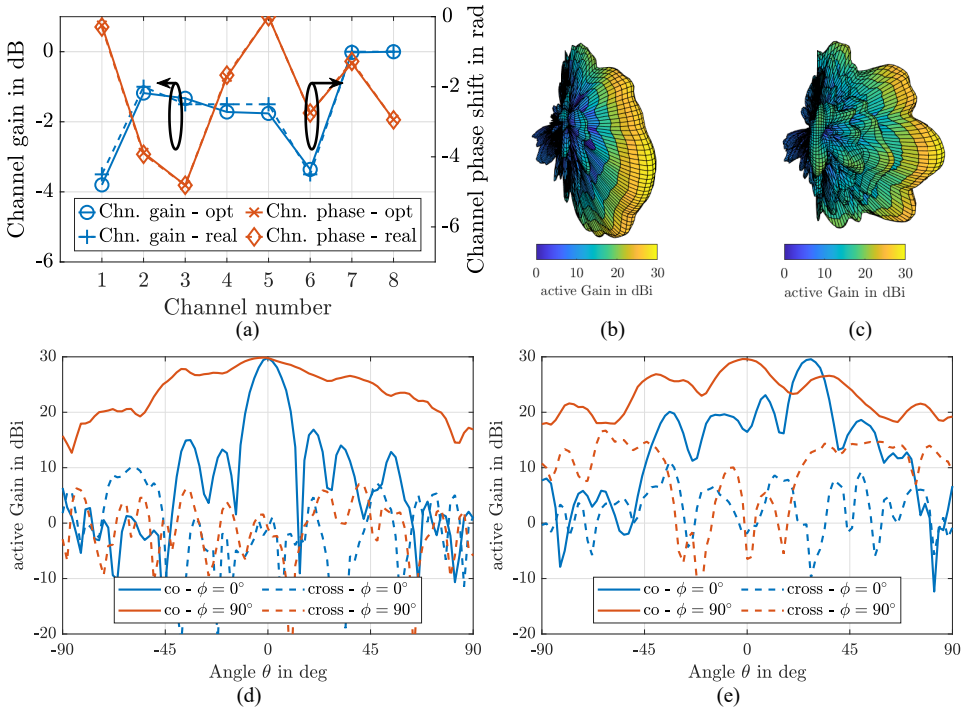

Figure 9.9: Array measurement results. (a) Extracted attenuation and phase offset calibration values from individual embedded element measurements at $\theta = 0$ and 20 GHz. (b),(d) Co- and cross-polarized realized gain values of the uniformly excited antenna array steered to $0°$ and $30°$ respectively as a function of the angle θ. (c),(e) 3D active gain patterns of the uniformly excited antenna array steered to $0°$ and $30°$ respectively.

due to the included low noise amplifier and internal channel differences.

9.5.3. Beamforming

While Figure 9.9a depicts the optimum calibration weights for uniform excitation at 20GHz, the Anokiwave AWMF0197 provides five- and six-bit digital control for attenuation and phase, respectively, on each individual channel which implies a non-optimal result for the combined antenna pattern. Nevertheless, the desired increase in directivity from combining the individual antenna elements as well the possibility of steering the beam can be observed in Figures 9.9d and 9.9e. The comparably high sidelobe level of ≈ -8dB in Figure 9.9e is most likely due to the non-optimal calibration.

9.6. Conclusion

This study demonstrates the feasibility of realizing K-band arrays for SatCom applications using low-cost additive manufacturing (AM) techniques. We designed and fabricated a multi-mode dielectric resonator phased array antenna using extrusion-based additive techniques combined with the dispensing of highly conductive silver particulate ink. The DRA

design incorporates both high- and low-permittivity extruded thermoplastic materials to engineer the effective permittivity of the DRA while integrating it into a mechanically robust holding structure for easy installation on the feed substrate. The entire manufacturing process was achieved using a low-cost system based on off-the-shelf components. A low-loss dielectric material, along with dispensed silver ink, was used to create a planar network to excite the individual antenna elements via an aperture-coupled microstrip line.

This work also addresses the particularities and challenges associated with the employed AM techniques, such as the influence of print settings on material parameters, the inherent anisotropy of the extrusion process, and dispersion in periodic dielectric lattices.

The manufactured antenna is validated through impedance and far-field measurements in both standalone and embedded configurations. Additionally, beamforming is demonstrated using a dedicated integrated circuit and a simple calibration procedure. Despite some remaining manufacturing imperfections, the fabricated design closely matches simulated and required performance criteria.

While hybrid manufacturing technology still requires significant advancements to reliably produce K-band components, this work highlights the substantial potential of low-cost hybrid additive techniques for mmWave applications. The results suggest a promising future for these technologies in the development of advanced antenna systems.

10

Conclusions and Outlook

This dissertation provides a comprehensive framework for the application of additive manufacturing in high-frequency electromagnetic devices. In particular, it carefully investigates challenges in the additive manufacturing of RF devices, extends foundations of effective dielectric theory to 3D printed materials and develops new solutions for a range of RF devices based on usage of engineered heterogeneous dielectrics and hybrid dielectric-conducting structures. A comprehensive review of the relevant literature in Chapter 2 identified six significant research gaps in the field, leading to the formulation of corresponding research questions (RQs). The theoretical foundation and methodology used to address these questions are outlined in Chapter 3.

10.1. Summary of Research Questions

The individual questions are repeated, their respective answers are presented, and the novelties of the work are highlighted below.

RQ-1: Homogenization and Characterization of AM Dielectric Crystals

What are the critical factors to consider when studying the effective dielectric material properties of additive manufactured periodic lattices, and what are suitable methods for homogenization and characterization?

This work identifies manufacturing-induced anisotropy and frequency dispersion as the two most significant factors affecting the dielectric behavior of AM periodic lattices. Additionally, periodic dielectrics exhibit effective anisotropy dependent on the symmetry of the lattice. Therefore, suitable homogenization and characterization methods are identified by their capability to capture these properties. In Chapter 4, it is demonstrated that standard effective medium theories fail to capture anisotropy and dispersion but provide simple isotropic approximations. The parallel plate capacitor model enables efficient anisotropic permittivity predictions, while eigenmode and Floquet port methods accurately capture frequency-dependent dispersion at the cost of computational complexity. For experimental characterization, guided-wave and free-space transmission methods are assessed. While the guided wave method provides the benefit of smaller sample sizes, it also exhibits the drawback of limited characterization bandwidth. In contrast, free space methods can be applied over an extensive frequency range but require comparably big sample sizes to obtain accurate measurements. The guided-wave approach used in this work enables compact sample sizes and anisotropic material characterization with a specialized quadratic waveguide sample holder. This eliminates the need for multiple samples, making it a more efficient method for characterizing anisotropic dielectric materials.

This research provides the first comprehensive comparison of homogenization and characterization techniques for periodic dielectric structures, offering future engineers a valuable resource for selecting appropriate methods based on the specific constraints of AM-based devices.

RQ-2: Anisotropy in Extrusion-Based AM Dielectrics

How does the layer-by-layer build approach of extrusion-based AM affect the dielectric properties of printed parts?

As demonstrated in Chapter 5, extrusion-based AM introduces uniaxial anisotropy due to

the deposition of stacked layers created through parallel extruded lines. A parallel plate capacitor model provides a closed-form expression relating anisotropy to extrusion parameters and material permittivity. This model is validated through numerical simulations and experimental measurements, showing reasonable accuracy for materials with low to moderate permittivity.

The findings fill a critical gap in understanding how AM process parameters influence dielectric material properties, providing engineers with a predictive tool to optimize extrusion-based AM for high-frequency EM applications. This research parallels well-documented studies on mechanical anisotropy in AM parts but uniquely extends the discussion to dielectric anisotropy, a previously unexplored topic.

RQ-3: Engineering the Effective Permittivity Tensor via Lattice Symmetry
How do lattice symmetries affect the effective anisotropy of periodic dielectric structures, and can this effect be exploited to engineer the effective permittivity tensor of AM dielectric crystals systematically?
The research presented in Chapter 6 demonstrates that the symmetry of a periodic dielectric lattice directly determines its effective permittivity tensor. Applying the Neumann principle from crystallographic theory, this research demonstrates that cubic lattice symmetries result in isotropic permittivity, while lower-symmetry configurations lead to engineered anisotropy. A parametric study confirms that breaking cubic symmetry allows for precise control of uniaxial and biaxial permittivity tensors. These findings provide a systematic approach to designing dielectric structures with precise anisotropic properties. Experimental characterization of extrusion-printed dielectric crystals validates the model, with maximum relative permittivity tensor errors below 7%.

This study establishes the first systematic methodology for engineering anisotropic dielectrics using AM. It provides a fundamental understanding of how lattice symmetry affects permittivity tensors, paving the way for custom-engineered materials for advanced microwave and millimeter-wave devices.

RQ-4: Applications of Spatially Modulated Dielectric Crystals
Besides GRIN lenses, how can controlled dielectric heterogeneity via spatially modulated dielectric crystals improve existing or enable novel high-frequency EM devices?
As the ability to spatially modulate permittivity within dielectric structures is a relatively recent advancement in AM, its full range of applications is still under exploration. This work introduces two novel applications in Chapter 7, demonstrating the impact of controlled heterogeneity in electromagnetic devices.
Circularly Polarized Dielectric Resonator Antennas (DRAs)
This study explores DRAs with radial and vertical linear permittivity gradients, demonstrating significant performance enhancements compared to the homogeneous counterpart:

- Radially inhomogeneous DRAs exhibit up to 94% increased impedance bandwidth and 116% enhanced axial-ratio bandwidth compared to a homogeneous DRA.
- Vertically inhomogeneous DRAs show a 96% improvement in impedance bandwidth

and 16% improvement in axial-ratio bandwidth.

- Both inhomogeneous demonstrate significantly enhanced polarization purity, as reflected in the 3 dB axial-ratio beamwidth improvement.

Spatially Modulated Dielectric Filters
A dielectric bandpass filter is designed and fabricated within a WR90 rectangular waveguide, using engineered volumetric infill to control its frequency response. The fabricated filter approximates a 3rd-order Chebyshev bandpass response centered at 10 GHz, with a passband insertion loss of $\approx$ 0.7 dB and a steep roll-off of -0.03 dB/MHz outside the passband. This research demonstrates that spatially modulated permittivity can be used to engineer desired reflection and transmission spectra in commonly utilized waveguide equipment, enabling compact, low-loss, and fully AM dielectric waveguide components.

The presented examples establish controlled dielectric heterogeneity as a viable design strategy for high-frequency EM devices. This approach enables greater design flexibility and enhanced device performance for next-generation antennas and filters.

RQ-5: Dielectric Bandgap Materials for High-Frequency Applications
What are suitable geometries for implementing dielectric bandgap materials, and how can they be applied in high-frequency EM devices?
Photonic bandgap materials exhibiting a complete 3D bandgap, which forbid the propagation of EM waves within specific frequency ranges, remain underutilized in EM applications due to difficulties in manufacturing the intricate 3D lattices. This work investigates two fundamental bandgap structures in Chapter 8, which are comparable and easy to manufacture with AM methods. Specifically, the diamond and woodpile lattice structures are designed and analyzed using eigenmode simulations to determine their bandgap properties. Experimental validation is performed by fabricating woodpile bandgap structures using AM, with measurements confirming the predicted bandgap around 30 GHz. A dielectric rod antenna incorporating a woodpile bandgap structure is designed to demonstrate the suppression of radiation at the third harmonic frequency, demonstrating the practical utility of AM photonic crystals for high-frequency EM applications.

This research validates the feasibility of AM-fabricated dielectric bandgap materials at millimeter-wave frequencies. The ability to engineer dispersion properties with low-cost AM techniques presents new opportunities for metamaterial-based antennas, waveguides, and filters.

RQ-6: Hybrid AM for High-Frequency EM Devices
Is it possible to deploy cost-effective AM systems capable of printing both dielectric and conductive materials for high-frequency EM devices?
A significant highlight of this work is the successful development and demonstration of hybrid AM techniques for fully printed RF components, as presented in Chapter 9. To this end, a cost-effective AM system with a micro-dispensing print head for conductive ink deposition is developed using commercial off the shelf components. This system enables the simultaneous deposition of dielectric and conductive materials, making it a

viable alternative to expensive commercial AM systems. With this setup, a fully printed 4-element phased array antenna operating in the K-band (20 GHz) is fabricated. The design integrates four different materials, including printed conductors, demonstrating the feasibility of cost-effective multi-material AM for RF components. The measured results confirm strong agreement with simulated performance, proving that hybrid AM can produce high-performance phased arrays with minimal fabrication costs.

This study represents one of the first demonstrations of a fully AM phased array antenna using a cost-effective hybrid AM approach. This work lowers the entry barrier for AM-based RF device fabrication by eliminating the need for expensive multi-material printers.

As a whole, this dissertation provides a comprehensive framework for the application of additive manufacturing in high-frequency electromagnetic devices, addressing challenges in:

1. Homogenization and characterization of periodic AM dielectrics.
2. Anisotropic material properties induced by AM processes.
3. Engineering effective permittivity tensors via crystal symmetries and geometric inclusion parameters.
4. Novel applications of spatially modulated dielectrics in antennas and filters.
5. Dielectric bandgap materials for high-frequency EM applications.
6. Hybrid AM strategies for cost-effective RF device fabrication.

The findings establish AM as a transformative tool for designing and fabricating next-generation electromagnetic structures. Moving forward, further research can optimize AM processes, explore new material formulations, and extend hybrid AM capabilities to more complex RF and microwave systems. This work bridges the gap between material science, AM and high-frequency EM applications, setting the foundation for future innovations in dielectric engineering, wave manipulation, and low-cost antenna fabrication.

10.2. Proposals for Future Research

Building on the findings of this dissertation, several key areas of future research emerge that can further enhance the role of additive manufacturing (AM) in high-frequency electromagnetic (EM) applications. These directions aim to address current limitations, explore new material formulations, and develop advanced fabrication techniques for next-generation EM devices.

1. **Improved Material Development for AM-Based Devices**
    - High-Permittivity, Low-Loss Dielectric Materials: The development of printable dielectric materials with higher relative permittivity ($\varepsilon r > 10$) for miniaturization and lower loss tangent ($\tan\delta < 0.001$) is crucial for improving the efficiency of antennas, filters, and waveguides.
    - Multi-functional Materials: Investigate the co-printing of dielectric, magnetic, and phase-change materials to develop structures with tunable EM properties.
    - Conductive Ink Performance Optimization: Current conductive inks exhibit higher resistivity compared to bulk metals, limiting their efficiency in printed antennas and waveguides. Research should focus on nanoparticle-based inks with post-processing techniques to enhance conductivity.
2. **Enhanced Homogenization and Characterization Techniques for AM Dielectrics**
    - Machine Learning for Material Property Prediction: Implement data-driven approaches to predict the effective permittivity tensor and loss characteristics of AM dielectrics based on printing parameters, material composition, and structural geometry.
    - In-Situ Dielectric Characterization: Develop real-time monitoring techniques that allow on-the-fly permittivity measurement during the printing process to improve consistency and repeatability.
3. **Exploring Dynamic Periodic Dielectric Architectures**
    - Reconfigurable Dielectric Crystals: Design tunable periodic lattices using ferroelectric or liquid-crystal-infused AM structures to enable dynamically adjustable permittivity tensors.
    - Active and Nonlinear Periodic Dielectrics: Explore the integration of active components such as varactors, MEMS actuators, or optical pumping techniques to create nonlinear and switchable dielectric lattices.
4. **Advanced Applications of Spatially Modulated Dielectric Structures**
    - Compact and Ultra-Wideband Antenna Designs: Extend the use of spatially modulated permittivity profiles beyond DRAs to develop low-profile, conformal, and miniaturized antennas with improved bandwidth and efficiency.
    - Integrated RF and Optical Components: Investigate the co-design of microwave and terahertz components with optical elements to create multi-functional AM devices for wireless communication and sensing.

- Dielectric Metasurfaces: Research the use of AM-based dielectric metasurfaces for applications in beam steering, polarization conversion, and holographic imaging.

5. **Expanding the Capabilities of Hybrid Additive Manufacturing**

   - Higher-Resolution Multi-Material Printing: Improve the resolution of hybrid AM systems to sub-micron scales, enabling precise deposition of both dielectric and conductive materials for high-frequency applications.
   - 3D-Printed Phased Array Antennas with Integrated Beamforming Networks: Extend hybrid AM capabilities to fabricate fully integrated phased arrays, including embedded feeding networks and control electronics.
   - Flexible and Wearable RF Systems: Investigate the use of hybrid AM to produce conformal and flexible antennas for applications in wearable communication, biomedical sensing, and Internet of Things (IoT) devices.

6. **Integration of AM with Emerging Electromagnetic Technologies**

   - AI-Driven Electromagnetic Design Optimization: Apply deep learning and evolutionary algorithms to optimize AM-based RF structures, reducing the time needed for design iteration.
   - AM for Quantum and Terahertz Applications: Investigate the feasibility of AM techniques for terahertz photonic crystals, quantum antennas, and superconducting RF structures.
   - 3D-Printed Energy Harvesting and Wireless Power Transfer Systems: Research the development of AM-enabled rectennas and metamaterial-based wireless power transfer devices for applications in energy-efficient IoT and space-based solar power.

Future research in AM for high-frequency EM applications should focus on material innovations, advanced fabrication techniques, new periodic structures, and hybrid AM integration. By addressing these challenges, AM can become a mainstream manufacturing method for next-generation electromagnetic devices, bridging the gap between cost-effectiveness, performance, and scalability in the RF and microwave engineering community.

Bibliography

[1] J. D. Kraus, *Antennas*. McGraw-Hill, 1988. Google-Books-ID: JHEbPQAACAAJ.

[2] H. Yagi and S. Uda, "Projector of the Sharpest Beam of Electric Waves," *Proceedings of the Imperial Academy*, vol. 2, no. 2, pp. 49–52, 1926. Number: 2.

[3] C. A. Balanis, *Antenna Theory: Analysis and Design*. John Wiley & Sons, Dec. 2012. Google-Books-ID: v1PSZ48DnuEC.

[4] R. J. Mailloux, *Phased Array Antenna Handbook*. Artech House, 2005.

[5] I. J. Bahl and P. Bhartia, *Microstrip Antennas*. Artech House, 1980. Google-Books-ID: gHEeAQAAIAAJ.

[6] V. Giannini, A. I. Fernández-Domínguez, S. C. Heck, and S. A. Maier, "Plasmonic Nanoantennas: Fundamentals and Their Use in Controlling the Radiative Properties of Nanoemitters," *Chemical Reviews*, vol. 111, pp. 3888–3912, June 2011. Number: 6 Publisher: American Chemical Society.

[7] N. Engheta and R. W. Ziolkowski, *Metamaterials: Physics and Engineering Explorations*. John Wiley & Sons, Sept. 2006. Google-Books-ID: 51e0UkEuBP4C.

[8] J. A. Slotwinski, "Additive Manufacturing: The Current State of the Art and Future Potential," *Johns Hopkins APL Technical Digest*, vol. 35, no. 4, 2021. Number: 4.

[9] J. C. Najmon, S. Raeisi, and A. Tovar, "2 - Review of additive manufacturing technologies and applications in the aerospace industry," in *Additive Manufacturing for the Aerospace Industry* (F. Froes and R. Boyer, eds.), pp. 7–31, Elsevier, Jan. 2019.

[10] M. Revilla-León, M. Sadeghpour, and M. Özcan, "A Review of the Applications of Additive Manufacturing Technologies Used to Fabricate Metals in Implant Dentistry," *Journal of Prosthodontics: Official Journal of the American College of Prosthodontists*, vol. 29, pp. 579–593, Aug. 2020. Number: 7.

[11] R. Kumar, M. Kumar, J. S. Chohan, and S. Kumar, "Overview on metamaterial: History, types and applications," *Materials Today: Proceedings*, vol. 56, pp. 3016–3024, Jan. 2022.

[12] J. C. Vasco, "Chapter 16 - Additive manufacturing for the automotive industry," in *Additive Manufacturing* (J. Pou, A. Riveiro, and J. P. Davim, eds.), Handbooks in Advanced Manufacturing, pp. 505–530, Elsevier, Jan. 2021.

[13] M. U. Naseer, A. Kallaste, B. Asad, T. Vaimann, and A. Rassõlkin, "A Review on Additive Manufacturing Possibilities for Electrical Machines," *Energies*, vol. 14, p. 1940, Jan. 2021. Number: 7 Publisher: Multidisciplinary Digital Publishing Institute.

[14] T. Whittaker, S. Zhang, A. Powell, C. J. Stevens, J. Y. C. Vardaxoglou, and W. Whittow, "3D Printing Materials and Techniques for Antennas and Metamaterials: A survey of the latest advances," *IEEE Antennas and Propagation Magazine*, vol. 65, pp. 10–20, June 2023. Number: 3 Conference Name: IEEE Antennas and Propagation Magazine.

[15] A. Paolini, S. Kollmannsberger, and E. Rank, "Additive manufacturing in construction: A review on processes, applications, and digital planning methods," *Additive Manufacturing*, vol. 30, p. 100894, Dec. 2019.

[16] "ISO/ASTM 52900:2021(en), Additive manufacturing — General principles — Fundamentals and vocabulary," June 2024.

[17] M. Rafiee, R. D. Farahani, and D. Therriault, "Multi-Material 3D and 4D Printing: A Survey," *Advanced Science (Weinheim, Baden-Wurttemberg, Germany)*, vol. 7, p. 1902307, June 2020. Number: 12.

[18] A. Haleem and M. Javaid, "Additive Manufacturing Applications in Industry 4.0: A Review," *Journal of Industrial Integration and Management*, vol. 04, p. 1930001, Dec. 2019. Number: 04 Publisher: World Scientific Publishing Co.

[19] U. M. Dilberoglu, B. Gharehpapagh, U. Yaman, and M. Dolen, "The Role of Additive Manufacturing in the Era of Industry 4.0," *Procedia Manufacturing*, vol. 11, pp. 545–554, Jan. 2017.

[20] H. S. Kang, J. Y. Lee, S. Choi, H. Kim, J. H. Park, J. Y. Son, B. H. Kim, and S. D. Noh, "Smart manufacturing: Past research, present findings, and future directions," *International Journal of Precision Engineering and Manufacturing-Green Technology*, vol. 3, pp. 111–128, Jan. 2016. Number: 1.

[21] T. D. Ngo, A. Kashani, G. Imbalzano, K. T. Q. Nguyen, and D. Hui, "Additive manufacturing (3D printing): A review of materials, methods, applications and challenges," *Composites Part B: Engineering*, vol. 143, pp. 172–196, June 2018.

[22] J. Chang, J. He, M. Mao, W. Zhou, Q. Lei, X. Li, D. Li, C.-K. Chua, and X. Zhao, "Advanced Material Strategies for Next-Generation Additive Manufacturing," *Materials*, vol. 11, p. 166, Jan. 2018. Number: 1 Publisher: Multidisciplinary Digital Publishing Institute.

[23] S. Ford and M. Despeisse, "Additive manufacturing and sustainability: an exploratory study of the advantages and challenges," *Journal of Cleaner Production*, vol. 137, pp. 1573–1587, Nov. 2016.

[24] N. Divakaran, J. P. Das, A. K. P v, S. Mohanty, A. Ramadoss, and S. K. Nayak, "Comprehensive review on various additive manufacturing techniques and its implementation in electronic devices," *Journal of Manufacturing Systems*, vol. 62, pp. 477–502, Jan. 2022.

[25] S. K. Dhinesh, J. Joshua Robert, S. Tushar Nair, D. H. Sharne Moni, S. Sona Fowzeya, K. L. Senthil Kumar, M. Raghunath, and P. Nagarajan, "Recent trends in additive manufacturing of electronics devices," *Materials Today: Proceedings*, vol. 66, pp. 928–941, Jan. 2022.

[26] M. García-Vigueras, L. Polo-Lopez, C. Stoumpos, A. Dorlé, C. Molero, R. Gillard, M. García-Vigueras, L. Polo-Lopez, C. Stoumpos, A. Dorlé, C. Molero, and R. Gillard, "Metal 3D-Printing of Waveguide Components and Antennas: Guidelines and New Perspectives," in *Hybrid Planar - 3D Waveguiding Technologies*, IntechOpen, Sept. 2022.

[27] A. Sihvola, *Electromagnetic Mixing Formulas and Applications*. IET Digital Library, Jan. 1999.

[28] Z. Hashin and S. Shtrikman, "A Variational Approach to the Theory of the Effective Magnetic Permeability of Multiphase Materials," *Journal of Applied Physics*, vol. 33, pp. 3125–3131, Oct. 1962. Number: 10.

[29] G. W. Milton, "Bounds on the complex dielectric constant of a composite material," *Applied Physics Letters*, vol. 37, pp. 300–302, Aug. 1980. Number: 3.

[30] V. Markel, "Introduction to the Maxwell Garnett approximation: tutorial," *Journal of the Optical Society of America. A Optics, Image Science, and Vision*, vol. 33, pp. 1244–1256, June 2016. Number: 7 Publisher: Optical Society of America.

[31] O. Levy and D. Stroud, "Maxwell Garnett theory for mixtures of anisotropic inclusions: Application to conducting polymers," *Physical Review B*, vol. 56, pp. 8035–8046, Oct. 1997. Number: 13 Publisher: American Physical Society.

[32] J. Vasseur, "The Plane Wave Expansion Method," in *Fundamentals and Applications of Acoustic Metamaterials*, pp. 107–141, John Wiley & Sons, Ltd, 2019. Section: 5 _eprint: https://onlinelibrary.wiley.com/doi/pdf/10.1002/9781119649182.ch5.

[33] Z. Q. Ni, Z. M. Zhang, L. Han, and Y. Zhang, "Study on the convergence of plane wave expansion method in calculation the band structure of one dimensional typical phononic crystal," *Optoelectronics and Advanced Materials - Rapid Communications*, vol. 6, pp. 87–90, Feb. 2012. Number: January-February 2012 Publisher: OAM-RC.

[34] S. Burger, R. Klose, A. Schaedle, F. Schmidt, and L. W. Zschiedrich, "FEM modeling of 3D photonic crystals and photonic crystal waveguides," (San Jose, California, United States), p. 164, Mar. 2005.

[35] A. Lavrinenko, P. Borel, L. Frandsen, M. Thorhauge, A. Harpøth, M. Kristensen, T. Niemi, and H. Chong, "Comprehensive FDTD modelling of photonic crystal waveguide components," *Optics Express*, vol. 12, pp. 234–248, Jan. 2004. Number: 2.

[36] C. D. Morales, C. Morlaas, A. Chabory, R. Pascaud, M. Grzeskowiak, and G. Mazingue, "3D-printed ceramics with engineered anisotropy for dielectric resonator antenna applications," *Electronics Letters*, vol. 57, no. 18, pp. 679–681, 2021. Number: 18 _eprint: https://onlinelibrary.wiley.com/doi/pdf/10.1049/ell2.12234.

[37] R. Clarke, "A guide to the characterisation of dielectric materials at RF and microwave frequencies. | NPL Publications," June 2024.

[38] M. S. Venkatesh and G. S. V. Raghavan, "An overview of dielectric properties measuring techniques," *CANADIAN BIOSYSTEMS ENGINEERING*, vol. 47, 2005.

[39] M. D. Deshpande and K. Dudley, "Estimation of Complex Permittivity of Composite Multilayer Material at Microwave Frequency Using Waveguide Measurements," Tech. Rep. NAS 1.15:212398, May 2003. Issue: NAS 1.15:212398 NTRS Author Affiliations: NASA Langley Research Center NTRS Document ID: 20030055680 NTRS Research Center: Langley Research Center (LaRC).

[40] L. A. Bronckers and A. B. Smolders, "Broadband Material Characterization Method Using a CPW With a Novel Calibration Technique," *IEEE Antennas and Wireless Propagation Letters*, vol. 15, pp. 1763–1766, 2016.

[41] Y. Wu, D. Isakov, and P. S. Grant, "Fabrication of Composite Filaments with High Dielectric Permittivity for Fused Deposition 3D Printing," *Materials*, vol. 10, p. 1218, Oct. 2017. Number: 10 Publisher: Multidisciplinary Digital Publishing Institute.

[42] B. Khatri, K. Lappe, M. Habedank, T. Mueller, C. Megnin, and T. Hanemann, "Fused Deposition Modeling of ABS-Barium Titanate Composites: A Simple Route towards Tailored Dielectric Devices," *Polymers*, vol. 10, p. 666, June 2018. Number: 6 Publisher: Multidisciplinary Digital Publishing Institute.

[43] I. Munina, I. Grigoriev, G. O'donnell, and D. Trimble, "A Review of 3D Printed Gradient Refractive Index Lens Antennas," *IEEE Access*, vol. 11, pp. 8790–8809, 2023. Conference Name: IEEE Access.

[44] S. Keyrouz and D. Caratelli, "Dielectric Resonator Antennas: Basic Concepts, Design Guidelines, and Recent Developments at Millimeter-Wave Frequencies," *International Journal of Antennas and Propagation*, vol. 2016, pp. 1–20, 2016.

[45] E. H. Lim, Y.-M. Pan, and K. W. Leung, "Dielectric Resonator Antennas," in *Handbook of Antenna Technologies* (Z. N. Chen, D. Liu, H. Nakano, X. Qing, and T. Zwick, eds.), pp. 955–1000, Singapore: Springer, 2016.

[46] A. Petosa and A. Ittipiboon, "Dielectric Resonator Antennas: A Historical Review and the Current State of the Art," *IEEE Antennas and Propagation Magazine*, vol. 52, pp. 91–116, Oct. 2010. Number: 5 Conference Name: IEEE Antennas and Propagation Magazine.

[47] A. Desai and P. Nayeri, "An Offset-Fed Wideband 3D Printed Aperture Coupled Trapezoidal Dielectric Resonator Antenna," in *2019 IEEE International Symposium on Antennas and Propagation and USNC-URSI Radio Science Meeting*, pp. 1987–1988, July 2019. ISSN: 1947-1491.

[48] J. Przepiorowski, I. Munina, M. J. Ammann, and D. Trimble, "Fully 3D-Printed Hemispherical Dielectric Resonator Antenna for C-band Applications," in *2023 17th European Conference on Antennas and Propagation (EuCAP)*, pp. 1–4, Mar. 2023.

[49] S. Diaz, M. Diaz, E. Rajo-Iglesias, and F. Pizarro, "Circular polarized 3D-printed cylindrical DRA using parasitic dielectric helix," *Scientific Reports*, vol. 13, p. 11838, July 2023. Number: 1 Publisher: Nature Publishing Group.

[50] J. Gielis, "A generic geometric transformation that unifies a wide range of natural and abstract shapes," *American Journal of Botany*, vol. 90, pp. 333–338, Mar. 2003. Number: 3.

[51] M. Simeoni, R. Cicchetti, A. Yarovoy, and D. Caratelli, "Supershaped dielectric resonator antennas," in *2009 IEEE Antennas and Propagation Society International Symposium*, pp. 1–4, June 2009. ISSN: 1947-1491.

[52] V. Basile, M. Grande, V. Marrocco, D. Laneve, S. Petrignani, F. Prudenzano, and I. Fassi, "Design and Manufacturing of Super-Shaped Dielectric Resonator Antennas for 5G Applications Using Stereolithography," *IEEE Access*, vol. 8, pp. 82929–82937, 2020. Conference Name: IEEE Access.

[53] J. Huang, S. J. Chen, Z. Xue, W. Withayachumnankul, and C. Fumeaux, "Impact of Infill Pattern on 3D Printed Dielectric Resonator Antennas," in *2018 IEEE Asia-Pacific Conference on Antennas and Propagation (APCAP)*, pp. 233–235, Aug. 2018. ISSN: 2381-5523.

[54] P. Nayeri and G. Brennecka, "Wideband 3D-Printed Dielectric Resonator Antennas," in *2018 IEEE International Symposium on Antennas and Propagation & USNC/URSI National Radio Science Meeting*, pp. 2081–2082, July 2018. ISSN: 1947-1491.

[55] Z.-X. Xia, K. W. Leung, and K. Lu, "3-D-Printed Wideband Multi-Ring Dielectric Resonator Antenna," *IEEE Antennas and Wireless Propagation Letters*, vol. 18, pp. 2110–2114, Oct. 2019. Number: 10.

[56] Q. Lamotte, G. Mazingue, J. Bhatker, M. Romier, N. Capet, N. Delhote, C. Menudier, O. Tantot, M. Thévenot, and K. Elis, "Multi-permittivity 3D-printed Ceramic Dual-Band Circularly Polarized Dielectric Resonator Antenna for Space Applications," in *2021 15th European Conference on Antennas and Propagation (EuCAP)*, pp. 1–5, Mar. 2021.

[57] I. Ederra, I. Khromova, R. Gonzalo, N. Delhote, D. Baillargeat, A. Murk, B. E. J. Alderman, and P. de Maagt, "Electromagnetic-Bandgap Waveguide for the Millimeter Range," *IEEE Transactions on Microwave Theory and Techniques*, vol. 58, pp. 1734–1741, July 2010. Number: 7 Conference Name: IEEE Transactions on Microwave Theory and Techniques.

[58] Q. Liang, D. Li, and G. Yang, "Rapid fabrication of diamond-structured ceramic photonic crystals with graded dielectric constant and its controllable stop band properties," *Ceramics International*, vol. 39, pp. 153–157, Jan. 2013. Number: 1.

[59] Y. Chen, D. Bartzos, Y. Lu, E. Niver, M. E. Pilleux, M. Allahverdi, S. C. Danforth, and A. Safari, "Simulation, fabrication, and characterization of 3-D alumina photonic bandgap structures," *Microwave and Optical Technology Letters*, vol. 30, no. 5, pp. 305–307, 2001. Number: 5 _eprint: https://onlinelibrary.wiley.com/doi/pdf/10.1002/mop.1297.

[60] R. C. Rumpf, J. Pazos, C. R. Garcia, L. Ochoa, and R. Wicker, "3D PRINTED LATTICES WITH SPATIALLY VARIANT SELF-COLLIMATION," *Progress In Electromagnetics Research*, vol. 139, pp. 1–14, 2013.

[61] A. Bellacicca, T. Santaniello, and P. Milani, "Embedding electronics in 3D printed structures by combining fused filament fabrication and supersonic cluster beam deposition," *Additive Manufacturing*, vol. 24, pp. 60–66, Dec. 2018.

[62] R. D. Crapnell, C. Kalinke, L. R. G. Silva, J. S. Stefano, R. J. Williams, R. A. Abarza Munoz, J. A. Bonacin, B. C. Janegitz, and C. E. Banks, "Additive manufacturing electrochemistry: An overview of producing bespoke conductive additive manufacturing filaments," *Materials Today*, vol. 71, pp. 73–90, Dec. 2023.

[63] Y. Yan, M. Han, Y. Jiang, E. L. L. Ng, Y. Zhang, C. Owh, Q. Song, P. Li, X. J. Loh, B. Q. Y. Chan, and S. Y. Chan, "Electrically Conductive Polymers for Additive Manufacturing," *ACS Applied Materials & Interfaces*, vol. 16, pp. 5337–5354, Feb. 2024. Number: 5 Publisher: American Chemical Society.

[64] Y. Wang and W. Feng, *Conductive Polymers and Their Composites*. Singapore: Springer Nature, 2022.

[65] O. Ulkir, "Conductive Additive Manufactured Acrylonitrile Butadiene Styrene Filaments: Statistical Approach to Mechanical and Electrical Behaviors," *3D Printing and Additive Manufacturing*, vol. 10, pp. 1423–1438, Dec. 2023. Number: 6 Publisher: Mary Ann Liebert, Inc., publishers.

[66] F. P. Chietera, G. A. Casula, R. Colella, G. Montisci, G. Muntoni, and L. Catarinucci, "3D Printing of Antenna Conductive Elements through Fused Filament Techniques," in *2022 IEEE 12th International Conference on RFID Technology and Applications (RFID-TA)*, pp. 47–50, Sept. 2022.

[67] V. K. R. R, V. A. K, K. P. S, and S. P. Singh, "Conductive silver inks and their applications in printed and flexible electronics," *RSC Advances*, vol. 5, pp. 77760–77790, Sept. 2015. Number: 95 Publisher: The Royal Society of Chemistry.

[68] B. Podsiadły, A. Skalski, and M. Słoma, "Soldering of Electronics Components on 3D-Printed Conductive Substrates," *Materials*, vol. 14, p. 3850, July 2021. Number: 14.

[69] R. Aradhana, S. Mohanty, and S. K. Nayak, "A review on epoxy-based electrically conductive adhesives," *International Journal of Adhesion and Adhesives*, vol. 99, p. 102596, June 2020.

[70] C. Bailey, S. Stoyanov, T. Tilford, and G. Tourloukis, "3D & printed electronics manufacturing strategies," in *2017 International Conference on Electronics Packaging (ICEP)*, pp. 312–315, Apr. 2017.

[71] A. Sihvola, "Metamaterials in electromagnetics," *Metamaterials*, vol. 1, pp. 2–11, Mar. 2007. Number: 1.

[72] A. Ali, A. Mitra, and B. Aïssa, "Metamaterials and Metasurfaces: A Review from the Perspectives of Materials, Mechanisms and Advanced Metadevices," *Nanomaterials*, vol. 12, p. 1027, Mar. 2022. Number: 6.

[73] R. A. Shelby, D. R. Smith, S. C. Nemat-Nasser, and S. Schultz, "Microwave transmission through a two-dimensional, isotropic, left-handed metamaterial," *Applied Physics Letters*, vol. 78, pp. 489–491, Jan. 2001. Number: 4.

[74] D. R. Smith, W. J. Padilla, D. C. Vier, S. C. Nemat-Nasser, and S. Schultz, "Composite medium with simultaneously negative permeability and permittivity," *Physical Review Letters*, vol. 84, pp. 4184–4187, May 2000. Number: 18.

[75] M. Kamran and M. Faryad, "Anti-reflection coatings of zero-index metamaterial for solar cells," *AIP Advances*, vol. 10, p. 025010, Feb. 2020. Number: 2.

[76] P. Alitalo and S. Tretyakov, "Electromagnetic cloaking with metamaterials," *Materials Today*, vol. 12, pp. 22–29, Mar. 2009. Number: 3.

[77] M. Alibakhshikenari, M. Khalily, B. S. Virdee, C. H. See, R. A. Abd-Alhameed, and E. Limiti, "Mutual Coupling Suppression Between Two Closely Placed Microstrip Patches Using EM-Bandgap Metamaterial Fractal Loading," *IEEE Access*, vol. 7, pp. 23606–23614, 2019. Conference Name: IEEE Access.

[78] X. Zhou and G. Hu, "Superlensing effect of an anisotropic metamaterial slab with near-zero dynamic mass," Apr. 2011. Issue: arXiv:1105.0001 arXiv:1105.0001.

[79] S. A. Tretyakov, "Meta-materials with wideband negative permittivity and permeability," *Microwave and Optical Technology Letters*, vol. 31, no. 3, pp. 163–165, 2001. Number: 3 _eprint: https://onlinelibrary.wiley.com/doi/pdf/10.1002/mop.1387.

[80] V. Pacheco-Peña and N. Engheta, "Temporal metamaterials with gain and loss," Aug. 2021.

[81] D. Cavallo, "Applications of Artificial Dielectric Layers for mm-Wave Antennas," in *2023 International Workshop on Antenna Technology (iWAT)*, pp. 1–4, May 2023.

[82] C. R. Garcia, J. Correa, D. Espalin, J. H. Barton, R. C. Rumpf, R. Wicker, and V. Gonzalez, "3D PRINTING OF ANISOTROPIC METAMATERIALS," *Progress In Electromagnetics Research Letters*, vol. 34, pp. 75–82, 2012.

[83] J. B. Pendry, D. Schurig, and D. R. Smith, "Controlling electromagnetic fields," *Science (New York, N.Y.)*, vol. 312, pp. 1780–1782, June 2006. Number: 5781.

[84] E. Yablonovitch, T. J. Gmitter, K. M. Leung, R. D. Meade, A. M. Rappe, K. D. Brommer, and J. D. Joannopoulos, "3-dimensional photonic band structure," *Optical and Quantum Electronics*, vol. 24, pp. S273–S283, Feb. 1992. Number: 2.

[85] J. D. Joannopoulos, S. G. Johnson, J. N. Winn, and R. D. Meade, *Photonic Crystals*. Princeton University Press, rev - revised, 2 ed., 2008.

[86] D. R. Paschotta, "photonic crystal fibers," Oct. 2024.

[87] L. Han, "1D Photonic Crystals: Principles and Applications in Silicon Photonics," in *Theoretical Foundations and Application of Photonic Crystals*, IntechOpen, Dec. 2017.

[88] M. Lončar, D. Nedeljković, T. Doll, J. Vučković, A. Scherer, and T. P. Pearsall, "Waveguiding in planar photonic crystals," *Applied Physics Letters*, vol. 77, pp. 1937–1939, Sept. 2000. Number: 13.

[89] F. Müller, A. Birner, U. Gösele, V. Lehmann, S. Ottow, and H. Föll, "Structuring of Macroporous Silicon for Applications as Photonic Crystals," *Journal of Porous Materials*, vol. 7, pp. 201–204, Jan. 2000. Number: 1.

[90] D. R. Solli and J. M. Hickmann, "Study of the properties of 2D photonic crystal structures as a function of the air-filling fraction and refractive index contrast," *Optical Materials*, vol. 33, pp. 523–526, Jan. 2011. Number: 3.

[91] S. Y. Lin, J. G. Fleming, D. L. Hetherington, B. K. Smith, R. Biswas, K. M. Ho, M. M. Sigalas, W. Zubrzycki, S. R. Kurtz, and J. Bur, "A three-dimensional photonic crystal operating at infrared wavelengths," *Nature*, vol. 394, pp. 251–253, July 1998. Number: 6690 Publisher: Nature Publishing Group.

[92] R. C. Rumpf, "Engineering the Dispersion and Anisotropy of Periodic Electromagnetic Structures," vol. 66, pp. 213–300, 2015. Book Title: Solid State Physics ISBN: 9780128034132 Publisher: Elsevier.

[93] J. L. Digaum, J. J. Pazos, J. Chiles, J. D'Archangel, G. Padilla, A. Tatulian, R. C. Rumpf, S. Fathpour, G. D. Boreman, and S. M. Kuebler, "Tight control of light beams in photonic crystals with spatially-variant lattice orientation," *Optics Express*, vol. 22, pp. 25788–25804, Oct. 2014. Number: 21 Publisher: Optica Publishing Group.

[94] J. Tribe, W. Whittow, R. Kay, and J. Vardaxoglou, "Additively manufactured heterogeneous substrates for three-dimensional control of local permittivity," *Electronics Letters*, vol. 50, no. 10, pp. 745–746, 2014. Number: 10 _eprint: https://onlinelibrary.wiley.com/doi/pdf/10.1049/el.2014.1174.

[95] T. Marc, M. Cyrille, D. Nicolas, T. Olivier, R. Maxime, and N. Capet, "A Dielectric Resonator Antenna designed with a structured dielectric material," in *2018 IEEE Conference on Antenna Measurements & Applications (CAMA)*, pp. 1–2, Sept. 2018.

[96] G. Mazingue, B. Byrne, M. Romier, and N. Capet, "3D Printed Ceramic Antennas for Space Applications," in *2020 14th European Conference on Antennas and Propagation (EuCAP)*, pp. 1–5, Mar. 2020.

[97] Z. Larimore, S. Jensen, P. Parsons, B. Good, K. Smith, and M. Mirotznik, "Use of space-filling curves for additive manufacturing of three dimensionally varying graded dielectric structures using fused deposition modeling," *Additive Manufacturing*, vol. 15, pp. 48–56, May 2017.

[98] J. W. Allen and B.-I. Wu, "Design and fabrication of an RF GRIN lens using 3D printing technology," in *Terahertz, RF, Millimeter, and Submillimeter-Wave Technology and Applications VI*, vol. 8624, pp. 164–170, SPIE, Mar. 2013.

[99] R. C. Rumpf and J. Pazos, "Synthesis of spatially variant lattices," *Optics Express*, vol. 20, pp. 15263–15274, July 2012. Number: 14 Publisher: Optica Publishing Group.

[100] D. M. Pozar, *Microwave Engineering: Theory and Techniques*. John Wiley & Sons, 2021. Google-Books-ID: PYPPEAAAQBAJ.

[101] R. E. Newnham, *Properties of Materials: Anisotropy, Symmetry, Structure*. OUP Oxford, 2005. Google-Books-ID: gSkTDAAAQBAJ.

[102] B. K. P. Scaife, *Principles of Dielectrics*. Oxford University Press, Sept. 1998.

[103] "Printer Tolerance Test von A_str8 | Kostenloses STL-Modell herunterladen," Feb. 2025.

[104] M. I. Mishchenko, J. M. Dlugach, and L. Liu, "Applicability of the effective-medium approximation to heterogeneous aerosol particles," *Journal of Quantitative Spectroscopy and Radiative Transfer*, vol. 178, pp. 284–294, July 2016.

[105] S. P. Hehenberger, A. P. T. Adithyababu, and S. Caizzone, "Effective Permittivity Measurement of 3D-Printed Dielectric Crystals," in *2022 16th European Conference on Antennas and Propagation (EuCAP)*, pp. 1–5, Mar. 2022.

[106] A. Goulas, S. Zhang, J. R. McGhee, D. A. Cadman, W. G. Whittow, J. C. Vardaxoglou, and D. S. Engstrøm, "Fused filament fabrication of functionally graded polymer composites with variable relative permittivity for microwave devices," *Materials & Design*, vol. 193, p. 108871, Aug. 2020.

[107] K. Brakora, C. Barth, and K. Sarabandi, "A plane-wave expansion method for analyzing propagation in 3D periodic ceramic structures," in *2005 IEEE Antennas and Propagation Society International Symposium*, vol. 2B, pp. 192–195 vol. 2B, July 2005. ISSN: 1947-1491.

[108] W. Setyawan and S. Curtarolo, "High-throughput electronic band structure calculations: Challenges and tools," *Computational Materials Science*, vol. 49, pp. 299–312, Aug. 2010. Number: 2.

[109] A. M. Nicolson and G. F. Ross, "Measurement of the Intrinsic Properties of Materials by Time-Domain Techniques," *IEEE Transactions on Instrumentation and Measurement*, vol. 19, pp. 377–382, Nov. 1970. Number: 4.

[110] W. Weir, "Automatic measurement of complex dielectric constant and permeability at microwave frequencies," in *Proceedings of the IEEE*, vol. 62, pp. 33–36, 1974. ISSN: 0018-9219 Issue: 1 Journal Abbreviation: Proc. IEEE.

[111] J. Baker-Jarvis, E. Vanzura, and W. Kissick, "Improved technique for determining complex permittivity with the transmission/reflection method," *IEEE Transactions on Microwave Theory and Techniques*, vol. 38, pp. 1096–1103, Aug. 1990. Number: 8.

[112] I. Waldron and S. Makarov, "Measurement of dielectric permittivity and loss tangent for bulk foam samples with suspended ring resonator method," in *2006 IEEE Antennas and Propagation Society International Symposium*, pp. 3175–3178, July 2006. ISSN: 1947-1491.

[113] S. Wilson, "Modal analysis of the 'gap effect' in waveguide dielectric measurements," *IEEE Transactions on Microwave Theory and Techniques*, vol. 36, pp. 752–756, Apr. 1988. Number: 4 Conference Name: IEEE Transactions on Microwave Theory and Techniques.

[114] A. Goulas, S. Zhang, D. A. Cadman, J. Järveläinen, V. Mylläri, W. G. Whittow, J. Y. C. Vardaxoglou, and D. S. Engstrøm, "The Impact of 3D Printing Process Parameters on the Dielectric Properties of High Permittivity Composites," *Designs*, vol. 3, p. 50, Dec. 2019. Number: 4 Publisher: Multidisciplinary Digital Publishing Institute.

[115] N. Zohdi and R. C. Yang, "Material Anisotropy in Additively Manufactured Polymers and Polymer Composites: A Review," *Polymers*, vol. 13, p. 3368, Jan. 2021. Number: 19 Publisher: Multidisciplinary Digital Publishing Institute.

[116] A. Knisely, M. Havrilla, and P. Collins, "Biaxial anisotropic sample design and rectangular to square waveguide material characterization system," in *2015 9th International Congress on Advanced Electromagnetic Materials in Microwaves and Optics (METAMATERIALS)*, pp. 346–348, Sept. 2015.

[117] J. L. Volakis, *Antenna Engineering Handbook*. New York, NY: McGraw-Hill Education, 5 ed., Dec. 2018.

[118] R. Cicchetti, E. Miozzi, and O. Testa, "A novel wideband multi-permittivity composite dielectric resonator antenna for wireless applications," in *2016 IEEE-APS Topical Conference on Antennas and Propagation in Wireless Communications (APWC)*, pp. 70–73, Sept. 2016.

[119] F. Wang, C. Zhang, H. Sun, and Y. Xiao, "Ultra-Wideband Dielectric Resonator Antenna Design Based on Multilayer Form," *International Journal of Antennas and Propagation*, vol. 2019, no. 1, p. 4391474, 2019. Number: 1 _eprint: https://onlinelibrary.wiley.com/doi/pdf/10.1155/2019/4391474.

[120] R. K. Chaudhary, K. V. Srivastava, and A. Biswas, "Variation of permittivity in radial direction in concentric half-split cylindrical dielectric resonator antenna for wideband application," *International Journal of RF and Microwave Computer-Aided Engineering*, vol. 25, no. 4, pp. 321–329, 2015. Number: 4 _eprint: https://onlinelibrary.wiley.com/doi/pdf/10.1002/mmce.20865.

[121] R. K. Chaudhary, V. V. Mishra, K. V. Srivastava, and A. Biswas, "Multi-layer multi-permittivity dielectric resonator: A new approach for improved spurious free window," in *The 40th European Microwave Conference*, pp. 1194–1197, Sept. 2010.

[122] F. P. Chietera, R. Colella, and L. Catarinucci, "Dielectric Resonators Antennas Potential Unleashed by 3D Printing Technology: A Practical Application in the IoT Framework," *Electronics*, vol. 11, p. 64, Jan. 2022. Number: 1 Publisher: Multidisciplinary Digital Publishing Institute.

[123] S. P. Hehenberger, W. Elmarissi, and S. Caizzone, "Design and Installed Performance Analysis of a Miniaturized All-GNSS Bands Antenna Array for Robust Navigation on UAV Platforms," *Sensors*, vol. 22, p. 9645, Jan. 2022. Number: 24 Publisher: Multidisciplinary Digital Publishing Institute.

[124] C. YANG, Y. XIAO, and K. W. LEUNG, "A 3D-Printed Wideband Multilayered Cylindrical Dielectric Resonator Antenna With Air Layers," in *2020 IEEE Asia-Pacific Microwave Conference (APMC)*, pp. 561–563, Dec. 2020.

[125] R. K. Mongia and P. Bhartia, "Dielectric resonator antennas—a review and general design relations for resonant frequency and bandwidth," *International Journal of Microwave and Millimeter-Wave Computer-Aided Engineering*, vol. 4, no. 3, pp. 230–247, 1994. Number: 3 _eprint: https://onlinelibrary.wiley.com/doi/pdf/10.1002/mmce.4570040304.

[126] L. Bui, D. Ball, and T. Itoh, "Broadband Millimeter-Wave E-Plane Bandpass Filters," in *1984 IEEE MTT-S International Microwave Symposium Digest*, pp. 236–237, May 1984. ISSN: 0149-645X.

[127] G. Craven and C. Mok, "The Design of Evanescent Mode Waveguide Bandpass Filters for a Prescribed Insertion Loss Characteristic," *IEEE Transactions on Microwave Theory and Techniques*, vol. 19, pp. 295–308, Mar. 1971. Number: 3 Conference Name: IEEE Transactions on Microwave Theory and Techniques.

[128] A. Aydoğan and F. Akleman, "Synthesis of dielectric-loaded waveguide filters as an inverse problem," *Applied Mathematics in Science and Engineering*, vol. 30, pp. 376–396, Dec. 2022. Number: 1 Publisher: Taylor & Francis _eprint: https://doi.org/10.1080/27690911.2022.2081321.

[129] M. Khalaj-Amirhosseini and H. Ghorbaninezhad, "Microwave impedance matching using waveguides filled by inhomogeneous dielectrics," *International Journal of RF and Microwave Computer-Aided Engineering*, vol. 19, no. 1, pp. 69–74, 2009. Number: 1 _eprint: https://onlinelibrary.wiley.com/doi/pdf/10.1002/mmce.20316.

[130] M. Khalaj-Amirhosseini, "MICROWAVE FILTERS USING WAVEGUIDES FILLED BY MULTI-LAYER DIELECTRIC," *Progress In Electromagnetics Research*, vol. 66, pp. 105–110, 2006.

[131] R. K. Cersonsky, J. Antonaglia, B. D. Dice, and S. C. Glotzer, "The diversity of three-dimensional photonic crystals," *Nature Communications*, vol. 12, p. 2543, May 2021. Number: 1 Publisher: Nature Publishing Group.

[132] F. Schwering and A. A. Oliner, "Millimeter-Wave Antennas," in *Antenna Handbook: Volume III Applications* (Y. T. Lo and S. W. Lee, eds.), pp. 1–148, Boston, MA: Springer US, 1993.

[133] R. C. Johnson, *Antenna Engineering Handbook*. McGraw-Hill, 1993. Google-Books-ID: xTSNJhVlHGgC.

[134] S. P. Hehenberger, S. Caizzone, S. Thurner, and A. G. Yarovoy, "Broadband Effective Permittivity Simulation and Measurement Techniques for 3-D-Printed Dielectric Crystals," *IEEE Transactions on Microwave Theory and Techniques*, vol. 71, pp. 4161–4172, Oct. 2023. Number: 10 Conference Name: IEEE Transactions on Microwave Theory and Techniques.

[135] D. Panusch, F. Hubert, F. Bachbauer, K. Lomakin, and G. Gold, "Additively Manufactured Helix Antenna for X-Band Applications," *2022 16th European Conference on Antennas and Propagation (EuCAP)*, pp. 1–4, Mar. 2022. Conference Name: 2022 16th European Conference on Antennas and Propagation (EuCAP) ISBN: 9788831299046 Place: Madrid, Spain Publisher: IEEE.

[136] X. Yu, M. Liang, C. Shemelya, D. A. Roberson, R. Wicker, E. MacDonald, and H. Xin, "3-D Printed Parts for a Multilayer Phased Array Antenna System," *IEEE Antennas and Wireless Propagation Letters*, vol. 17, pp. 2150–2154, Nov. 2018. Number: 11.

[137] M. Li, Y. Yang, F. Iacopi, J. Nulman, and S. Chappel-Ram, "3D-Printed Low-Profile Single-Substrate Multi-Metal Layer Antennas and Array With Bandwidth Enhancement," *IEEE Access*, vol. 8, pp. 217370–217379, 2020. Conference Name: IEEE Access.

[138] B. Niese, P. Amend, T. Frick, S. Roth, and M. Schmidt, "Fast and flexible production of mechatronic integrated devices by means of additive manufacturing," in *2016 12th International Congress Molded Interconnect Devices (MID)*, pp. 1–6, Sept. 2016.

[139] S. P. Hehenberger, S. Caizzone, and A. Yarovoy, "Low-Cost Hybrid Additive Manufacturing of a Miniaturized Dual Band Stacked Patch Antenna for GNSS Applications," in *2024 18th European Conference on Antennas and Propagation (EuCAP)*, pp. 01–05, Mar. 2024.

[140] K. H. Church, N. B. Crane, P. I. Deffenbaugh, T. P. Ketterl, C. G. Neff, P. B. Nesbitt, J. T. Nussbaum, C. Perkowski, H. Tsang, J. Castro, J. Wang, and T. M. Weller, "Multimaterial and Multilayer Direct Digital Manufacturing of 3-D Structural Microwave Electronics," *Proceedings of the IEEE*, vol. 105, pp. 688–701, Apr. 2017. Number: 4.

[141] T. P. Ketterl, Y. Vega, N. C. Arnal, J. W. I. Stratton, E. A. Rojas-Nastrucci, M. F. Córdoba-Erazo, M. M. Abdin, C. W. Perkowski, P. I. Deffenbaugh, K. H. Church, and T. M. Weller, "A 2.45 GHz Phased Array Antenna Unit Cell Fabricated Using 3-D Multi-Layer Direct Digital Manufacturing," *IEEE Transactions on Microwave Theory and Techniques*, vol. 63, pp. 4382–4394, Dec. 2015. Number: 12 Conference Name: IEEE Transactions on Microwave Theory and Techniques.

[142] N. A. Abd Rahman, M. N. Mohd Yasin, I. M. Ibrahim, M. Jusoh, S. K. Noor, M. R. Ekscalin Emalda Mary, N. Zamin, and N. Nurhayati, "A Review of Circularly Polarized Dielectric Resonator Antennas: Recent Developments and Applications," *Micromachines*, vol. 13, p. 2178, Dec. 2022. Number: 12 Publisher: Multidisciplinary Digital Publishing Institute.

[143] S. Fakhte, H. Oraizi, L. Matekovits, and G. Dassano, "Cylindrical Anisotropic Dielectric Resonator Antenna With Improved Gain," *IEEE Transactions on Antennas and Propagation*, vol. 65, pp. 1404–1409, Mar. 2017. Number: 3 Conference Name: IEEE Transactions on Antennas and Propagation.

List of Acronyms

1D	One-Dimensional
2D	Two-Dimensional
3D	Three-Dimensional
ABS	Acrylonitrile Butadiene Styrene
AI	Artificial Intelligence
AM	Additive Manufacturing
AUT	Antenna Under Test
CNC	Computerized Numerically Controlled
COC	Cyclo Olefin Copolymere
CST	Computer Simulation Technology
DRA	Dielectric Resonator Antenna
DRA-H	DRA homogeneous
DRA-IHR	DRA inhomogeneous as a function of its radial coordinate
DRA-IHZ	DRA inhomogeneous as a function of its z coordinate
EM	Electromagnetic
EMT	Effective Cedia Theories
FCC	Face Centered Cubic
FDM	Fused Deposition Modeling
FDTM	Finite-Difference Time-Domain
FEM	Finite Element Method
FFF	Fused Filament Fabrication
FOV	Field of View
GNSS	Global Navigation Satellite Systems
GRIN	Graded Index
HF	High-Rrequency
HFSS	High-Frequency structure simulator
HIPS	High-impact Polystyrene
HPBW	Half power Beamwidth
IBZ	Irreducible Brillouin Zone
IEEE	Institute of Electrical and Electronics Engineers
IC	Integrated Circuit
IoT	Internet of Things
LHCP	Left Hand Circular Polarization
MAG	Maxwell-Garnett Approximation
mmWave	Millimeter Wave
MUT	Material Under Test
PBG	Photonic band gap
PCB	Printed Circuit Board
PEC	Perfectly Electrically Conducting
PEEK	Poly-ether Ether Ketone
PhC	Photonic Crystal
PLA	Poly-lactic Acid
PWEM	Plane Wave Expansion Method
QWG	Quadratic Waveguide
RF	Radio Frequency
RHCP	Right Hand Circular Polarization
RWG	Rectangular Waveguide
SatCom	Satellite Communications
SC	Simple Cubic
SLA	Stereolithography
STL	Standard Ressellation
SVL	Spatially Varied Lattice
TO	Transformation Optics
TRL	Through-Reflect-Line
UV	Ultra-Violet

List of Symbols

π	ratio of a circles circumference to its radius
e	Eulers number
$\jmath$	imaginary unit
$\mathbf{q}$	bold letters indicating vectors
$\hat{\mathbf{q}}$	bold letters with hat indicating unit vectors
∇	nabla operator
$\cdot$	inner product
$\times$	outer product
$[\mathbf{I}]$	identity matrix
$[\cdot]$	square brackets denoting material properties presented as tensors of rank 2
$\mathbf{r}$	Spatial coordinate vector
x	cartesian coordinate - x axis
y	cartesian coordiante - y axis
z	cartesian coordinate - z axis
c_0	Speed of light
$\mathbf{E}$	electric field vector
E_x	electric field vector - x component
E_y	electric field vector - y component
E_z	electric field vector - z component
$\mathbf{D}$	electric flux vector
D_x	electric flux density vector - x component
D_y	electric flux density vector - y component
D_z	electric flux density vector - z component
ε_0	Permittivity of free space
ε_r	relative Permittivity - indicating isotropy
$[\varepsilon]$	Permittivity tensor
$[\varepsilon_\mathrm{r}]$	relative Permittivity tensor - indicating anisotropy
$\varepsilon_{\mathrm{r,xx}}$	relative Permittivity - coupling D_x and E_x
$\varepsilon_{\mathrm{r,xy}}$	relative Permittivity - coupling D_x and E_y
$\varepsilon_{\mathrm{r,xz}}$	relative Permittivity - coupling D_x and E_z
$\varepsilon_{\mathrm{r,yx}}$	relative Permittivity - coupling D_y and E_x
$\varepsilon_{\mathrm{r,yy}}$	relative Permittivity - coupling D_y and E_y
$\varepsilon_{\mathrm{r,yz}}$	relative Permittivity - coupling D_y and E_z
$\varepsilon_{\mathrm{r,zx}}$	relative Permittivity - coupling D_z and E_x
$\varepsilon_{\mathrm{r,zy}}$	relative Permittivity - coupling D_z and E_y
$\varepsilon_{\mathrm{r,zz}}$	relative Permittivity - coupling D_z and E_z
μ_0	Permeability of free space
μ_r	relative Permittivity tensor - indicating isotropy
$[\mu]$	Permeability tensor
$[\mu_\mathrm{r}]$	relative Permittivity tensor - indicating anisotropy
$\mathbf{H}$	magnetic field density vector
$\mathbf{B}$	magnetic flux density vector
$\mathbf{J}$	electric current density vector
$\mathbf{M}$	magnetic current density vector
$\mathbf{k}$	wave vector
β	Bloch wave vector
f	frequency
ω	angular frequency
λ	wavelength
λ_0	wavelength in free space
$\mathbf{a}$	crystal reference vector
$\mathbf{b}$	crystal reference vector
$\mathbf{c}$	crystal reference vector
a	crystal unit cell size
b	crystal unit cell size
c	crystal unit cell size
α	angle between crystal reference vectors $\mathbf{b}$ and $\mathbf{c}$

β	angle between crystal reference vectors **a** and **c**
γ	angle between crystal reference vectors **a** and **b**
a'	geometric extension of ellipsoidal inclusion along the x axis
b'	geometric parameter of ellipsoidal inclusion along the y axis
c'	geometric parameter of ellipsoidal inclusion along the z axis
$[\varepsilon_{\mathrm{r,m}}]$	relative Permittivity tensor - dielectric crystal manufacturing material
$[\varepsilon_{\mathrm{r,b}}]$	relative Permittivity tensor - dielectric crystal background material
$\mathbf{t}_1$	primitive lattice vector 1
$\mathbf{t}_2$	primitive lattice vector 2
$\mathbf{t}_3$	primitive lattice vector 3
$\mathbf{T}_1$	reciprocal lattice vector 1
$\mathbf{T}_2$	reciprocal lattice vector 2
$\mathbf{T}_3$	reciprocal lattice vector 3
Ψ	spatial harmonic superposition
$\bar{\Psi}$	normalized real part of a spatial harmonic superposition
ψ_{i}	amplitude of spatial harmonic with index i
$\mathbf{g}_{\mathrm{i}}$	grating vector of a spatial harmonic with index i
$g_{\mathrm{i,x}}$	x component of grating vector with index i
$g_{\mathrm{i,y}}$	y component of grating vector with index i
$g_{\mathrm{i,z}}$	z component of grating vector with index i
L	lattice extracted from spatial harmonic superposition
th	threshold parameter to extract lattice from spatial harmonic superposition
$th_{\max}$	maximum threshold parameter to result in a connected lattice from spatial harmonic superposition
D	plate separation in a parallel plate capacitor
A	area
C	capacitance
Q	charge
U	voltage
C_{x}	capacitance along x axis in the equivalent parallel plate capacitor model
C_{y}	capacitance along y axis in the equivalent parallel plate capacitor model
C_{z}	capacitance along z axis in the equivalent parallel plate capacitor model
$[\varepsilon_{\mathrm{r}}]_{\mathrm{i,j,k}}$	discretized relative permittivity tensor with i,j,k denoting index variables along The x,y,z axis
N_{x}	Number of discretized steps along the x axis
N_{y}	Number of discretized steps along the y axis
N_{z}	Number of discretized steps along the z axis
$\varepsilon_{\mathrm{r,xx,i,j,k}}$	xx component of the discretized permittivity tensor
$\varepsilon_{\mathrm{r,yy,i,j,k}}$	yy component of the discretized permittivity tensor
$\varepsilon_{\mathrm{r,zz,i,j,k}}$	zz component of the discretized permittivity tensor
C_{x}	capacitance along x axis in one discretized volume section
C_{y}	capacitance along y axis in one discretized volume section
C_{z}	capacitance along z axis in one discretized volume section
d_{x}	discretization distance along x axis
d_{y}	discretization distance along y axis
d_{z}	discretization distance along z axis
n_{eff}	effective refractive index
ω_{n}	normalized frequency
$\omega_{\mathrm{n,c}}$	normalized cutoff frequency
S_{11}	scattering parameter - reflection coefficient (self term) port 1
S_{21}	scattering parameter - transmission coefficient (mutual term) port 1 to port 2
$\varepsilon_{\mathrm{r,p}}$	print material relative permittivity
$\tan\delta_{\mathrm{p}}$	print material loss tangent
d	print setting - extrusion width
h	print setting - extrusion height
d'	modeled width of rectangular inclusion in a ”100%” dense print
h'	modeled height of rectangular inclusion in a ”100%” dense print
ε_{O}	ordinary permittivity
ε_{E}	extraordinary permittivity

η	birefringence
$\varepsilon_{\mathrm{O,CST}}$	ordinary permittivity predicted from numerical simulations
$\varepsilon_{\mathrm{E,CST}}$	extraordinary permittivity predicted from numerical simulations
$[\varepsilon_{\mathrm{r,target}}]$	effective relative permittivity tensor target as input for the material synthesis procedure
$[\varepsilon_{\mathrm{r,synth}}]$	measured effective relative permittivity tensor of the synthesized periodic dielectric lattice
$error_{\mathrm{O}}$	error on the ordinary permittivity
$error_{\mathrm{E}}$	error on the extraordinary permittivity
a_{DRA}	radius of a cylindrical dielectric resonator antenna
h_{DRA}	height of a cylindrical dielectric resonator antenna
a_{feed}	radial offset of the feed probe from the center of the cylindrical DRA
l_{feed}	length of the feed probe within the cylindrical DRA
$\tilde{\varepsilon}_{\mathrm{r,max}}$	maximum manufacturable effective relative permittivity
$\tilde{\varepsilon}_{\mathrm{r,min}}$	minimum manufacturable effective relative permittivity
f_{res}	resonance frequency
B_{Z}	impedance bandwidth
B_{AR}	axial ratio bandwidth
G_{r}	realized Gain
θ	elevation angle
ϕ	azimuth angle
$H(f)$	transfer function
$[ABCD]_{\mathrm{n}}$	chain matrix of the nth homogeneous section of a heterogeneous dielectric slab
A_{n}	A component of the chain matrix of the nth homogeneous section of a heterogeneous dielectric slab
B_{n}	B component of the chain matrix of the nth homogeneous section of a heterogeneous dielectric slab
C_{n}	C component of the chain matrix of the nth homogeneous section of a heterogeneous dielectric slab
D_{n}	D component of the chain matrix of the nth homogeneous section of a heterogeneous dielectric slab
d	thickness of a homogeneous section of a heterogeneous dielectric slab
$\beta_{\mathrm{z,n}}$	z component of the wave vector in the nth homogeneous section of a heterogeneous dielectric slab
$\eta_{\mathrm{z,n}}$	wave impedance in the nth homogeneous section of a heterogeneous dielectric slab
η_0	wave impedance of free space
$[ABCD]_{\mathrm{slab}}$	chain matrix of a heterogeneous slab
A_{slab}	A component of the chain matrix of a heterogeneous dielectric slab
B_{slab}	B component of the chain matrix of a heterogeneous dielectric slab
C_{slab}	C component of the chain matrix of a heterogeneous dielectric slab
D_{slab}	D component of the chain matrix of a heterogeneous dielectric slab
Z_{TE}	characteristic impedance of the fundamental TE mode
M	number of discrete frequencies considered in the optimization of a heterogeneous dielectric slab
err	cost function considered in the optimization of a heterogeneous dielectric slab
V	volume
n_{m}	refractive index of the manufacturing material
n_{b}	refractive index of the background material
Δn	contrast between the refractive indices of the manufacturing and background material
$\omega_{\mathrm{n,L}}$	normalized lower bandgap frequency
$\omega_{\mathrm{n,U}}$	normalized upper bandgap frequency
$\varepsilon_{\mathrm{r,rod}}$	relative permittivity of the dielectric rod
L_{rod}	length of the dielectric rod
W_{rod}	width of the dielectric rod
l_{t}	length of the radiation taper of the dielectric rod
l_{b}	length of body of the dielectric rod
l_{f}	length of the feed taper of the dielectric rod
l_{s}	length of the insert section of the dielectric rod
l_{m}	length of the matching taper of the dielectric rod
h_{t}	width of the end of the radiation taper of the dielectric rod
h_{b}	width of the body of the dielectric rod
h_{m}	height of the end of the matching taper of the dielectric rod
$f_{\mathrm{d,rod}}$	design frequency of the dielectric rod antenna
a_{RWG}	width of a rectangular waveguide
b_{RWG}	height of a rectangular waveguide

a_{GP}	lateral dimension of a groundplane
h_{sub}	height of the substrate
w_{h}	width of the DRA holding structure
h_{h}	height of the DRA holding structure
a_{MSL}	width of the microstrip line feeding the DRA
o_{MSL}	offset length of the microstrip line from the aperture feeding the DRA
l_{slot}	length of the aperture feeding the DRA
w_{slot}	width of the aperture feeding the DRA
h_{l}	height of the liner substrate used in the printing process
h_{co}	height of the conductive ink layer
d_{array}	inter-element distance in the DRA array
$[\varepsilon_{r,DRA}]$	effective permittivity tensor of the DRA

List of Publications

Journal

Topics aligned with the PhD Thesis

1. **S. P. Hehenberger**, S. Caizzone, S. Thurner and A. G. Yarovoy, ”Broadband Effective Permittivity Simulation and Measurement Techniques for 3-D-Printed Dielectric Crystals,” in IEEE Transactions on Microwave Theory and Techniques, vol. 71, no. 10, pp. 4161-4172, Oct. 2023, doi: 10.1109/TMTT.2023.3259479

2. **S. P. Hehenberger**, S. Caizzone and A. G. Yarovoy, ”Additive Manufacturing of Linear Continuous Permittivity Profiles and Their Application to Cylindrical Dielectric Resonator Antennas,” in IEEE Open Journal of Antennas and Propagation, vol. 4, pp. 373-382, 2023, doi: 10.1109/OJAP.2023.3258147

3. **S. P. Hehenberger**, S. Caizzone and A. G. Yarovoy, ”Modeling and Measurement of Dielectric Anisotropy in Material Manufactured via Fused Filament Fabrication Processes” in Material Research Bulletin, vol. 179, doi: 10.1016/j.materresbull.2024.112938.

4. **S. P. Hehenberger**, S. Caizzone and A. G. Yarovoy, ”Dielectric Rod Antenna with Third Harmonic Suppression via Photonic Crystal Bandgap Material”, in IEEE Transactions on Antennas and Propagation, vol. 73, no. 8, pp. 5044-5051, Aug. 2025, doi: 10.1109/TAP.2025.3573601.

5. **S. P. Hehenberger**, S. Caizzone, S. Thurner and A. G. Yarovoy, ”Design and Manufacturing of a Heterogeneous Dielectric Waveguide Filter at X-Band” currently under review for publication in IEEE Transactions on Devices, Packaging and Manufacturing.

6. **S. P. Hehenberger**, S. Caizzone, A. G. Yarovoy, ”Homogenization and Synthesis of Additive Manufactured Dielectric Crystals” currently being prepared for submission to the IEEE Transactions on Microwave Theory and Techniques

Topics, not aligned with PhD Thesis, but prepared during PhD

1. **S. P. Hehenberger**, W. Elmarissi, S. Caizzone, ”Design and Installed Performance Analysis of a Miniaturized All-GNSS Bands Antenna Array for Robust Navigation on UAV Platforms,” in Sensors 2022, vol. 24, no. 9645, 2022, doi: /10.3390/s22249645

2. S. Caizzone, Ramy A. Gerguis, Ernest O. Addo, **S. P. Hehenberger**, W. Elmarissi, ”Spatial Filtering of Multipath at GNSS Reference Stations Through Metamaterial-Based Absorbers” in IEEE Transactions on Aerospace and Electronic Systems, vol. 59, no. 6, pp. 7764-7771, Dec. 2023, doi: 10.1109/TAES.2023.3294896

3. **S. P. Hehenberger**, S. Caizzone, ”A Miniaturized Multi-Band Hybrid Dielectric Resonator Antenna Array for Precise and Robust GNSS Applications”, currently under review for publication IEEE Antennas and Wireless Propagation Letters

Conference

1. **S. P. Hehenberger**, A. P. T. Adithyababu and S. Caizzone, ”Effective Permittivity Measurement of 3D-Printed Dielectric Crystals,” 2022 16th European Conference on Antennas and Propagation (EuCAP), Madrid, Spain, 2022, pp. 1-5, doi: 10.23919/EuCAP53622.2022.9769370

2. **S. P. Hehenberger**, S. Caizzone, A. G. Yarovoy, ”Low Cost Additive Manufacturing of Bandgap Photonic Crystals for mmWave Applications.” 12th International Conference on Metamaterials, Photonic Crystals and Plasmonics, July 19 – 22, 2022, Torremolinos, Spain.

3. **S. P. Hehenberger**, S. Caizzone, S. Thurner and A. Yarovoy, ”Broadband Waveguide Characterization of 3D-Printed Anisotropic Dielectric Crystals,” 2023 17th European Conference on Antennas and Propagation (EuCAP), Florence, Italy, 2023, pp. 1-5, doi: 10.23919/EuCAP57121.2023.10133599

4. **S. P. Hehenberger**, S. Caizzone, and A. Yarovoy, ”Anisotropy of Additively Manufactured Dielectric Substrates via Fused Filament Fabrication Process,” 2023 12th International Conference on Microwave Materials and their Applications

5. **S. P. Hehenberger**, S. Caizzone and A. Yarovoy, ”Low-Cost Hybrid Additive Manufacturing of a Miniaturized Dual Band Stacked Patch Antenna for GNSS Applications,” 2024 18th European Conference on Antennas and Propagation (EuCAP), Glasgow, United Kingdom, 2024, pp. 01-05, doi: 10.23919/EuCAP60739.2024.10501211

6. **S. P. Hehenberger**, A. P. T. Adithyababu, S. Caizzone, Y. Aslan and A. Yarovoy, ”Hybrid Additive Manufacturing of a Dielectric Resonator Phased Array Antenna at K Band,” 2024 IEEE International Symposium on Phased Array Systems and Technology (ARRAY), Boston, MA, USA, 2024, pp. 1-8, doi: 10.1109/ARRAY58370.2024.10880394

7. **S. P. Hehenberger**, S. Caizzone, A. Yarovoy, ”Leveraging Extrusion-Based Additive Manufacturing for Integrated Antenna Applications,” 42nd ESA Antenna Workshop, Antenna Technologies for Future Space Missions, ESA-ESTEC, Noordwijk, Netherlands

8. **S. P. Hehenberger**, S. Caizzone, A. Yarovoy, ”Hybrid Additive Manufacturing of a Planar Dielectric Resonator Antenna Array at K-Band,” 2025 European Conference on Antennas and Propagation, Stockhom, Sweden

9. **S. P. Hehenberger**, S. Caizzone, A. Yarovoy, ”A 3D Printed Multi-Material GRIN Lens with an Integrated Matching Layer at 20 GHz,” 2025 European Microwave Conference, Utrecht, Netherlands

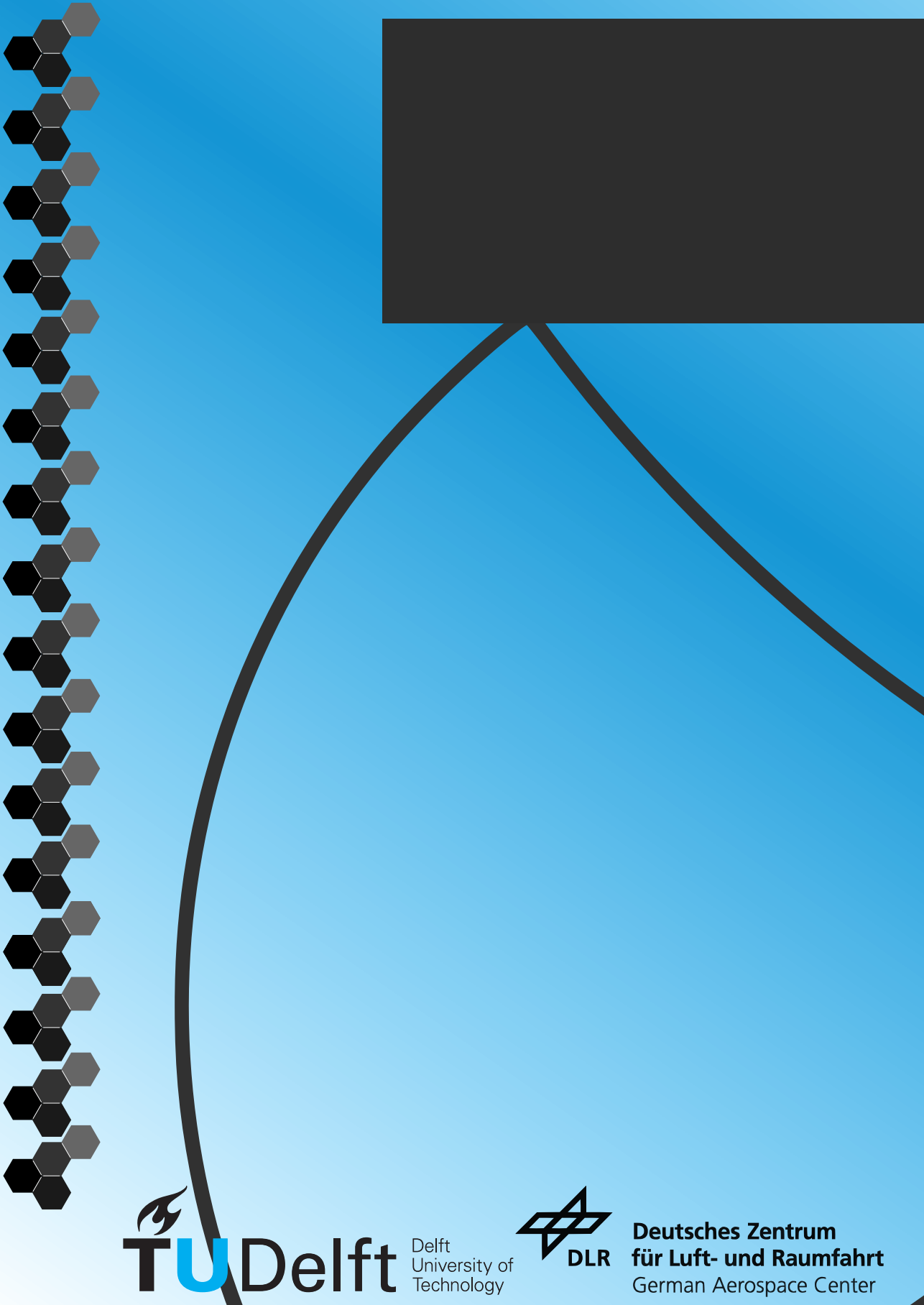

Delft University of Technology

Deutsches Zentrum für Luft- und Raumfahrt
German Aerospace Center